Title
Generalized Approach for Selecting Plasma Chemistries in Metal Etch

Permalink
https://escholarship.org/uc/item/0fq9f0q8

Author
CHEN, KUN-CHIEH

Publication Date
2016

Peer reviewed|Thesis/dissertation

UNIVERSITY OF CALIFORNIA

Los Angeles

Generalized Approach for Selecting Plasma Chemistries in Metal Etch

A dissertation submitted in partial satisfaction of the

requirements for the degree Doctor of Philosophy

in Chemical Engineering

by

Kun-Chieh Chen

2016

ABSTRACT OF THE DISSERTATION

Generalized Approach for Selecting Plasma Chemistries in Metal Etch

by

Kun-Chieh Chen
Doctor of Philosophy in Chemical Engineering
University of California, Los Angeles, 2016
Professor Jane Pei-Chen Chang, Chair

A generalized methodology, combining thermodynamic assessment and kinetic verification of surface reactions, is established in this work and shown great promise in developing effective etching chemistries for patterning complex magnetic metals in magnetic tunnel junction (MTJ) based magnetic random access memory (MRAM). To screen various chemistries, reactions between the dominant vapor phase/condensed species at various partial pressures of reactants are first considered. The volatility of the etch product is determined to aid the selection of viable etch chemistry. Selected metals (Fe, Co, Pt) and their alloys within the MRAM were studied by this generalized approach. To validate the thermodynamic calculation, films were patterned using a modified reactive ion etch process of halogen discharge with subsequent hydrogen plasma exposure. This sequential chemical processing is shown to be much more viable than a pure halogen chemistry in that, not only the etch rate of Fe, Co, and Pt were enhanced by 40%, 25%, and 20% respectively, the deteriorated coercive field strength after halogen exposure was nearly completely restored after hydrogen exposure. Surface compositional analysis by X-ray photoelectron spectroscopy confirmed chemical removal of non-volatile metal chlorides by hydrogen plasma.

To further improve the etch rate and selectivity, organic chemistry capable of generating highly volatile etching products was investigated. Through the thermodynamic calculations, acetyleacetone (acac) and hexafluoroacetyleacetone (hfac) were selected for Co and Fe etch. A series of etching experiments verified the theoretical calculation through etch rate measurement and identification of etch products. Ion beam assisted chemical etch (IBACE) using Ar was then investigated to develop a vacuum-compatible and highly effective process in patterning magnetic metal stacks. The etching of Co by alternating Ar ion and acac vapor showed an enhancement of the etch rate by approximately 180% compared to that of Ar ion alone. The etch rate of Co by alternating Ar ion and acac vapor was much greater than the sum of the two, suggesting a synergistic effect of chemical etching. The final validation of this generalized approach was to assess the chemical etching efficacy in order to avoid the sputtering effect. A sequential etch process including surface modification by oxygen plasma followed by organic vapor etch in formic acid was developed to pattern Fe, Cu, Co, Pd, and Pt, and the etch rates were 4.2, 3.7, 2.8, 1.2, 0.5 nm/cycle, respectively. A high etch selectivity of metal oxide to metal by formic acid vapor was achieved, suggesting one of the most important requirement in atomic layer etch, self-limiting reaction, was fulfilled. By controlling the thickness of oxides with oxygen plasma oxidation, the etch rates of metals could be controlled at the atomic scale. The patterned samples of Co and MTJ stack were investigated in the optimized condition, and an isotropic etching profile, high selectivity of mask to metals, and retaining of magnetic characteristic were observed, suggesting a process with solely chemical etch was realized. An anisotropic etching profile of Co was demonstrated by biasing the samples in O_2 plasma to achieve directional oxidation, and a much higher etch rate of 7.5 nm/cyc was achieved.

The dissertation of Kun-Chieh Chen is approved.

Vasilios Manousiouthakis

Yvonne Y. Chen

Richard E. Wirz

Jane Pei-Chen Chang, Committee Chair

University of California, Los Angeles

2016

iv

TABLE OF CONTENTS

LIST OF FIGURES

xv

LIST OF TABLES

xviii

ACKNOWLEDGEMENTS

Zillions of great, invaluable ideas and actions have supported me during the journey. Unfortunately, I am not able to include everyone's name due to space constraints, and for that I apologize.

My advisor, Professor Jane Chang, brought me into academia, exhibited a professional standard of research, and planted the seeds of hope in my mind that I could contribute to the plasma society. She also led me to industry and demonstrated that our research definitely promoted the progress of science and technology. A conversation we had on the day I received an award from the Semiconductor Research Corporation at Tucson will always remind me to keep moving forward. I would also like to thank my committee members. Professor Vasilios Manousiouthakis walked me through the prospectus individually with insightful comments. Professor Yvonne Chen always gave me constructive feedback. Professor King-Ning Tu helped me to improve my conversation skills. Professor Richard Wirz pointed out critical facts at my defense. Industrial sponsors have also contributed to my study. Dr. Meihua Shen at Lam Research not only supported me during the entire journey of my PhD but also offered me a job. Dr. Satyarth Suri at Intel supported my study through SRC, and we have appreciated his critical feedback.

Special thanks are due to my lab mentor, Dr. Nathan Marchack, for his advice on how to make things work out. My knowledge of science increased greatly thanks to his dedication and patience in mentoring me. If I have any accomplishments in the field of science, it must be a consequence of his guidance and mentorship. Based on my experience of working with my successors, I believe the royal lineage of the etch crew will be successful. Nicholas Altieri is eager to help teammates, and he has shown his strong willingness in taking the SRC project further. The patience of Luke Minardi drives him to the world of simulation (IMPACT), which

matches his hobby of watching Fish Center. I am genuinely inspired by Ernest Chen, who always brings up brilliant ideas in designing a new chamber (Lam), and he also shows enthusiasm to continue some of the work. Long live the etch crew!

The Chang Lab group has always been a great source of imagination, patience, and fulfillment. Dr. Taeseung "Father" Kim, a master of problem solver, was my best teammate, and together we have conquered numerous etching projects. He was the one who inspired me to execute my vision and make those dreams come true. My knowledge of science was acquired from those intelligent senior students. James Dorman passed down all the tricks of wet chemistry in the 1st quarter of my PhD as my temporary mentor. Sandy Perng not only taught me the skills of vacuum science but also sheltered me while interviewing at Intel. Vladan Jancovic was the philosopher of the lab who taught me to never give up. Captain Jea Cho, the soul of the gang, made me both optimistic and sober through his unique and insightful opinions. Without Calvin and Diana's skills at XPS, I could not have gotten as far as I did. Cyrus accompanied me throughout my PhD, and I will never forget the nights we spent working in the dry lab. Colin is the best teacher for broadening my horizons, and I already miss the parties after the group meetings. Jeff is a hardworking friend, and I want to thank him for all the discussions and instructions on new ideas. Kevin has a strong desire for knowledge, and he will guide and improve the PZT project. Ryan will be the master of the LASO battery project. It was also nice having friends outside the world of the Chang Lab, and I would like to thank the NTU gang (Candy and Paul) and Friday Night club for making life at UCLA more fascinating. Lastly, I am thankful to my mother, father, brother, sister, and grandparents, I would never have been able to get where I am today if it was not for my family. Finally, I would love to thank the person closest to my heart, my wife, Iris, for your continual love, endless support, and faith in my abilities.

VITA

2007-2010	Presidential Award 4 times through 4 years National Taiwan University Taipei, Taiwan
2010	B. S., Chemical Engineering National Taiwan University Taipei, Taiwan
2010	College Student Research Award National Science Council Taiwan
2010-2011	Political Warfare Officer Ministry of National Defense Taiwan
2011-2014	Graduate Student Researcher Department of Chemical Engineering University of California, Los Angeles
2015	Teaching Assistant Department of Chemical Engineering University of California, Los Angeles
2015	Simon Karecki Award Semiconductor Research Corporation
2015	AVS Coburn and Winters Award Finalist 62th AVS International Symposium

PUBLICATIONS

1. T. Kim*, Y. Kim*, **J. K. Chen*** and J. Chang, "A viable alternating chemical approach for patterning technology of nanoscale MRAM devices," *J. Vac. Sci. Technol. A,* Vol. 33, (2015) 021308 *Shared first author

2. T. Kim*, **J. K. Chen*** and J. Chang, "Thermodynamic assessment and experimental verification of reactive ion etching of magnetic metal elements," *J. Vac. Sci. Technol. A,* Vol. 32, No.4, (2014) 041305 *Shared first author

3. **J. K. Chen**, C. Y. Hsu, C. W. Hu and K. C. Ho, "A novel complementary electrochromic device based on Prussian blue and Poly(ProDOT-Et$_2$) with high-contrast and high-coloration

efficiency", *Sol. Energy Mater. Sol. Cells,* 2010.

4. C. W. Hu, K.M. Lee, **J. K. Chen**, C. Y. Hsu, T. H. Kuo, and K. C. Ho, "High contrast all-solid-state electrochromic device based on 2,2,6,6-tetramethyl-1-piperidinyloxy (TEMPO), heptyl viologen, and succinonitrile," Sol. Energy Mater. Sol. Cells, Vol. 99, (2012) 135.

PRESENTATIONS

1. <u>**J. K. Chen,**</u> N. Altieri, L. and J. Chang, "Generalized Approach for Selecting Plasma Chemistries in Metal Etch," AVS 62th International Symposium & Exhibition, San Jose, CA, October, (2015) (Oral Presentation - Nominated for Coburn and Winters Award)

2. <u>**J. K. Chen,**</u> N. Altieri, L. Minardi, and J. Chang, "Benefit of Modeling-Based Process Development," IMPACT program, San Jose, CA, March 6, (2015)

3. <u>**J. K. Chen,**</u> N. Altieri, M. Paine, and J. Chang, "Non-PFC plasma chemistries for patterning low-k dielectric materials," AVS 61th International Symposium & Exhibition, Baltimore, MD, November 10, (2014)

4. <u>**J. K. Chen**</u>, T. Kim, and J. Chang, "Thermodynamic approach to select viable etch chemistry for magnetic metals," Plasma Processing Science, Gordon Research Conference, Bryant University, U.S., July 26, (2014)

5. <u>**J. K. Chen**</u>, N. Marchack, and J. Chang, "Selection of non-PFC chemistries for Through-silicon via etch," 2013 AICHE Annual Meeting, San Francisco, CA, November, (2013)

6. <u>**J. K. Chen**</u>, N. Marchack, and J. Chang, "Selection of non-PFC chemistries for Through-silicon via etch," AVS 60th International Symposium & Exhibition, Long Beach, CA, October 28, (2013)

7. <u>T. Kim</u>**, J. K. Chen** (contribute equally) and J. Chang, "Thermodynamic Approach to Select Viable Etch Chemistry for Magnetic Metals," AVS 60th International Symposium & Exhibition, Long Beach, CA, October 27, (2013)

8. <u>**J. K. Chen**</u>, T. Kim and J. Chang, "Selection Generalized approaches for selecting plasma chemistries in metal etch," IMPACT program, Albany, NY, March 25, (2013)

9. N. Marchack, <u>**J. K. Chen**</u>, and J. Chang, "Predictions of the Etch Behavior of Complex Oxide Films for High-k Applications," AVS 59th International Symposium & Exhibition, Temple, FL, November 1, (2012)

10. N. Marchack, <u>**J. K. Chen**</u>, and J. Chang, "Predictions of the Etch Behavior of Complex Oxide Films for High-k Applications," 2012 AICHE Annual Meeting, Pittsburgh, PA, November (2012)

11. <u>**J. K. Chen**</u>, N. Marchack, and J. Chang, "Selection of non-PFC chemistries for Through-silicon via etch," Plasma Processing Science, Gordon Research Conference, Bryant University, U.S., July 21, (2012)

12. <u>**J. K. Chen**</u>, C. Y. Hsu, C. W. Hu and K. C. Ho, "A novel complementary electrochromic device based on Prussian blue and Poly(ProDOT-Et$_2$) with high-contrast and high-coloration efficiency," 9th International Meeting on Electrochromism (IME-9), Bordeaux, France, September 5-9, (2010)

CHAPTER 1:   INTRODUCTION

Nowadays, mobile electronics such as smart phones, tablet PC's and laptops have benefited from downscaling that allows for higher performance processors and higher capacity memory to store and process enormous amounts of data at lower cost. However, as we continue to push the envelope for micro- and nano-electronics, major challenges arise for plasma patterning. Since novel materials form the backbone of certain emerging technologies such as spintronic devices, a solution to patterning materials that are intrinsically hard to etch is required. Meanwhile, the structural complexity of high aspect ratio and multilayer features, present challenges in achieving the desired final products. Furthermore, the continual downscaling of integrated circuit (IC) devices requires precision at the atomic scale, and minor deviations from those pattern dimensions can result in unbearable degradation in device performance. Ultimately, to address these challenges, developing a new generalized approach for the patterning process is necessary. Physics- and chemistry-based modeling affords a tremendous understanding of the elementary reaction mechanisms in plasma patterning; however, the parameters necessary for kinetic modeling are sometimes difficult to obtain experimentally for novel multifunctional compounds. Developing a comprehensive framework for selecting viable chemistries in plasma patterning of magnetic metals has the potential to reduce the time and cost associated with the design of experiments. A brief introduction to the basic concepts as they apply to magnetic metals has been given, followed by the discussion of today's state-of-the-art techniques of patterning the metal stack. Finally, a thermodynamic analysis of the etching process was demonstrated with a copper etch case study, which has been applied to screening the potential plasma chemistries for patterning magnetic metals in this work.

1.1 Motivation

The conventional metal-oxide-semiconductor field-effect transistor (MOSFET) has been shrinking exponentially in dimensions over the past century. As a result, the number of transistors in a microelectronic chip has been increasing exponentially. The MOSFET is the foundation of microprocessors, memory chips, and telecommunications microcircuits. For example, there are more than 2 billion MOSFETs in a modern microprocessor, and more than 256 billion transistors in a 32 gigabyte (GB) memory. In 1965, Gordon Moore, the co-founder of Intel and Fairchild Semiconductor, published a famous paper, where he predicted that the density of transistor on a chip would double every 18 months. (Moore 1965, Moore 1998) Reducing the dimension of transistors allows an increase of density on a chip, resulting in an increase of the functionality of the circuit. Besides the benefits of performance, shrinking feature size on an integrated circuit (IC) also reduces the cost, typically 30% per linewidth generation, (Jones 2004) which shown in Figure 1-1.

Dennard and co-workers have demonstrated that scaling down the device by a factor of two, increases the switching speed twice, reduces the power dissipation by four times and improves the power-delay product by eight times, which based on the assumption of maintaining a constant electric field in the transistor. (Dennard, Gaenssle.Fh et al. 1974) However, due to the limit of the threshold voltage, the benefits from the scaling predicted by Dennard were interrupted by the short-channel effects, which arise when the distance separating the source from the drain becomes very small. From the Figure 1-2, the gate length in the current generation of microprocessor is around 30 nm, and the feature size can be reduced to 5 nm in several

technology nodes, which is only 10 times larger than the lattice parameter of a silicon crystal, resulting in much more severe of short-channel effects on MOSFET.
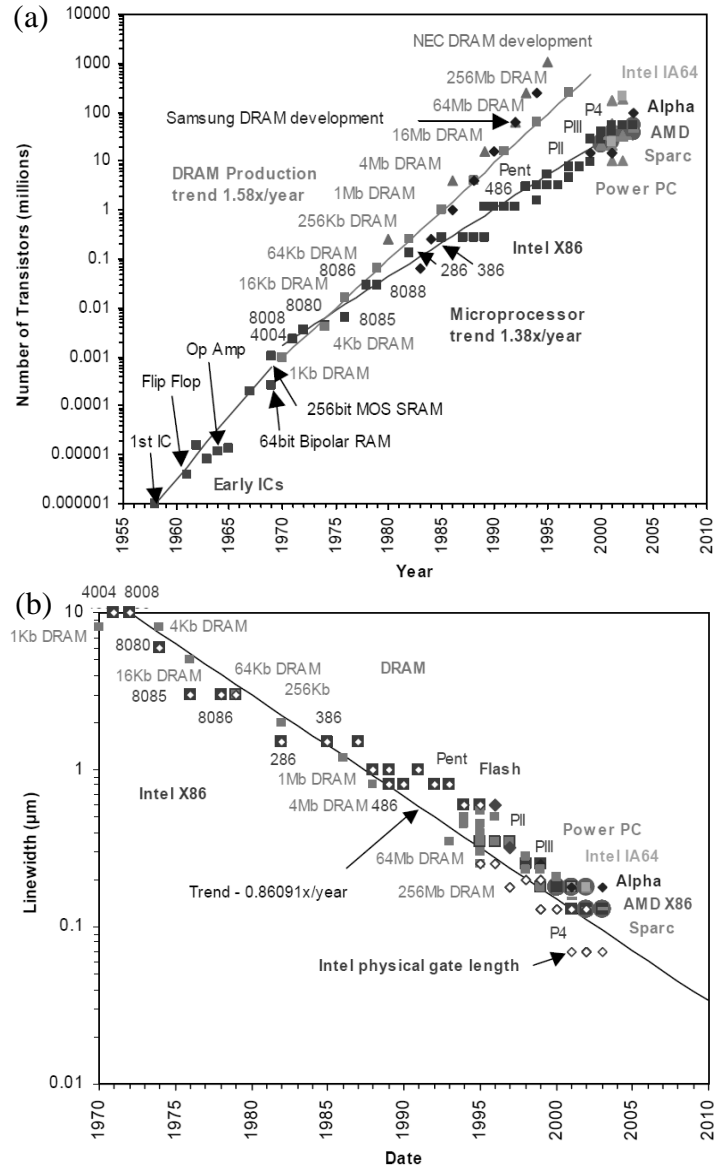
Figure 1-1 (a) Trends in number of transistors over a period of time for several DRAM and microprocessor technologies, (b) Trend in the linewidth over time. (Jones 2004)
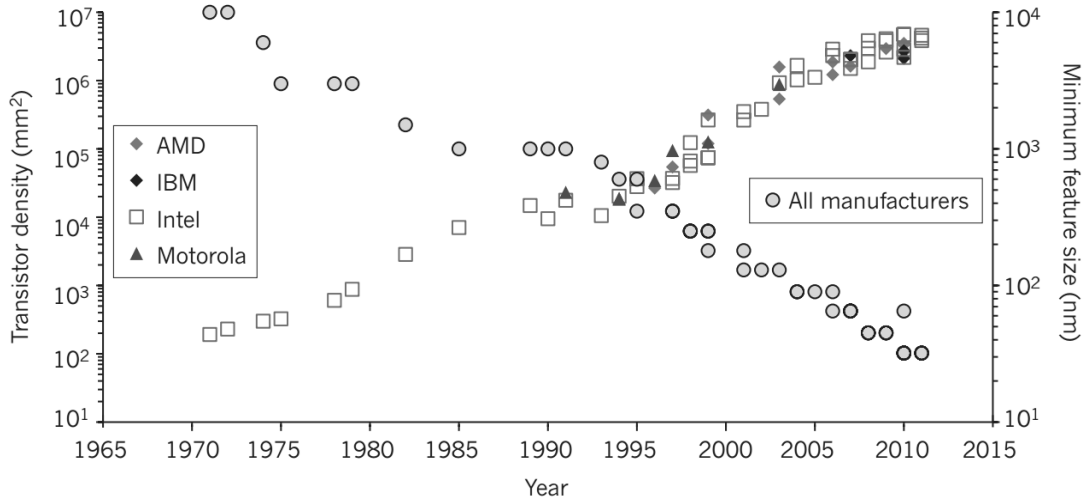
Figure 1-2 The evolution of transistor gate length (minimum feature size) and the density of transistors in microprocessors over time. Between 1970 and 2011, the gate length of MOSFETs shrank from 10μm to 28nm (yellow circles; y axis, right), and the number of transistors per square millimetre increased from 200 to over 1million (diamonds, triangles and squares show data for the four main microprocessor manufacturers; y axis, left). AMD, Advanced Micro Devices; IBM, International Business Machines. (Ferain, Colinge et al. 2011)

The configuration of MOSFET in the beginning was planar, where the gate electrode is situated on top of an insulator that covers the channel region of the device between the source and the drain, and it has evolved to multigate MOSFET, in which the shape is modified and shown in Figure 1-3. Multigate MOSFET takes advantage of a third dimension to approach the issue of short-channel effects by having several sides of the channel region covered the electrode. Figure 1-3 presents the various multigate devices, (a) FinFET, (Huang, Lee et al. 1999) (b) tri-gate MOSFET, (Doyle, Datta et al. 2003) (c) Π-gate MOSFET, (Jong-Tae, Colinge et al. 2001) (d) Ω-gate MOSFET, (Fu-Liang, Hao-Yu et al. 2002) (e) gate-all around MOSFET, (Colinge, Gao et al. 1990) and (f) bulk tri-gate MOSFET. (Cho, Choe et al. 2004, Okano, Izumida et al. 2005). Most of the devices were made using silicon-on-insulator (SOI) substrates (a-e), but bulk tri-gate with bulk silicon under MOSFET has been shown to have good short-channel effect immunity down to the sub-20-nm gate-length regimes. (Cho, Choe et al. 2004) Therefore, in

4

order to shrink the feature dimension of the transistor and avoid the short-channel effect, a complex architecture has been proposed, resulting in a complicated patterning process where silicon fins need to be patterned on a bulk silicon before the ion implantation to form the source and drain.
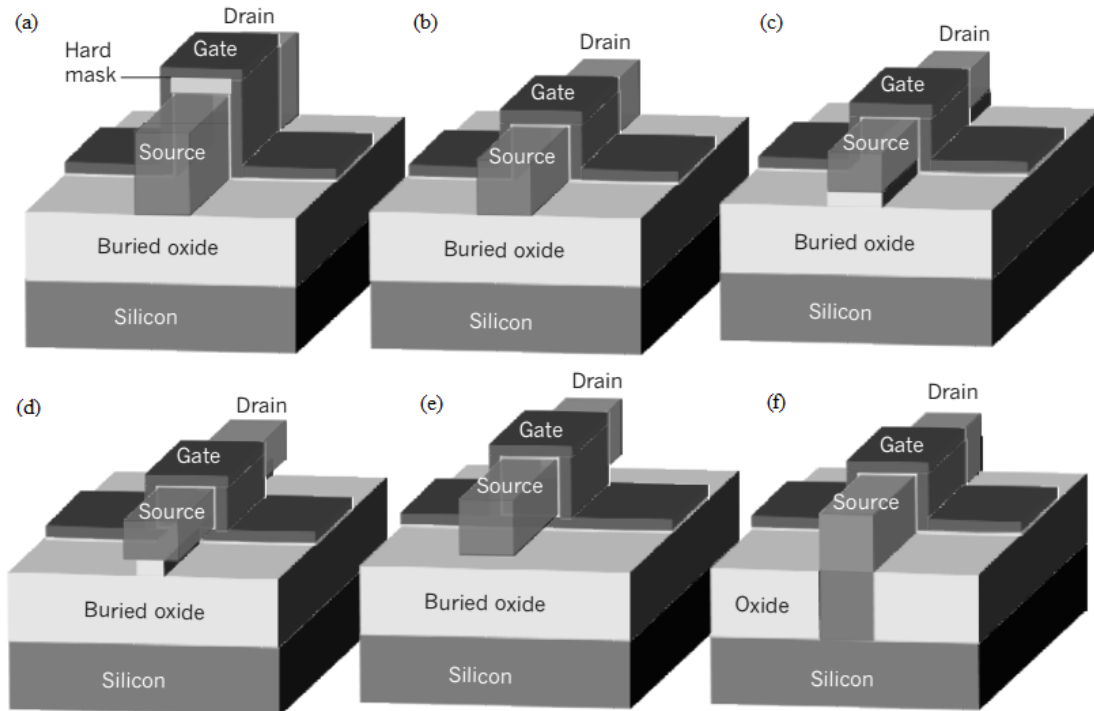
Figure 1-3 Types of multigate MOSFET. a, A silicon-on-insulator (SOI) fin field-effect transistor (FinFET). b, SOI triple-gate (or tri-gate) MOSFET. c, SOI Π-gate MOSFET. d, SOI Ω-gate MOSFET. The names Π gate and Ω gate reflect the shape of the gates. e, SOI gate-all-around MOSFET. f, A bulk tri-gate MOSFET. Gate control is exerted on the channel from three sides of the device (the top, the left and the right). In this case, there is no buried oxide underneath the device. (Ferain, Colinge et al. 2011)

Although the development of the MOSFET has advanced both microprocessor and memory device to the higher level in the past 4 decades, a shift of focus from processor to memory has slowly occurred due to a continuous growing gap between CPU and memory speeds in the computer performance as shown in Figure 1-4. (Patterson, Anderson et al. 1997) The

enhancement rate in microprocessor speed so far exceeds that of DRAM memory since speed is the main focus for processor while capacity is the goal for memory. As a result, the improvement rate of 60% per year presented in microprocessor performance is much greater than that of 10% per year of memory. A practical example is shown in Figure 1-4, considering a hypothetical computer with a processor that operates at 800 MHz (Pentium III) attached to a memory through a 100 MHz bus, meaning that the processor manipulated 800 million items per second needs to wait for the memory working at 100 million items per second.
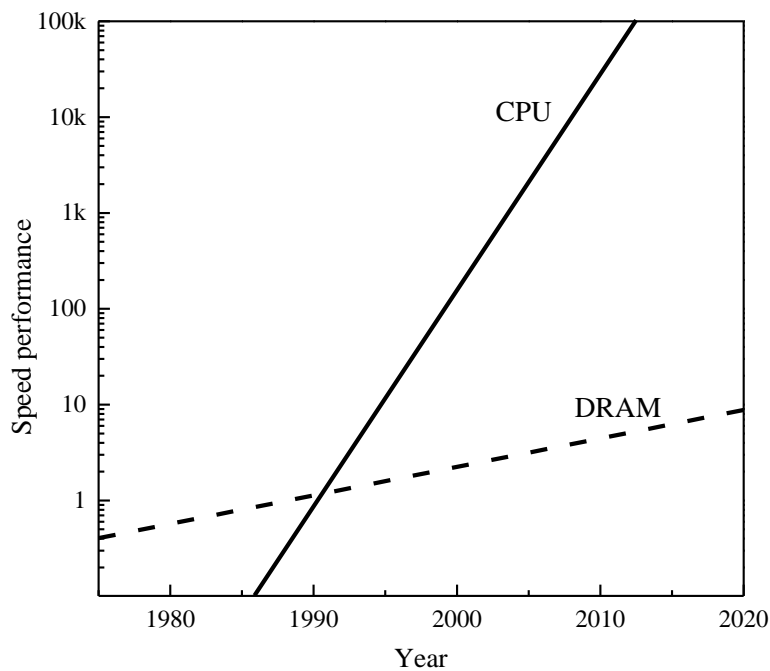
Figure 1-4 Processor-DRAM Memory Gap (latency). (Patterson, Anderson et al. 1997)

In order to shrink the gap between processor and memory, a number of solid-state memory devices such as flash, ferroelectric random access memory (FeRAM), magnetoresistive random access memory (MRAM), static random access memory (SRAM), and phase-change memory (PCM) were created. Each memory device employs one or more types of electronic

component such as diodes, resistors, and capacitors. Non-volatile flash memory was able to follow Moore's law for the past two decades, but physical limitations of read-write time, high operational energy consumption, and cell size have forced semiconductor manufacturers to develop other potential memory devices such as MRAM, FeRAM, and PCM. A comparison of these devices is shown in Table 1-1 (ITRS(2011)).

Table 1-1. Solid-state memory comparison. (ITRS(2011))

	DRAM (Embedded)	SRAM	NAND Flash	FeRAM	MRAM	PCM
Volatility	Volatile Memory			Non-Volatile Memory		
Feature size, F, (nm)	65	45	22	180	65	45
Cell Area (F^2)	12	140	4	22	20	4
Density (Gb/chip)	8	-	64	0.125	0.03	-
R/W Time(ns)	2/2	0.2/0.2	10/100	40/65	25/25	12/100
Program Energy/bit (nJ)	5	0.5	0.2	30	25	6000
Retention time	64ms	-	>10y	>10y	>10y	>10y

Magnetoresistive random access memory (MRAM) utilizes ferromagnetic storage devices to provide non-volatile memory with the high performance characteristics of short read and write times and low energy consumption. Many ideas have been explored by both academia and industry for developing the properties of MRAM materials. The main idea of MRAM is to store data by adjusting the magnetic configuration of materials to specific stable states and retrieve data by measuring the resistance of the device with a small current. The shift from dynamic random access memory (DRAM), in which data is stored by charging a capacitor, to MRAM results in three main benefits: (i) non-volatile magnetic polarization, allowing data retention; (ii) data stability despite small reading currents; (iii) lack of electron movement in the

write mode, eliminating expend ability. (Sbiaa, Meng et al. 2011) The magnetoresistance ratio (MR) is used to determine the magnetic quality of an MRAM cell and is defined as:

$$MR = \frac{R_{high} - R_{low}}{R_{low}} \tag{1.1}$$

R_{high} and R_{low} represent the resistance of the device in a high and low magnetic state, respectively. In the early years of MRAM research, the anisotropic magnetoresistance (AMR) properties of ferromagnetic alloys such as NiFe alloy showed an MR of only a few percent. AMR utilized the change of angle between the magnetization and the current to provide the change of resistance. The small resistance resulted in a small read signal that limited the development of memory devices. In the 1980s, giant magnetoresistance (GMR) was discovered by Albert Fert and Peter Grünberg, who received the 2007 Nobel Prize in physics. When the magnetic polarities of the layers of a device are oriented in the same direction, the spin-dependent scattering of minority electrons results in a small resistance. The phenomenon of GMR occurs with anti-parallel magnetization, where both majority and minority electrons are scattered and the resistance is significantly increased. These two states represent "1" and "0" respectively. The MR values achieved using GMR, 14%, were observed in multilayered metallic films of Fe/Cr superlattices at 4.2 K. (Baibich, Broto et al. 1988) Numerous studies in both industry and academia have significantly improved the magnetoresistive effect through development of tunneling magnetoresistance (TMR),

$$TMR = \frac{R_{AP} - R_P}{R_P} = \frac{2P_1P_2}{1 - P_1P_2} \tag{1.2}$$

Where R_{AP} is the electrical resistance in the anti-parallel state, R_P is the resistance in the parallel state, and P is the spin polarization of the ferromagnetic material. The spin polarization is calculated from the spin dependent density of states (DOS) at the Fermi energy. High MR values

were observed at room temperature in the development of magnetic tunnel junctions (MTJ), which provide sufficiently high read signals for MRAM devices. The main difference between GMR and TMR is the conductivity of the spacer; GMR utilizes a conductive spacer, while TMR uses an insulating spacer. In 1991, Miyazaki first observed a 2.7% MR at room temperature, and in 1994 he found 18% in junctions of iron separated by an amorphous aluminum oxide insulator. (Miyazaki and Tezuka 1995) Substantial progress has been made in improving the MR for TMR by searching for the best oxidation method to improve the AlO_x barriers. The highest reported TMR value of amorphous AlO_x-based MTJs to date is 70% with CoFeB electrodes. (Wang, Nordman et al. 2004) From Figure 1-5, magnesium oxide began gradually replacing aluminum oxide in 2000 based on theoretical work that MgO provides the best possible interface. (Butler, Zhang et al. 2001, Ikeda, Hayakawa et al. 2007), (Mathon and Umerski 2001) In 2004, Parkin et al. were able to make Fe/MgO/Fe junctions with over 200% TMR at room temperature, (Yuasa, Nagahama et al. 2004) and in 2009, effects of up to 604% TMR at room temperature were observed in junctions of CoFeB/MgO/CoFeB. (Ikeda, Hayakawa et al. 2008)
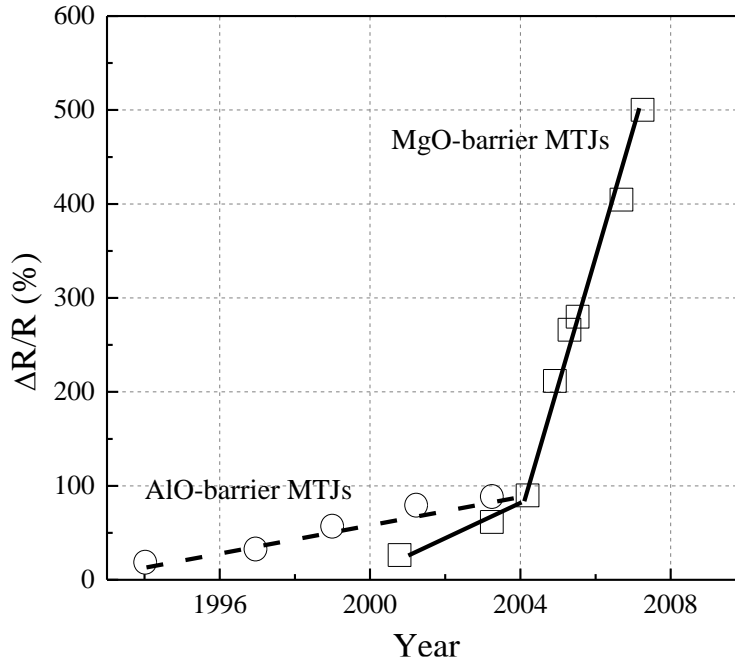
Figure 1-5 Trend in TMR ratio for Al_2O_3 and MgO barriers. (Ikeda, Hayakawa et al. 2007)

1.2 Complex Materials and Architecture for MTJ

The MTJ stack requires improvement to make it beneficial for memory applications. The evolution of tunneling magnetoresistance (TMR) structure is described in Figure 1-6 (Parkin, Jiang et al. 2003). In (a) and (b), the free layer in a magnetoresistive device is oriented based on the purpose of the device. For example, the free layer is designed to be orthogonal to the moment of the pinned layer in field sensor devices such as read heads. Conversely, in MRAM devices, the magnetic direction in free layer must be parallel or anti-parallel to that of pinned layer. Figure 1-6 (c) shows the fundamental structure of GMR and TMR stacks, which include a pinned layer, a free layer, a conduction spacer layer between the ferromagnetic layers, and an exchange-biased pinned layer. Exchange-bias is an induced magnetic anisotropy, which occurs in ferromagnetic materials when coupled to an antiferromagnetic layer. The antiferromagnetic layer

10

leads to an internal exchange field at the interface with the adjacent ferromagnetic layer whose direction is fixed by cooling from above the Neel Temperature of the antiferromagnetic layer in a magnetic field. Due to the exchange coupling, the ferromagnetic layer exhibits a unidirectional magnetic anisotropy so that its magnetic moment direction is fixed in one direction. Therefore, the external magnetic field required to rotate the moment of the ferromagnetic layer increases inversely with the thickness of the ferromagnetic layer. In the Figure 1-6 (d), the pinned layer is coupled through a Ru spacer layer, and the lower layer is pinned via exchange bias. The flux closure stabilizes the magnetic properties of the pinned layer and reduces the coupling to the free layer. In stack (e), the exchange bias layer has been removed to discourage rotation of the pinned layer. Stack (f) shows both pinned and free layers consisting of antiferromagnetic (AF)-coupled pairs, and (g) depicts a double tunnel junction element in which the current tunnels from the first pinned layer to the free layer to the second pinned element. These schematics show the complexity of the evolution of magnetically engineered MTJ stack. (Parkin, Jiang et al. 2003)

Legend:

- Magnetic Free Layer
- Magnetic Pinned Layer
- Spacer Layer – Metallic or Tunnel Barrier
- Ru Spacer Layer
- Antiferromagnetic Exchange Bias Layer
- Underlayers
- Seed Layer
- Substrate

(a) Memory – free layer easy axis parallel to pinned layer moment

(b) Sensors – free layer easy axis perpendicular to pinned layer moment in xy plane

(c) Exchange-biased pinned layer

(d) Flux-closed "Artifical Antiferromagnet" Exchange-biased pinned layer

(e) Flux-closed "Artifical Antiferromagnet" unbiased pinned layer

(f) Flux-closed "Artifical Antiferromagnet" pinned layer & Free layer

(g) **Double Junction:** Center flux-closed Free Layer structure 2 barriers 2 flux-closed exchange biased Pinned Layer structures

Figure 1-6 Evolution of magnetically engineered multilayers. (Parkin, Jiang et al. 2003)

12

1.2.1 Materials in magnetic tunnel junctions (MTJ)

Materials in magnetic tunnel junctions are transition metals such as Co and Fe and noble metals such as Pd, Pt and Au. These materials show perpendicular magnetic anisotropy (PMA) with a specific range of thicknesses and layers. For example, Broeder et al reported that Pd/Co multilayers have a higher saturation magnetization than pure Co, which is attributed to an induced ferromagnetism on Pd interfacial atoms. (Denbroeder, Donkersloot et al. 1987) Carcai et al showed that Co/Pd films with Co thickness less than 8 Å are easy to magnetize along a direction normal to the film surface. (Carcia, Meinhaldt et al. 1985) Magnetic properties like saturation magnetization and anisotropy energy can be easily controlled by tailoring the thickness and number of periods in metal stacks. Transition metals, Pd/Pt, Co/Pd, Co/Pt, and Co/Ni are commonly used multilayers in MRAM stack due to their relatively high PMA properties. Although spin valve has been studied intensively, the interest of using multilayers with PMA in MTJ devices is being vigorously studied as well. Since MTJ consists of two ferromagnets separated by a thin insulator, the AlO_x tunnel barrier has been investigated since it is easier to deposit than a crystalline MgO barrier. However, with coherent tunneling of the MgO (001) phase, MgO can theoretically provide much higher TMR values than AlO_x. One challenge researchers face is the precise control of the growth of the magnetic electrode deposited under the MgO layer. Therefore, a solution to find the best ferromagnetic materials for MgO (001) growth is crucial (Zhang, Wang et al. 2004). In 2005, Yuasa et al. observed TMR ratios up to 230% at room temperature by replacing the polycrystalline CoFe ferromagnetic electrodes surrounding the MgO layer with amorphous CoFeB, as seen in Figure 1-7. (Djayaprawira, Tsunekawa et al. 2005) In 2010, Yakushiji et al. showed that with very thin Co and Pd films –

about 0.2 nm – a TMR of 62% with ultralow resistance-area product (3.9 Ω μm^2) in MgO based junctions was achieved, enabling a development of gigabit-scale nonvolatile memory (Yakushiji, Saruya et al. 2010). The superlattice of multilayers can be annealed at high temperature to promote the formation of the MgO (001) phase. To summarize the materials in MRAM, Figure 1-8 shows the typical materials such as Co, Fe, Pd and MgO used in MTJ stack. (Slaughter 2009) The approach of patterning these materials with high fidelity and selectivity is the focal point in this work.
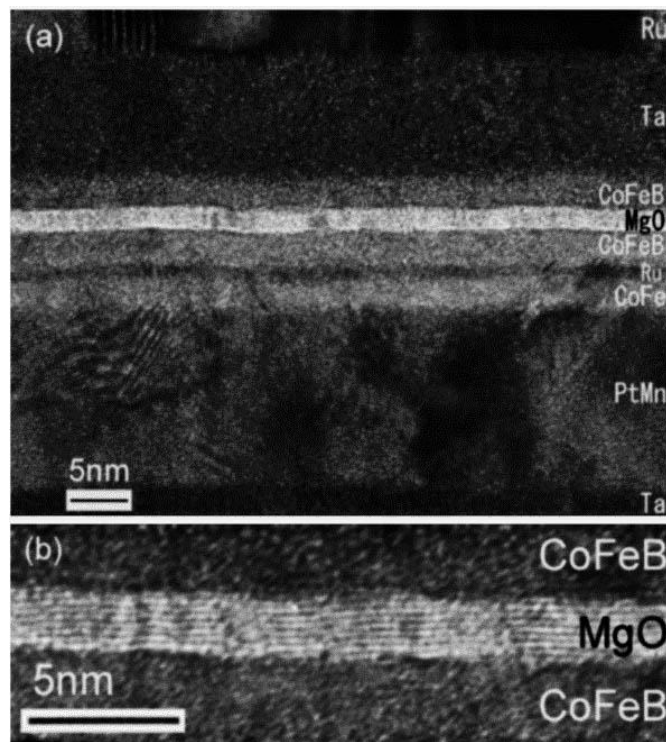
Figure 1-7 (a) Cross-section HRTEM images of CoFeB/MgO/CoFeB MTJs. (b) Enlarged cross-section HRTEM image of MTJs shown in (a). (Djayaprawira, Tsunekawa et al. 2005)

Top electrode	Top electrode		Ta
Ferromagnetic layer (Free layer)	Metal 2	⇢	NiFe, CoPd, CoFeB
	Spacer		Ru
	Metal 1	⇢	NiFe, CoPd, CoFeB
Tunnel barrier	Insulator		AlO$_x$, MgO
Ferromagnetic layer (Fixed layer)	Fixed	⇢	CoFe, CoFeB
	Spacer		Ru
	Pinned	⇢	CoFe, CoFeB
AF pinning layer	AF pinning layer	⇢	PtMn, IrMn
Bottom electrode	Bottom electrode		Ta/TaN
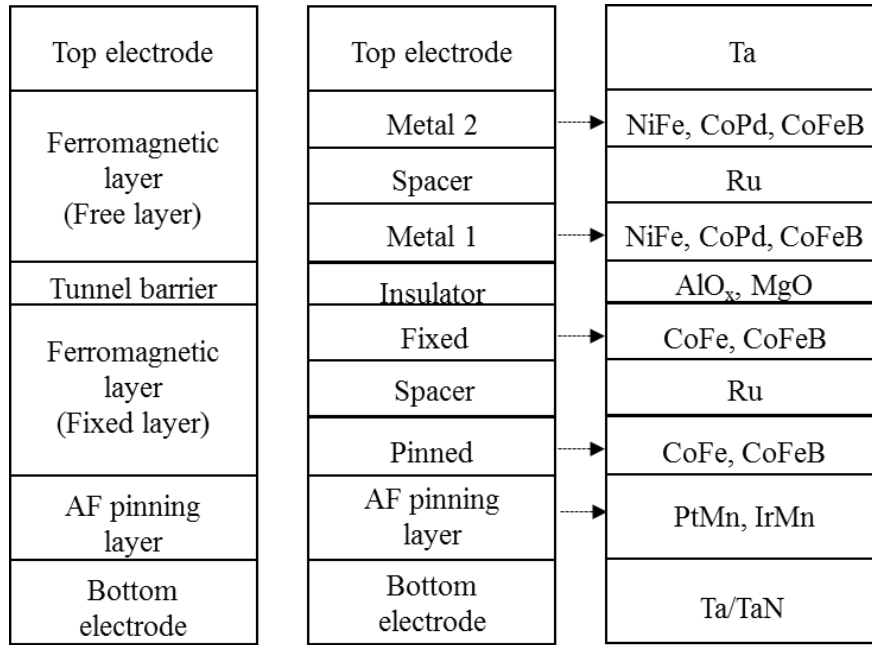
Figure 1-8 Typical materials used in MTJ stack. (Slaughter 2009)

1.3 Plasma Etching of Metal Stack

Etching is a semiconductor manufacturing technique used to remove material selectively from pre-defined locations. There are two major etching methods, wet etching and dry etching. Wet etching removes the material with chemical solutions and has several advantages including high etch rate, high throughput, and low cost. The removal of native silicon oxide on the top of a silicon wafer usually involves wet etching with hydrofluoric acid, a highly corrosive acid capable of dissolving many materials -- especially oxides (Greenwood and Earnshaw 1984). However, wet etching cannot transfer patterns with high aspect ratio or narrow line-width in very large scale integrated (VLSI) devices due to the lack of anisotropic properties. Dry etching, also called plasma etching, uses the free radicals and ions generated in plasma to remove material with anisotropic characteristics. The small linewidth achieved by dry etching is necessary to achieve

the wafer density improvements dictated by Moore's Law. Due to its preciseness, dry etching has become more important in semiconductor processes over the last few decades.

Various chemistries have been chosen in plasma etching to etch different materials such as oxides, nitrides, metals and polymers. (Kastenmeier, Matsuo et al. 1996) This section focuses on the application of plasma etching of the aforementioned MRAM materials. Ar^+ ion milling has been using widely in pattern transfer techniques for magnetic materials. However, side wall redeposition and low etch rates are two major challenges with this technique. (Hsiao 1999) Jung et al. reported a significantly higher etch rate of 5 nm/s for magnetic multilayer structures by high ion density Cl_2/Ar plasmas. (Jung, Lambers et al. 1997) Nevertheless, the chlorinated etch products of magnetic materials lack the volatility of conventional materials and tend to severely corrode the magnetic material. Therefore, non-corrosive CO/NH_3 plasma has been developed to decrease corrosion and maintain high etch rate. (Orland and Blumenthal 2005) Each of these processes are described in more detail below.

1.3.1 Ar^+ Ion Milling for Etching Magnetic Metals

Ar^+ ion beams are typically capable of etching materials in an MTJ multilayer stack with Ta capping. This capping acts as a hard mask material due to the low sputter yield compared to other magnetic materials. Features with size around 100 nm can be transferred by Ar^+ ion milling. The energy and momentum of Ar^+ is used to knock off an atom on the surface of material by exceeding the binding energy of the etched material. (Kaufman, Cuomo et al. 1982) However, R. E. Lee reported particular limitations imposed by ion-beam etching such as mask erosion and faceting, side wall re-deposition, and trenching. (Lee 1979) First, the etching rate of

Ar$^+$ ion beam is strongly dependent on the angle between incoming Ar$^+$ ion beam and the surface. The etch rates of different materials with various incidence angles of the Ar$^+$ ion beam are depicted in Figure 1-9. The angle of maximum etch rate is important due to formation of stable facets transference of etched material. (Smith, Melngail.J et al. 1973)
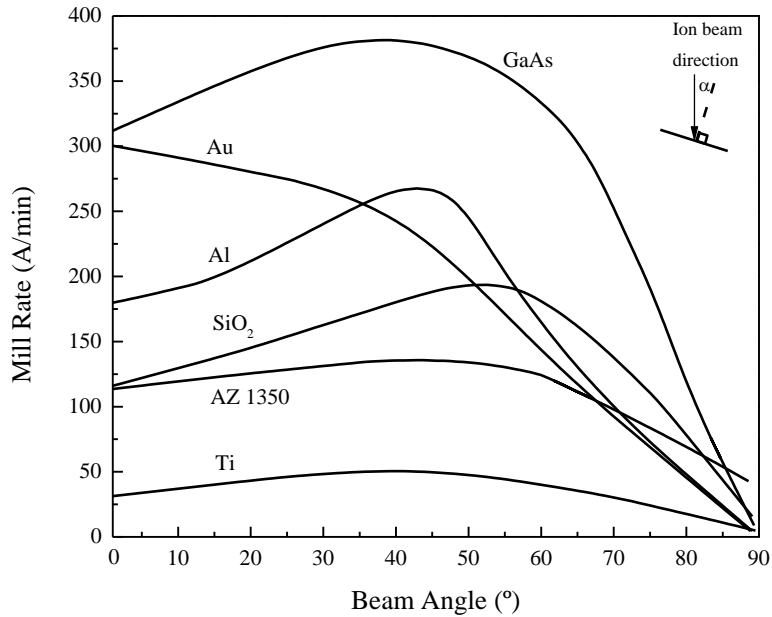
Figure 1-9 Ar$^+$ ion etch rate of different materials as function of the beam incidence angle. (Smith, Melngail.J et al. 1973)

Second, back-sputtering caused by the ion beam tends to redeposit the material around the edges of steep surface features, resulting in the interconnection of isolated regions or the prevention of complete coverage by a subsequent deposition. Figure 1-10 shows the three undesirable phenomena in ion beam etching caused by backsputtered material accumulating on the vertical sidewalls of the mask. (Gloersen 1976)

Ion beam

Back sputtering

1. Before etch

Target film

Substrate

2. After etch

3. Mask removed
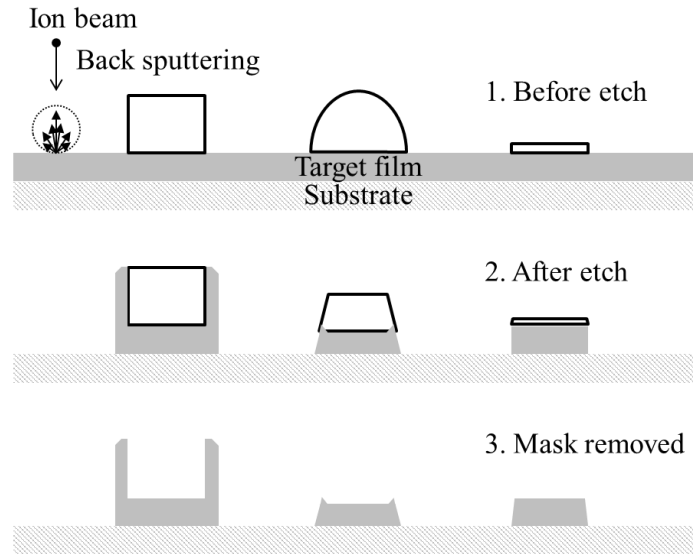
Figure 1-10 Masking strategies for ion-beam etching. (Lee 1979)

Finally, R. E. Lee developed a method to control facet and trench formation during ion beam etching by tilting the material under etching. In Figure 1-11, the sample with 20 degree tilt shows a much more uniform etch rate distribution than that of non-tilted sample. (Lee 1979)

MASK

(A)

SUBSTRATE

0° tilt

(B)

10° tilt

(C)

20° tilt

(D)
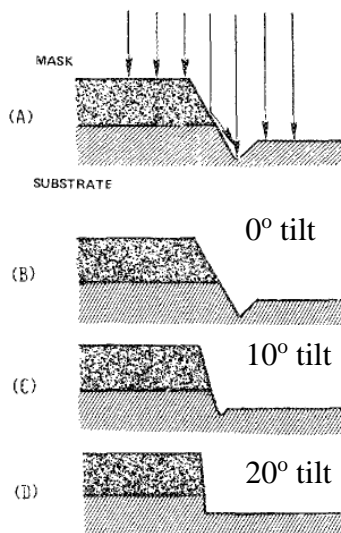
Figure 1-11 Method to control facet and trench formation during ion-beam etching. Ions incident on mask (a) cause facet formation, which leads to trenching because of the concentrated ion flux at the base. (Lee 1979)

In Figure 1-12, M. Gajek et al have demonstrated the removal of side wall deposition by Ar^{+} ion beam post etch with 80 degree tilt from sample normal. (Gajek, Nowak et al. 2012)
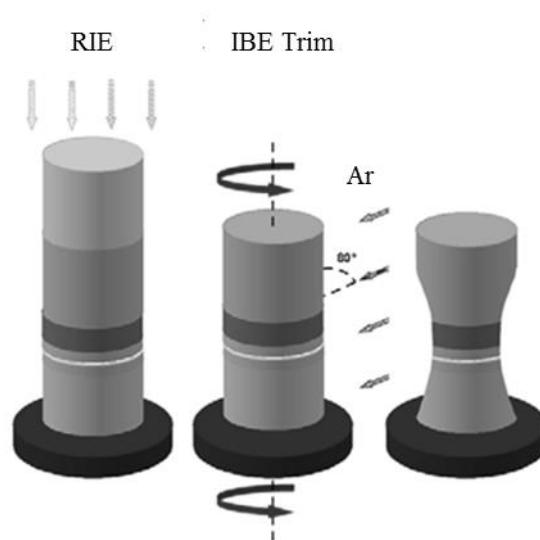
Figure 1-12 Schematic of the junction fabrication processes, from left to right: Reactive ion etching of hard mask and magnetic stack structure, photoresist strip and ion beam trimming at glancing incidence and resulting structure. (Gajek, Nowak et al. 2012)

1.3.2 Halogen-based Plasma for Etching Magnetic Metals

The first inclination towards etching stable materials is the use of highly reactive chemistry, e.g. fluorine-based chemistries. However, due to environmental considerations, there is a need to seek alternatives that are not as damaging, e.g. chlorine-based chemistries. Nevertheless, it is still important to analyze the properties of potential etch products. From the CRC handbook, Table 1-2 indicates all metal-halogenated species have high boiling points, resulting in low volatility and difficulties in etching with halogen chemistries. (Phillips and Perry 1995)

Table 1-2 Boiling point of metal fluoride, chloride and bromide. All values taken from "Handbook of Inorganic Compounds." (Phillips and Perry 1995)

Element	Fluoride : T_B (°C)	Chloride : T_B (°C)	Bromide : T_B (°C)
Co	CoF_2 : 1400	$CoCl_2$: 1049	$CoBr_2$: unknown
Fe	FeF_2 : unknown	$FeCl_2$: 1023	$FeBr_2$: decompose
	FeF_3 : unknown	$FeCl_3$: 316	
Mn	MnF_2 : 1820	$MnCl_2$:1190	$MnBr_2$: unknown
Pd	PdF_2 : unknown	$PdCl_2$: decompose	$PdBr_2$: unknown
Ni	NiF_2 : 1750	$NiCl_2$: decompose	$NiBr_2$: unknown
Ti	TiF_4 : 284 (subl.)	$TiCl_4$: 136.4	$TiBr_4$: 230
Ru	RuF_5 : 227	$RuCl_3$: >500 (subl.)	$RuBr_4$: unknown
Ta	TaF_5 : 229.5	$TaCl_5$: 242	$TaBr_5$: 348.8
W	WF_6 : 17	WCl_5 : 275.6	WBr_5 : 333
Ir	IrF_6 : 53	$IrCl_4$: non-volatile	$IrBr_3$: non-volatile

Cl_2-based plasmas have much higher etch rates in MTJ stack etching than Ar^+ ion beam etching. K. B. Jung et al. have etched NiFe and NiFeCo at >300nm/min at <80° K in a Cl_2/Ar plasma in electron cyclotron resonance (ECR) condition with post etch of in situ H_2 plasma. Although the etch products $NiCl_x$, $FeCl_x$, and $CoCl_x$ are nonvolatile, the high ion current under ECR conditions increases the efficiency of ion-assisted desorption while preventing the formation of a side wall chlorinated selvedge layer. (Jung, Lambers et al. 1997)

However, the maximum etch rate is limited by the unbalanced formation of etch products and an inefficient ion-assisted desorption. (Jung, Cho et al. 1999) Although high etch rate of MTJ materials can be achieved, the disadvantage of Cl-based plasma is the corrosion of chlorinated etch residues on the surface or in the side wall features. Y. B. Hahn et al. observed that post etch cleaning with H_2 or SF_6 plasmas or H_2O rinsing is necessary to prevent the corrosion of the metal layers from chlorinated etch residues for high density Cl_2/Ar plasma etch of NiFe, NiFeCo, TaN and CrSi. (Cho, Lee et al. 2000) In Figure 1-13, despite van Delft's prediction that high temperatures of plasma etching are needed to increase the efficiency of

desorption of etch products by Arrhenius plot, high temperature also deteriorates the magnetic properties of most soft-magnetic materials and decrease the selectivity of materials over mask (Vandelft 1995).
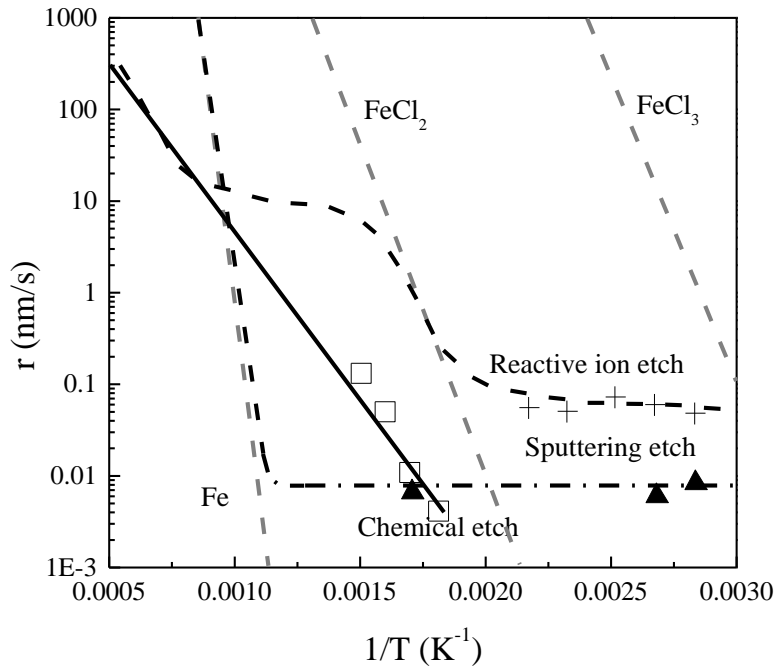
Figure 1-13 Arrhenius plot of etch rate versus temperature: experiments on F for 10 sccm 10 Pa Ar plasma 400 W rf power (triangle), 20 sccm 10 Pa HCl plasma 400 W rf power (+) and 20 sccm 10 Pa HCl resistive heating only (square). Model calculation for sputter etching (dash dot line), chemical etching (solid line), and reactive ion etching (dash line). (Vandelft 1995)

To increase the chemical etch rate instead of only physical sputtering, M. S. P. Andriesse et al. reported that a few percent of BCl_3 or $SiCl_4$ in an ICP Cl_2 plasma combines the spontaneous and ion enhanced chemical etching. Etch rates of Fe up to 300nm/min at 190°C have been observed. (Andriesse, van der Drift et al. 2001) For the etching of Co and related alloy such as CoNbZr, Andriesse et al. not only observed the 35% etch rate enhancement from the addition of BCl_3 but also 40% enhancement from the exposure of deep ultraviolet radiation. A

fast anisotropic dry etching process of CoNbZr has been developed with 300 nm/min at 220 ºC. (Andriesse, Zijlstra et al. 2000)

1.3.3 Noncorrosive Plasma for Etching Magnetic Metals

In the search for noncorrosive gas, CO seemed to be a promising alternative due to increased volatility of metal carbonyl compounds over analogous chlorinated products. However, results indicated deposition of carbonaceous materials as organic molecules broke down in plasma conditions, resulting in etch stop. Nakatani and Pearton suggested addition of NH_3 to the CO plasma in RIE to avoid the deposition of carbide. (Nakatani 1996), (Jung, Hong et al. 1999), (Jung, Hong et al. 1999) Etch rate in NH_3 plasma was approximately 20 nm/min; however, etch rates as high as 50 nm/min was observed with 15% CO addition. Orland et al. attempted to investigate CO/NH_3 plasma by mass spectral signals, however they also proved that it is difficult to assign unequivocally. (Orland and Blumenthal 2005) Therefore, CO/H_2 plasma was investigated as a tool to understand more about CO/NH_3 plasmas. Using the mass spectra in Figure 1-14, CO/H_2, CO/D_2, and $^{13}CO/D_2$ was analyzed to determine the major compounds generated in each plasma. Combining all the results, the chemical composition of this family peaks can be confirmed as CO_2H_{2-x}. Three possible chemical structures can be assigned to this composition: formic acid, a van der Waals cluster of carbon monoxide and water, and a van der Waals cluster of carbon dioxide and hydrogen. However, van der Waals bonds are too weak to exist in these conditions. It can be concluded that formic acid has been generated in the CO/H_2 plasma. Under the same analysis, the peak around m/z=55-60 can be assigned to $C_2O_2H_{4-x}$, which could be acetic acid, methylformate, hydroxyacetetadehyde, ethenediol, or dioethane. By

comparing every peak, the only possible chemical structure is ethenediol. It was proven that

volatile ethenediol complexes were formed. (Orland and Blumenthal 2005)
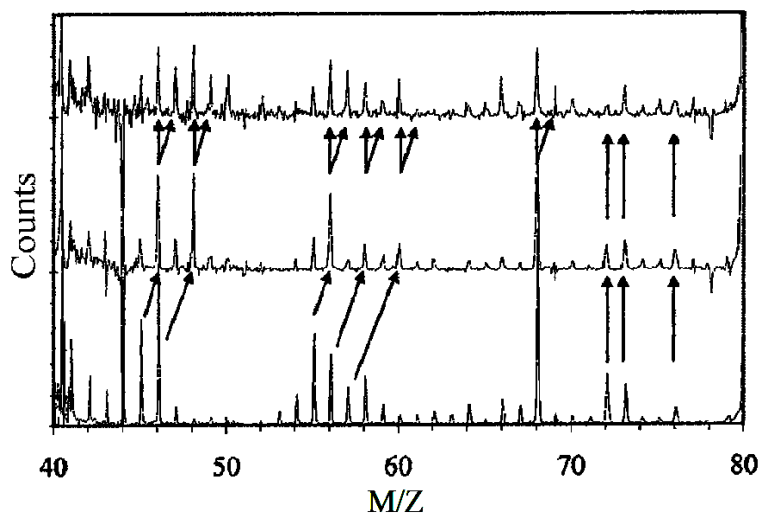
Figure 1-14 Mass spectra of $^{13}CO/D_2$ (top), $^{12}CO/D_2$ (middle), and $^{12}CO/H_2$ (bottom) plasmas. The anticipated isotopic shifts for chemical identifications have observed. (Orland and Blumenthal 2005)

Although it is difficult to image the suitable gas reactions needed to create CO_2H_{2-x} and

$C_2O_2H_{4-x}$ species from CO and H_2, the proposed surface chemical mechanism is introduced in

Figure 1-15. The method, known as the Fischer-Tropsch process, is one of the synthesis

mechanisms of hydrocarbons and other aliphatic compounds by hydrogen and carbon monoxide

on the surface of a catalytic metal (e.g., iron, cobalt, or nickel). In industrial Fischer-Tropsch

processes the products are methane, sysnthetic gasoline and waxes, and alcohols with water or

carbon dioxide produced as a by-product. With the variety of surface sites created by ion

bombardment during plasma exposure, the opportunity for a number of reaction pathways are

dependent primarily upon the neighbors of the reacting species. Formic acid (HCO_2H),

formaldehyde (HCOH), large alkanes and metal carbide are generated in the gas phase reacts with the sites to synthesize the metal formate and metal ethenediol complexes.
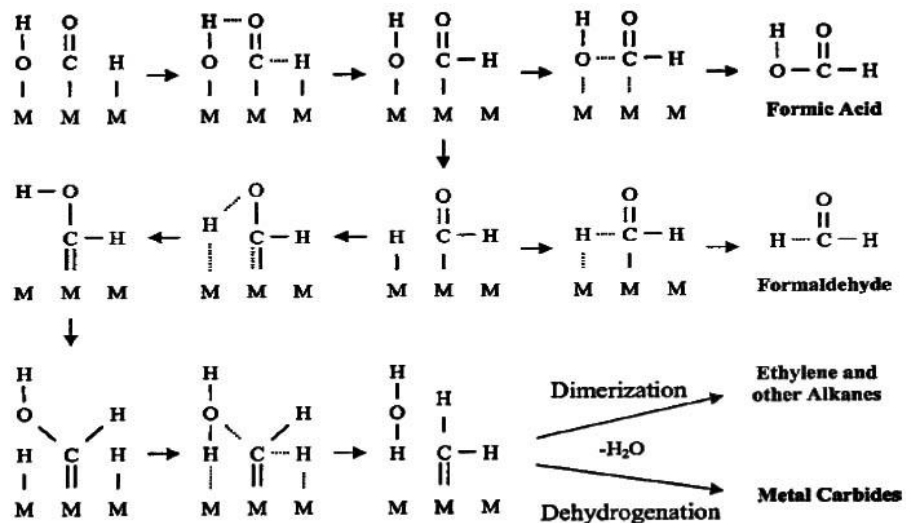
Figure 1-15 Proposed surface chemical mechanism of potential products, including formic acid, formaldehyde, large alkanes and metal carbide produced through Fischer-Tropsch reaction with CO, H_2, CO_2H_{2-x}, and $C_2O_2H_{4-x}$ as reactants. (Orland and Blumenthal 2005)

With the reference of CO/H_2 plasmas completed, the next stage was to prove the formation of a metal complex in CO/NH_3 plasma etch processes. From the mass spectroscopic results shown in Figure 1-16, the chemical processes have been found to be consistent with Fischer-Tropsch chemistry, resulting in the formation of formamide in plasma conditions. Meanwhile, the metal formamide complex has been suggested as being responsible for the etch rate enhancement in CO/NH_3 plasmas. (Orland and Blumenthal 2005)

24
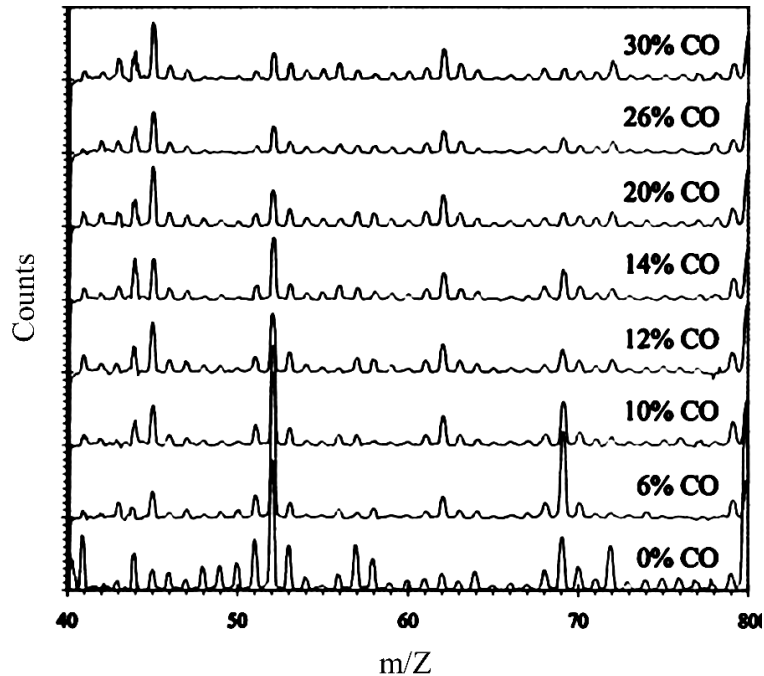
Figure 1-16 Mass spectra of CO in NH₃ plasmas over the range from m/z=40 to 80. (Orland and Blumenthal 2005)

Although the NH₃ addition enhanced the etch rate of magnetic metal in CO plasma chemically, the major etch mechanism in high density CO/NH₃ plasma continues to be physical sputtering. Therefore, the selectivity between the CoFe of the free layer over the MgO of the tunnel junction is not significant due to the strong physical component. Therefore, the discovery of a new chemistry for MTJ etching is still necessary.

1.4 Organo-metallic Chemistry for Etching Magnetic Metal

Table 1-3 illustrates the bulky volatile ligands acetylacetone (acac) (Mane, Shalini et al. 2002), 2,2,6,6-tetramethyl-3,5-heptanedionate (tmhd) (Barreca, Massignan et al. 2001), trifluoroacetylchloride (tfac), hexafluoroacetylacetone (hfac), acetic acid (Maruyama and Nakai

25

1991), as well as the nitrogen containing ligands N,N-dimethylethylenediamine (dmen) (Senocq, Urrutigoity et al. 1999), N,N-diethylethylenediamine (deen) (Senocq, Urrutigoity et al. 1999) and acetylacetonime (acim) (Gorbenko, Kaul et al. 1997) commonly used in organo-metallic precursors for atomic layer deposition (ALD). Table 1-4 lists the melting points, boiling points, and vapor pressures of organometallics with these ligands compared to conventional chlorinated compounds. The boiling points of these organometallics are much lower than those of chlorinated compounds. The vapor pressure of organo-metallic complexes are very high at 150° C, which is still in the acceptable operating temperature range to protect the magnetic properties of metals.

Table 1-3 Traditional organometallic precursors of beta diketonates for CVD process. (Orland and Blumenthal 2005)

Organics	Acetylacetonate	2,2,6,6-tetra-methyl-3,5-heptanedionate	Trifluoroacetyl-acetonate	Hexauoroacetyl-acetonate
Abbr.	ACAC	TMHD	TFAC	HFAC
Structure of organics				

Table 1-4 Melting point, boiling point and vapor pressure of metal complex species vs. chlorinated species. (Phillips and Perry 1995)

Product	MP (°C)	BP/T_{sub}(°C)	Vapor pressure @ 150°C (Torr)
$CoCl_2$	737	1049	-
$CoCO_3$	280*	181 (exp~200)	-
$Co_2(CO)_8$	51*	170 (exp~190)	-
$Co_4(CO)_{12}$	60*	171 (exp~192)	-
$Co(acac)_2$	170	161 (exp~179)	-
$Co(acac)_3$	211	131	1.059
$Co(tmhd)_2$	254	90	-
$Co(tmhd)_3$	143		-
$Co(tfac)_3$	-		3.319
$Co(hfac)_3$	-		9.132
$FeCl_3$	308	316	-
$Fe(C_5H_5)_2$	172.5	249	-
$Fe(CO)_4H_2$	-70	-20*	-
$Fe(CO)_5$	-20.5	103	-
$Fe_2(CO)_9$	100*	161 (exp~182)	-
$Fe_3(CO)_{12}$	140	150 (exp~177)	-
$Fe(acac)_3$	184	121	2.781
$Fe(tmhd)_3$	164	81	-
$Fe(tfac)_3$	-		8.34
$Fe(hfac)_3$	-		25.021
$NiCl_2$	1031	985 (subl)	-
$Ni(CO)_4$	-19	42 (exp~60)	

According to Le Chatelier's principle (equilibrium law), if an organo-metallic complex can deposit metal and release the ligands reversibly, an excess of ligands on the metal surface would give rise to spontaneous etching. The reverse engineering of ALD points to organometallic chemistry as a viable alternative to halogens. Several common ligands used in metal organic chemical vapor deposition (MOCVD) have been shown above. Each has a property in common, the ability to act as bidentate ligands. Selective chemical vapor-phase etching of copper and iron has been reported by Hess's group. (George, Hess et al. 1995, George,

Hess et al. 1996) For Cu etched by 1,1,1,5,5,5- hexafluoro-2,4-pentadione (H+hfac), the following chemical reaction has been proposed:

$$2H^+hfac_{(g)} + CuO_{(s)} \rightleftharpoons Cu(hfac)_{2(g)} + H_2O_{(g)} \tag{1.2}$$
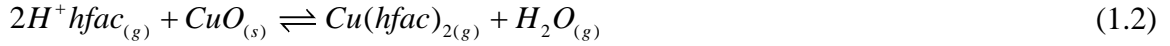
For the reaction of Cu^{2+} with h+hfac results in copper disproportionation:

$$2H^+hfac_{(g)} + Cu_2O_{(s)} \rightleftharpoons CuO_{(s)} + Cu(hfac)_{2(g)} + H_2O_{(g)} \tag{1.3}$$
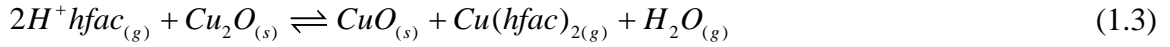
However, no reaction takes place with H+hfac on Cu^0 surface, resulting in an accumulation of Cu^0 and a termination of the copper removal process. Fe behaves similarly to Cu above, (George, Hess et al. 1996) with the following reaction:

$$6H^+hfac_{(g)} + Fe_2O_{3(s)} \rightleftharpoons 2Fe(hfac)_{3(g)} + 3H_2O_{(g)} \tag{1.4}$$
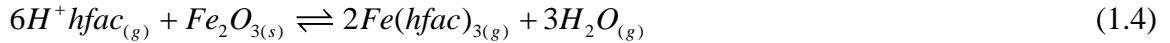
In Figure 1-17, the H_2O peak appearing in hfac treated Fe_2O_3 film is strong evidence for the reaction proposed above. Angle resolved X-ray photoelectron spectroscopy suggests H_2O is localized on the surface.
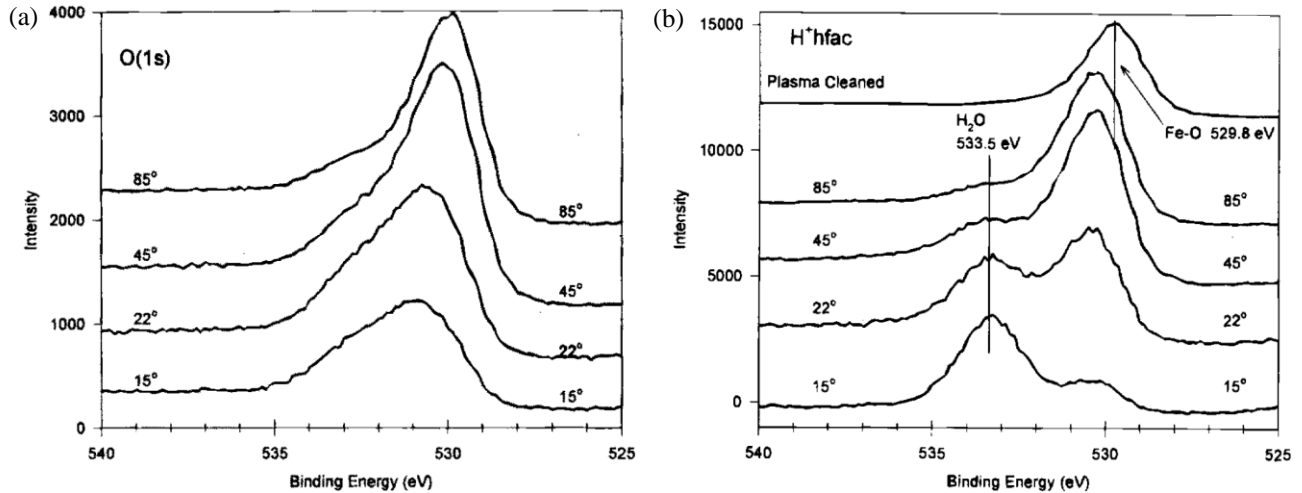
Figure 1-17 XPS spectrum of hfac-treated (a) Fe film and (b) Fe_2O_3 film. (George, Hess et al. 1996)

Although the H$^+$hfac can decompose on an iron surface, it appears to have a limited effect on the etching process. Similar experiments have shown that the reactivity of acac on a Ni surface and an oxygen covered Ni surface is different. (Nigg and Masel 1998) Figure 1-18 (a) shows that acac on a pure nickel surface did not lead to any Ni-containing desorption species. However, Ni(acac)$_2$ was desorbed from oxygen covered Ni surfaces, confirming that Ni surfaces are etched by acac. Similar results were also shown with tfac and hfac ligands as shown in Figure 1-18(b).
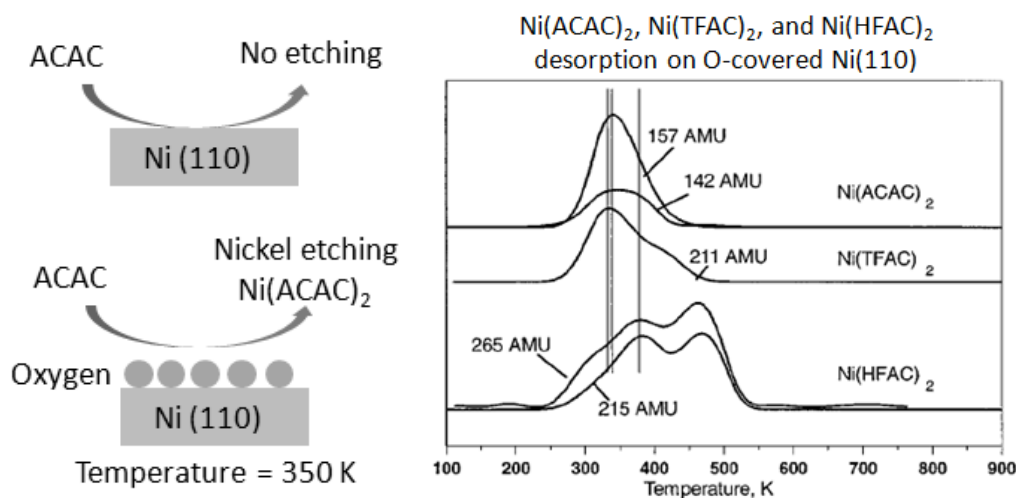
Figure 1-18 (a) The different desorption species on a Ni(110) surface and on an oxygen covered Ni(110) surface. Acac ligand was dosed at 100K and the surface was heated with 10K/ sec. (b) The desorption species are detected by mass spectrometer. (Nigg and Masel 1998)

1.4.1 Organo-metallic Complex Synthesis

Since the goal in this section is to generate volatile organometallic complex with metal film and organic ligand, an in-depth understanding of organo-metallic synthesis is necessary. The definition of organo-metallic chemistry is the possession of a metal carbon bond in the chemical

structure. As a result, it combines aspects of inorganic chemistry and organic chemistry. In the past, such numerous interests in this field are owing to the application of organo-metallic compounds as catalysts in industrial chemistry. However, there has been a dramatic growth in the field of ALD and CVD over the past ten years, driven by the needs of the semiconductor industry such as high-k dielectric in transistor, DRAM capacitors, metal film of interconnection and so on. The precursor chemistry plays an important role in ALD process. The precursor must be volatile and thermally stable without restricting to gases but also liquids and solids. Metal halides, metal alkyls, and metal alkoxides have been widely applied in ALD, but the beta-diketonates are the most studied compounds of these metals due to its high volatility (Tiitta and Niinistou 1997, Leskela and Ritala 2002). Since the concept of organo-metallic chemical etch is based on the reverse process of ALD, the synthesis of beta-diketonate is the concentration in this section.

The fundamental structure of beta-diketonate is 2,4-pentanedione, usually denoted as acac (acetylacetone). Acac is the most common representative of a large group of ligands that form especially stable and useful chelate complexes with a large variety of metals. The structures of acac and its anion are shown in Figure 1-19 (a). Acac exists as an equilibrium mixture of keto and enol tautomers in Figure 1-19 (b). (Caminati and Grabow 2006, Czech and Wojciechowicz 2006) Enol tautomer provides much stable structure due to the formation of intramolecular hydrogen bond and an extended π system, namely, conjugated system. The negative charge is highly delocalized by resonance since the enolate form of acac anion. Due to the conjugated system of acac, planar structure has been observed. Although there are two potential geometries, cis and trans of the anion, the cis conformation is encountered normally while the anion acts as a ligand. Under cis conformation, the conjugated system of the enolate provides the favorable

30

position of oxygen for coordination, resulting in the most stable structure as the six-membered chelating ring has little strain energy and electrophilic substitution of the methine hydrogen. Figure 1-20 shows the sample structure of Co(acac)$_3$. (Jensen and O'Brien 2001) Furthermore, not only Co(acac)$_3$, but also Na(acac), Be(acac)$_2$, Zn(acac)$_2$, Ni(acac)$_2$, Al(acac)$_3$, Fe(acac)$_3$, La(acac)$_3$, Zr(acac)$_4$, Cr(acac)$_3$, Cu(acac)$_2$, Mn(acac)$_2$, VO(acac)$_2$, Pd(acac)$_3$, Ru(acac)$_3$ and Ir(acac)$_3$ have been synthesized. (Lamprey 1960, Beck 1965, Habeeb, Tuck et al. 1978, Bennett, Heath et al. 1998, Isakova, Baidina et al. 2000, Hamid, Zeller et al. 2005)
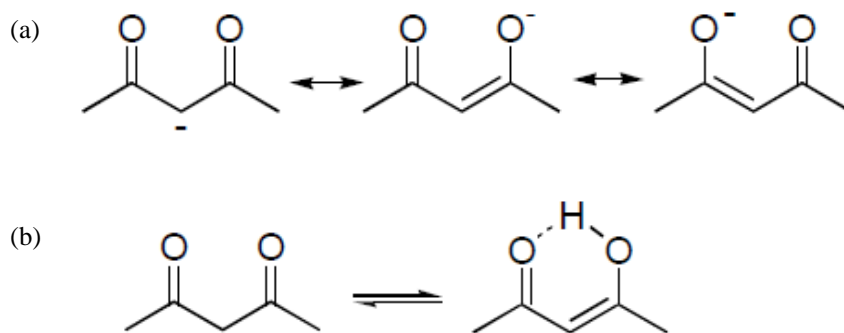
Figure 1-19 (a) The structures of acac and its anion, (b) keto in left and enol tautomer in right. (Caminati and Grabow 2006, Czech and Wojciechowicz 2006)
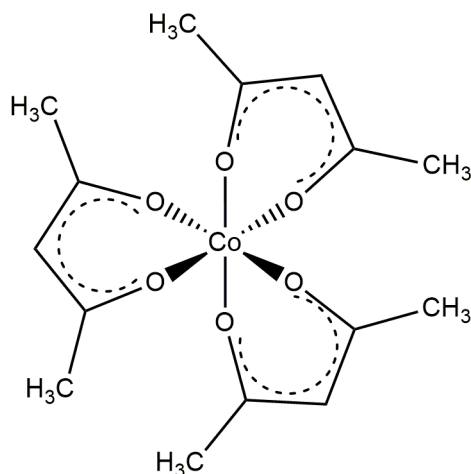
Figure 1-20 The structure of Co(acac)₃. (Jensen and O'Brien 2001)

It is usually straightforward to synthesize acac organo-metallic complex, because of the stability of the reaction products. Unlike most of ketone, diketones have much lower pKa, which allows it to be extensively deprotonated by mild bases such as carbonate or ammonia. For example, pKa of acac is 9, which is much lower than that of acetone, 20. Because the 6 fluorine atoms serve as electron-withdrawing groups, Hfac (1,1,1,5,5,5-Hexafluoro-2,4-pentanedione) provides an even lower pKa, 4.3. The synthesis of Co(acac)₃ and Co(hfac)₃ are introduced as samples here: the preparation of Co(acac)₃ begins with cobalt carbonate and a large excess of acac which serves as the reaction solvent as well as for generation of the enolate. Meanwhile, oxidation of Co^{2+} to Co^{3+} with hydrogen peroxide is necessary to generate Co(acac)₃ instead of Co(acac)₂ (Shalhoub 1980). By using the excess hfac as a reactant and solvent, the synthesis of Co(hfac)₃ has a similar procedure to that of Co(acac)₂. Since the metal is surrounded by hydrophobic methyl group, the complex tends to have higher solubility in the organic solvent. Furthermore, the intermolecular forces within the molecules are relatively low, resulting in relative high volatility. Even higher volatility has been discovered in hfac due to the low polarizability of fluorine makes the van der Waals force within the molecules exceptionally

weak. Based on this phenomenon, the complex can be purified by sublimation or distillation. (Shalhoub 1980, Jensen and O'Brien 2001)

1.5 Thermodynamic Assessment for Etching Magnetic Metal

According to previous sections, patterning a magnetic metal individually or in stack via plasma etching is a challenging process. One issue in realizing the etching process is that it is not clear which metal gaseous species is responsible for the primary etching mechanism. Although the measurement of partial pressure of metal gaseous species by mass spectrometer along with other techniques could determine the major etch products in gas phase and condensed phase, it is a tedious and costly diagnostic. To save resources and eliminate the need for trial and error methods, a systematic approach in determining the possibility of etch chemistries is needed. Theoretical approaches based on thermodynamics, which provide the foundation for analyzing the respective probabilities of competing mechanisms, may be preferable to experiments. In making the selection, several crucial thermodynamics parameters such as melting point, boiling point, heat of formation, heat of reaction, Gibbs free energy, and vapor pressure must be considered. These data for magnetic metals, such as iron, cobalt and nickel, are available in the NIST JANAF tables, (Chase 1998) HSC Chemistry, (Smith 1996) and CRC handbook. (Phillips and Perry 1995) There are certain methods based on thermodynamic calculations, one is the Ellingham diagram, which is a plot of Gibbs free energy change as a function of reaction temperature, (Ellingham 1944) and the Pourbaix diagram, which plots the potential with respect to standard hydrogen electrodes as a function of pH. Since the species in plasma etching conditions are mostly in gaseous and condensed phases, the volatility diagram is the most

suitable tool for depicting thermodynamic analysis. The volatility diagram is a plot of the partial pressure of a particular gaseous product as a function of the pressure of the reactant gas. It was first used in ceramic reaction analysis (Gulbranse and Jansson 1972) and metals. (Gulbransen 1970) The etching capability of plasma chemistries can be determined by the vapor pressure of gaseous etching product, suggesting that the weight loss due to the loss of the volatile etching species should be appreciable to be considered as etchable. In more detail, the weight loss in a thermogravimetric analyzer (TGA) can be registered provided the vapor pressure of the evaporating species is higher than 10^{-8} atm. (Lou, Mitchell et al. 1985) Therefore, the volatility diagram can be applied to any material with available Gibbs free energy data. In 2002, Kulkarni and DeHoff applied the volatility diagrams to analyze the dry etching of copper by chlorine plasma at various temperatures. (Kulkarni and DeHoff 2002) Reactions of copper with molecular and atomic chlorine were investigated, and molecular and atomic hydrogen reactions were also considered. To construct the volatility diagram, the dominant species in gas and condensed phase needs to be determined in order to assess the possible reaction. A list of relevant reactions in the Cu-Cl system with equilibrium constants is given in Table 1-5.

Table 1-5. Reactions utilized for plotting volatility diagrams in the Cu-Cl system.(Kulkarni and DeHoff 2002)

Reaction	log(K) = -ΔG°/RT			
	50C	100C	150C	200C
(1) $Cu(c) + 1/2\ Cl_2(g) \rightarrow CuCl(c)$	19.17	16.21	13.95	12.18
(2) $CuCl(c) + 1/2\ Cl_2(g) \rightarrow CuCl_2(c)$	8.34	6.60	5.27	4.23
(3) $Cu(c) \rightarrow Cu(g)$	-47.63	-40.32	-34.74	-30.34
(4) $CuCl(c) \rightarrow Cu(g) + 1/2\ Cl_2(g)$	-66.8	-56.32	-48.69	-42.51
(5) $CuCl_2(c) \rightarrow Cu(g) + Cl_2(g)$	-75.13	-63.12	-53.96	-46.74
(6) $Cu(c) + 1/2\ Cl_2(g) \rightarrow CuCl(g)$	-9.91	-7.95	-6.45	-5.27
(7) $CuCl(c) \rightarrow CuCl(g)$	-29.09	-24.15	-20.40	-17.45
(8) $CuCl_2(c) \rightarrow CuCl(g) + 1/2\ Cl_2(g)$	-37.43	-30.75	-25.67	-21.67
(9) $Cu(c) + Cl_2(g) \rightarrow CuCl_2(g)$	8.16	7.22	6.50	5.93
(10) $CuCl(c) + 1/2\ Cl_2(g) \rightarrow CuCl_2(g)$	-11.02	-8.99	-7.45	-6.25
(11) $CuCl_2(c) \rightarrow CuCl_2(g)$	-19.36	-15.59	-12.72	-10.47
(12) $3\ Cu(c) + 3/2\ Cl_2(g) \rightarrow Cu_3Cl_3(g)$	39.61	34.27	30.19	26.97
(13) $3\ CuCl(c) \rightarrow Cu_3Cl_3(g)$	-17.91	-14.35	-11.66	-9.56
(14) $3\ CuCl_2(c) \rightarrow Cu_3Cl_3(g) + 3/2\ Cl_2(g)$	-42.93	-34.14	-27.47	-22.24

The list of reactions can be separated into certain groups by the equilibrium between condensed phases. For example, the first group of Cu(g) equilibrium includes reactions 1 - 5, the second group detailing CuCl(g) equilibrium is reactions 6 - 8 and the third (reactions 9-11) and fourth (reactions 12-14) are the equilibrium of $CuCl_2(g)$ and Cu_3Cl_3 respectively. The complete volatility diagram, combining every reaction on the list, is shown in Figure 1-21 (a). The line segments of maximum equilibrium vapor pressure are solid, the stable portions of the equilibrium vapor pressure lines that are less than the maximum are dashed, and the metastable extensions are dotted. Therefore, the most volatile species in the Cu-Cl system is Cu_3Cl_3. However, the maximum partial pressure, 10^{-18} atm, is much lower than that of the threshold pressure, 10^{-8} atm. Since thermodynamic properties are a function of temperature, the volatility diagram for Cu-Cl from 50 to 200° C is shown in Figure 1-21 (b).
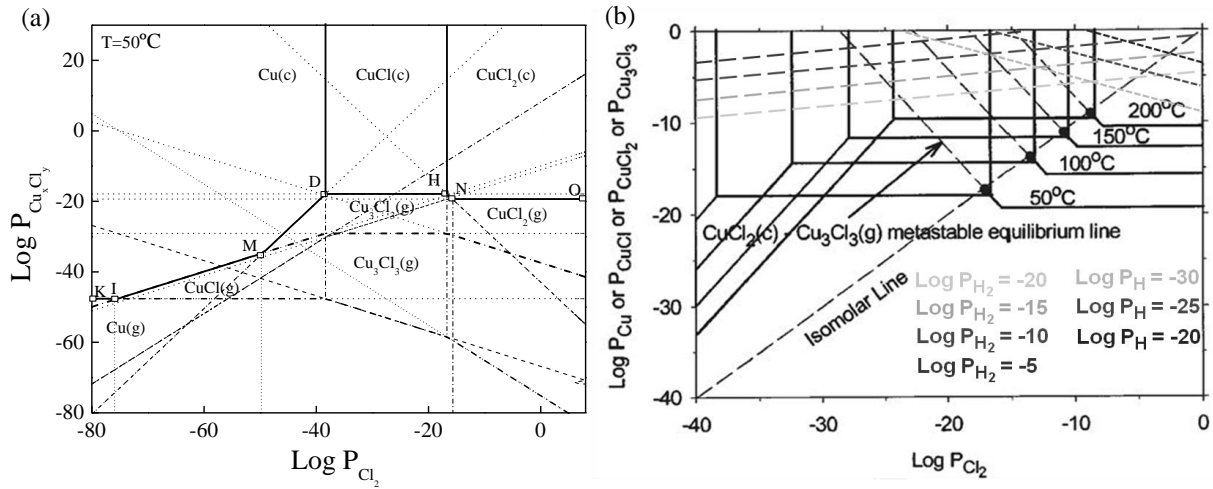
Figure 1-21 Volatility diagrams for (a) Cu/Cl$_2$ system at 50°C and (b) Cu/Cl$_2$-H/H$_2$ system at varying pressures of H/H$_2$ and varying temperatures. (Kulkarni and DeHoff 2002)

The isomolar line (dash) in Figure 1-21 (b) represents the mass balance criterion that the reactions that lie above this line are technically metastable and are in violation of the principle of mass conservation. The vapor pressure of Cu$_3$Cl$_3$ is sufficiently high (10^{-8} atm) at temperatures greater than 200° C. In order to increase the pressure of etch products under operating temperature, the introduction of molecular and atomic hydrogen has been investigated. The reactions of hydrogen considered are:

$$3CuCl_{2(c)} + \frac{3}{2}H_{2(g)} \rightleftharpoons Cu_3Cl_{3(g)} + 3HCl_{(g)} \tag{1.5}$$

$$3CuCl_{2(c)} + 3H_{(g)} \rightleftharpoons Cu_3Cl_{3(g)} + 3HCl_{(g)} \tag{1.6}$$

The reaction for the same partial pressure of hydrogen falls on a straight line known as the isobaric line, shown in Figure 1-21 (b) as a dashed line. The line with positive slope represents molecular hydrogen and the negative slope represents atomic hydrogen. As a result, the pressure of Cu$_3$Cl$_3$ for a given pressure of atomic hydrogen is extremely high at low

temperatures. By utilizing the results from thermodynamics analysis, a two-step reaction scheme for a dry etching process of copper has been proposed. Meanwhile, this process has been verified experimentally. (Tamirisa, Levitin et al. 2007) This two-step etch process includes a chlorine plasma followed by a hydrogen plasma. From the XPS results, a $CuCl_x$ layer was generated by the chlorine plasma, while H_2 plasma assisted the removal of the $CuCl_x$ layer by forming Cu_3Cl_3, which confirmed the etch mechanism from the thermodynamic prediction.

In this work, a thermodynamic approach was used to assess the feasibility of various etch chemistries, beginning with the consideration of reactions between the dominant vapor phase/condensed species and the surface at various temperatures and reactant partial pressures. The volatility of etching product was determined to aid the selection of viable etch chemistry leading to improved etch rate. As mentioned in previous sections, a few magnetic metals were considered (Co, Fe, and Ni) along with various halogen and organometallic based chemistries. The thermodynamically favorable reactions were investigated and the vapor pressures of its products were calculated. In addition, the vapor pressure enhancement induced by adding secondary gas such as hydrogen were investigated. Since experimental validation is an important part to verify the thermodynamic prediction, the etch rate of different magnetic metals applied in plasmas were compared by cross-sectional image by scanning electron microscopy (SEM). Furthermore, optical emission spectroscopy (OES) and quadrupole mass spectrometry (QMS) applied to plasma chamber to measure the relative amount of predicted etching products. Finally, the SEM was utilized to observe the morphology of surface and the etching profile of patterned sample, determining the physical sputtering, chemical etching or synergetic chemical sputtering in pattering magnetic metals.

1.6 Scope and Organization

To continue to push the envelope for micro- and nano-electronics, there are certain major challenges that arise for plasma etching. Firstly, as novel materials form the backbone of such emerging technologies such as magnetoresistive RAM (MRAM), the need of patterning materials that are intrinsically hard to etch such as Co, Fe, Pt and Pd is inevitable. Secondly, the structural complexity of high aspect ratios and multilayered features presents challenges in achieving the desired final product. Finally, the downscaling of devices suggests that a minor deviation from pattern dimensions could result in unbearable degradation in device performance. Ultimately to address these challenges, developing a new generalized approach to select the viable chemistries for patterning magnetic metal is inevitable. Figure 1-22 presents the flow diagram of this work that the first step of the generalized approach was screening of the potential plasma chemistries for patterning MRAM stack, including several transition and noble metals by conducting thermodynamic calculations. The plasma chemistries predicted by thermodynamic calculation have been verified by reactive ion beam etch and organic chemical etch in Chapter 3, 4 and 5.

Thermodynamic calculation to select viable etch chemistry		
Reactive ion etching (RIE)	**Organic Chemical Etch**	
Surface modification	Surface modification	
Sequential Cl_2/H_2 plasma	Ar^+ assisted chemical etch	Sequential O_2 plasma and organic
Transition metal	Transition metal	Transition metal
Co, Fe, Ni & CoFe alloy	Co, Fe & CoFe alloy	Co, Fe, CoFe alloy & Cu
Noble metal	Multiple layers	Noble metal
Pt	MRAM stack	Pt & Pd
Etch rate(SEM), surface analysis(XPS), magnetic property(SQUID), mass spectrometry(MS), optical emission spectroscopy(OES),		

Figure 1-22 Flow diagram of this work. RIE has been introduced in Chapter 3, organic chemical etch with different surface modifications has been described in Chapter 4 and 5.

Chapter 2 describes the apparatus used to conduct the experimental work in this study, focusing primarily on the inductively coupled plasma (ICP) reactor and the *in situ* diagnostic probes equipped for the purpose of characterizing the plasma, etch products and macroscopic etch rate of the complex metal films. An ultra-high vacuum transfer system and surface characterization techniques are discussed. On the other hand, a low vacuum setup of organic solution, vapor, ion beam assisted organic vapor etch chambers, and the solution characterization are introduced. Since the magnetic device is the final product of the study, the measurement of magnetic properties for metal film is also included. In addition, theoretical methods of thermodynamic such as Gibbs free energy minimization and volatility diagram analysis are described in detail using specific model systems.

Chapter 3 discusses the generalized approach for reactive ion etch of magnetic metals, including the detailed analysis of volatility diagram for etching Co, Fe, Ni, and CoFe alloy by

halogen plasmas such as chlorine, fluorine, and bromine. The introduction of secondary chemistries such as oxygen and hydrogen radicals after halogen gases treatment are also studied, and the theoretical works are verified by the experiments, including etch rate measurement, etching product characterization, surface chemical analysis, etching profile observation, and magnetic properties study.

Chapter 4 presents the ion beam assisted organic chemical etch of magnetic materials such as Co and Fe. Although an enhancement of etching performance of reactive ion etch has shown in Chapter 3, a highly volatile etching products are required to increase the selectivity of mask to metal in patterning MRAM stack. A reversed engineering of ALD is proposed for patterning metal. First, thermodynamic calculation is performed to select a viable organic chemistry for each metal, followed by verification of experiments with solution and vapor etch. Second, due to the low density of organic molecules in vapor phase, an ion beam is selected to activate the metal surface and assist the desorption of organometallic complex. Finally, etch rate measurement, etching product characterization, and surface chemical analysis are conducted for understanding the etching efficacy.

Chapter 5 further explores the organic chemical etch of metals with surface modification. Various processes of surface modification including O_2, Cl_2, SO_2, CF_4, SF_6 plasma and O_2 ion source for metal are studied through XPS to understand the conversion of metallic to oxidized state on surface. Multiple organic ligands are also examined in etching metal in both solution and vapor phase, and XPS, ICP-MS, and ellipsometer are applied to analyze the etching efficacy of organic ligands. Finally, the patterned samples of Co and MRAM stack are chosen to demonstrate the etching performance. Etch rate, surface morphology, etching profile evolution

and magnetic property of patterned sample are studied for realizing the atomic scale control of etching.

Finally, the accomplishment of this work is summarized in Chapter 6 that a comprehensive framework for selecting viable chemistries in patterning magnetic metals has been developed, and the surface modification prior to organic chemical etch was realized to be necessary in chemically etching metals. A high selectivity of metal oxide to metal by formic acid vapor is achieved, suggesting that one of the most important requirement in atomic layer etch, self-limiting reaction, is fulfilled. By controlling the thickness of oxides in oxidation, the etch rate of metals could be controlled in atomic scale level. High density MRAM fabrication can be achieved based on the results of this work.

CHAPTER 2: EXPERIMENTAL SETUP

This chapter is a description of the systems that have been used for the experimental work of the study, including wet and plasma etching. The synthesis of the several materials and patterned samples investigated in this work are introduced. Additionally, the various analytical tools that are used to characterize the plasma environment have also been described. Furthermore, the measurement of etching performance such as etch rate and etching profile are presented. Finally, analyses of surface chemical compositions, surface morphology, magnetic properties, and reaction products have been presented.

2.1 UHV Transfer Tube and Load Lock

An ultra high vacuum transfer tube system provides the capability for processing and analyzing in a variety of chambers without having to expose samples to ambient conditions. Each chamber is separated from the main tube by a gate valve. Figure 2-1 shows the relevant chambers to this experimental work attached to the tube: an inductively coupled plasma reactor and X-ray photoelectron spectroscopy system.

The main tube is connected to three pumps, an Edwards E2M-18 mechanical pump, a Leybold 360 turbomolecular pump, and a CTI CT-8 croygenic pump each utilized to achieve a separate pressure regime. Pressure is monitored by a cold cathode gauge or an ion guage. Samples are introduced to the tube via a load lock pumped by an additional Leybold 360 turbomolecular pump (base pressure $\sim 10^{-6}$ Torr), which is in turn backed by the same E2M-18

mechanical pump connected to the tube. A linear transfer arm on the other side of load lock

allows the sample to be transferred to a cart which is utilized to ferry samples along the tube to

various chambers. The cart runs along a metal track secured to the floor of the transfer tube and

is towed by a motorized pulley system. Linear transfer arms connected to the tube allow samples

to be loaded from the cart into various chambers.
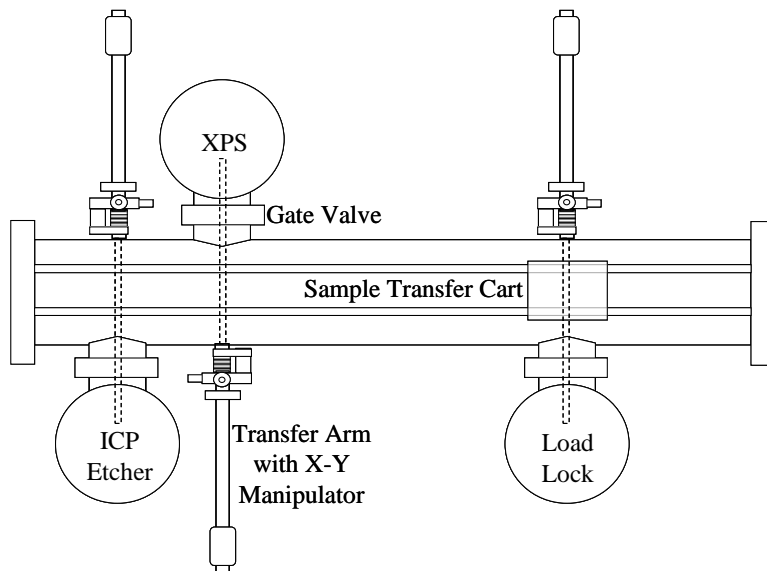
Figure 2-1 A schematic illustration of a UHV Transfer Tube Setup.

2.2 ICP Plasma Etcher

The main experimental system used in this study was a custom-built inductively coupled plasma etcher. The system can be operated in both capacitively coupled (E) and inductively coupled (H) modes based on the magnitude of the RF power supplied as observed and described by numerous authors. (Amorim, Maciel et al. 1991, Hopwood 1992, Kortshagen, Gibson et al. 1996) At low RF powers the E mode (driven by an electrostatic field) dominates. As the RF power is increased there is a transition to the H mode (driven by electromagnetic induction) which is marked by a dramatic increase in plasma density. However, it is possible for the H mode to be sustained at lower power values owing to its more efficient sustaining mechanism. (Miyoshi, Petrovic et al. 2002) This reactor's main chamber is constructed from stainless steel and is divided into two sections as depicted in Figure 2-2.
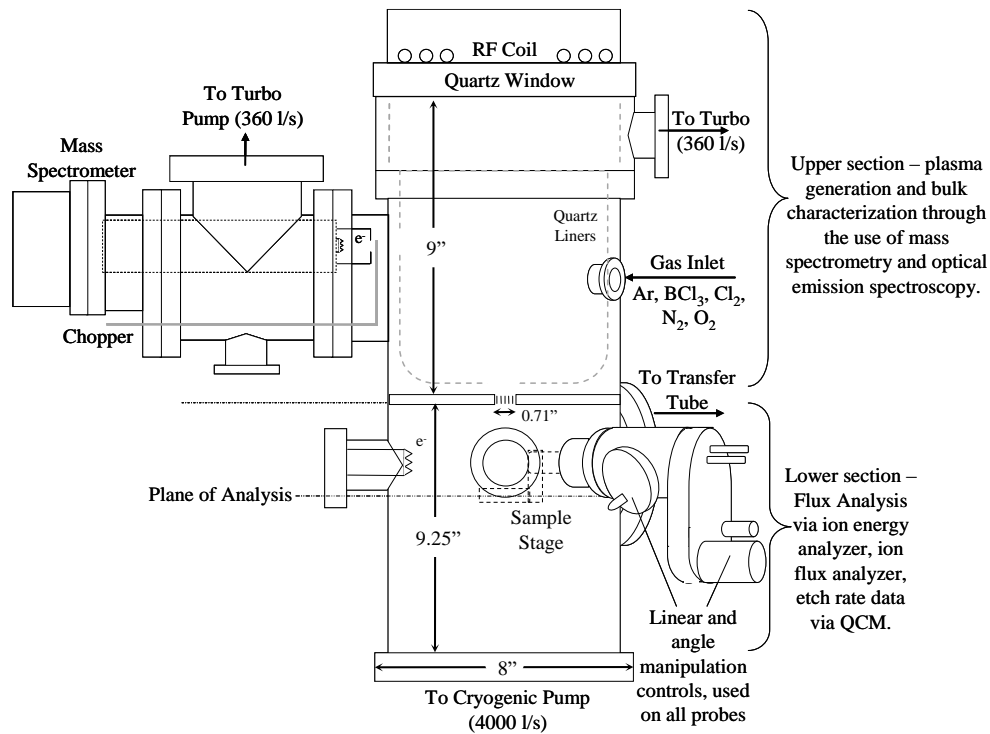
Figure 2-2 Schematic of ICP etcher showing divisions in chamber.

The upper section is capped by a quartz window upon which rests a coil connected to a 13.56 MHz RF power source. Plasma is generated via inductive coupling through the top quartz window, while a quartz liner serves to isolate the plasma from the metal walls of the chamber. A metal electrode located in the interior of the beam source allows DC biasing of up to 500 V.

A roughing valve connected to this section allows for pumping via a Leybold D25B mechanical pump. This mechanical pump also backs a Leybold Turbovac 361C turbomolecular pump directly connected to the upper section, allowing a base pressure of 4.0×10^{-7} Torr to be achieved. This section also contains the gas inlet through which the process gases – Ar, BCl_3, Cl_2, N_2 and O_2 – are fed. The gas flow rates are controlled by MKS mass flow controllers. The upper section can also be exposed to a UTI 100C quadrupole mass spectrometer. The lower boundary of this section is a metal barrier with a grounded, gridded orifice 0.71 inches in diameter. This design allows a plasma beam to be extracted from the upper section and directed

45

into the lower area. For a 13.56 MHz RF ICP system using Cl_2 as the feed gas (with 1% each of He, Ne, Ar, Kr, and Xe) with an incident power of 400 W and operating pressure of 2 mTorr, typical ion density (n_i) and electron density (n_e) values are 6×10^{10} cm^{-3} (Malyshev and Donnelly 2001) with an average electron temperature (T_e) of 3 eV. (Malyshev and Donnelly 2000) In a similar system utilizing CF_4 as the feed gas, with an incident power of 300 W and operating pressure of 10 mTorr, n_i and n_e were 2.75 and 1.6×10^{11} cm^{-3}, with $T_e \sim 6.2$ eV. The mean free path of particles in the chamber is given by the equation:

$$\lambda = \frac{KT}{\sqrt{2}\, p\pi d_o^2}$$

(2.1)

Where p is the pressure, and d_0 is the collision diameter of the gas molecule. For diatomic Cl_2 with collision diameter of 4.11 Å (Ono and Tuda 1997), the mean free path at the given operating pressure of 2 mTorr and a neutral gas temperature of 590 K (Donnelly and Malyshev 2000) is estimated as 4.07 cm. CF_4 with collision diameter of 4.1Å (Cui, He et al. 2000) at 10 mTorr and an estimated neutral gas temperature of 750 K (Cruden, Rao et al. 2002) the mean free path is calculated to be 1.04 cm. However, it should be noted that at the pressure of the extracted beam chamber (~1×10^{-4} Torr) the mean free paths are accordingly higher: 81 cm for the Cl_2 plasma and 104 cm for the CF_4 plasma.

The lower area of this system is connected to a CTI CT-8 cryogenic pump with a pumping speed of 4000 L/s which maintains a base pressure of 10^{-8} Torr and a processing pressure of ~1.0×10^{-4} Torr. The cryo pump is necessary in this reactor as the small conductance of the extraction grid hole prevents the turbo pump in the upper chamber from efficiently evacuating the entire reactor. An ion gauge connected to this area provides the current pressure inside the chamber, and viewports allow for visual confirmation of the plasma generation. A 0.004 inch diameter tungsten filament minimizes spreading of the aforementioned plasma beam

by emitting low energy electrons, while also preventing charge accumulation on insulated samples. This section houses a rotatable, grounded sample stage which can hold wafer chips roughly 1.5 cm^2 in area. The lack of biasing means that ions are accelerated toward the substrate solely by the bias potential applied to the extraction grid. The sample holder is physically mounted on a pin protruding from the stage without electrostatic chucking. The rotational capability of the stage allows for variation in the beam impingement angle relative to the substrate surface. The stage and a variety of analytical tools, including an ion flux analyzer, ion energy analyzer and an optical emission spectrometer, lie in the analytical plane of the lower section. The ion flux analyzer and ion energy analyzer can be rotated and manipulated in the x, y and z directions, and can be positioned away from the center of the chamber if necessary. These diagnostic tools are discussed in greater detail in Section 2.7.

2.3 Wet Etching System of Organic Chemistry

Wet etching is a material removal process involving multiple chemical reactions between liquid solution and solid state materials to consume the reactants and generate favorable etch products. The specific patterns are usually defined via masking in the standard semiconductor process; however, the wet etching in this work focused on etching efficacy of organic chemistry toward hard-to-etch metals. Therefore, the etch rate of metals, surface composition and post-etch solution have been analyzed to quantify the etching efficacy.

In Figure 2-3, the wet etching procedure applied in this work is described. Since the organic chemistries used in this work are quite volatile, the interface between etched and un-etched area is ambiguous. In order to increase the accuracy of measurement of etch rate, a

47

mixture of Loctite 1C and EPKC epoxy paste were applied to define the un-etched area to improve the clarity of the boundary separating the etched and un-etched areas. After 24-hour solidification of epoxy, the components were placed in a vial and heated to 80°C. The water bath has been chosen to increase the uniformity of heat in the vial. After the predetermined etching time, the metal sample was immersed in dichloridemethane (DCM) to remove the epoxy on the un-etched area. The post-etch solutions were analyzed via inductively coupled plasma mass spectrometry (ICP-MS) to determine the etch products. With the change of surface composition analyzed by XPS and etch rate measured by Dektak profiler, the etch efficacy of metals with specific organic chemistry can be determined.
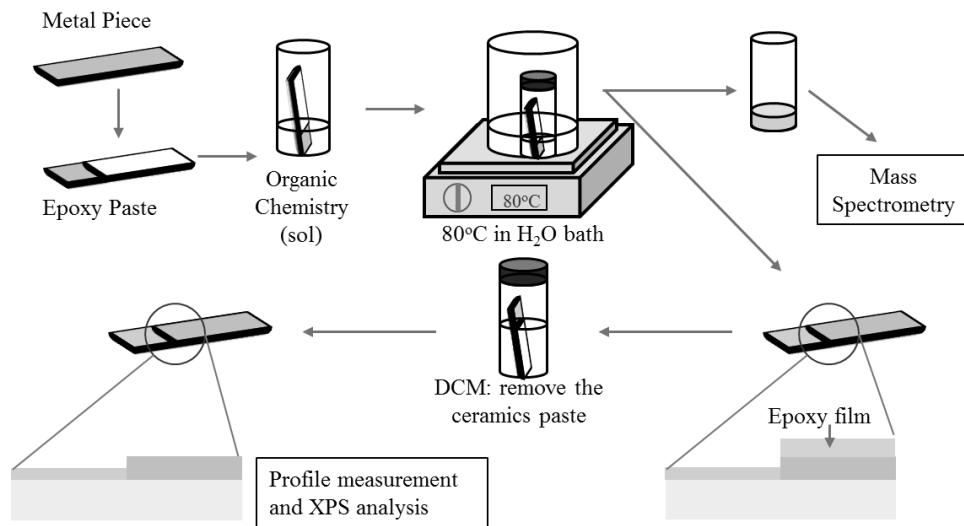
Figure 2-3 Schematic of wet etching standard operating procedure.

2.4 Ion Beam Assisted Chemical Etch System

In order to carry out the chemical etch with assistance of ion beam, a customer-designed ion beam assisted chemical etch system equipped with a 3-cm Commonwealth Scientific Kaufman ion source has been built (Figure 2-4). The main system is connected to two pumps, an Edwards E2M-18 mechanical pump and a Leybold 361 turbomolecular pump, each for a separate pressure regime. Meanwhile, a Pfeiffer Vacuum TCP-040 turbo pump serves as a differential pump of the ion source. Pressure is monitored by a MKS 627B Baratron gauge and a nude ion gauge.

A brief introduction of the principle of the broad beam ion source is provided here, but detailed information including the designs of the multi-aperture ion optics can be found in literature (Kaufman 1978, Kaufman, Harper et al. 1979, Harper, Cuomo et al. 1982, Kaufman, Cuomo et al. 1982). A schematic of the ion source is shown in Figure 2-4. By applying a potential difference between anode and cathode, a DC discharge can be generated in the discharge chamber.
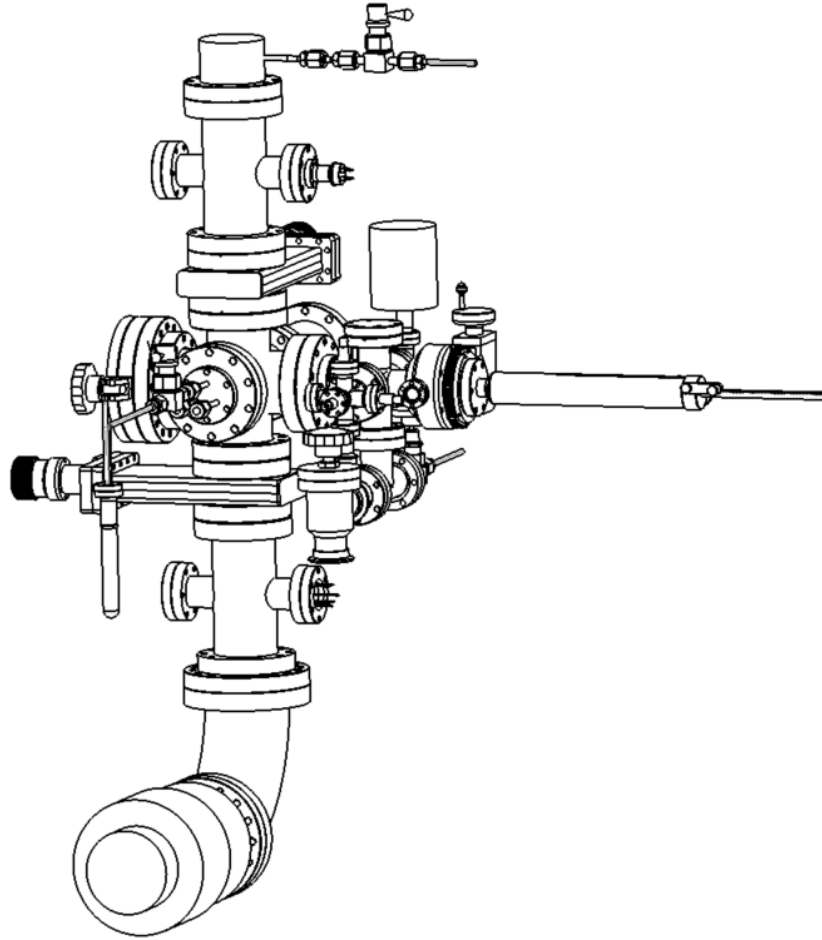
Figure 2-4 The schematic diagram of the ion beam assisted chemical etch system.

The cathode filament, made of 0.25 mm tungsten wire, in the discharge chamber is used to sustain the discharge through thermionic emission of electrons. The neutral argon (Ar) feed gas is supplied to the discharge chamber through a built-in 1/8" outer-diameter tube. Although the primarily ionizations are Ar^+ generation of single electron impacts, in order to maximize dissociation, a discharge voltage of 40V was used to maintain the low probability of Ar^{2+} formation. To confine the energetic electrons generated from cathode in discharge chamber and prevent the neutralization before colliding with Ar gas molecules, a permanent magnet was designed to situate beneath the anode to generate a magnetic field directed parallel to the axis. The floated potential of anode determines the energy of extracted ions with respect to a grounded

sample. Two grids outside the discharge chamber serve as the ion optics to facilitate ion extraction. The first screen gird was designed to confine the plasma, which possesses a similar potential to that of cathode. The second grid serves as accelerator which is biased negatively to extract the Ar$^+$ through the discharge chamber to sample surface. In order to extend the lifetime of the grids, low sputtering yields of graphite have been chosen as the material. An external neutralizer made of a 0.25 mm-diameter tungsten wire is needed to not only reduce the Ar$^+$ beam spreading due to the repulsion of positive Ar$^+$ ions, but also prevent surface charging of insulated substrate. Since the typical operating pressure of ion source is in several millitorr, the recombination rate of electrons and Ar$^+$ is negligible due to the large mean free path. Meanwhile, the negative-biased accelerator also avoids the backstreaming of electrons. Based on the Child's law (Kaufman 1978), the current density j of the extracted ion beam can be expressed as following,

$$j = \frac{4\varepsilon_0}{9}\left(\frac{2q}{m}\right)^{1/2}\frac{V^{3/2}}{l^2}$$

(2.2)

Where, ε_0 is the vacuum permittivity, q/m is the charge-to-mass ratio of extracted ions, V is the voltage difference between the screen and the accelerator grid, and l is the spacing between the two grids. Usually around 5 sccm of Ar feed gas is used to sustain the high ion flux without too high background pressure (10^{-4} torr), the maximum current density of 1keV Ar$^+$ can be achieved approximately 50 μA/cm^2.
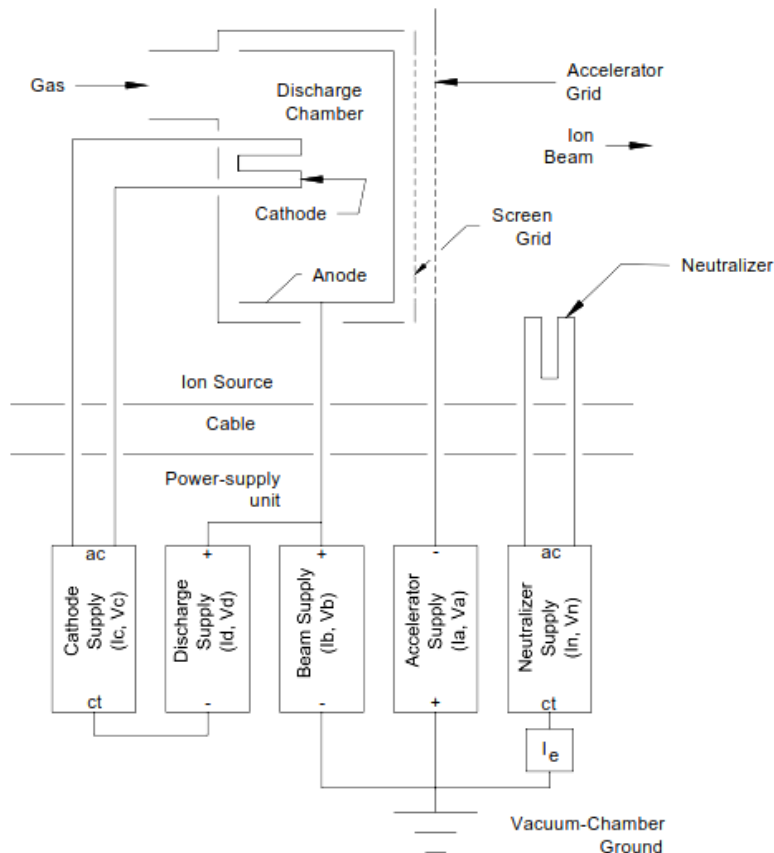
Figure 2-5 Schematic diagram of the 3 cm ion source installation. (Image courtesy of Kauffmann ion source manual)

Since the entire system is designed to perform the ion beam assisted chemical etch, a system for delivering organic vapor is built next to the sample stage. A special shape of shutter is made of 0.01"-thick-stainless steel shim and both 2D and 3D schematic of shutter is shown in Figure 2-6. The dimension of top, side and bottom surface is 2.5 by 5 cm^2, 2 by 5 cm^2, and 1.25 by 5 cm^2, respectively, and the side face is vertical to both top and bottom faces. The sample stage is placed right under the shutter, and the dimension of stage is 2.5 by 5 cm^2. While the shutter is off, the entire sample is exposed to the Ar ion beam from the ion source as mentioned above. When the shutter is on, half of the sample is covered by the shutter, another half of sample is exposed to the organic vapor through a doser as shown in Figure 2-6. The mean free

path of acac molecule, 5 cm, has been calculated based on following parameters: P=1 mtorr, T=300 K and ζ (diameter of acac) = 1.19×10^{-9} m. It is much larger than 1-mm-gap between sample and shutter, resulting in high concentration of acac on the exposed area, but extremely low concentration of acac on the surface covered by the shutter.
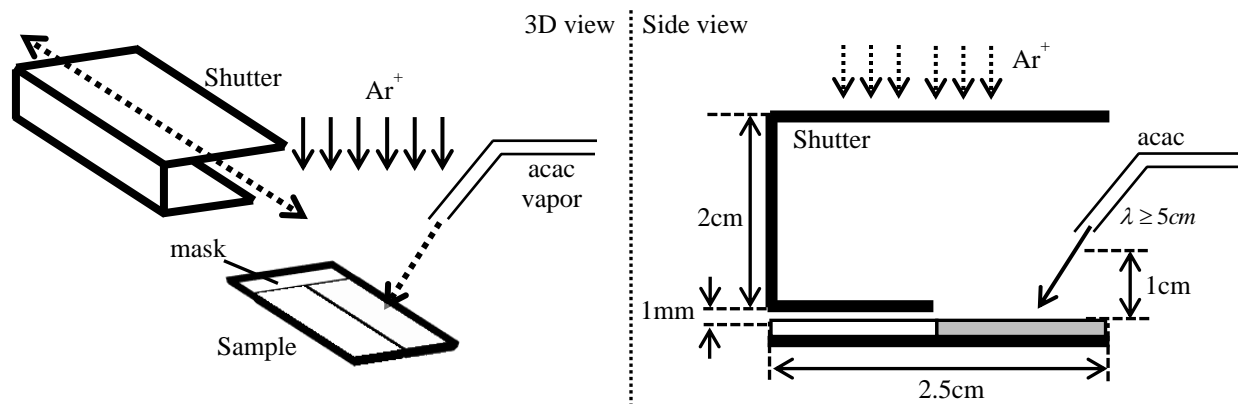
Figure 2-6 Schematic diagram of the design of sample holder and shutter in 3D and side view of organic doser and the shutter to block Ar+ beam.

2.4.1 Vapor Etch Chamber Coupled With ICP Chamber

Once the etching efficacy of organic chemical is examined by solution etch, a study of vapor etch is required for incorporating the etching approach into vacuum-compatible semiconductor process. The result from the organic solution etch suggests that the surface modification by O_2 plasma treatment is necessary to achieve higher reactivity between metal and organic ligand. Therefore, a vapor etch chamber is attached onto ICP chamber with a gate valve for isolation is shown in Figure 2-7. A 1.33" six-way-cross nipple is selected as a vapor etch chamber due to the temperature control issue and the usage of organic solution. The main system is connected to a pump, an Edwards E2M-18 mechanical pump, and the pressure is monitored by

a MKS 627B Baratron gauge, ranging from 1 to 1000 Torr. In order to maintain an 80ºC environment to avoid condensation of organic, several heating wires are placed uniformly on the chamber wall externally. If the vapor etch chamber is too large, the temperature of environment would be easily perturbed, resulting in local condensation of organic chemical. Meanwhile, a small etch chamber reduces the usage of organic chemical due to the high density of organic molecule could be obtained easily. Since a sequential process of surface oxidation and organic vapor exposure is desired, a gate valve is needed to isolate the plasma from vapor etch chamber. A precision magnetic transporter is designed to move the sample between the ICP chamber and the vapor etch chamber. By rotating the transporter, an alignment of sample to the organic doser is available in the vapor etch chamber. A doser is connected to a vaporizer system, allowing the delivery of organic vapor.

In order to deliver the organic chemical efficiently onto sample, the commercially available M1-1141-PN liquid vaporizer provided by Horiba^{TM} allows the fine control of the organic chemical vapor. Three steps are carried out by vaporization systems to inject the chemical vapor. First, a flow rate varied from 0.02 to 0.1 g/min of liquid is measured, and controlled by LF-F20M-A liquid mass flow rate controller (MFC). Second, a carrier gas of N_2 is measured and controlled by SEC-E40 gas MFC, and facilitate the vaporization for liquid. Third, the vaporized gas is released into the reactor.
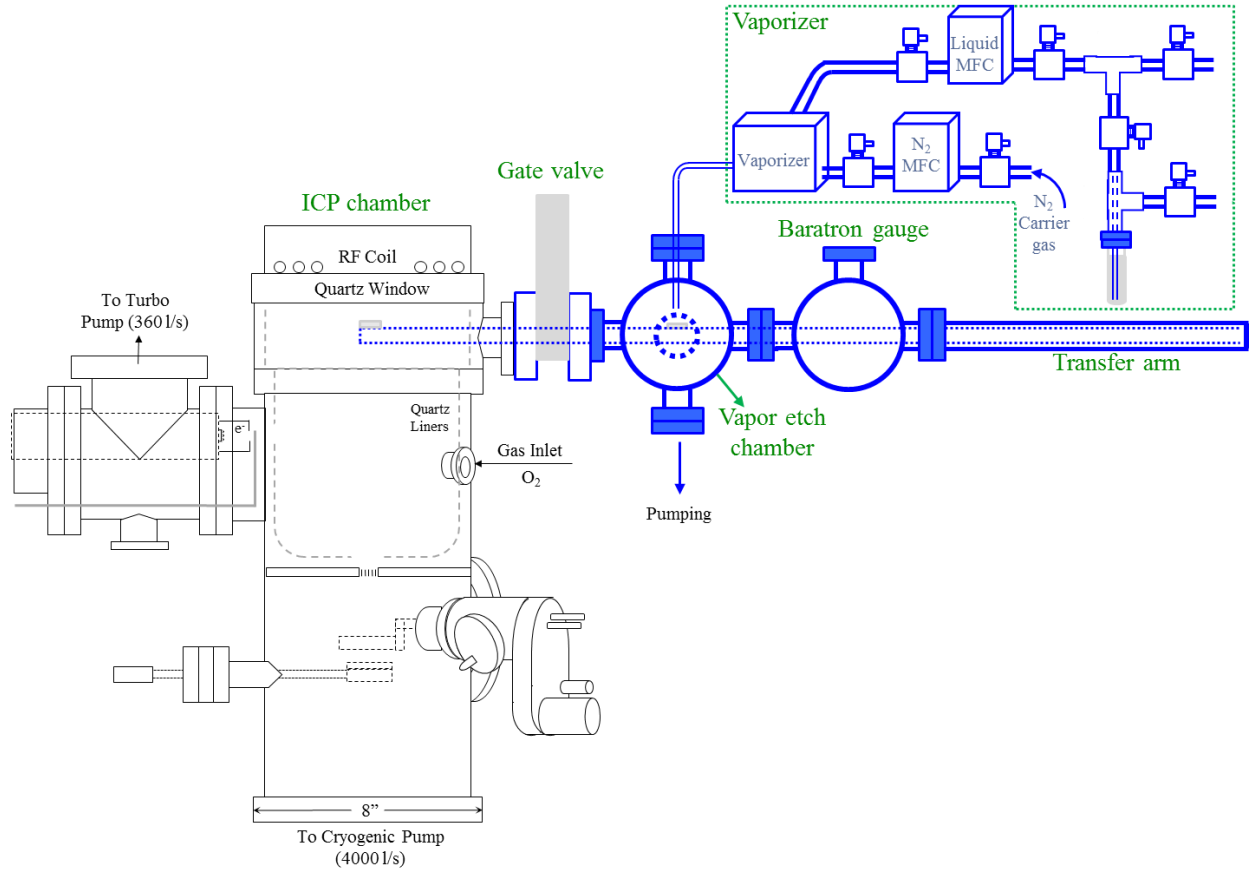
Figure 2-7 A coupled vapor etch chamber with ICP chamber for conducting metal etch with sequential surface oxidation and organic vapor exposure.
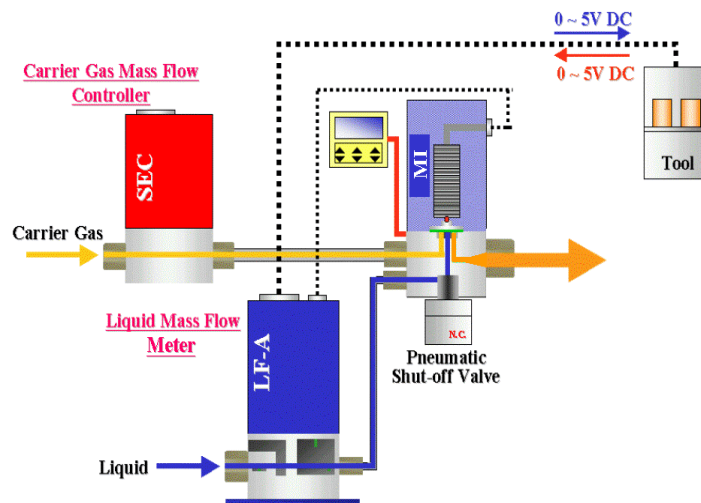
Figure. 2-8 Schematic diagram of the design of Horiba liquid vaporizer system. (Image courtesy of Horiba, 2013)

A fundamental of vaporization is described in a phase diagram, Figure. 2-9. There are two ways to get from a liquid to a gaseous state. The first method involves increasing the temperature while holding the pressure steady, as indicated by the arrow with the dash line. This method is commonly used in everyday settings of boiling water. In the second approach which is applied in the vaporizer system, one can also heat the liquid in advance and then abruptly reduce the pressure, as depicted by the arrow with the solid line. The pressure in the vaporization section of the injector can be reduced instantaneously, and this makes it possible to vaporize a liquid source instantaneously.
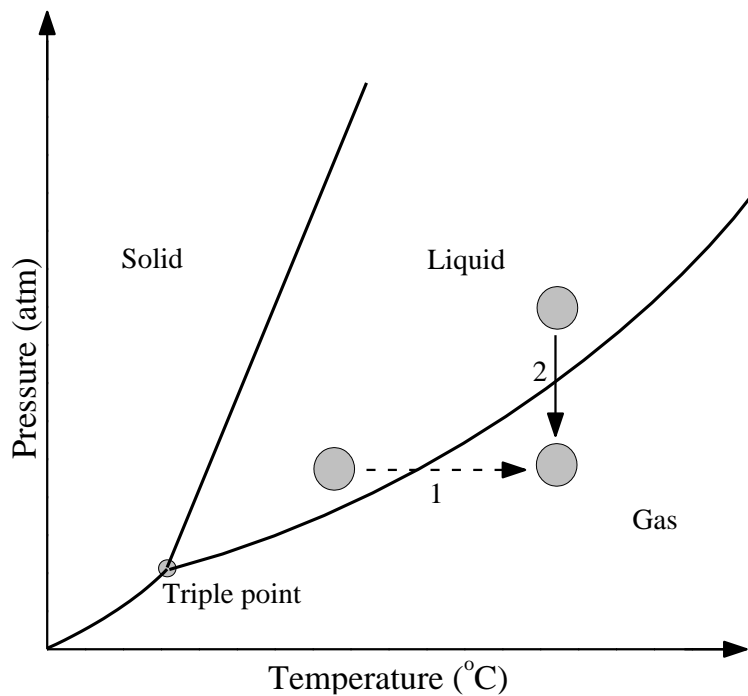
Figure. 2-9. Generic phase diagram with two approaches to vaporize the liquid instantaneously.

A method of mixing gas and liquid is illustrated in Figure 2-10. Since the pressure on the carrier gas is higher at the front of the nozzle inside the injector, it can be heated efficiently. The liquid source and the heated carrier gas are mixed together in the front of nozzle, and the

pressure is reduced as they pass through the nozzle, which vaporizes the mixture. A large flow

rate can be generated steadily without applying high energy to keep the temperature.
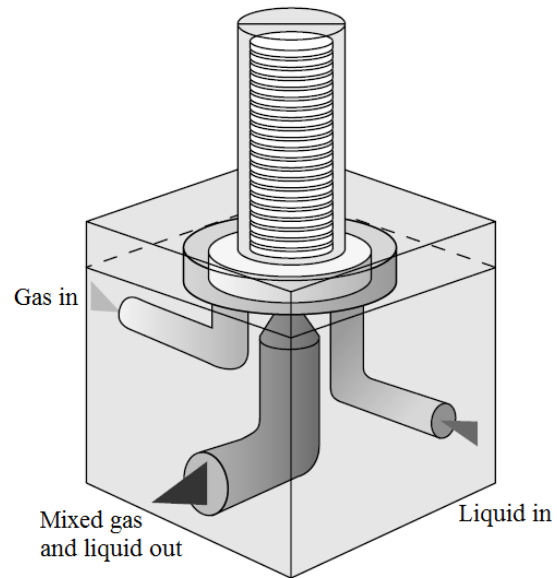
Figure 2-10 A method of mixing gas and liquid utilized in vaporizer system. (Image courtesy of Horiba, 2013)

2.5 Material Systems for MRAM Applications

Although the target of this work is to develop a generalized approach for fabricating

MRAM memory stack, fundamental studies on each metal utilized in MTJ stack are required.

Blanket film is required for fundamental studies such as surface chemical state, etching product

identification and quantification which required a large amount of material. Thus, for the purpose

of this work it is important to obtain blanket films of the materials of interest as shown on Table

2-1. The synthesis method, film thickness, and source of the films are listed on Table 2-1 as well.

Table 2-1 Detailed listing of the material blanket films investigated in this work.

Material	Synthesis Method	Film Thickness (Å)	Source
Co	E-beam evaporation (PVD)	100, 200, 500, 1k	CNSI (UCLA)
Fe	E-beam Evaporation (PVD)	100, 500, 1k	CNSI (UCLA)
Ni	E-beam Evaporation (PVD)	500	CNSI (UCLA)
Pd	E-beam Evaporation (PVD)	100	Nanolab (UCLA)
Pt	Sputtering Deposition (PVD)	270	Lam Research Crop.
$Co_{0.3}Fe_{0.7}$	Sputtering Deposition (PVD)	500	CNSI (UCLA)
$Co_{0.9}Fe_{0.1}$	Sputtering Deposition (PVD)	10k	Lam Research Crop.
$Co_1Fe_2\ Co_4$	Sol-Gel	1500	Tolbert's lab (UCLA)
$Co_1Fe_2B_1$	Sputtering Deposition (PVD)	500	Nanolab (UCLA)
$Co_1Fe_2B_1$	Sputtering Deposition (PVD)	300	Intel
$Co_{0.5}Pt_{0.5}$	Sputtering Deposition (PVD)	240	Lam Research Crop.
$Co_{0.5}Pd_{0.5}$	Sputtering Deposition (PVD)	270	Lam Research Crop.

Ultimately, the etching behavior of materials in the MTJ stack is of great importance for

the goal of understanding the feature profile evolution, as achieving the desired profile for all of

the components involved is largely dependent on the relative selectivity of the chemistries

chosen. For example, the etching of a blanket film may not able to distinguish the pure physical

sputtering, pure chemical etch, or combination of two, not to mention the undercut or sidewall

re-deposition. Due to the intellectual property and proprietary technology, the publication of etched profiles in cutting edge devices is rare, and when such profiles are available, the complete details of the process parameters used are often withheld. Thus, in this work, limited number of patterned Co film shown in Figure 2-11 is used to study the organic chemical etch with surface modification.
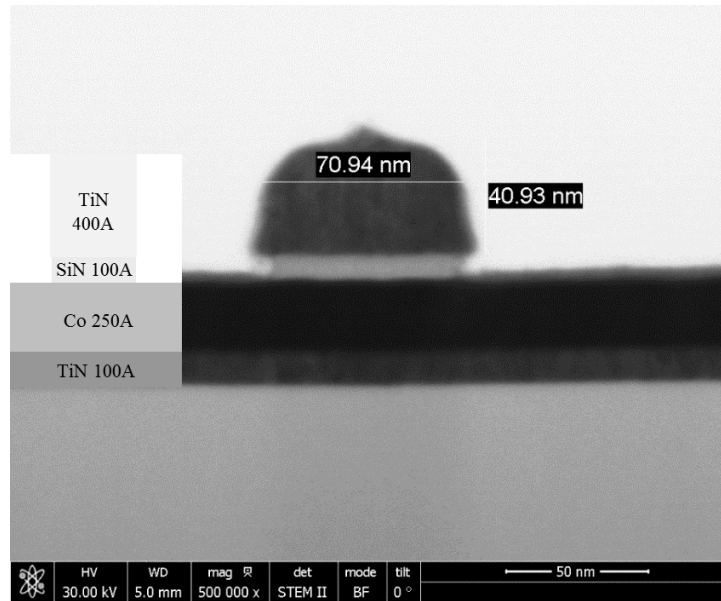
Figure 2-11 SEM images of the Co film patterned by a TiN hard mask and a SiN protecting layer with a TiN barrier layer at the bottom as the etch stop layer.

2.6 Plasma Diagnostics

2.6.1 Langmuir Probe

Langmuir probe is one electric probe for plasma diagnostics, and it was developed by Irving Langmuir in early 1924. A detailed introduction of the device can be found in the original paper published by Mott-Smith and Langmuir (Mott-Smth and Langmuir 1926). Basically, the

electric probe measures the electron density (n_e), space potential (V_s), and the electron temperature (T_{ev}) in local plasmas by using stationary or slow-scanning-rate of electric fields to emit or to collect charged particles. A metallic electrode in spherical, cylindrical, or planar geometries have been used as a probe, which first immersed into the plasma and polarized to the potential V_p by external power supply. The probe current of I_p can be measured due to the voltage drop in between V_p and plasma potential, V_{sp}, and a characteristic curve of voltage-current (I-V) is recorded for extracting the plasma parameters. In this study, an ESPIon Langmuir Probe from Hiden Inc. was utilized, with a 3 mm long cylindrical tungsten tip of radius 0.075 mm. The probe voltage range was -200 to +100 V, while the current range was -100 mA to 1000 mA. A typical voltage step of -0.1 V was used, the resolution of voltage and current data obtained by the system was 10^{-4} V and 10^{-8} A, respectively. A diagram of this setup and a typical I-V curve from an O_2 plasma are shown in Figure 2-12. (Chen 2015)
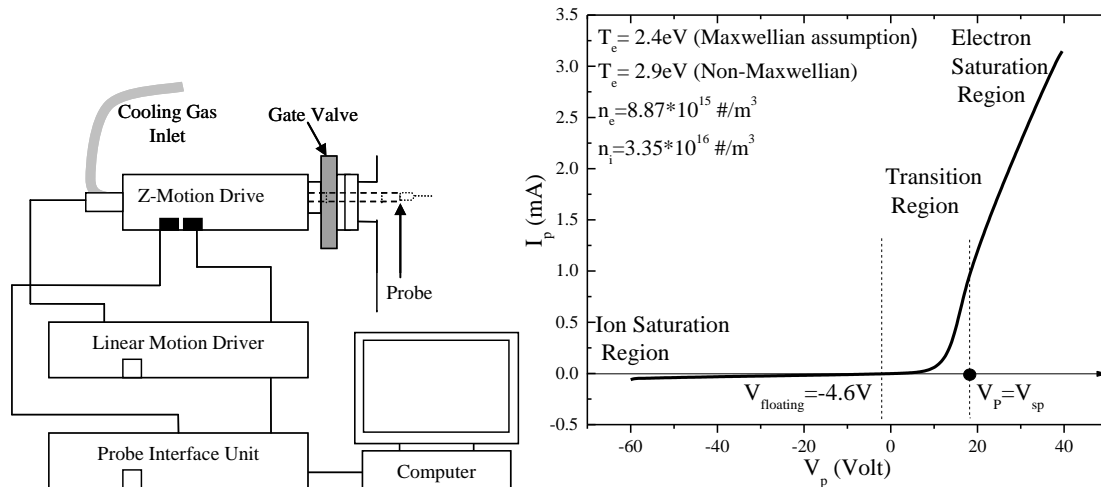
Figure 2-12 Schematic of Langmuir Probe Setup and sample I-V curve for O_2 plasma taken in the ICP reactor at 500 W, 0 W bias power with 2.5 mT.

To qualitatively interpret the I-V curve, an idealized, non-equilibrium, collisionless, Maxwellian and unmagnetized plasma is considered. Some assumptions have proposed, for example, the collisional mean free paths of all particles are greater than all characteristic lengths such as radius of Langmuir probe and Debye length, as well as the electron temperature is higher than those of ions and neutrals. The plasma potential of V_{sp} in Figure 2-12 corresponds to the electric potential at the point of local plasma, resulting in a probe current of I_p, which is composed of an ion (I_i) and electron currents (I_e) ($I_p = I_i + I_e$). While the bias is far negative, $V_p \ll V_{sp}$, the electrons are repelled, resulting in domination of ion current of I_p, which is called ion saturation current, I_{is}. On the other hand, when it is at positive bias, $V_p \gg V_{sp}$, the ions are repelled, leaving electrons attracted by the probe. In this case, the electrons are responsible for the electric shielding of the probe, and it is called electron saturation current, I_{es}. If the potential of V_p is equal to V_{sp}, leaving no current passes through the probe, the floating potential is obtained where the contribution of the ion and electron currents are equals. (Axford, Goodings et al. 1998, Goodings, Guo et al. 2001, Merlino 2007)

To consider the ion current (I_i) with a Maxwellian ion distribution at the temperature T_i, the ion current I_i can be expressed as a function of applied voltage (V_p), (Auciello and Flamm 1989)

$$I_i(V_p) = -I_{is} \exp[e(V_{sp} - V_p)/kT_i], \text{ when } V_p \geq V_{sp}, \tag{2.3}$$

$$I_i(V_p) = -I_{is}, \text{ when } V_p < V_{sp}, \tag{2.4}$$

where e is the electron's charge, and k is the Boltzmann constant. When T_i is comparable to the electron temperature T_{ev} as proposed above, the ion saturation current can be expressed as (Cherrington 1982)

$$I_{is} = \frac{1}{4} e n_i \upsilon_{i,th} A_{probe} \tag{2.5}$$

where n_i is the ion density, $\upsilon_{i,th} = \sqrt{8kT_i / \pi m_i}$ is the ion thermal motion speed,

However, when $T_{eV} \gg T_i$, the ion saturation current is not a function of T_i but T_{eV},

$$I_{is} = I_{Bohm} = 0.6 e n_i \sqrt{T_{eV} / m_i} A_{probe} \qquad (2.6)$$

If an electrode in the plasma has a potential different from the local plasma potential, the electrons and ions distribute themselves spatially around the electrode in order to shield the effect of this potential on the bulk plasma. An electron shielding cloud would surround the positively biased electrode, and the negatively biased electrode acquires positive space charge cloud to cover the electrode, and the characteristic shielding distance for negatively biased electrode can be expressed by Debye length, $\lambda_D = \sqrt{\left(\dfrac{\varepsilon_0 T_{eV}}{e^2 n_e} \right)}$. A positive space charge sheath can form only when the ion density exceeds that of electron at the sheath edge, which the velocity of ion must surpass Bohm velocity, $u_B = \sqrt{T_{eV} / m_i}$. To achieve the speed of Bohm velocity, the corresponding energy is acquired to overcome a potential drop of $0.5(kT_e / e)$. The factor of 0.6 = $e^{-1/2}$ comes from the approximation of the plasma potential at the end of the presheath. (Chen 2015)

On the other hand, electron current (I_i) with a Maxwellian ion distribution at the temperature T_e, the electron current I_e can be expressed as a function of applied voltage (V_p), (Chen 2015)

$$I_e(V_p) = I_{es} \exp[-e(V_{sp} - V_p) / kT_e], \text{ when } V_p \leq V_{sp}, \qquad (2.7)$$

$$I_e(V_p) = I_{es}, \text{ when } V_p > V_{sp}, \qquad (2.8)$$

Similar to ion saturation current, the electron saturation current is given by $I_{is} = \frac{1}{4} e n_i \upsilon_{i,th} A_{probe}$,

where n_e is the electron density, $\upsilon_{e,th} = \sqrt{8kT_e / \pi m_e}$ is the electron thermal speed, and m_e is the

electron mass. Since the electron density is similar to that of ion by assumption of

quasineutrality, and the m_i is much higher than m_e, resulting in greater electron saturation current

compared to ion saturation current. Figure 2-12 presents the Langmuir Probe measurement taken

at the O_2 operating condition (500 W, 2.5 mT), T_{eV} and n_i were calculated as 2.4 eV and 3.35 $\times$

10^{10} #/cm^{-3} respectively, translating to an ion flux of 8.9 $\times$ 10^{15} cm^{-2} s^{-1} by equation below. (Chen

2015)

$$J_{ion} = n_i \left(\frac{T_{eV}}{M} \right)^{1/2} \tag{2.9}$$

The next parameter that may be determined is the electron temperature, T_{ev} (eV). A

Maxwellian distribution of electrons is commonly assumed, but since this is not necessarily true.

A useful concept to implement is the electron energy distribution function (EEDF) – $g_e(\varepsilon)$ from

which both n_e and an effective electron temperature T_{eff} can be calculated. The EEDF is defined

as:

$$g_e(\varepsilon) d\varepsilon = 4\pi v^2 f_e(v) dv \tag{2.10}$$

where v is the electron velocity and f_e is the electron distribution function. In terms of energy (ε =

½ mv^2/e) this equation takes the form:

$$g_e(\varepsilon) = 2\pi \left(\frac{2e}{m} \right)^{3/2} \varepsilon^{1/2} f_e[v(\varepsilon)] \tag{2.11}$$

which can then be expressed in terms of I_e and probe potential V as:

$$g_e(V) = \frac{2m}{e^2 A} \left(\frac{2eV}{m} \right)^{1/2} \frac{d^2 I_e}{dV^2} \tag{2.12}$$

where *m* is the electron mass, *e* is the electron charge and A is the area of the probe tip. For a Maxwellian distribution of electrons, the electron energy distribution function, expressed as the electron energy probability function (EEPF) $g_p(\varepsilon) = \varepsilon^{-1/2} g_e(\varepsilon)$ then can be expressed as:

$$g_p(\varepsilon) = \frac{2}{\sqrt{\pi}} n_e T_{eV}^{-3/2} e^{-\varepsilon/T_e} \qquad (2.13)$$

when $\ln[g_p(V_p - V_s)]$ is plotted versus $V_p - V_s$, T_e can be determined from the slope of the linear region. However in the case of a non-Maxwellian distribution, the slope is not linear and thus the effective electron temperature is more suitable, defined as:

$$T_{eff} = \frac{2}{3}\langle\varepsilon\rangle = \frac{2}{3n_e}\int_0^\infty \varepsilon g_e(\varepsilon)d\varepsilon \text{ , where } n_e = \int_0^\infty g_e(\varepsilon)d\varepsilon \qquad (2.14)$$

Thus, by integrating the curves of both $g_e(V_p - V_s)$ and $(V_p - V_s)g_e(V_p - V_s)$ vs. $(V_p - V_s)$, n_e and T_{eff} can be calculated. For the I-V characteristic from the Figure 2-12 calculated n_e and T_{eff} using this method were 3.5×10^{16} m^{-3} and 4.17 eV respectively. Once the plasma density and electron temperature are known, the Debye length of the plasma (the characteristic distance scale over which significant charge densities can spontaneously exist) can be calculated by the following equation:

$$\lambda_{De} = \left(\frac{\varepsilon_0 T_{eV}}{n_e e}\right)^{1/2} \qquad (2.15)$$

where ε_0 is the permittivity of free space, and e is the fundamental charge of an electron. Based on the values of T_{eV} and n_e above, the calculated Debye length for the ICP system was 0.08 mm.

2.6.2 Optical Emission Spectroscopy

      The Ocean Optics S2000 system used in this study is comprised of five fiber optic cables (designated as Master and Slaves 1-4) with a total wavelength range of 200-1000 nm. These are connected to an analyzer which interfaces with a computer workstation for data collected. The fiber optic cables are attached to a viewport in the ECR reactor through a machined cover held in place by screws. The described system and a sample OES spectrum are shown in Figure 2-13.
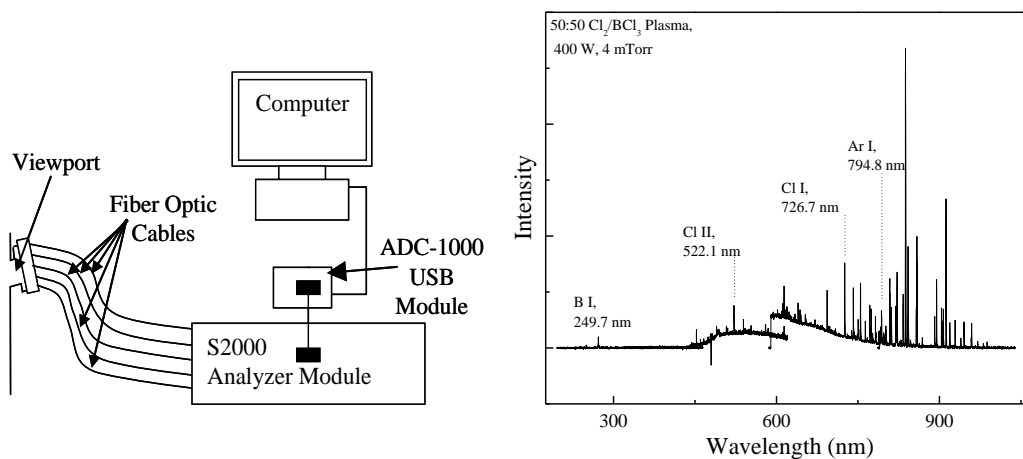
Figure 2-13 Schematic of OES setup, and sample spectrum of Cl_2 plasma with 5% Ar addition.

      The interaction between plasma species such as electrons, ions and neutrals results in the creation of particles with excited electronic states. These excited species can subsequently undergo electric dipole radiation to emit photons, returning to a relaxed state. The energy of these photons is characteristic of a particular transition in the plasma species, corresponding to the difference between initial and final quantum energy states of the relaxed electron. The use of this measured energy to ascertain the identity of species present in the plasma is known as optical emission spectroscopy (OES). Among the primary advantages of OES is its non-intrusive nature.

OES has been utilized to monitor the endpoints of plasma etching experiments (Litvak 1996), quantify the relative percentages of plasma species present, calculate the reaction kinetics of said species through actinometry (Booth, Joubert et al. 1991, Booth and Sadeghi 1991), and obtain bulk plasma information such as T_e, n_e and EEDF using Trace Rare Gases OES (Donnelly and Schabel 2002).

As OES spectra are gathered periodically over the time span of an experiment, the endpoint of etching can be estimated by the appearance of certain lines (e.g. atomic Si) in the spectra. Additionally, species can be quantified using the principle of actinometry, which is described as follows. For an electron impact excitation from the ground state to an excited state, the equation relating the measured emission intensity to the concentration of the free radical species is as follows:

$$I_\lambda = \alpha_{\lambda A} n_A \tag{2.16}$$

where $\alpha_{\lambda A}$ is defined by the following equation:

$$\alpha_{\lambda A} = k_D(\lambda) \int_0^\infty 4\pi v^2 dv Q_{A^*}(p, n_e) \sigma_{\lambda A}(v) v f_e(v) \tag{2.17}$$

In the above equations I_λ is the optical emission intensity, n_A is the concentration of free radical A, $\sigma_{\lambda A}$ is the cross section for the emission of a photon having wavelength λ due to electron impact excitation of A to A^*, k_d is the detector response constant, Q_{A^*} is the quantum yield for photon emission from the excited state, and f_e is the electron distribution function. However, since the aforementioned variables are not normally obtainable, it is impossible to solve for n_A and thus the measured intensities can only provide qualitative information. To circumvent this problem, a trace amount (generally < 5% of the inlet flow) of a known

66

concentration of inert gas (the actinometer) is fed into the plasma. An emission line (T) with an excited state that possesses excitation threshold energy close to that of the chosen radical A is then selected so that the cross sections for the radical and the actinometer are similar near the excitation energy. The intensity of the emission line from the actinometer can then be described in a manner analogous to the first set of equations:

$$I_{\lambda'} = \alpha_{\lambda'T} n_T \tag{2.18}$$

where

$$\alpha_{\lambda'T} = k_D(\lambda') \int_0^\infty 4\pi v^2 dv Q_{T^*}(p, n_e) \sigma_{\lambda'T}(v) v f_e(v) \tag{2.19}$$

On an energy scale, only the energetic tail end of the electron distribution is above the threshold energy for the photon emission cross sections, which allows the cross sections near the threshold energy to be approximated as linear functions of electron velocity:

$$\sigma_{\lambda A} \approx C_{\lambda A}(v - v_{thr}) \tag{2.20}$$

and

$$\sigma_{\lambda'T} \approx C_{\lambda'T}(v - v_{thr}) \tag{2.21}$$

where $C_{\lambda A}$ and $C_{\lambda'T}$ are proportionality constants. The ratio of intensities of the two emission lines can then be taken to yield the radical density:

$$n_\lambda = C_{AT} n_T \frac{I_\lambda}{I_{\lambda'}} \tag{2.22}$$

where

$$C_{AT} = \frac{k_D(\lambda) Q_{A^*} C_{\lambda A}}{k_D(\lambda') Q_{T^*} C_{\lambda'T}} \tag{2.23}$$

If the chosen emission wavelengths are similar to each other, i.e. $\lambda' \sim \lambda$ and $Q_{A^*} \sim Q_{T^*}$, then $C_{AT} \sim C_{\lambda A}/C_{\lambda'T}$ can be determined and an absolute value of the radical density n_A can be

calculated. (Coburn and Chen 1980) In general for the experimental section of this work the actinometer used is five percent of argon in the inlet gas feed. The normalized intensities of the BCl (272 nm), Cl (738.62 nm) and Cl (792.54 nm) lines to Ar (750.42 nm) in a pure BCl$_3$ discharge is shown in Figure 2-14 from Sha et al. (Sha and Chang 2004)
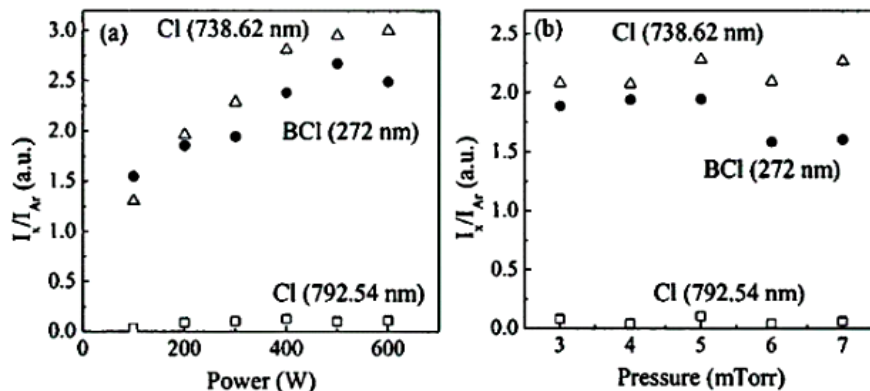
Figure 2-14 OES intensity ratio of Cl (738.62 nm), BCl (272 nm) and Cl (792.54 nm) to Ar (750.42 nm) as a function of the power at 5 mTorr (left) and chamber pressure (right) at 300 W in a pure BCl$_3$ plasma. (Sha and Chang 2004)

2.6.3 Quadrupole Mass Spectrometry

A UTI 100C line of sight quadrupole mass spectrometer is set up on this reactor in order to analyze the ion and neutral compositions of the plasma discharges in the ICP chamber. (Figure 2-15) The mass spectrometer assembly is housed within a stainless steel manifold which is evacuated by a Leybold 361C turbomolecular pump. An orifice 0.065 inches in diameter and 0.0625 inches deep allows the passage of ions from the plasma in the upper section of the ICP reactor to the QMS. For ionization of neutral species, a potential of -50.0 V at a current of approximately 2.0 mA is applied to the filament electrons. A quadrupole - a precise square array

of four parallel metal rods between which a combined RF/DC field is maintained serves as a mass filter and also increases the sensitivity and speed of analysis. (Yinon and Klein 1971)
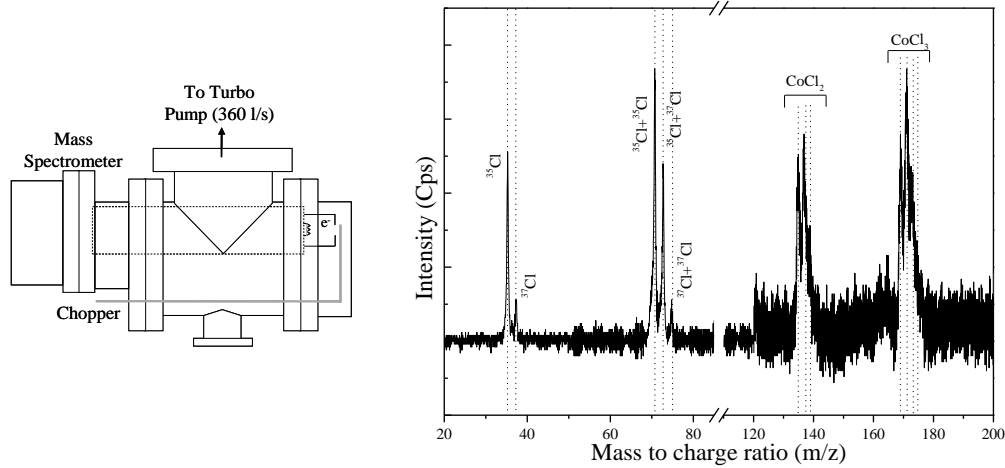
Figure 2-15 Schematic of UTI 100C Mass Spectrometer and mass spectrum for an etch of Co film in Cl_2 plasma, the Cl, Cl_2, $CoCl_2$ and $CoCl_3$ peaks have been discovered.

Since its inception, mass spectrometry has become an important tool in physics, chemistry and biology (Mayne 1952). In the context of this study, it is a versatile analytical technique that allows for detailed compositional analysis of the bulk plasma. Unlike OES, mass spectrometry allows for the identification of complicated molecules over a wide range of masses, rather than simple atomic and diatomic species. The basic principle of mass spectrometry lies in the fact that when a beam of charged species is passed through a variable magnetic field, species with a fixed mass to charge ratio can be focused into a collector and spectra dependent only on mass can be obtained. (Aston 1920) By comparing these spectra to calculated isotope patterns of the various molecules that may be present in the plasma, the composition of the discharge can be verified. Figure 2-16 depicts the isotope composition patterns of the Cl_2 that was encountered in this study.
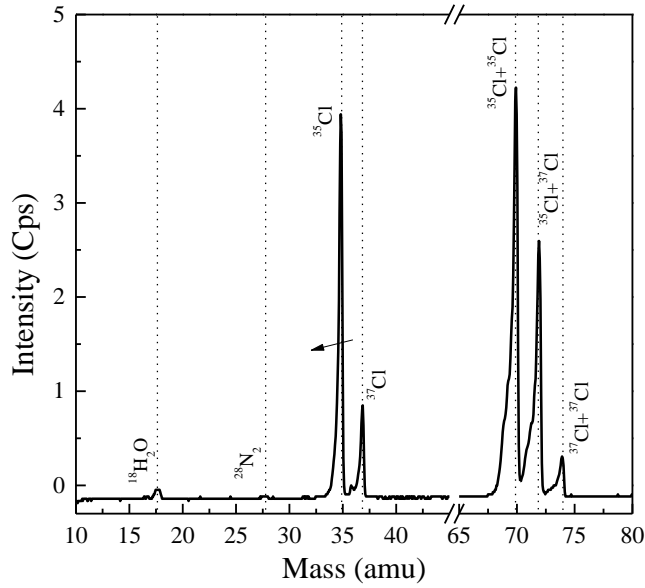
Figure 2-16 Naturally occurring isotope composition patterns of the Cl_2.

For QMS systems, there is an inverse relationship between the mass to charge ratio of species and the sensitivity of the spectrometer. It is important to determine this sensitivity change as a function of mass to charge ratio in order for quantitative analysis to be considered accurate. For this particular QMS, the relationship is as follows.

$$I \propto \frac{1}{m_c^k} \tag{2.24}$$

where I is the signal intensity and m_c is the mass to charge ratio. The constant k varies between 1.0 and 1.2. (Chae, Vitale et al. 2003)

2.7 Surface Characterization

2.7.1 X-Ray Photoelectron Spectroscopy

Originally known as Electron Spectroscopy for Chemical Analysis (ESCA), x-ray photoelectron spectroscopy (XPS) is based on the fact that when a material sample is bombarded with ionizing radiation or high energy particles, electrons possessing energies specific to each element are emitted from either inner or outer valence shells. By measuring the kinetic energy of these electrons, the ionization potential or binding energy can be derived using the following equation:

$$E_k = h\upsilon - E_b - \Phi \tag{2.25}$$

where E_k is the kinetic energy of the electron, $h\upsilon$ is the energy of the incident radiation, E_b is the binding energy of the electron, and Φ is the work function of the spectrometer (Hagström, Nordling et al. 1964). When the radiation source used is an X-ray source (Mg Kα, 1254 eV or Al Kα, 1487 eV), this technique is known as XPS. Use of a crystal monochromator can further enhance the resolution of the electron spectra and increase the accuracy in interpretation of results by reducing some of the uncertainty associated with inherent linewidths and degree of chemical shifts (Siegbahn, Barnett et al. 1972).

The XPS system used to take the measurements in this study was a Kratos XPS Axis Ultra DLD unit. The Al Kα anode (1486.6 eV emission) was used with a monochromator at a 30° takeoff angle. Survey scans were performed at 160 eV pass energy, 1 eV step size and 100 ms dwell time, while detailed scans were performed at 20 eV, 0.1 eV step size and 400 ms dwell time.

XPS can also be used to obtain information about the local structure of solid surfaces. The immediate environment, charge and oxidation state of a particular atom can all have effects on the binding energies of its electrons. By comparing the shift in energy of an atom relative to a standard value, specific details about the aforementioned parameters can be deduced.

The integrated intensity of a specific peak is proportional to the number of photoelectrons per second from that peak, given by the following equation:

$$I = nf\sigma\theta y\lambda AT \tag{2.26}$$

where n is the number density of atoms of that element in the sample, f is the x-ray flux, σ is the photoelectric cross-section for the atomic orbital of interest, θ is the angular efficiency factor for the instrumental arrangement, y is the efficiency of the photoelectric process for formation of photoelectrons with the normal photoelectron energy, λ is the mean free path of the photoelectrons in the sample, A is the area of the sample from which photoelectrons are detected, and T is the detection efficiency. If rearranged in terms of the density:

$$n = \frac{I}{f\sigma\theta y\lambda T} = \frac{I}{ASF} \tag{2.27}$$

where the denominator is defined as the atomic sensitivity factor ASF and used only in calculations involving a ratio of sensitivity factors. This is because quantities in ASF can vary based on references used, yet the ratio remains unaffected. The atomic fraction of an element in the film can be determined from the fraction of corrected integrated intensity of one peak from the element of interest over the summed corrected integrated intensities of each peak from all of the elements in the film as shown in the following equation:

$$C_x = \frac{n_x}{\sum_i n_i} = \frac{I_x / ASF_x}{\sum_i I_i / ASF_i}$$

(2.28)

The atomic sensitivity factors are XPS equipment dependent and the elements encountered in this study are tabulated along with the spin orbital splitting (S.O.S.) values and peak binding energy (B.E.) in Table 2-2.

Table 2-2 XPS Atomic Sensitivity Factors (ASFs) for elements of interests.

Element	Line	B.E. (eV)	S.O.S	ASF
B	1s	186.5	-	0.159
C	1s	284.6	-	0.278
N	1s	396.8	-	0.477
O	1s	529.2	-	0.780
F	1s	684.8	-	1.000
Mg	2p	49.6	0.30	0.168
Si	2p	99.7	0.50	0.328
Cl	2p	198.6	1.50	0.891
Fe	2p	706.7	13.20	2.957
Co	2p	778.3	15.10	3.59
Ni	2p	852.7	17.50	4.044
Cu	2p	932.7	19.60	5.321
Pd	3d	334.8	5.25	5.356
Pt	4f	17.1	3.35	5.575
Ta	4f	230	12.00	5.158

The XPS system used to take the measurements in this study was a Kratos XPS Axis Ultra DLD unit. The Al Kα anode (1486.6 eV emission) was used with a monochromator at a 30° takeoff angle. Survey scans were performed at 160 eV pass energy, 1 eV step size and 100 ms dwell time, while detailed scans were performed at 20 eV, 0.1 eV step size and 400 ms dwell time. A schematic and sample spectrum of the XPS is shown in Figure 2-17.
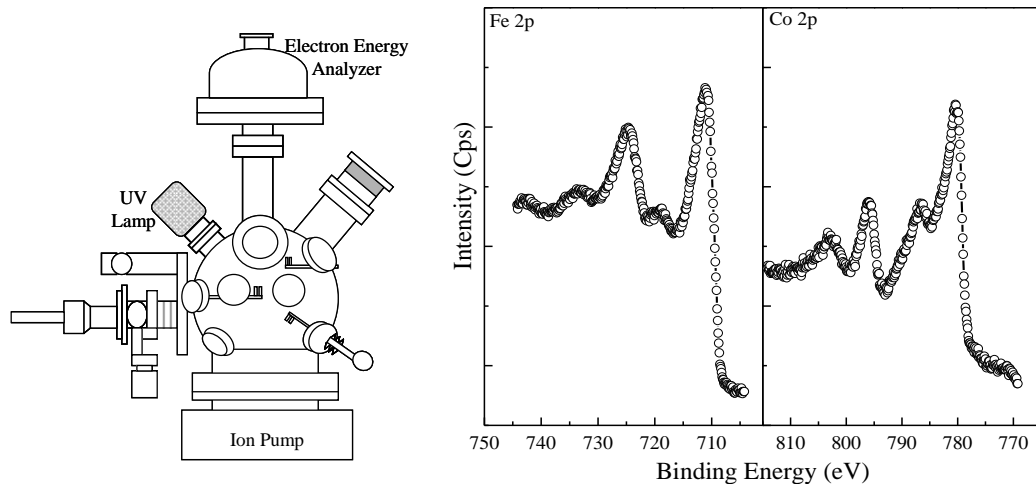
Figure 2-17 Schematic of XPS system and sample spectra for the Fe 2p and Co 2p peaks after etching a CoFe alloy film in a Cl_2 plasma.

Other variation on the XPS process involves adjusting the take-off angle at which electrons are detected. Doing so allows the effective depth from which an electron emitted (and thus the maximum depth that can be probed) is controlled. This is due to the restricted mean free path of the electrons within a surface film. The effect is illustrated in the following Figure 2-18:
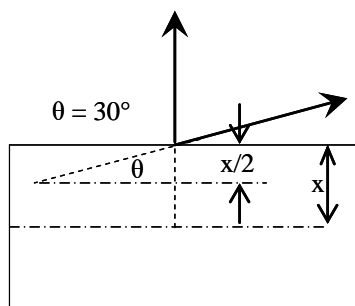
Figure 2-18 Illustration of the variation in escape length from a planar surface at take-off angles of 90° and 30°. At a take-off angle of 30° an excited electron can only exit from a depth half that of one from a surface oriented at 90°.

This technique is referred to as angle-resolved XPS (ARXPS) and can be used to conduct depth profiling of a surface film, allowing a greater degree of insight into the composition of a film (Layadi, Donnelly et al. 1997). The percentages of elements present are often normalized to

the intensity of the substrate peak for each variation in take-off angle. Figure 2-19 shows the Pt

4f spectra taken at three different electron take-off angles of 30°, 60°, and 90° (measured from

the substrate normal) for the Pt (20 nm) treated by 500 W ICP O_2 plasma for 5 min. First of all,

the area under the spectra remained the same through all the angles, suggesting a normalized

intensity has achieved. Second, the intensity of Pt^{0+} peak increased while that of Pt^{4+} decreased

from 30° to 90°, implying a thin layer of platinum oxide on the metallic platinum film. By

quantitatively comparison, the amount of Pt^{4+} in 30°, 60°, and 90° are 23%, 20%, and 5%,

respectively.
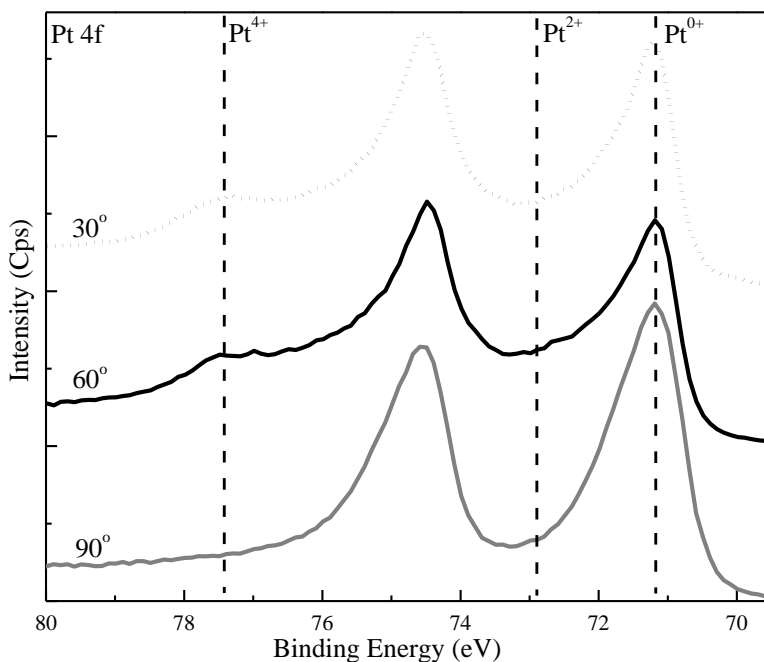
Figure 2-19 XPS spectra taken for Pt (20 nm) treated by 500 W O_2 ICP plasma for 5 min. The Pt 4f spectra taken at three electron take-off angles. From the top to bottom are 30° (dash line), 60° (solid line), 90° (gray line), respectively.

XPS can not only characterize the surface chemical state, but it can also be utilized to

estimate the thickness of thin films less than 10 nm thick by quantification. A good example of

XPS quantification would be estimating the thickness of the oxide on the top of metal by O_2 plasma treatment shown in Figure 2-20.

Pre-treated Pt

O₂ plasma treated Pt

PtO$_x$

Pt

Pt
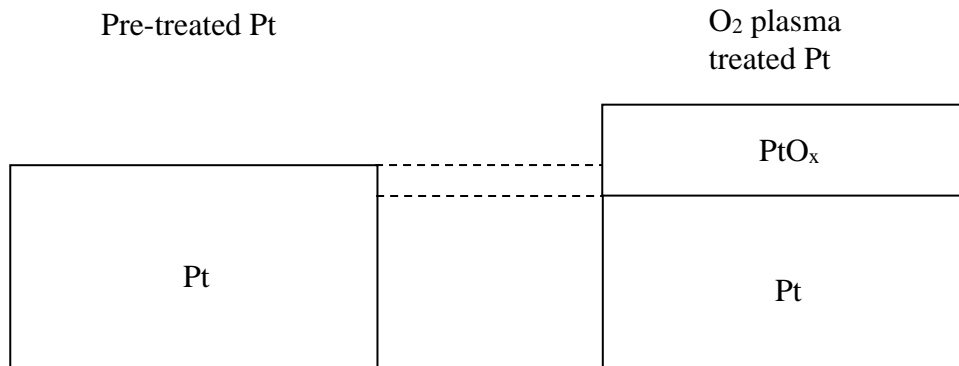
Figure 2-20 Basic model assumed for the formation of platinum oxide on a metallic Pt surface through O_2 plasma treatment.

The basic model of metallic platinum to platinum oxide conversion for Pt film via O_2 plasma treatment is shown. Based on the mass balance criteria, the formation of platinum oxide via O_2 plasma needs to consume corresponding amount of metallic Pt on the surface. The volume density of the platinum oxide (Pt(IV)O_2), 11 g/cm^3, is much lower than that of metallic Pt, 21 g/cm^3, suggesting the expansion of volume for converting platinum to platinum oxide. The basic model would be helpful on interpreting XPS data for thickness quantification.

XPS quantification of the plasma-produced platinum oxide on 20 nm metallic platinum film utilizes Pt 4f, O 1s spectra and survey. The survey scan is needed to confirm no other element is found except platinum, oxygen, and adventitious carbon. Although the adventitious carbon would attenuate signal of electron of platinum, the exposure time of platinum film in the air was controlled, suggesting a negligible amount of carbon left on the platinum surface. Meanwhile, a thick Pt film (20 nm) was chosen in quantifying oxide thickness to avoid the signal from the underlying Si substrate. An example of XPS spectra for both pre-treated and O₂ plasma

76

treated Pt is shown in Figure 2-21. First, the survey in Figure 2-21 (c) shows platinum, oxygen, and carbon without contamination. A qualitative comparison of two samples in Pt 4f shows a significantly change with an additional peak, and the intensity of O 1s increased dramatically after O_2 plasma treatment. Quantitatively deconvolution of the range of spectra actually reveals that at least two new peaks, Pt $^{4+}_{7/2}$ and Pt $^{4+}_{5/2}$, emerge in Pt 4f. All the peaks were fitted by the same asymmetric Gaussian-Lorentzian sum function, and the separation of the doublet peaks for Pt 4f chemical state is held constant. For the Pt 4f region in Figure 2-21 (a), a minimum of three doublet peaks are required in order to reasonably fit the data. On the other hand, the pre-treated Pt (metallic) only presents Pt^{0+} doublet peak with weak Pt^{2+} doublet peaks. For the O 1s region, a background oxygen signal was detected due to the adventitious oxygen in physisorbed molecules in pre-treated sample, but an obvious O-Pt peak appeared after O_2 plasma treatment.
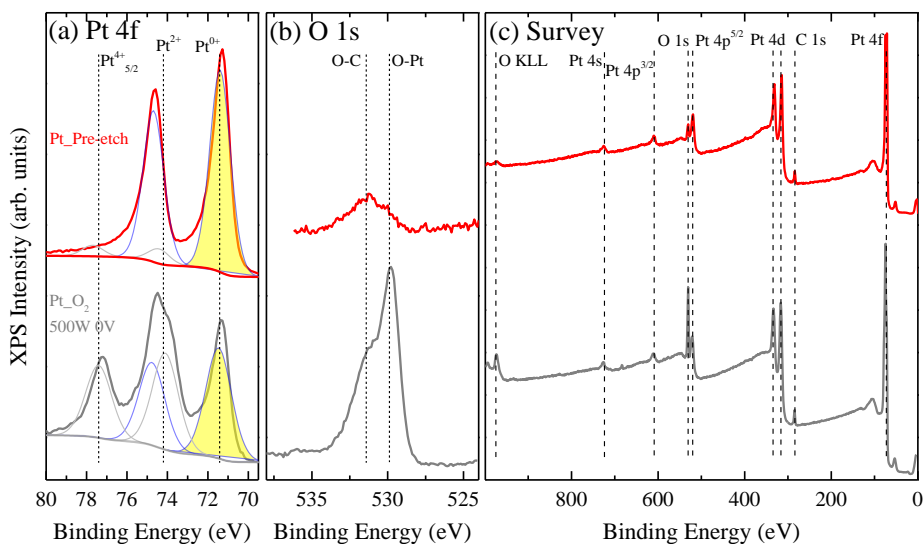
Figure 2-21 XPS spectra taken for pre-treated and O_2 plasma treated Pt with (a) Pt 4f, (b) O 1s, and (c) Survey.

A basic model presented in Figure 2-20 was employed for the purposes of quantifying oxide thickness. According to the model, the intensity of metallic doublet Pt 4f peaks should be

attenuated by $\exp\left(\dfrac{-d}{\lambda\cos\theta}\right)$, where d is the thickness of oxide on the top of metallic Pt, λ is the

inelastic mean free path (IMFP) of an electron in platinum oxide at the kinetic energy associated

with the peak, and θ is the electron take-off angle. The ratio of oxide thickness to inelastic mean

free path can be calculated by the ratio of Pt^{0+} intensity of Pt with O_2 plasma treatment to that

without O_2 plasma treatment:

$$\frac{d}{\lambda} = -\ln\left[\frac{Pt^{0+}(\text{Pt with } O_2 \text{ plasma treatment})}{Pt^{0+}(\text{Pt without } O_2 \text{ plasma treatment})}\right] \qquad (2.29)$$

The advantage of the model is that the ratio of platinum oxide thickness to inelastic mean free

path can be extracted independently from the platinum oxide properties, but the platinum oxide

thickness would still requires inelastic mean free path of an electron in platinum oxide.

A database of electron effective-attenuation-length released from the US National

Institute of Standards and Technology (NIST) (Jablonski and Powell 2002) with the empirical

approximation formula developed by Tanuma et al. (Tanuma, Powell et al. 1994) provide the

estimation of inelastic mean free path of electron as a function of electron kinetic energy in

Figure 2-22. The detailed information for estimating inelastic mean free path (λ) of metal oxide,

including, Pt, Pd, Co, Fe, and Cu are shown in Table 2-3, where E_g is band gap in eV, N_v is the

number of electron in the valence band, and bulk density of film is utilized in g/cm^3. Since the

kinetic energy of electron at PtO$_x$ peak is around 1415.5 eV, the corresponding IMFP is

estimated to be 1.96 nm. Therefore, the thickness of platinum oxide could be calculated by the

equation above, which the platinum oxide generated by O_2 plasma 500 W without bias is around

0.83 nm.

Table 2-3 The detail information required for estimating the inelastic mean free path of electron (λ) in metal oxide including Pt, Pd, Co, Fe, and Cu. (Jablonski and Powell 2002).

Metal	Pt		Pd		Co		Fe			Cu	
Compound	PtO	PtO$_2$	PdO	PdO$_2$	CoO	Co$_3$O$_4$	FeO	Fe$_2$O$_3$	Fe$_3$O$_4$	Cu$_2$O	CuO
E$_g$ (eV)	1.40	1.25	4.50	2.00	2.40	1.96	2.40	2.20	0.10	2.17	1.55
N$_v$ (#)	16	22	16	22	15	51	14	34	48	28	17
Density(g/cm^3)	14.10	10.20	8.30	4.23	6.44	6.11	5.7	5.2	5.0	6.0	6.3
λ (nm)	1.74	1.96	1.82	2.40	1.43	1.47	1.59	1.67	1.67	1.23	1.22
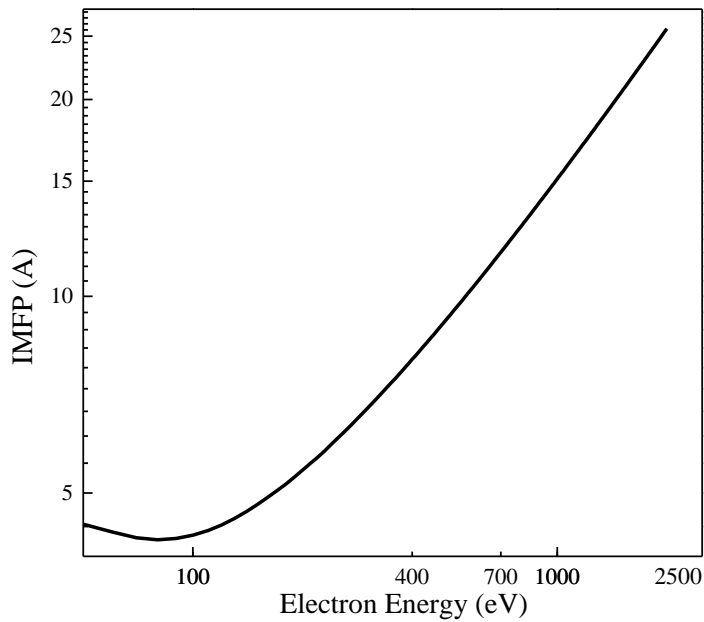
Figure 2-22 Inelastic-Mean-Free-Path in (nm) as a function of electron energy (eV) of electron in platinum oxide (Jablonski and Powell 2002).

2.7.2 Scanning Electron Microscopy

The scanning electron microscope (SEM) allows observation of a surface at significantly higher resolutions than that of an optical microscope, with a depth of field that is orders of magnitude larger. Figure 2-23 displays a schematic of the essential components of an SEM, as

well as an image of a patterned Pt sample. A 120-nm-thick of Pt was deposited on Si substrate, and a 50-nm-thick Ti hard mask was patterned by lift-off process. The spacing of Ti was 10nm with a 30 nm pitch on Pt film. Most of the SEM images taken in this work were using Nova 600 at 10 kV and 0.54 nA with a processed resolution of 1 nm. The current of filament is 0.27 mA at 1×10^{-5} torr, which was controlled by a mechanical pump and turbo pump. The magnification of image was ranging from 500 to 250,000×.

A simple explanation of the operational concept follows. Electrons are accelerated toward the anode with energies ranging from volts to tens of kilovolts and subsequently pass through one or more lenses which serve to reduce the image of the electron source to a nanometer scale as it impinges on the plane of the surface. A scanning generator is used to deflect the path of the electron beam, allowing the beam to be moved over the sample surface in a pattern. The interaction between the electron beam and the surface generates secondary electrons which are collected and passed through an amplifier before being transmitted to a display cathode ray tube (CRT). Other types of emission such as light, x-rays, IR and UV radiation may also be produced, and collected.

From the obtained images, information about the physical dimensions of the pre- and post-etched samples can be derived, which can be used to calculate effect of the plasma parameters and chemistry on the etch rate and sidewall angles of the features.
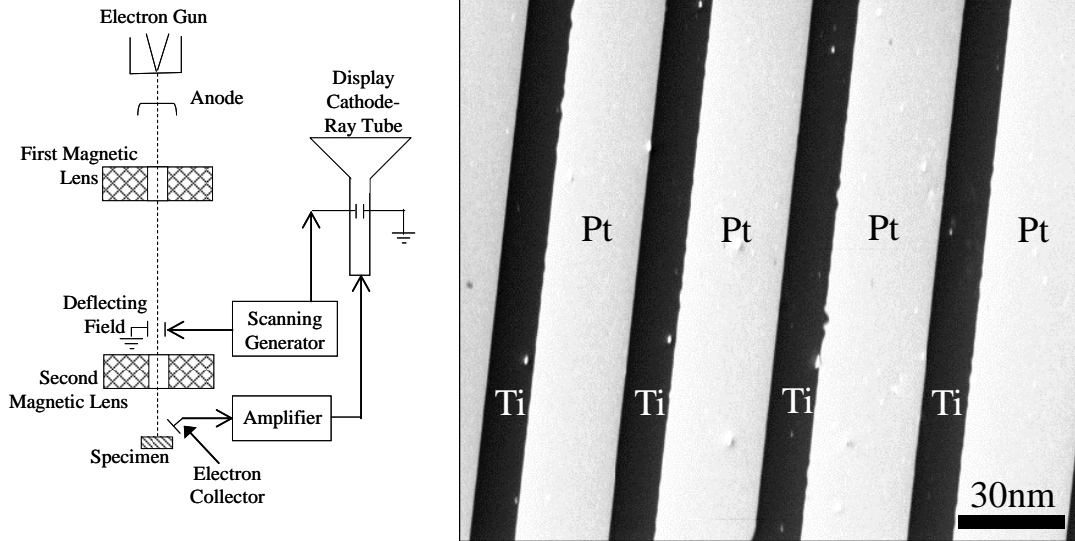
Figure 2-23 Components of a scanning electron microscope and cross-sectional image taken of a patterned cobalt sample.

2.7.3 Dektak Surface Profiler

Stylus profiling is a technology of surface metrology that is used to determine the thickness change of two different surface treatment. Stylus profilers are versatile functional tools that not only measure the film thickness but also surface roughness, thin film stress, and waviness. The movement of a small-diameter stylus can record the surface morphology in both vertical and horizontal directions. Via direct contact with the surface, the stylus measurement provides highly precise and repeatable results. Therefore, it becomes the standard for monitoring thin film deposition or etching processes. A stylus is composed of metal with a diamond tip, mounted on an arm as shown in the Figure 2-24, and coupled with a linear variable differential transformer (LVDT). The LVDT is the heart of the profiler and is driven by a special electromechanical transducer which composed of one primary coil, two secondary coils and a movable coil in between. The signal detected by the primary coil can vary the displacement of

the two secondary coils. The output of multiplexed signal is then filtered to provide a varying DC signal. In the end, the varying DC signal is digitized and stored to represent the surface profile of the sample. A schematic and sample spectra of the profiler are shown in Figure 2-24.

To prepare the sample for measuring the thickness change by profiler, the part of sample is first covered by the Kapton® Tape and followed by etching process. And the Kapton® Tape is removed for measuring the step under the profiler once the etching process is done. In the Figure 2-24, a Co film is etched by Ar ion beam (top) and Ar ion beam assisted acac vapor etch (bottom). The removal thickness of Co etched by Ar ion beam and Ar ion beam assisted acac vapor are 37.1, and 57.5 nm. All of the spectra taken in this work were using Dektak 150 surface profiler, which allowed sample size in maximum of six inch diameter and one centimeter thick. The tool can measure steps less than 10 nm as well as measure surface roughness, and the step-height repeatability is 0.6 nm. The standard stylus of 25 µm wide and stylus force of 3.0 mg is selected, and a scan resolution of 0.513 µm/sec is applied onto the samples in this work. (Thomas, Hartnett et al. 1988)
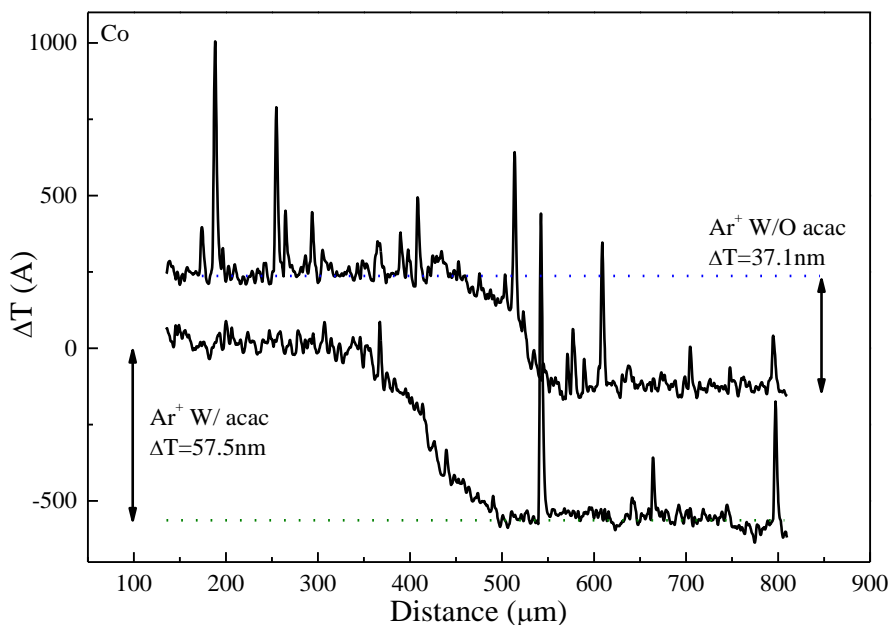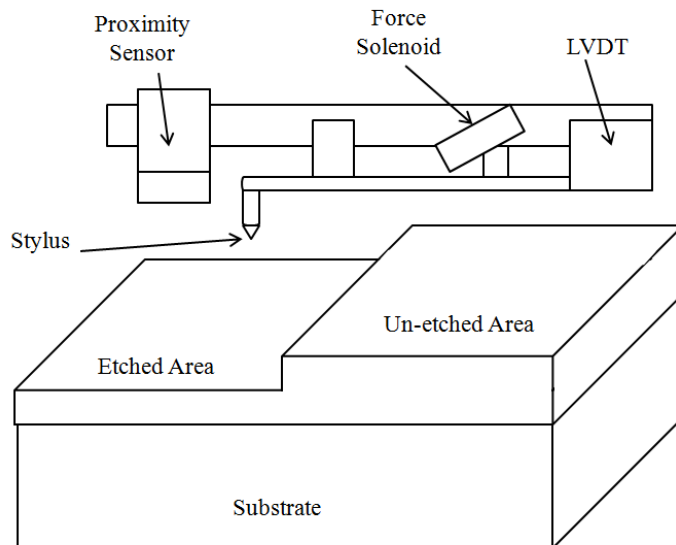
Figure 2-24 Schematic of Dektak profiler system and sample spectra for the Co etched by Ar$^+$ beam with and without acac alternative etch.

2.7.4 Spectroscopic Ellipsometry

Spectroscopic ellipsometry is a power tool to detect the optical properties of materials through the change of polarization state after interaction with the sample. It provides a sensitive, nondestructive and comprehensive approach to achieve a highly accurate measurement of film thickness and optical properties.

As Figure 2-25 presents, a beam of linearly polarized light with known wavelength incidents onto the sample surface, and the polarization state of the incident light is interfered to elliptical polarization. The polarization state depends on multiple parameters such as the incident angle of light and the refractive index of the sample. The ratio ρ of the Fresnel amplitude reflection coefficients for p- and s-wave polarized light is defined by

$$\rho = \frac{r_p}{r_s} \tag{2.30}$$

Where, r_p and r_s stand for amplitude reflection coefficients for p- and s-wave, respectively. (Tompkins and McGahan 1999, Fujiwara 2007) All the terms of ρ, r_p and r_s are complex, which can be expressed by amplitude (Ψ) in real part and phase (Δ) in imagine part as follows,

$$\rho = \tan \Psi \exp(i\Delta) \tag{2.31}$$
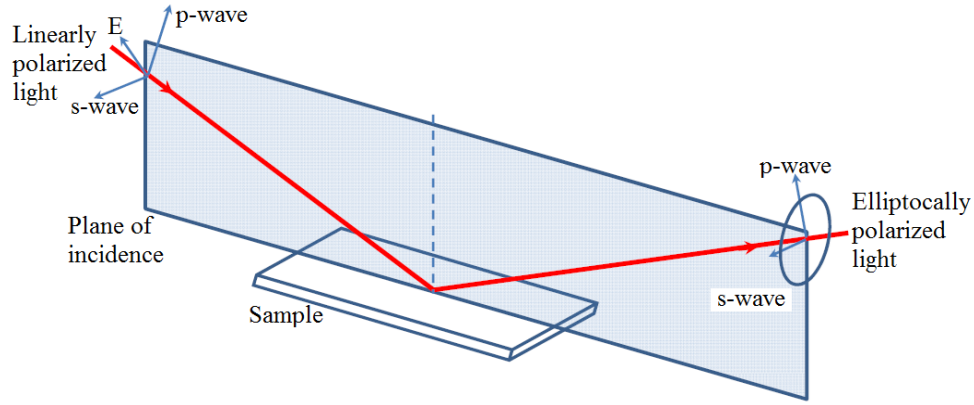
Figure 2-25 Schematic view of a ellipsometric measurement in reflection configuration. The polarized beam is incident on the sample from the left side. After reflection the polarization state of the beam has changed and pursuits its propagation to the right side. (Zheng, Zhang et al. 2012)

In order to determine the thickness of the film, the process of ellipsometry data fitting and model analysis are shown here. First, the two ellipsometry parameters of Ψ and Δ can be measured by ellipsometer directly as a function of wavelength of incident polarized light. Second, a suitable model for either single or multiple films can be constructed by optical properties of material such as refractive index (n), extinction coefficient (k), band gap (Eg), and density (d). Third, a proper model is required for fitting, such Sellimeier model, Cauchy model, Lorentz model, Drude model, effective medium approximation (EMA) model etc., for each material. Finally, a comparison of measured and theoretical values of Ψ and Δ can be calculated by mean squared error (MSE), which is shown here,

$$MSE = \sqrt{\frac{1}{2n-m-1}\sum_{i=1}^{n}\left[\left(\Psi_i^{cal}-\Psi_i^{mea}\right)^2+\left(\Delta_i^{cal}-\Delta_i^{mea}\right)^2\right]} \tag{2.32}$$

where the mea and cal stand for measured and calculated parameters, respectively, n and m are the numbers of the measured data points and the analytical parameters, respectively. To get the accurate thickness of the film, several unknown parameters such as optical constant and

85

thickness are varied to produce a best fitting of the measured Ψ and Δ. Once a global minimum

of MSE is reached in the equation above, an accurate thickness in the model would be achieved.

(Tompkins and McGahan 1999, Fujiwara 2007)

A JA Woollam M88 Spectroscopic Ellipsometer has been utilized to measure the film

thickness in the work, and the spectral wavelength ranging from 280 to 760 nm is covered by this

model. Two examples for single film of Co and Pt are shown in Figure 2-26 that refractive index

(n), extinction coefficient (k) are expressed as a function of wavelength. Since cobalt is one of

the group of transition metals, at long wavelengths in the infrared region, may be expected to

behave according to the classical Drude formulas for free-electron materials, namely,

$$
\begin{aligned}
\varepsilon_1 &= n^2 - k^2 = 1 - Av_c / 2\pi(v^2 + v_c^2) \\
\varepsilon_2 &= 2nk = Av_c^2 / 2\pi v(v^2 + v_c^2)
\end{aligned}
\tag{2.33}
$$

where, A is a constant, proportional to the DC electrical conductance, v is the frequency and

v_c is the electron collision frequency. These formulas predict that in the infrared the optical

constants n and k should have large values with both increasing with wavelength. A further

review by Ordal *et al.* showed a Drude-model fit to the various experimental results. (Ordal, Bell

et al. 1985) Similar to cobalt, platinum displays Drude behavior in dielectric function above 1

eV, but deviations from a free-electron metal behavior are seen at lower energies due to

interband transitions from the d-electron to s-electron bands near the Fermi level. (Zollner 2000)

(Palik 1985, Palik 1991, Palik and Ghosh 1998) With known optical parameters such as n and k,

an appropriate fitting of the measured Ψ and Δ can be achieved with global minimum MSE in

Figure 2-27, which MSE for Co and Pt are 5.69 and 7.02, respectively. Although MSE for Co

and Pt are not extremely low, the MSE lower than 10 would be acceptable empirically. The

thickness of Co and Pt measured by ellipsometer are 40.7 and 32.8 nm, which are verified by the

measurement of SEM, 39.0 and 35.0 nm, respectively.
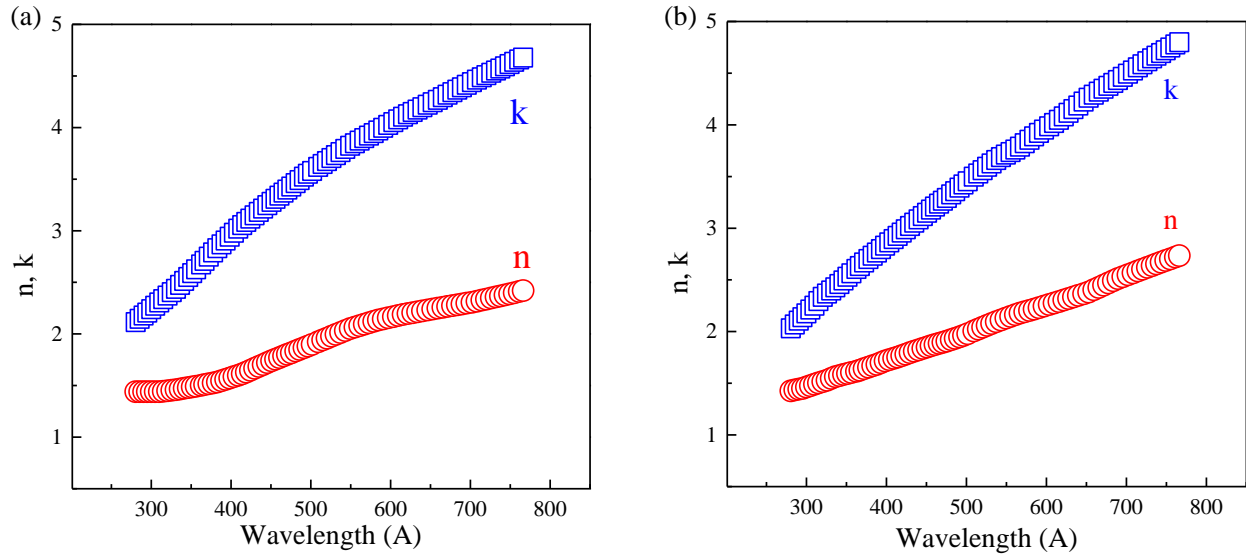
Figure 2-26 Refractive index (n) and extinction coefficient (k) as a function of wavelength for (a) Co and (b) Pt.
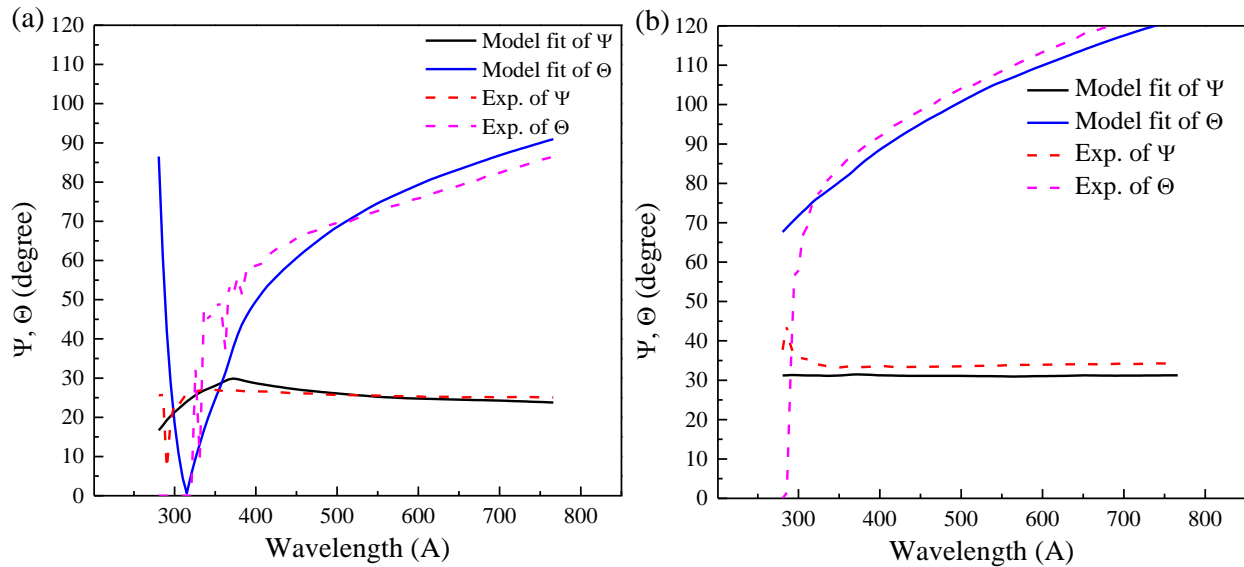
Figure 2-27　A fitting of refractive index (n) and extinction coefficient (k) measured by ellipsometer to the model of (a) Co and (b) Pt.

However, the data of refractive index (n) and extinction coefficient (k) would not available for alloy such as CoPt. A unique model for alloy to fit experimental data is built by a Bruggeman Effective Medium Approximation (EMA), which has been developed to predict the effect of inclusions of a given material within a host medium. (Aspnes 1982) The following equation has shown the approach for EMA to estimate the thickness,

$$f_{Co}\frac{\tilde{\varepsilon}_{Co} - \tilde{\varepsilon}}{\tilde{\varepsilon}_{Co} + 2\tilde{\varepsilon}} + f_{Pt}\frac{\tilde{\varepsilon}_{Pt} - \tilde{\varepsilon}}{\tilde{\varepsilon}_{Pt} + 2\tilde{\varepsilon}} = 0 \tag{2.34}$$

where, f_{Co}, f_{Pt} are the volume fractions of Co and Pt, ε_{Co}, and ε_{Pt} are the dielectric function of Co and Pt, and ε is the effective dielectric function. The fitting of the CoPt alloy is shown in Figure 2-28 that MSE is 2.67 which is relatively low compared to Co and Pt single films. The thickness measured by ellipsometer is 25.0 nm, which is within 7% difference from SEM measurement, 27.0 nmÅ, suggesting an EMA model is adequate in calculating thickness of CoPt alloy.
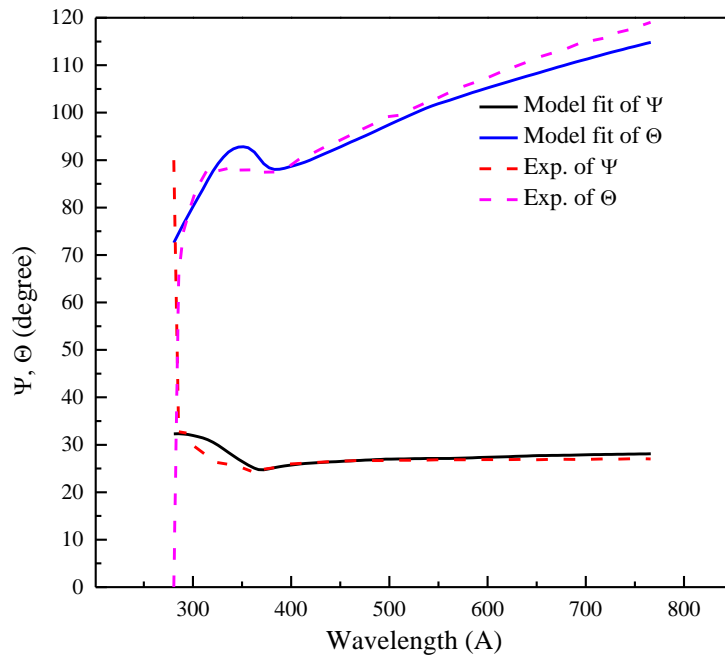
Figure 2-28 A fitting of refractive index (n) and extinction coefficient (k) measured by ellipsometer to the model developed for CoPt alloy thin films.

2.7.5 Superconducting quantum interference device (SQUID)

Superconducting quantum interference device (SQUID) magnetometer provides the highest sensitivity for magnetic field measurement, and a resolution of 10^{-12} G can be obtained. The fundamental theories behind SQUID contained quantization of the magnetic flux in a superconducting ring and the Josephson effect, which allows the tunneling of Copper pairs through a normal conducting barrier. Flux quantization suggests that magnetic flux enclosed by a superconducting loop can be quantized by,

$$\Phi_0 = \frac{h}{2e} \approx 2.07 \times 10^{-15} \, Tesla - m^2 \tag{2.35}$$

Where, h is Plank's constant and e is the electron charge (Kleiner, Koelle et al. 2004). On the other hand, a Josephson effect involves the coherent tunneling of Cooper pairs through a thin insulator sandwiched between two superconductors as shown in Figure 2-29, and only when a current passes the critical value, a voltage across the junction can be detected.
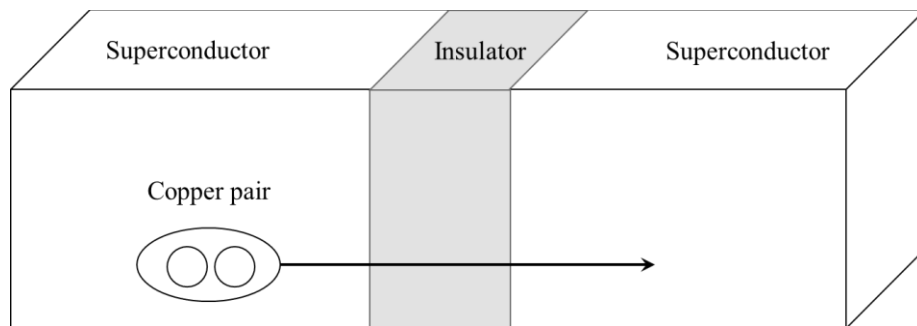
Figure 2-29 A Josephson junction is composed of two bulk superconductors separated by a thin insulating layer through which Cooper pairs can tunnel, and the Josephson junction is served as a nonlinear inductor (You and Nori 2011).

Based on the operation mode of alternating current (AC) or direct current (DC), a superconducting ring in SQUID is interrupted by one or two Josephson junctions. A DC SQUID

consists of two Josephson junctions connected in parallel on a superconducting loop and is operated in the voltage state with a current bias, and eventually a magnetic flux can be measured by the oscillation of voltage (Jaklevic, Silver et al. 1964) For AC SQUID, only a single Josephson junction inserted into a superconducting loop, which is inductively coupled to the inductor of an LC-resonant circuit excited by a current at a frequency from megahertz to gigahertz. The flux change can be detected by the amplitude of the oscillating voltage across the resonant circuit. (Silver and Zimmerma.Je 1967), (Kleiner, Koelle et al. 2004)

A magnetic property measurement system (MPMS) XL from Quantum Design with a resolution higher than 10^{-8} emu at an external magnetic field of 5.5 Tesla, and the standard setup allows the measurements at the temperature between 1.9 and 400 K with 0.5% accuracy. MPMS SQUID XL allows the measurements with the applied field pointing out-of-plane or in-plane with respect to the sample surface. A straw holder made of plastic is selected as a sample holder due to the total vertical dimension of the pickup coils is smaller than the length of the straw, which shows no contribution to the magnetic flux. However, the silicon substrate of the metal film produces a diamagnetic background signal and contributed to the magnetic flux measurement. A careful background subtraction by linear fit of the raw data at the high end of magnetic field is required. Some examples of magnetic hysteresis loop measured by SQUID for ferromagnetic, paramagnetic, and the combination of ferro- and para-magnetic materials are described below. (Cullity 1972)

A sample hysteresis loop of ferromagnetic Co with and without surface oxidation is shown in Figure 2-30 (a). In order to observe the coercivity field which the ability of a ferromagnetic material to withstand an external magnetic field, a spectrum is shown in Figure 2-30 (b). The coercivity increased from 33 to 54 Oe, and the saturated magnetization decreased

from 1125 to 923 emu/cm^3 after surface oxidation of cobalt. It is confirmed by the literature that the magnetic property of ferromagnetic Co becomes harder after surface oxidation. (Apatiga and Castano 2006)
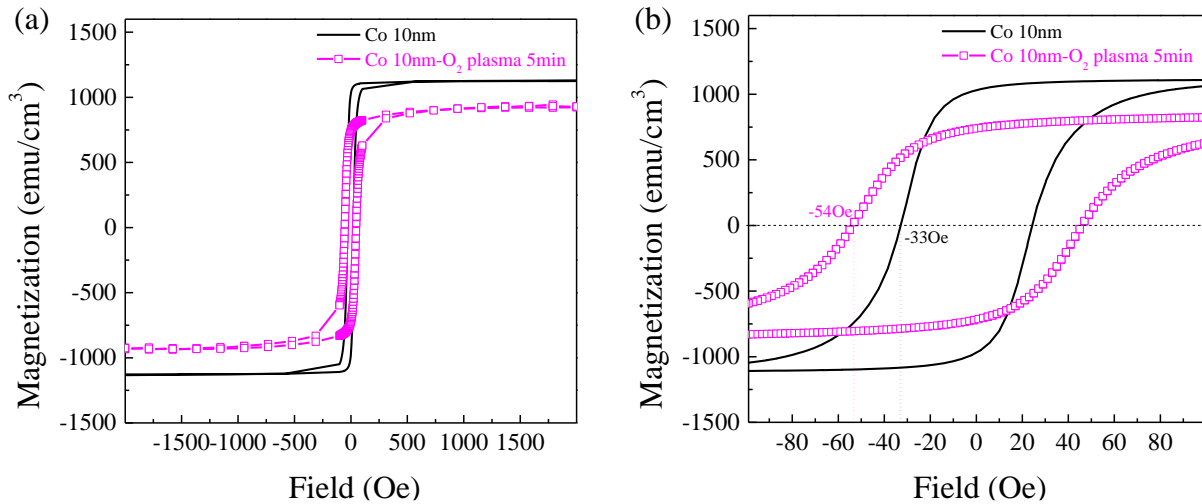
Figure 2-30 (a) Magnetic hysteresis loop of pristine Co 10 nm film (solid line) and Co treated by surface oxidation by 500 W O$_2$ plasma for 5 min (hollow square). The SQUID measurement was conducted at 300 K from -2000 to 2000 Oe. (b) Enlarged hysteresis loop from -100 to 100 Oe.

The magnetic hysteresis loop of Pt with and without surface oxidation is shown in Figure 2-31. Due to the paramagnetic characteristic of Pt, the magnetization is proportional to the applied magnetic field as shown in Figure 2-31 (a). A coercivity field of 85 Oe and saturated magnetization of 11 emu/cm^3 are found after surface oxidation in Figure 2-31 (b). (Cullity 1972)
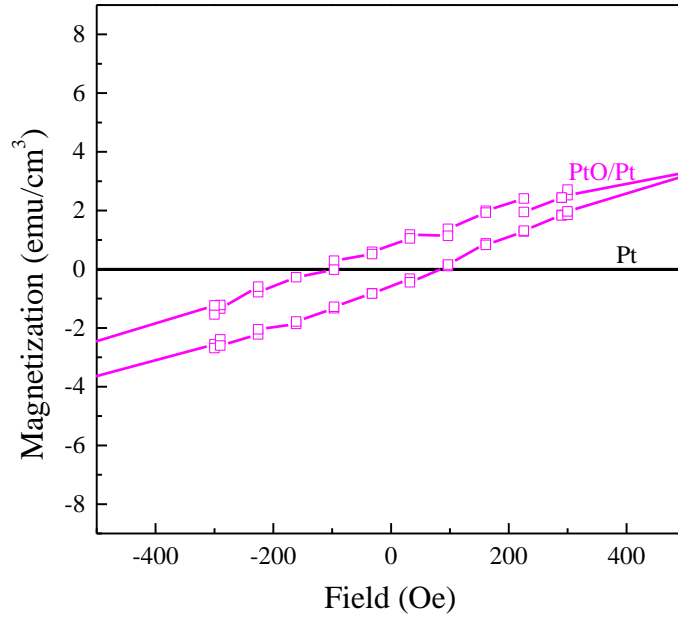
Figure 2-31 Magnetic hysteresis loop of pristine Pt 15 nm film (solid line) and Pt treated by surface oxidation by 500 W O_2 plasma for 5 min (hollow square). The SQUID measurement was conducted at 300 K from -2000 to 2000 Oe.

Finally, a magnetic hysteresis loop of CoPt alloy is measured and shown in Figure 2-32 (a), and an increase of coercivity field from 202 to 245 Oe and a decrease of saturated magnetization from 459 to 429 are observed in Figure 2-32. This increase in coercivity field is due to the formation of metal oxides on the surface of the film, changing the electron bonding states, resulting in a hard magnetic property of material. A material provides higher coercivity field may require higher applied magnetic field to switch the magnetic domains in the film, which is not preferred in memory application.
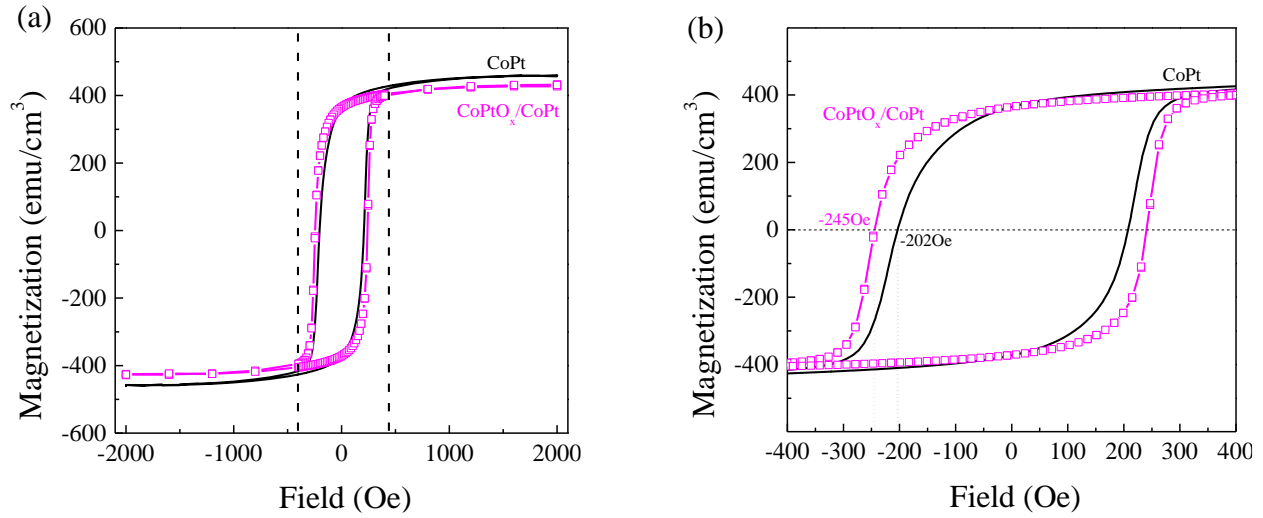
Figure 2-32 (a) Magnetic hysteresis loop of pristine CoPt 27 nm film (solid line) and CoPt treated by surface oxidation by 500 W O_2 plasma for 5 min (hollow square). The SQUID measurement was conducted at 300 K from -2000 to 2000 Oe. (b) Enlarged hysteresis loop from -400 to 400 Oe.

2.8 Solution Etching Characterization

2.8.1 Electrospray Ionization - Mass Spectrometry (ESI-MS)

A mass spectrometry using electrospray ionization (ESI) technique has been applied in the study of the formation of organometallic complex in organic chemistry etching. ESI is a technique used to assist the transfer of ions from liquid to gas phase, allowing the ions to be analyzed by ESI-MS. Neutral compounds with ionic conversion such as protonation or cationaisation can also be subjected to ESI-MS. Three main steps have been proposed to transfer ionic species from liquid to gas phase: (1) dispersal of charged droplets, followed by (2) evaporation of solvent and finally (3) ion ejection from the highly charged droplets (Figure 2-33).
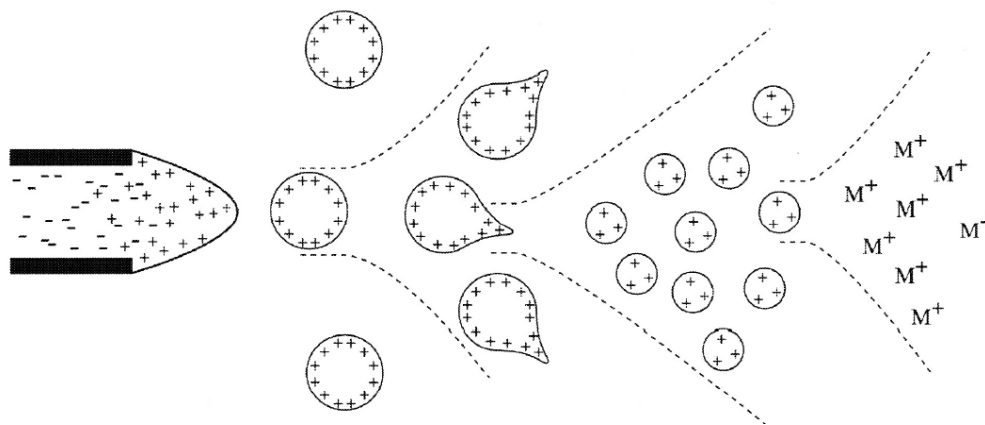
Figure 2-33 Three steps of electrospray ionization (Ho, Lam et al. 2003).

In the beginning, the sample solution is passed through the quartz capillary tube to which a high voltage is applied relative to the surrounding chamber. At the same time, the charged droplet has been generated by a biased capillary tube with identical polarity. The nebulising gas (e.g. N_2) increased the flow rate of charged droplet and reduced the size by evaporation of the

94

solvent. At the exit of the electrospray tip, the electric field strength in the charged droplet overcomes the kinetic energy barrier resulting in the ejection of ions from the surface of droplet. Finally, the emitted ions are accelerated into quadrupole mass analyzer. Depending on the mass to charge ratio (m/z), the movement of ionic species can be affected by electrical and magnetic field, and the different ion can be distinguished. Moreover, Figure 2-33 shows the tandem triple quadrupole system designed in the ESI-MS equipment which can potentially investigate the structure of molecule by analyzing the fragment of compound (Ho, Lam et al. 2003).
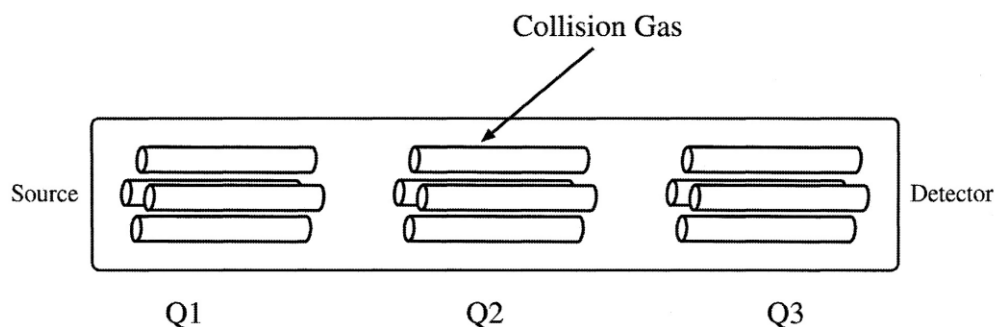
Figure 2-34 Schematic diagram of a tandem triple quadrupole system. First (Q1) and third (Q3) are mass spectrometers and the second (Q2) is a collision cell (Ho, Lam et al. 2003).

The post-etch solutions have been analyzed by the Waters Micromass LCT Premier Mass Spectrometer. The ionization of liquid species was performed by 10 µA with sample cone voltage of 100 V. Propranolol of 260.16 amu was selected as a reference mass, which allows the acquisition range of 100 – 1000 m/z (mass to charge ratio). The scanning rate is about one spectrum per second, and the full width half maximum (FWHM) is 5500, presenting an ultrahigh signal to noise ratio.

An isotope of given element is an atom with the same number of protons but a different number of neutrons, resulting in a different mass. For example, carbon shows six protons but

various neutrons of 6, 7, and 8, represented by ^{12}C, ^{13}C, and ^{14}C, respectively. The amount of ^{12}C, ^{13}C, and ^{14}C are 98.89%, 1.11%, and trace, resulting in an isotope pattern for particular species. A sample spectrum from the ESI-MS is shown in Figure 2-35. The spectra were taken from two post-etch solutions that Co and Fe films etched in 10 M acac solution at 80°C for 30 min separately. The intensity of Co(acac)$_2$ is pronounce compared to that of Fe(acac)$_3$, suggesting a higher reactivity of cobalt to acac compared to Fe.
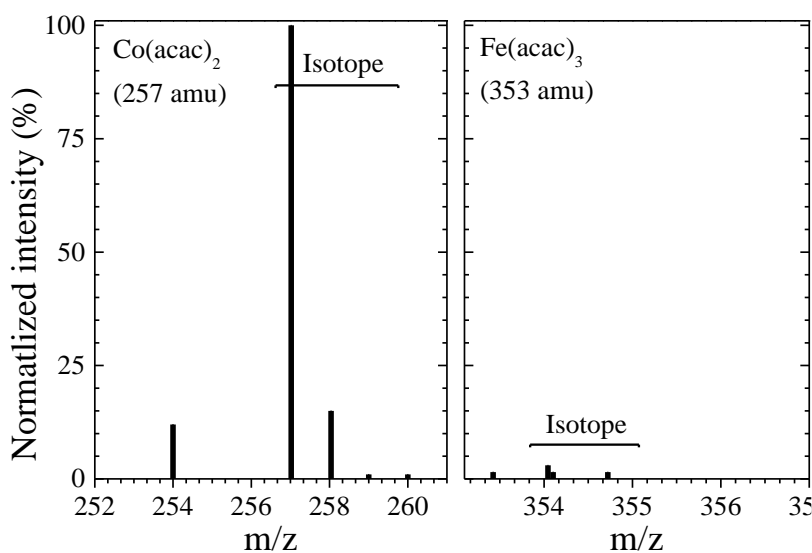
Figure 2-35 Sample spectra for the Co(acac)$_2$ and Fe(acac)$_3$ in the post-etch solution of Co and Fe etched by 10 M acac solution at 80°C for 30 min.

2.8.2 Inductively Coupled Plasma - Mass Spectrometry (ICP-MS)

Inductively Coupled Plasma - Mass spectrometry (ICP-MS) is an analytical technique utilized for detecting the element in the solution. An ICP-MS contains a high-temperature ICP source, ionizing the neutral molecule in the sample, in order to let the element to be detected by mass spectrometer. Usually, argon gas is selected to flow inside the concentric channels of the

ICP torch which is connected to a radio-frequency (RF) generator as shown in Figure 2-36, and an oscillating electric and magnetic fields can be established at the end of the torch once power is supplied to the load coil. After ignition of plasma, argon molecule is converted to argon ion, becoming a stable argon discharge, which can ionize the sample that introduced as an aerosol. Once the elements in the sample are ionized, they are brought into the mass spectrometer via the interface cones. Sampler, and skimmer cone are the first, and second interface cone, respectively, as they can reduce the pressure of the sample stream from 1 to 10^{-5} torr by a small hole of 1 mm in the center. A shadow stop blocks the photon generated from ICP which may interfere the lens of determining the elements. In order to avoid the clogging of the small hole on the interface cones, a low concentration sample from dilution is required. Finally, the ions from the ICP source are then focused by the electrostatic lenses into the entrance aperture or slit of the mass spectrometer, which contains a quadrupole mass filter that allows only single mass-to-charge ratio (m/e) pass through the rods to the detector at a given instant in time. (Niu and Houk 1996)
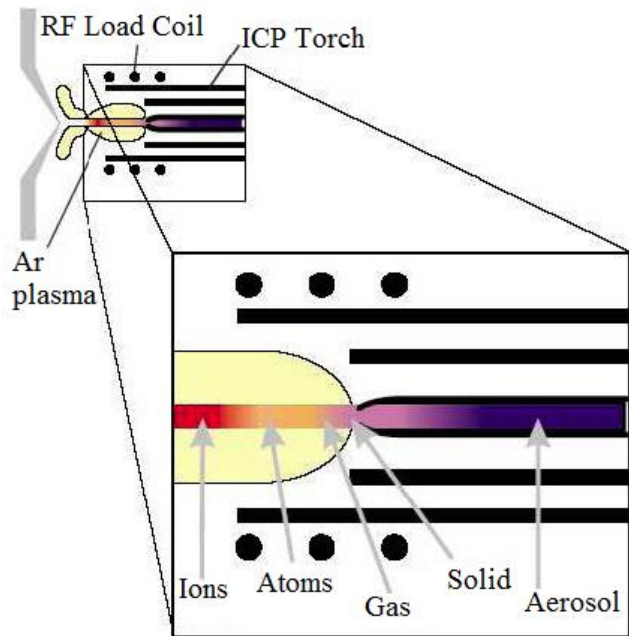
Figure 2-36 The ICP torch with RF load coil generate the argon plasma in the end of torch which ionize the species in the aerosol (Wolf 2005).
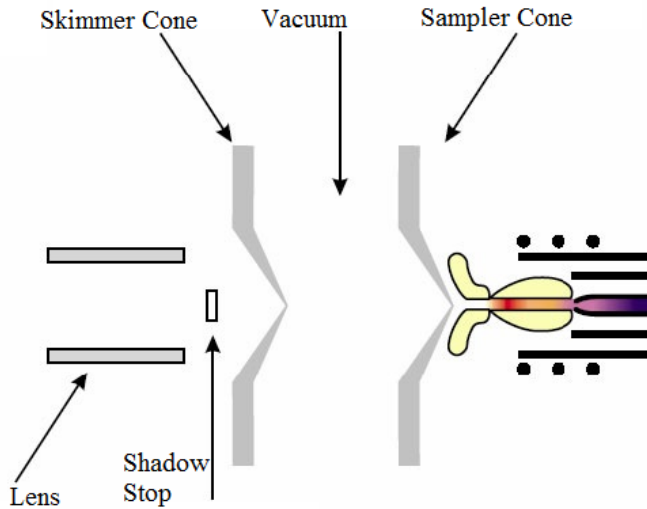
Figure 2-37 The interface region of an ICP-MS, including a plasma torch, sampler, skimmer cones and a shadow stop with lens for detector (Wolf 2005).

The ELAN DRCII was utilized for all the samples in this work. A 20 L/min flow rate of Ar is used as a carrier gas with a 175 μL/min of sample uptake rate, and the maximum RF power

is 1500 W for ionization of sample spices. An Instrumental detection limit (IDL) of and the isotopes pattern of all the elements are shown in Figure 2-38. And the detection limit depends upon many factors, including: lab and instrument background levels, sample matrix, sample collection and preparation methods, and operator skill level. However, the IDL can be used as a general guide as to the relative capabilities of the ICP-MS technique as compared to other analytical techniques. (Wolf 2005)

Figure 2-38 Approximate detection capabilities of the ELAN 6000/6100 quadrupole ICP-MS (Wolf 2005).

The concentration of sample preparation for ICP-MS is critical. If the sample concentration is too high, the excess of species would block the small hole on the interface cones and it could potentially contaminate the quartz in the ICP-MS as well. However, if the concentration is lower than the instrumental detection limit (IDL), for example, 0.03 µg/L for Co, 0.39 µg/L for Pd, and 0.14 µg/L for Pt, the detector would not be able to distinguish the

signal and the background noise. Therefore, a standard sample preparation is designed. First, the metal film for etching is prepared approximately in a rectangle of 7 by 10 cm, and the volume of the etchant is controlled in 10 mL. Second, the post-solution is stored in the metal-free VWR 50 mL vial with 1:10 (v:v) dilution. One of the most important studies with ICP-MS is to confirm the etching efficacy of the meal by organics with and without surface modification. For instance, the concentration of post-etch solution with surface modification prior to etch is found 2.61 and 2.76 μg/L, for Co and Pt respectively, which is much higher than that without surface modification, 0.08 μg/L Co and 0.39 μg/L Pt, suggesting an enhancement of etching efficacy with surface modification prior to organic etch.

2.9   Theoretical Methods

2.9.1 MATLAB^{TM} code

MATLAB^{TM} is a multi-paradigm numerical computing environment and fourth-generation programming language, and it allows matrix manipulations, plotting of functions and data, implementation of algorithms, creation of user interfaces, and interfacing with programs written in other languages such as C, C++, Java, Fortran and Python. In this work, Gibbs free energy minimization adopted MATLAB^{TM} as a tool to predict the etching product in various plasma environments. The Gibbs energy minimization method first applies a linear constraint of atomic conservation matrix. This constraint designates the limitations set on the atoms in each of the system constituents. The equilibrium chemical potentials of the constituents are obtained as a linear combination of the component-specific contributions, which are solved with the Lagrange method of undetermined multipliers. Basically, if a list of etching products and byproducts are

available, by considering all of them and their respective Gibbs free energies of formation, a global minimum of Gibbs free energy would be obtained with a selected combination of compounds within the system at equilibrium. Figure 2-39 presents a plot of composition as a function of temperature for the system of 1 kmol $SiOCH_2$ and 6 kmol CF_4 at $P = 10^{-5}$ atm based on the Gibbs free energy minimization through $MATLAB^{TM}$ code. The detail of $MATLAB^{TM}$ code utilized in this work is included in the Appendix L.
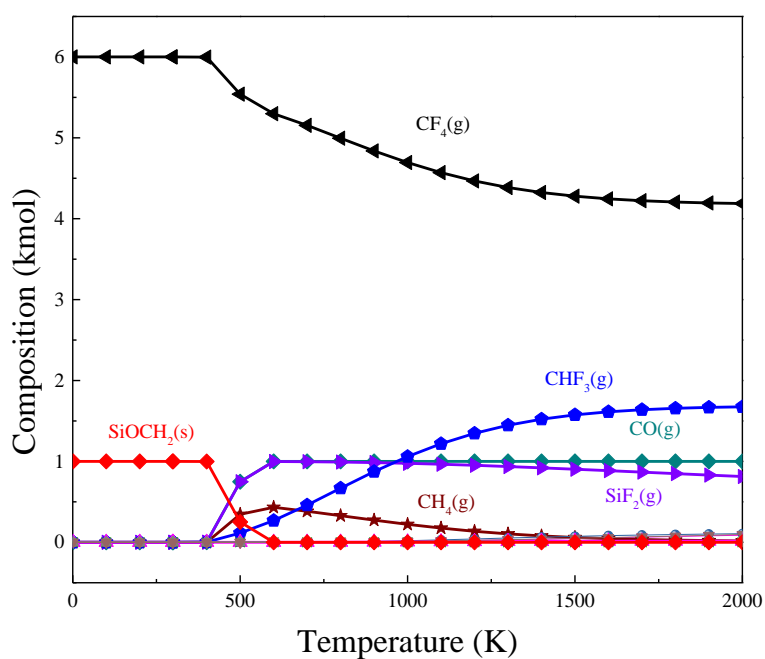
Figure 2-39 The plot of composition as a function of temperature for the system of 1 kmol $SiOCH_2$ and 6 kmol CF_4 at $P = 10^{-5}$ atm based on the Gibbs free energy minimization.

CHAPTER 3: GENERALIZED APPROACH FOR REACTIVE ION ETCH OF

MAGNETIC METALS

A thermodynamic analysis of etch chemistries for Co, Fe, and Ni using a combination of hydrogen, oxygen and halogen gases suggested that a single etchant does not work at 300K; however, a sequential exposure to multiple etchants results in sufficiently high partial pressure of the reaction products for the process to be considered viable. This sequential dose utilized the two reactions, a surface halogenation followed by the secondary etchant exposure. (MX_2 (c) + 3Y $\rightarrow$ MY(g) + 2XY(g), where M = Co, Fe, Ni; X = F, Cl, Br; Y= O, H) The volatilization reaction induced by sequential plasma exposure changed the equilibrium point, increasing the partial pressure of the etch product. Amongst all combinations, Cl_2 or Br_2 plasmas followed by H_2 plasma were the most effective. Followed by the thermodynamic calculation, the experimental kinetic verification was performed. From both the gas phase diagnostics and surface composition analysis, H_2 plasma alone could not etch metallic Co, Fe, and Ni films, but alternating doses of Cl_2 and H_2 plasmas resulted in more effective removal of chlorinated metals and increased the overall etch rate. Since the generalized approach has been proven to work for single metal films, the alloy of CoFe, which is actually utilized in the MRAM device has been studied. Starting with systematic thermodynamic calculations assessing various chemistries and reaction pathways leading to the highest possible vapor pressure of the etch products reactions, the potential chemical combinations were verified by etch rate investigation and surface chemistry analysis in plasma treated CoFe films. An approximately ~20% enhancement in etch rate was observed with the alternating use of Cl_2 and H_2 plasmas, in comparison with the use of only Cl_2 plasma. This chemical combination was effective in removing metal chloride layers thus

maintaining the desired magnetic properties of the CoFe films. Scanning electron microscopy (SEM) equipped with energy-dispersive X-ray spectroscopy (EDX) showed visually and spectroscopically that the metal chloride layers generated by Cl_2 plasma were eliminated with H_2 plasma to yield a clean etch profile. This work suggests that the selected chemistries can be used to etch magnetic metal alloys with a smooth etch profile and this general strategy can be applied to design chemically based etch processes to enable the fabrication of highly integrated nanoscale MRAM devices.

3.1 Thermodynamic Calculation of Etching Efficacy

Motivated by the above, this work focuses on a systematic thermodynamic approach to examine potentially viable etch chemistries for magnetic metals. While conventional phase diagrams, such as Richardson-Ellingham diagrams and Pourbaix diagrams, (DeHoff 1993) are useful exhibits summarizing thermodynamic properties, we adopted the use of a volatility diagram to summarize the thermodynamic calculations of the partial pressure of reactants as a function of the partial pressure of the main etchants. The volatility diagram was first shown in the work of Wagner et al. who analyzed the silicon oxidation process (Wagner 1958) and later used in assessing the feasibility of etching of copper by chlorine and hydrogen chemistries.(Kulkarni and DeHoff 2002) The viable chemistry and operating conditions predicted by thermodynamics for copper etching were subsequently verified experimentally. (Tamirisa, Levitin et al. 2007, Wu, Levitin et al. 2010) According to the thermodynamic calculation for Cu-Cl$_2$ system, an atomic hydrogen addition on CuCl$_2$(c) can generate Cu$_3$Cl$_3$(g) by utilizing a reaction (3CuCl$_2$(c) + 3H $\rightarrow$ Cu$_3$Cl$_3$(g) + 3HCl(g)).(Kulkarni and DeHoff 2002) Although this thermodynamic calculation is based on equilibrium conditions, which is not a realistic representation of what happens in a plasma system that is by definition non-equilibrium, (Coburn and Winters 1979, Coburn and Winters 1979),(McNevin and Becker 1985) nonetheless this work inspired a series of experimental work that proved that Cu can indeed be etched by a two step plasma etching processing employing chlorine and hydrogen(Wu, Levitin et al. 2010) and under specific conditions by hydrogen plasma alone.(Wu, Levitin et al. 2010, Wu, Levitin et al. 2011) This set of literature based on independent theoretical prediction and experimental

verification established the feasibility of using the thermodynamic calculations as a *guide* to help search of viable etch plasma chemistries.

3.1.1 Volatility Diagrams for Co, Fe and Ni Etched in Cl_2 System

In this work, several simple reactions leading to the generation of gaseous and condensed phase metal chlorides were chosen. The generation of metal clusters such as dimerized $Co_2Cl_4(g)$ and $Fe_2Cl_4(g)$ were considered because the species are relatively stable in the gas phase. However, $Ni_2Cl_4(g)$ was not considered because its formation was constrained by that of monomeric counterparts. Table 3-1 lists the probable reactions that were considered in the thermodynamic calculations involving chlorine etching of Co, Ni, and Fe films. Reactions (1)-(10) represent the sublimation of pure cobalt, chlorination reaction of cobalt, and formation of $CoCl(g)$, $CoCl_2(g)$, $CoCl_3(g)$ and $Co_2Cl_4(g)$. Because the Gibbs free energies of reactions (2), (3), (8), and (9) were negative, the partial pressures of $CoCl_2(g)$, $CoCl_3(g)$ and $Co_2Cl_4(g)$ in general increase as that of $Cl_2(g)$ increases and are determined by the vapor pressure of $CoCl_2(c)$ (reaction (4),(5),(7), and (10)). The reaction sets, (11)-(15), considered for nickel were very similar to those for cobalt, but more reactions were considered for iron because of the attainable valency (+2 and +3) of its condensed phase.

Table 3-1 Reactions utilized for plotting volatility diagrams in the M-Cl systems (M = Co, Fe, Ni) at 300K.

	Reaction	ΔG (kJ/mol)
(1)	$Co(c) \rightarrow Co(g)$	379.8
(2)	$Co(c) + Cl_2(g) \rightarrow CoCl_2(c)$	-269.3
(3)	$Co(c) + Cl_2(g) \rightarrow CoCl_2(g)$	-107.2
(4)	$CoCl_2(c) \rightarrow CoCl_2(g)$	162.1
(5)	$CoCl_2(c) \rightarrow Co(g) + Cl_2(g)$	593.8
(6)	$Co(c) + 1/2Cl_2(g) \rightarrow CoCl(g)$	141.3
(7)	$CoCl_2(c) \rightarrow CoCl(g) + 1/2Cl_2$	382.9
(8)	$CoCl_2(c) + 1/2Cl_2(g) \rightarrow CoCl_3(g)$	-148.4
(9)	$2Co(c) + 2Cl_2(g) \rightarrow Co_2Cl_4(g)$	-323.1
(10)	$2CoCl_2(c) \rightarrow Co_2Cl_4(g)$	160.3
(11)	$Ni(c) \rightarrow Ni(g)$	384.3
(12)	$Ni(c) + Cl_2(g) \rightarrow NiCl_2(c)$	-258.8
(13)	$Ni(c) + Cl_2(g) \rightarrow NiCl_2(g)$	-86.4
(14)	$NiCl_2(c) \rightarrow NiCl_2(g)$	172.3
(15)	$NiCl_2(c) + 1/2Cl_2(g) \rightarrow NiCl_3(g)$	-222.3
(16)	$Fe(c) \rightarrow Fe(g)$	369.4
(17))	$Fe(c) + Cl_2(g) \rightarrow FeCl_2(c)$	-301.6
(18)	$FeCl_2(c) + 1/2Cl_2(g) \rightarrow FeCl_3(c)$	-32.0
(19)	$Fe(c) + Cl_2(g) \rightarrow FeCl_2(g)$	-155.7
(20)	$FeCl_2(c) \rightarrow FeCl_2(g)$	145.9
(21)	$FeCl_2(c) \rightarrow Fe(g) + Cl_2(g)$	671.6
(22)	$FeCl_3(c) \rightarrow Fe(g) + 3/2Cl_2(g)$	703.0
(23)	$Fe(c) + 1/2Cl_2(g) \rightarrow FeCl(g)$	215.4
(24)	$FeCl_2(c) \rightarrow FeCl(g) + 1/2Cl_2(g)$	517.5
(25)	$FeCl_3(c) \rightarrow FeCl(g) + Cl_2(g)$	548.9
(26)	$FeCl_3(c) \rightarrow FeCl_2(g) + 1/2Cl_2(g)$	177.8
(27)	$Fe(c) + 3/2Cl_2(g) \rightarrow FeCl_3(g)$	-247.8
(28)	$FeCl_2(c) + 1/2Cl_2(g) \rightarrow FeCl_3(g)$	54.285
(29)	$FeCl_3(c) + FeCl_3(g)$	85.7
(30)	$2Fe(c) + 3Cl_2(g) \rightarrow Fe_2Cl_6(g)$	-598.3
(31)	$2FeCl_2(c) + Cl_2(g) \rightarrow Fe_2Cl_6(g)$	5.8
(32)	$2FeCl_3(c) \rightarrow Fe_2Cl_6(g)$	68.7

[1] Reaction (28) is equal to $2FeCl_2(c) + Cl_2(g) \rightarrow 2FeCl_3(g)$.

The vapor pressures of metal chlorides at temperatures between 300 K and 500 K were determined and shown in Figure 3-1 as a function of the chlorine partial pressure. To assess the volatility of a reaction product, the square symbol and gray line at 10^{-8} atm represented a reference point at which the weight loss of a material is measurable by a thermogravimetric analyzer and considered etchable.(Lou, Mitchell et al. 1985)
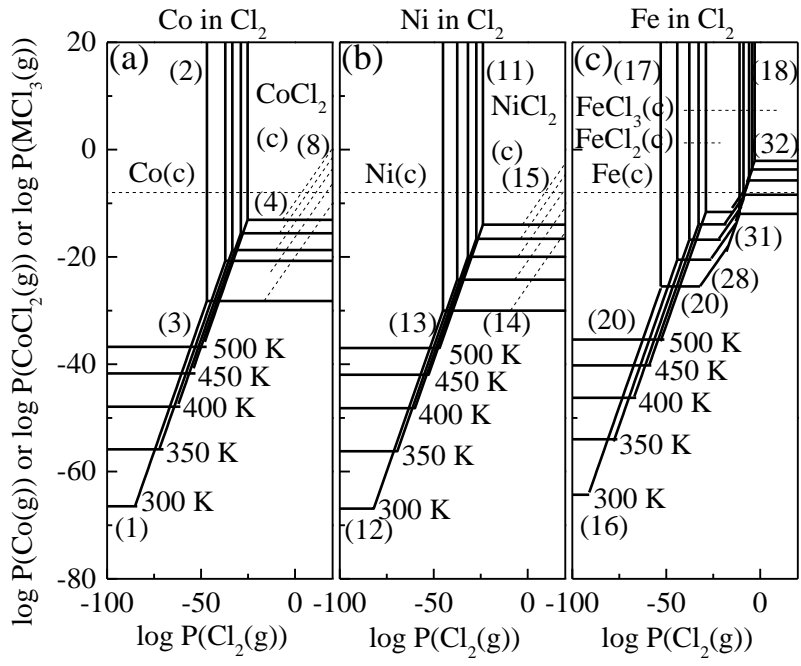
Figure 3-1 Volatility diagram for (a) Co in Cl_2, (b) Fe in Cl_2, and (c) Ni in Cl_2 system at 300, 350, 400, 450, and 500K. The reactions in the figure are presented in Table 3-1. The square and dashed line at 10^{-8} atm infers the reactant volatility, corresponding to a weight loss that is detectable in a thermogravimetric analyzer (Lou, Mitchell et al. 1985).

In the volatility diagram of Co in Cl_2, the horizontal lines of reaction (1) represent the sublimation from Co(c) to Co(g). The corresponding vapor pressure at 300 K was lower than 10^{-60} atm. The vertical lines correspond to the equilibrium state between Co(c) and $CoCl_2$(c), showing that $CoCl_2$(c) is preferred as the partial pressure of Cl_2 increases. $CoCl_2$(c) vapor pressure increases as Cl_2 pressure increases in reaction (3) and is limited at the equilibrium of

107

$CoCl_2$(c) sublimation, reaction (4). This is because the reaction to generate $CoCl_2$(c) is significantly more favorable than Co(c), even at low temperatures. As a result, the attainable vapor pressure is dictated by the sublimation of $CoCl_2$(c) which shows the highest vapor pressure in this diagram. In addition, it is well known that the dihalide state is the only known condensed halides of cobalt.(Greenwood and Earnshaw 1998) The reaction (8) does not have an intermediate state to make a reaction because $CoCl_2$(c) is saturated with chlorine, so an equilibrium line of the reaction is displayed as a dashed line.

Very similar trends were observed for chlorine reacting with Ni; however, the volatility diagram for Fe was different from Co and Ni since Fe can form $FeCl_3$(c) in a +3 valance state. In the reaction between Fe and Cl, $FeCl_3$(c) is thermodynamically preferred over $FeCl_2$(c) since the enthalpy of the former reaction is lower.(Kiihamaki and Franssila 1999) In addition, it was reported that the chlorine-based plasma etching of an Fe/Si alloy film generated $FeCl_3$ rather than $FeCl_2$.(Kinoshita, Yamada et al. 1991) A temperature-dependent volatility diagram is presented from 300 to 500 K (Figure 3-1). The required temperatures to make $CoCl_2$, $FeCl_3$, and $NiCl_2$ volatile were calculated to be 613 K, 392 K, and 633 K, respectively.

The vapor pressures of various metal halides were plotted against temperature in Figure 3-2. Metal chloride and bromide (Metal = Co, Fe, or Ni) have higher vapor pressures than metal fluoride, consistent with their melting and boiling points.(Lide 1995) The metal halide compounds were not volatile below 473 K except $FeCl_3$ and $FeBr_3$. The incorporation of an additional chemistry is necessary to etch these metals.
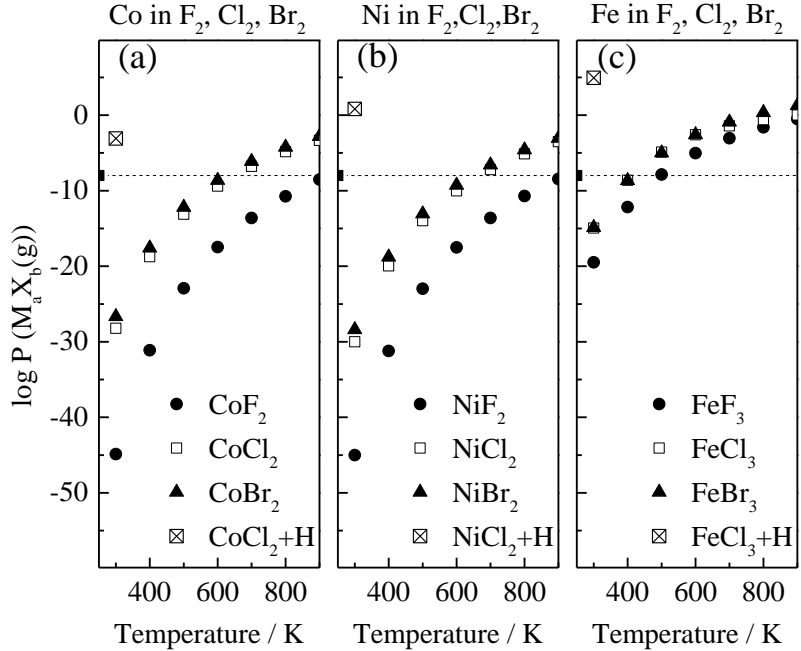
Figure 3-2 Calculated vapor pressure from the sublimation reaction of metal halide condensed phase at 300, 400, 500, 600, 700, 800, and 900 K. (a) Co in Cl_2, (b) Fe in Cl_2, and (c) Ni in Cl_2 system. Hollow stars represent the partial pressure of MH(g) (M = Co, Fe, and Ni) at an equilibrium when metal chloride is exposed to hydrogen radicals.

3.1.2 Secondary Chemistries Addition in Cl_2 System

The addition of the secondary plasma was investigated on a $CoCl_2$(c) layer. The first chemistry examined was molecular and atomic oxygen addition as summarized in Table 3-3. The addition of an oxygen plasma enabled access to the meta-stable extension of the CoO(g)-$CoCl_2$(c) equilibrium line. In Figure 3-3(a), a dashed line (35) represents an equilibrium line to generate CoO(g) from the reaction between a meta-stable $CoCl_2$(c) layer and an oxygen atom. Three equilibrium lines were shown, depending on the partial pressure of oxygen. The equilibrium pressure increased as the oxygen partial pressure varied from 10^{-30} to 10^{-10} atm. The maximum attainable partial pressure of CoO(g) was decided by the mass balance of a

thermodynamically favorable reaction (36), which was represented as hollow squares in Figure

3-3. At the oxygen radical pressure of 10^{-10} atm, the partial pressure of CoO(g) was 10^{-11} atm

which is higher than the $CoCl_2$(c) vapor pressure but lower than the required pressure to be

considered etchable (10^{-8} atm). O_2 addition by reaction (33) and (34) does not enhance the partial

pressure of CoO(g) compared to $CoCl_2$(g) pressure at the equilibrium.

Table 3-2 Reactions utilized for plotting volatility diagrams in $CoCl_2$ etching with O, Co etching with O, and CoO etching with Cl systems at 300K.

	Reaction	ΔG (kJ/mol)
(33)	$CoCl_2(c) + 1/2O_2(g) \rightarrow CoO(g) + Cl_2(g)$	526.7
(34)	$CoCl_2(c) + 3/2O_2(g) \rightarrow CoO(g) + 2OCl(g)$	723.3
(35)	$CoCl_2(c) + O(g) \rightarrow CoO(g) + Cl_2(g)$	295.1
(36)	$CoCl_2(c) + 3O(g) \rightarrow CoO(g) + 2OCl(g)$	28.5
(37)	$Co(c) + 1/2O_2(g) \rightarrow CoO(c)$	-214.1
(38)	$3CoO(c) + 1/2O_2(g) \rightarrow Co_3O_4(c)$	-152.0
(39)	$Co(c) + 1/2O_2(g) \rightarrow CoO(g)$	257.3
(40)	$CoO(c) \rightarrow CoO(g)$	471.4
(41)	$1/3Co_3O_4(s) \rightarrow CoO(g)+1/6O_2(g)$	522.1
(42)	$CoO(c) + 1/2Cl_2(g) \rightarrow CoCl(g) + 1/2O_2(g)$	375.2
(43)	$CoO(c) + Cl_2(g) \rightarrow CoCl(g) + ClO(g)$	473.5
(44)	$CoO(c) + Cl(g) \rightarrow CoCl(g) + 1/2O_2(g)$	270.0
(45)	$CoO(c) + 2Cl(g) \rightarrow CoCl(g) + ClO(g)$	263.1

[1]Reaction (33) is equal to $2CoCl_2(c) + O_2(g) \rightarrow 2CoO(g) + 2Cl_2(g)$.
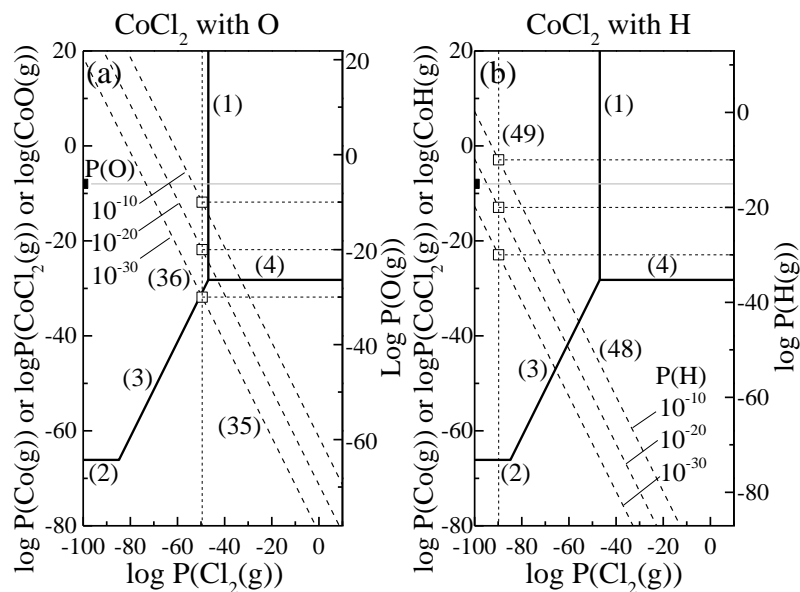
Figure 3-3 A partial pressure of CoO(g) generated from atomic oxygen (left) addition on $CoCl_2(c)$ and that of CoH(g) generated from atomic hydrogen (right) addition on $CoCl_2(c)$ at 300K. The hollow square symbol was achieved from the mass balance from reaction (19) and (32).

Another chemistry examined was hydrogen with reactions involving molecular and atomic hydrogen for etching Co as summarized in Table 3-4. A reaction with hydrogen was considered because it results in a more negative Gibbs free energy of the reaction compared to the CoO(g) generation reaction. In Figure 3-3(b), a dashed line (48) represents an equilibrium line derived from the reaction between a meta-stable $CoCl_2(c)$ layer and hydrogen. The maximum partial pressure of CoH(g) was represented as a hollow square at which point the thermodynamically favorable state and mass balance are simultaneously satisfied. The partial pressure of CoH(g) was estimated to be higher than 10^{-8} atm, indicating that the addition of an atomic hydrogen on $CoCl_2(c)$ is a promising etch chemistry. While the vapor pressure of a compound is an intrinsic property and thus constant at a given temperature, the cobalt chloride surface acts as an intermediate state to the subsequent reaction path and generates CoH(g) at an

enhanced rate. The result indicates that the kinetics changed during this sequential reaction process.

Table 3-3 Reactions considered in hydrogen plasma reacting with $CoCl_2$.

	Reaction	ΔG (kJ/mol)
(46)	$CoCl_2(c) + 1/2H_2(g) \rightarrow CoH(g) + Cl_2(g)$	678.5
(47)	$CoCl_2(c) + 3/2H_2(g) \rightarrow CoH(g) + 2HCl(g)$	487.9
(48)	$CoCl_2(c) + H(g) \rightarrow CoH(g) + Cl_2(g)$	475.3
(49)	$CoCl_2(c) + 3H(g) \rightarrow CoH(g) + 2HCl(g)$	-121.7

[1] Reaction (46) is equal to $2CoCl_2(c) + H_2(g) \rightarrow 2CoH(g) + 2Cl_2(g)$.

Having established that a hydrogen exposure to a chlorinated cobalt surface is a potentially effective route to chemically etch cobalt, the combination of hydrogen and chlorine plasmas was tested on nickel, where one chemistry was used first followed by the exposure to the other chemistry. This analysis was done only for nickel because the thermodynamic data existed for condensed nickel hydride but not for cobalt hydride or iron hydride. The left panel of Figure 3-4 represents an equilibrium line (50) derived from the hydrogen addition reaction on the meta-stable $NiCl_2(c)$. The maximum pressure achieved from the mass balance of reaction (51) was marked as a hollow square, showing the enhanced partial pressure of an etch product. An atomic chlorine addition on a nickel hydride film was shown in the right panel of Figure 3-4. The maximum partial pressure of $NiCl(g)$ achieved from the mass balance of reaction (56) was $\sim 10^{-2}$ atm which is significantly higher than the reference point (10^{-8} atm). This result indicates that both an $H(g)$ addition on $NiCl_2(c)$ and a $Cl(g)$ addition on NiH_x can increase the partial pressure of etch products to make the etch chemistry viable. The driving force to enhance the equilibrium pressure is the highly reactive H atom's propensity to form $MH(g)$. In addition, a stable byproduct such as $HCl(g)$ ($\Delta G_f = -95.3$) contributes to the Gibbs free energy of a reaction being

negative, so an equilibrium point forms at the point to generate CoH(g) with a higher partial pressure. (NiCl$_2$(c) + 3H $\rightarrow$ NiH(g) + 2HCl(g), ΔG_r = -190.9 kJ/mol) This reaction can be compared with that to generate CoH(g) directly from Co(c), which has a positive Gibbs free energy. Because of the negative Gibbs free energy of a reaction, the equilibrium point moved to the forward reaction to generate CoH(g) and to increase the vapor pressure of an etch product.

Table 3-4 Reactions considered in hydrogen plasma reacting with NiCl$_2$ and chlorine plasma reacting with NiH$_{0.5}$.

	Reaction	ΔG (kJ/mol)
(50)	NiCl$_2$(c) + H(g) $\rightarrow$ NiH(g) + Cl$_2$(g)	406.1
(51)	NiCl$_2$(c) + 3H(g) $\rightarrow$ NiH(g) + 2HCl(g)	-190.9
(52)	Ni(c) + 1/4H$_2$(g) $\rightarrow$ NiH$_{0.5}$(c)	5.9
(53)	Ni(c) $\rightarrow$ Ni(g)	384.3
(54)	Ni(c) + 1/2H$_2$(g) $\rightarrow$ NiH(g)	350.5
(55)	NiH$_{0.5}$(s) +1/2H(g) $\rightarrow$ NiH(g)	239.4
(56)	NiH$_{0.5}$(c) + Cl(g) $\rightarrow$ NiCl(g)+1/4H$_2$(g)	37.7
(57)	NiH$_{0.5}$(c)+3/2Cl(g) $\rightarrow$ NiCl(g)+1/2HCl(g)	-62.6
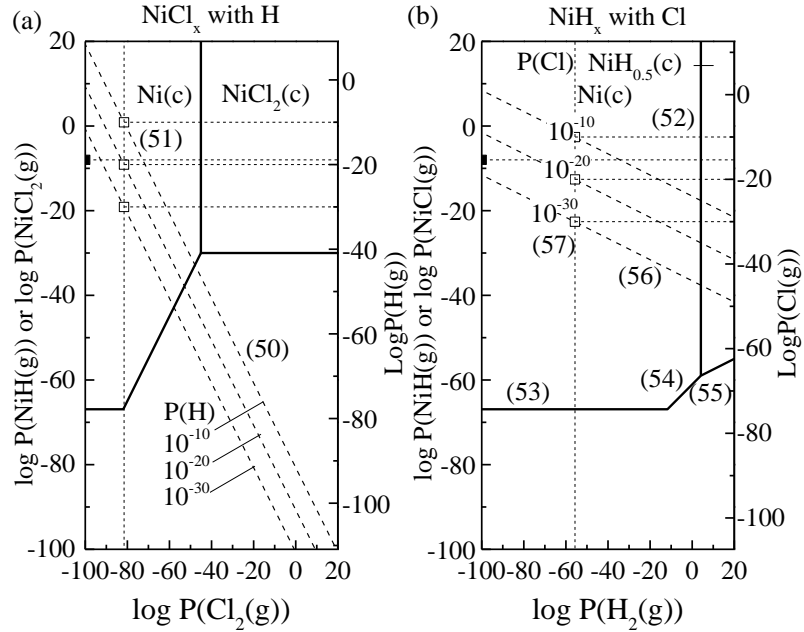
Figure 3-4 A partial pressure of NiH(g) at equilibrium generated from an atomic H addition on NiCl₂(c) (left) and that of NiCl(g) generated from an atomic Cl addition on NiH₀.₅(c). The hollow square symbol was achieved from the mass balance from reaction (34) and (40).

3.1.3 Summary of Thermodynamic Calculation

This general framework for thermodynamic calculations was applied to various combinations of H_2, O_2, Cl_2, Br_2, and F_2 plasmas. (Figure 3-5) There are common trends observed for Co, Fe, and Ni metals. First, an etch product generated by a single gas plasma, such as $MCl_x(s)$, $MBr_x(s)$ and $MO(s)$, is not volatile at 300 K (M=Co, Fe, or Ni). Atomic oxygen addition to a metal halide enhanced the partial pressure of an etch product, but is still considered non-volatile. The addition of atomic hydrogen to metal halides appeared to be the most viable in terms of increasing the partial pressure of an etch product. According to the calculation, the combinations of Cl_2/H_2 and Br_2/H_2 plasmas were proposed as feasible chemistries to etch Co, Ni, and Fe.

114
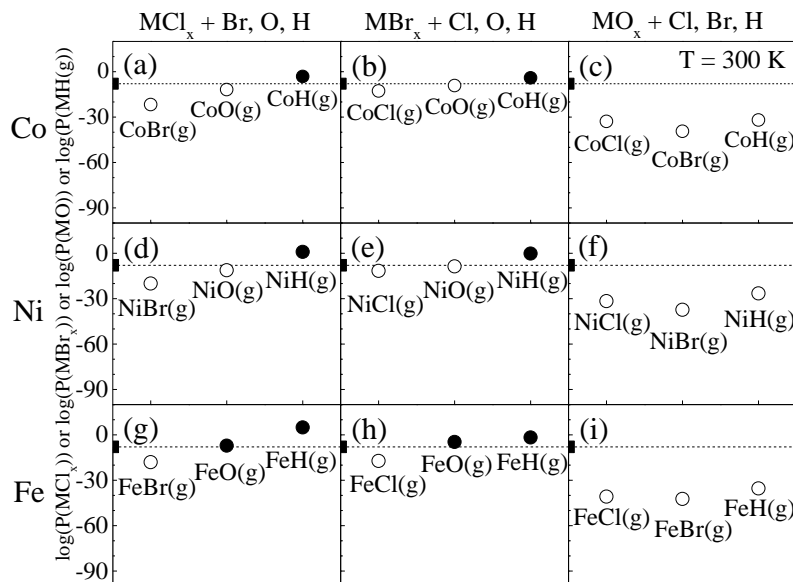
Figure 3-5 Summary of a partial pressure enhancement induced by chlorine, bromine, oxygen, and hydrogen addition to $MCl_x(c)$, $MBr_x(c)$, and $MO(c)$. (M=Co, Fe, and Ni).

3.2 Experimental Verification of Thermodynamic Calculation

3.2.1 Surface Chemical Characterization and Etch Rate of Co, Fe, and Ni in Cl_2/H_2 Plasma

In the experiments to prove the thermodynamic calculations, Cl_2 and H_2 plasma were exposed sequentially to measure surface composition and etch rate. Figure 3-6 represents XPS data for pre-etch, Cl_2 plasma (30 sec), Cl_2 plasma (30 sec) followed by H_2 plasma (30 sec) and Cl_2 plasma (30 sec) followed by H_2 plasma (90 sec) on Co film at 300K. A Co 2p spectrum taken after a Cl_2 plasma dose does not change significantly because the electron binding energies of cobalt chloride and cobalt oxide are similar. However, the Cl 2p peak increased significantly,

indicating the formation of a $CoCl_2$ layer. When this layer was exposed to H_2 plasma, the Cl 2p

peak decreased significantly, indicating that the metal chloride layer had been etched. Surface

composition measurements for Fe and Ni also showed similar results.

Table 3-5 Plasma condition of Cl_2 and H_2 plasma.

	Cl_2 plasma	H_2 plasma
Plasma power (W)	400.0	800.0
Sample bias (W)	100.0	100.0
Electron temperature (eV)	1.6	1.9
Self-bias (V)	8.0	9.5
Frequency (MHz)	2.0	2.0
Flow rate (sccm)	20.0	50.0
Pressure (mtorr)	10.0	30.0
Pulse time (sec)	20.0	20.0
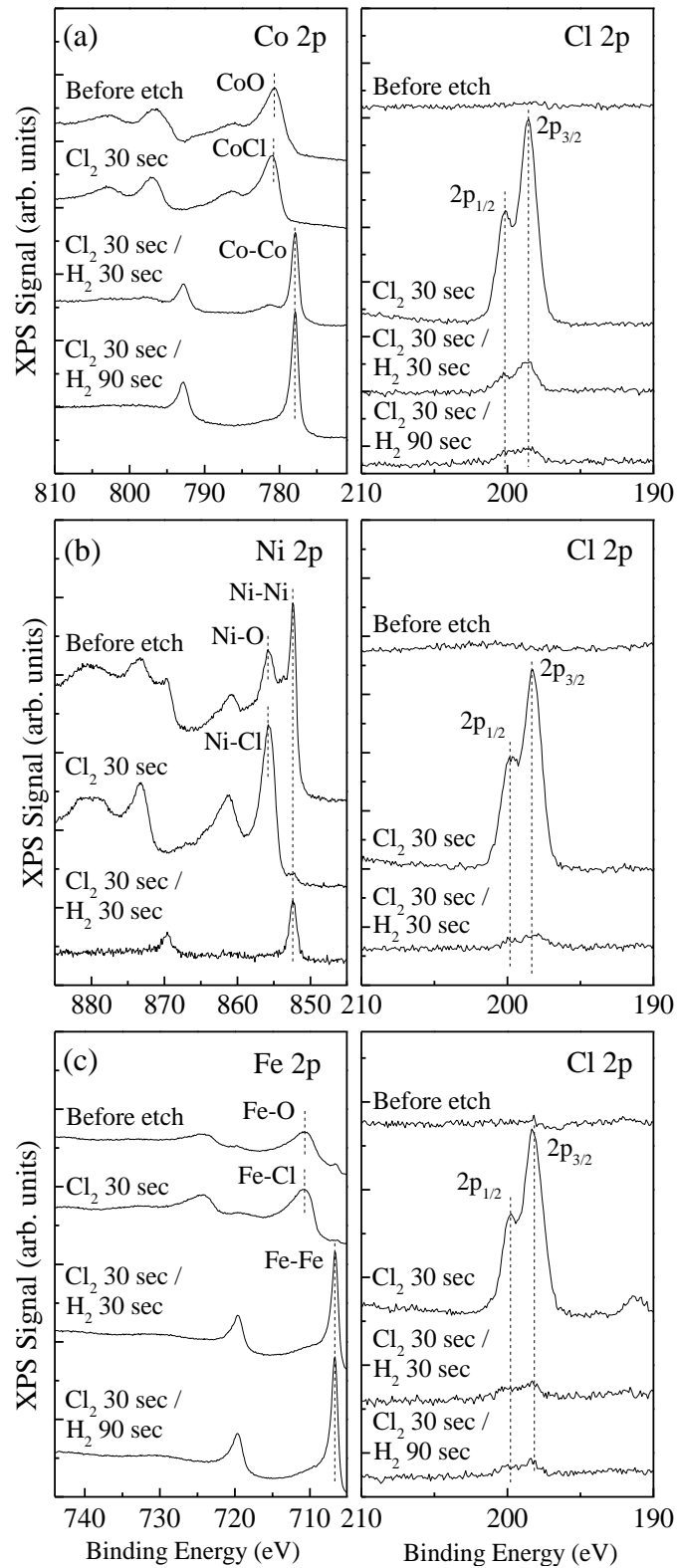
Figure 3-6 Surface composition measurements of Co, Ni, and Fe thin films using XPS representing before-etch, Cl₂ plasma 30 sec, Cl₂ plasma 30 sec followed by H₂ plasma 30 sec, and Cl₂ plasma 30 sec followed by H₂ plasma 90 sec.

117

3.2.2 Surface Chemical Characterization and Etch Rate of Co, Fe, and Ni in Cl_2/H_2 Plasma

The etch rate measurement was also consistent with the thermodynamic calculation. The etch rates of Co, Fe, and Ni by Cl_2 plasma were 3.9, 8.0, and 4.8 nm/cycle, corresponding to 11.8, 24.0, and 14.3 nm/min, respectively. (1 cycle = 20 sec) (Figure 3-7).
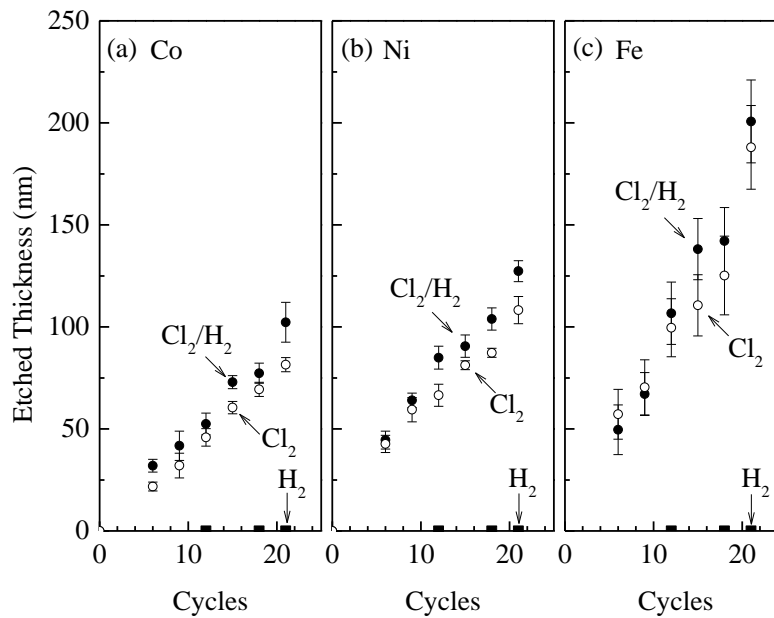
Figure 3-7 Etch rate measurement using profilometer. Cl_2 and H_2 plasma were exposed alternating manner. The etch rate by hydrogen plasma was zero (filled square symbol in the figure). Co etch rates in Cl_2 and Cl_2/H_2 cycle were 4.61 and 3.94 nm/cycle, respectively. Fe etch rates in Cl_2 and Cl_2/H_2 cycle were 8.50 and 8.01 nm/cycle, respectively. Fe etch rates in Cl_2 and Cl_2/H_2 cycle were 5.74 and 4.77 nm/cycle, respectively.

Though chlorine chemistry seems to yield limited chemical etching, the physical sputtering component is still significant. In terms of physical sputtering, a sputtering yield with an ion energy below 1 keV can be expressed as follows:(Steinbrüchel 1985)

$$Y = \frac{4.6}{U} \times \frac{Z_t}{(Z_t^{2/3} + Z_i^{2/3})^{3/4}} \times \left(\frac{M_p}{M_t + M_p}\right)^{1/2} \times E^{1/2} \qquad (3.1)$$

In (3.1) U is the surface binding energy in eV, Z_t and Z_p are target and ion atomic numbers, M_t and M_p are the respective masses and E is the ion energy in keV. The binding energies of Co, Ni, and Fe are known to be 4.4, 4.4 and 4.3 eV, respectively.(Gshneider 1964) The sputtering yield of a Cl ion on a Co film was therefore ~ 0.28. The vapor pressure of $CoCl_2$ was lower than the reference point in the volatility diagram, however the film was etched with the rate of 11.8 nm/min. This can be explained by the physical sputtering or the ion assisted etching. Although the surface binding energies and atomic masses of Co, Fe, and Ni are similar to within 2%, the etch rate of Fe by Cl_2 plasma was two times higher than that of Co, a trend that is similar to the vapor pressure evaluation.

The next step is to consider the reaction kinetics to assess the rate constant (k) = A×exp(-E_a/RT) where A, E_a, R, and T represent the pre-exponential factor, activation energy of reaction, ideal gas constant (= 8.314 J/mol·K), and temperature, respectively. Assuming that the concentration of atomic hydrogen is at least 5-10 orders of magnitude of smaller than that of H_2(Kulkarni and DeHoff 2002) under the experimental condition (30mtorr), the pre-exponential factor is related with the flux of H(g), which is calculated to be 1.53×10^{14} atoms/cm²·sec when the partial pressure of H(g) was 1×10^{-10} atm. Assuming that all the impinged H(g) react to make CoH(g), the maximum etch rate for a Co film was calculated to be 1.02 nm/min. This quantitative analysis indicates that an equilibrium pressure estimated from the thermodynamic calculation is high enough to etch a $CoCl_2$(c) film if the pressure is kept constant by CoH(g) supplemented from the reaction of hydrogen with the film. However, the etch rate in the

experiment was limited by the impingement rate of H(g) because the flux on the surface was not sufficient to convert all $CoCl_2$(g) to CoH(g).

The etch rates of Co, Fe, and Ni by Cl_2/H_2 plasma were 4.6, 8.5, and 5.7 nm/cycle, which was enhanced by 17, 6, and 20% compared to Cl_2 plasma, respectively. Cl_2 plasma on cobalt film showed a rough etch profile. Soaking the chlorinated samples in ethanol and water did not result in any additional removal of surface species.   However, exposure to H_2 plasma after Cl_2 plasma on the cobalt film resulted in a clean etch profile (SEM not shown). The etch rate measurement from SEM analysis of the etch profile before and after the etching corroborated the XPS analysis. If the reduction of the Cl 2p peak in XPS came from the abstraction reaction to generate HCl(g) ($CoCl_2$(c) + H(g) $\rightarrow$ Co(c) + HCl(g)), the etch rate by Cl_2 and Cl_2/H_2 plasma would be similar since Co atoms could not be etched by H_2 plasma.

3.2.3 Etching Products Analysis by Optical Emission Spectrum for Cobalt in Cl_2/H_2 Plasma

OES spectra of Cl_2 plasma etching Co, H_2 plasma etching $CoCl_x$, and Cl_2/H_2 plasma etching Co have been recorded to study the etch chemistry. In Figure 3-8(a), atomic Cl peaks appear from 700 nm to 900 nm in Cl_2 plasma.(Donnelly 1996, Lee, Chang et al. 2000) When H_2 plasma was used after Cl_2 plasma, the spectrum showed H_α, H_β, H_γ and H* emission corresponding to n=3, n=4, and n=5 excited states of H, and excited state of H_2, respectively. In the magnified spectrum (b), four peaks at 441.6, 442.6, 444.3 and 449.8 nm appeared in H_2 plasma etching $CoCl_x$ and Cl_2/H_2 plasma etching Co, but not in H_2 plasma etching SiO_2. This confirms that they did not originate from H_2 excitation, but from CoH. The representative excitation states of CoH were reported as $A^3\Phi_4$ and $A^3\Phi_3$ which are located 2.76 and 2.80 eV

120

above $X^3\Phi_4$ state,(Freindorf, Marian et al. 1993) corresponding to the peaks at 442.6 and 449.8

nm in the OES spectrum. Other peaks at 444.3 and 441.6 nm are overlapped with atomic cobalt

spectra. The electronic excitation to $A^3\Phi_4$ and $A^3\Phi_3$ states support the CoH generation induced

by H_2 plasma etching $CoCl_x$. The surface composition and etch rate measurements support the

thermodynamic calculation. First, the Co, Fe, and Ni etch rate induced by Cl_2 plasma is plausible

by thermodynamic calculations. Second, the cobalt chloride layer was removed by H_2 plasma

even though H_2 plasma cannot etch pure Co film. As a result, an atomic hydrogen addition could

enhance the etch rate, which is consistent with thermodynamic calculation.
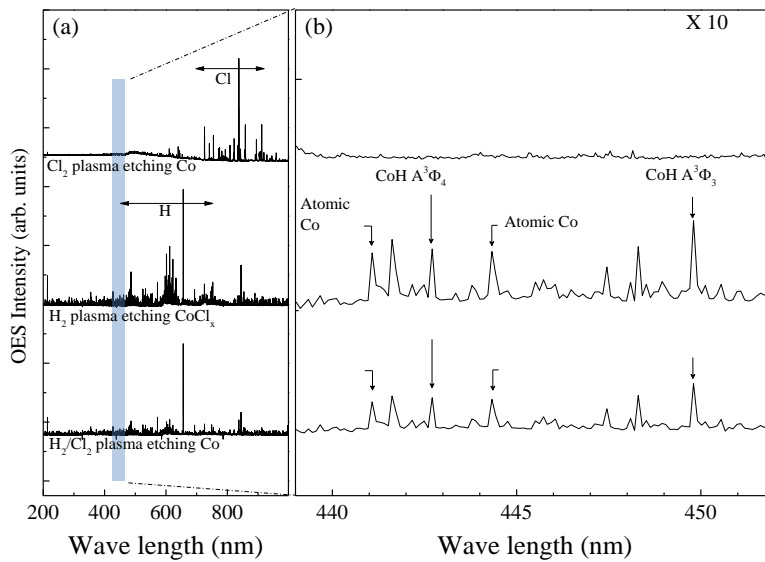
Figure 3-8 OES spectra of Cl_2 plasma etching Co, H_2 plasma etching Cl_2-plasma pretreated Co, and H_2/Cl_2 plasma etching Co. (a) OES with the wave length from 200 to 1000 nm. (b) Magnified spectra of (a) from 435 to 455 nm. The peaks assigned as CoH(g) and Co(g) do not appear in H_2 plasma on SiO_2.

In this work, an atomic hydrogen addition on a metal chloride layer was investigated to

generate MH(g) (M = Co, Fe, or Ni). According to the thermodynamic calculation, this reaction

could generate MH(g) with a high attainable partial pressure, making this a viable etching

process. Similarly, atomic chlorine addition on metal hydride layer ($NiH_{0.5}$) resulted in a higher attainable partial pressure of NiCl(g), making this two step etching process a viable approach to etch magnetic metal elements.

3.2.4 Summary of Experimental Verification on Thermodynamic Calculation

The attainable partial pressure of an etch product was evaluated by thermodynamic calculations. The metal hydride was not volatile, but oxygen radical addition on MCl_x (M = Co, Fe, or Ni) could enhance the vapor pressure of the etch product. Hydrogen radical addition on chlorinated surfaces appears to be the most effective combination to etch metals, showing that the partial pressure of MH(g) can be higher than the reference value ($\sim 10^{-8}$ atm). According to the surface composition measurements, hydrogen plasma could etch a MCl_x layer but not pure metals. As a result, the etch rates of Co, Fe, and Ni by Cl_2/H_2 plasmas were enhanced by 17, 6, and 20%, respectively, compared to those measured in a Cl_2 plasma. The thermodynamic expectation was consistent with the experimental result: 1) Co and Ni etch rate by a Cl_2 plasma was similar, while Fe etch rate was higher than those metals and 2) atomic hydrogen addition could etch a metal chloride layer with an increased etch rate. A reactive hydrogen atom and the stable byproduct such as HCl acted as driving forces for the enhanced attainable partial pressure.

3.3 CoFe Alloy Thin Film Patterned by Cl_2/H_2 Plasma

3.3.1 Etch Rate and Surface Chemical Characterization of CoFe Alloy Etched by Cl_2/H_2 Plasma

The etch rate analysis of CoFe films with Cl_2 and Cl_2/H_2 plasma support the fact that H_2 plasma induces a higher partial pressure of the etch product than that generated by Cl_2 plasma. In Figure 3-9 (b), etch rates with Cl_2 plasma itself and with the subsequent H_2 plasma have been found to be 3.2 and 4.2 nm/min, extracted from linear fits, shown with black and gray dashed lines, respectively. The enhanced etch rate of Cl_2/H_2 plasma demonstrates that H_2 plasma etches the surface modified by Cl_2 plasma although H_2 plasma itself cannot etch CoFe magnetic film as shown in the supporting information. The surface reactions resulting from halogen-based plasma have been demonstrated in Figure 3-10. The XPS spectrum of Cl_2-plasma exposed CoFe film presents a significant increase of spectral weight for Cl 2p peak, indicating the formation of metal chloride layers such as $CoFeCl_x$, on the CoFe film surface (Figure 3-10 (c)), while the spectral weight of the Co 2p and Fe 2p peaks were barely affected by Cl_2 plasma since the CoO and $CoCl_2$ electron binding energies are comparable (Figure 3-10 (a)) and Fe 2p peak of FeO overlaps with Co Auger electron peak (Figure 3-10b). Afterwards, the chemical effect of H_2 plasma in the metal chloride layers was studied. The spectral weight of Co $2p_{3/2}$ peak, measured at approximately 781.1 eV, is diminished, and a peak around 777.9 eV corresponding to metallic cobalt appears when the metal chloride product is exposed to H_2 plasma for 30 sec as shown in Figure 3-10a. As the exposure time of H_2 plasma is increased up to 90 sec, the peak related to metallic cobalt has an increased spectral weight indicating clearly that the metal chloride layers react with H_2 plasma. The H_2 plasma causes the emergence of Fe metallic peak at approximately 706.4 eV as shown in Figure 3-10. As the metallic Co and Fe peaks develop in the spectra, the

spectral weight of the Cl 2p peak decreases significantly as the time of H_2 plasma exposure is increased, e.g. H_2 plasma doses for 30 and 90 sec reduce Cl 2p area to 6.1 % and 3.2 % as shown in Figure 3-10 (c). An enhanced etch rate of Cl_2/H_2 plasma compared to Cl_2 plasma indicates that the surface composition variation of Figure 3-10 was not the result of de-chlorination reaction, but from the removal of metal chloride layer. Combining the etch thickness and the surface composition measurements, the resulting thermodynamic calculation implies that the surface modification prior to H_2 plasma exposure changes the reaction path, and H_2 plasma enhances the equilibrium partial pressure of those etch products including metal atoms.
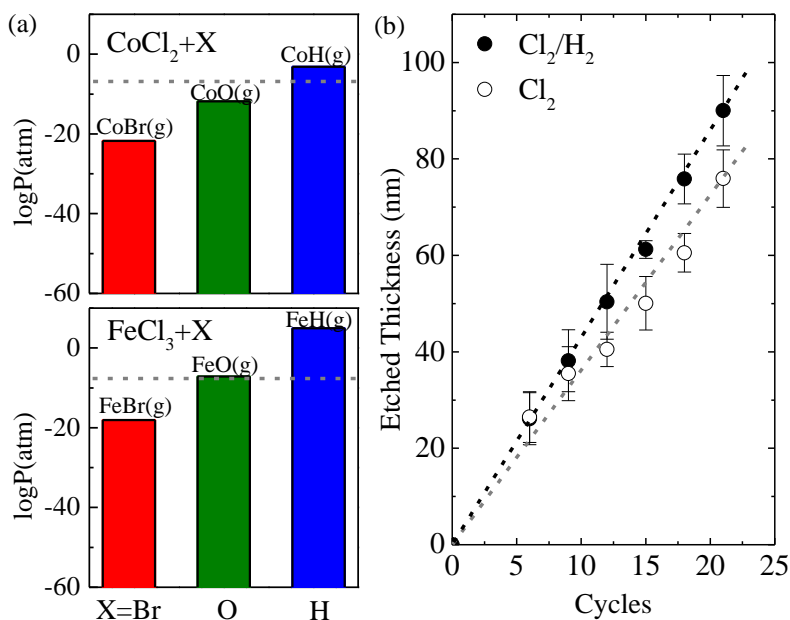
Figure 3-9 (a) Calculated partial pressures of etch products generated from atomic Br, O, and H addition on $CoCl_2$ and $FeCl_3$. Detailed calculation can be found in the supporting information. (b) Etched thickness is shown as a function of chlorine and hydrogen plasma cycles after 20 sec exposure with Cl_2 plasma and 20 sec exposure individually with Cl_2/H_2 plasma. A Cl_2 cycle is 20 sec Cl_2 plasma and Cl_2/H_2 cycle is composed of 20 sec Cl_2 followed by 20 sec H_2. The dashed lines represent linear fittings of etched thicknesses for Cl_2 and Cl_2/H_2 cycles.
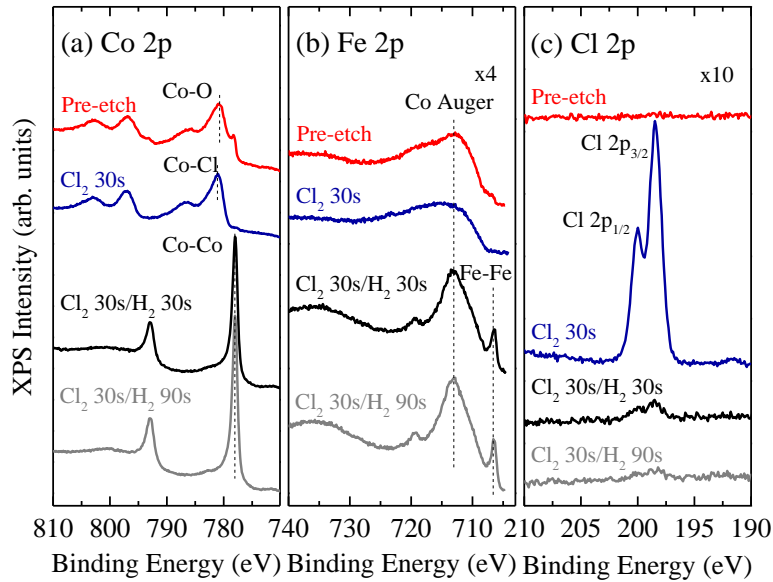
Figure 3-10 XPS spectra of (a) Co 2p, (b) Fe 2p, and (c) Cl 2p. From the top, the spectra represents pre-etch, Cl_2(30sec), Cl_2(30sec)/H_2(30sec), and Cl_2(30sec)/H_2(90sec) plasma exposure on 500 nm $Co_{0.8}Fe_{0.2}$ films. For each element analyzed, each chemical state is represented by a spin-orbit split doublet, $2p_{3/2}$ and $2p_{1/2}$, which is constrained to have a 2:1 peak area ratio, equal full-width-at-half-maximum, and their energy separations are 15.0 eV, 12.9 eV, and 1.53 eV, for Co, Fe and Cl, respectively. For simplicity, only the $2p_{3/2}$ peaks are labeled in the figure. In Fe 2p spectra, the Co Auger LMM peak at ~714.3 eV is overlapped with Fe-O and Fe-Cl peak at ~710.7 eV and ~711 eV.

3.3.2 Etching Feature Profile Analysis of CoFe Etched in Cl_2/H_2 Plasma

To demonstrate the potential of the halogen-based plasma-etching method for fabricating a high-density integrated circuit, SEM was used to assess the effects on patterns with various plasma etching processes. Figure 3-11 indicates SEM images obtained from pre-, post-Cl_2, post-Cl_2/H_2, and post-Ar plasma assisted etching on patterned wafers, which has the layer structure of TiN(300nm)/CoFe(45nm)/Ti(10nm) on Si wafer. In the case of Cl_2 with subsequent H_2 plasma, pure gases rather than a mixture were introduced to comprehend the effect of etch chemistry. Figure 3-11 (a) and (b) show SEM images of the CoFe patterned wafer prior to etching, where a

steep slope and a smoothed surface are visible. Figure 3-11 (c) and d display etch profile after a 4 min Ar plasma exposure, where a 45 nm CoFe film is completely removed above a 10nm Ti adhesion layer under the following conditions: RF1 (plate power) of 100 W, RF2 (coil power) of 500 W, and 20 mTorr pressure. The image indicates that the Ar plasma induces a sidewall re-deposition and/or TiN hard mask corrosion and further coarsens the film surface as shown in Figure 3-11 (c) and (d). It is known that Ar plasma causes a rough surface due to defect sites induced by the ion bombardment. (Kinoshita, Utsumi et al. 2010, Gajek, Nowak et al. 2012). Figure 3-11 (e) and (f) indicate that a 2 min Cl_2 plasma exposure removes the CoFe film entirely under the conditions of RF1 of 50 W, RF2 of 500 W, and 20 mTorr pressure with supporting evidence as shown in the cyan colored EDX spectrum in Figure 3-11 (i). The metal chloride layers formed by Cl_2 plasma have accumulated on the border between CoFe and TiN films as shown in Figure 3-11 (f). The time-dependent Cl_2 plasma influence on patterned wafers has been presented to demonstrate experimentally the accumulated metal chlorides on the border in the supporting information. SEM-EDX spectroscopy was performed to systematically confirm the existence of metal chloride after Cl_2 plasma treatment. Figure 3-11 (i) shows the EDX spectra measured in three different positions marked with colored circles in the SEM image of Figure 3-11 (f). The cyan colored circular region where the CoFe film was exposed to Cl_2 plasma shows the absence of Co-Lα, Fe-Lα, and Cl-Kα peaks because the film was etched by Cl_2 plasma. The Cl-Kα is observed only in the red colored spectrum, which was measured at the border as shown in Figure 3-11 (f). This spectrum is an indication that most of the metal chloride has accumulated on the edge of the TiN hard mask, and the CoFe film after the metal chloride layers were partially removed. The black colored spectrum measured on the TiN hard mask shows Ti-Lα, Co-Lα, and Fe-Lα peaks with the absence of Cl-Kα, indicating the metal chloride is induced

from the CoFe film. The Co-Lα and Fe-Lα peaks were detected because the penetration depth of the emitted X-ray is larger than 1 μm. In Figure 3-11 (g) and (h), a 4 min exposure to H$_2$ plasma chemistry totally removes the metal chlorides with the conditions of RF1 of 100 W, RF2 of 800 W, and 20 mTorr pressure. In addition, the reactive ion etch by Cl$_2$/H$_2$ plasma renders the etched surface smooth compared to the Ar sputtering-assisted surface as presented in Figure 3-11 (h). The red colored EDX spectrum in Figure 3-11 (j) demonstrates the extinction of the Cl-Kα peak induced by the Cl$_2$ plasma.
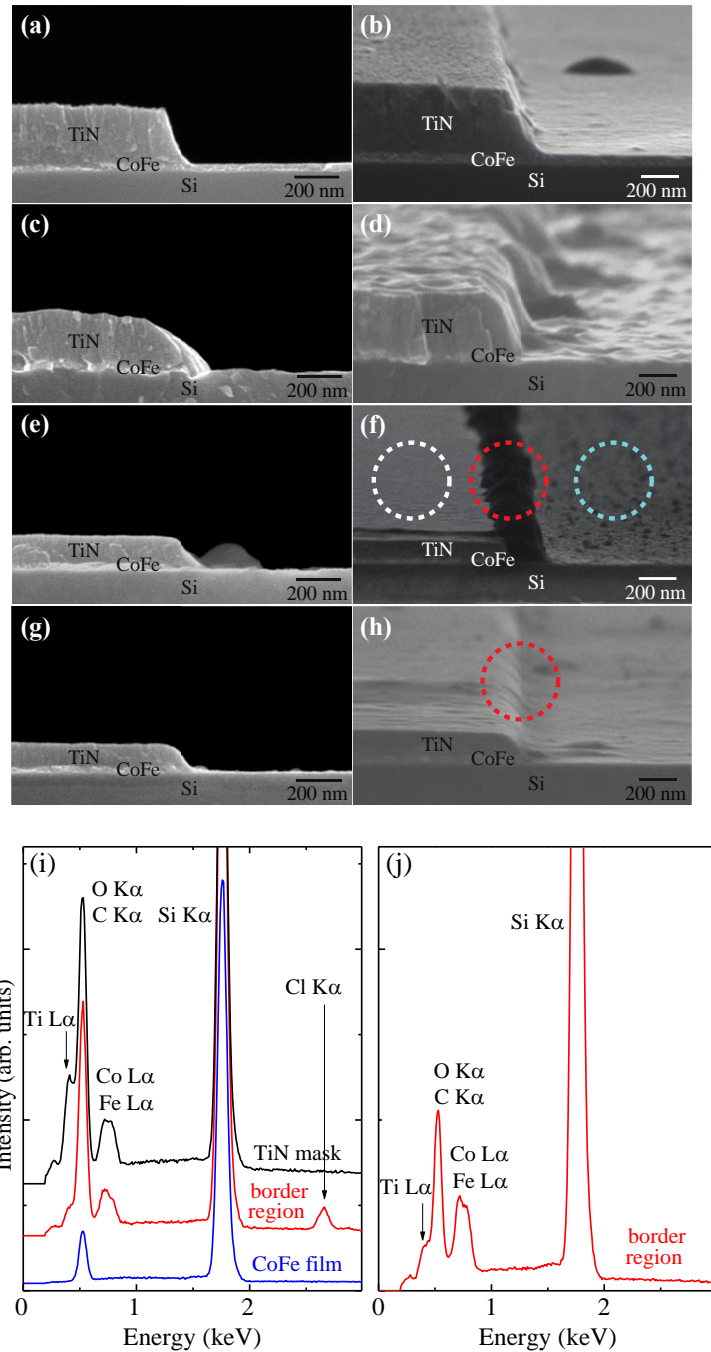
Figure 3-11 Cross-sectional ((a), (c), (e), and (g)), and bird eye ((b), (d), (f), and (g)) view SEM images of 300 nm TiN- masked 45 nm CoFe films. (a, b) CoFe pattern prior to plasma etching; (c, d) after 4 min Ar plasma etching with RF1 power of 100 W, RF2 power of 500 W and 20 mTorr pressure, (e, f) 2 min Cl_2 plasma etching with RF1 power of 50 W, RF2 power of 500 W and 20 mTorr pressure, (g, h) 4 min subsequent H_2 plasma etching with RF1 power of 50 W, RF2 power of 500 W and 20 mTorr pressure. Figure 3-11(i) and (j) present EDX spectra measured at the positions denoted by circles in Figure 3-11 (f) and (h), respectively.

3.3.3 Etching Profile Analysis of CoFe Etched in Cl_2/H_2 Plasma

In addition, the surface modification by Cl_2 and Cl_2/H_2 plasma is closely related with the restoration of magnetic properties in the magnetic metallic film. Figure 3-12 presents magnetic hysteresis loops for magnetization as a function of applied magnetic field of the pre-etched CoFe film, as a reference, and Cl_2 and Cl_2/H_2 plasma-treated CoFe films. The inset of Figure 3-12 shows coercive field and saturation magnetization extracted from the magnetic hysteresis loops as a function of hydrogen plasma duration. The hysteresis loop measured in the pre-etched CoFe film indicates the film exhibits soft magnetic properties characterized by low coercive field.(Osaka, Yokoshima et al. 2003) In Figure 3-12, formation of metal chloride layers renders the soft magnetic material harder, where the coercive field increases from ~20.9 Oe to ~63.6 Oe, and the saturation magnetization decreases from ~1300 emu/cm^3 to ~520 emu/cm^3. We have systematically studied the effect of H_2 plasma exposure time on the chlorinated CoFe film to reduce the amount of metal chloride as suggested in Figure 3-12. As the H_2 plasma treatment time is increased, the hard magnetism in the Cl_2 plasma exposed CoFe film is gradually reverted to soft magnetism as indicated by the coercive field and saturation magnetization. The existence of an optimal H_2 plasma exposure time can be explained by the hydrogenation of the magnetic metallic film, in which the magnetic moments and the coercive fields in the hydrides decrease and increase with increasing hydrogen concentration, respectively.(Antonov 2002, Lin, Tsai et al. 2013) The Cl_2 plasma treated ferromagnetic free layer in a MTJ device increases on/off energy triggered by a large amount of dissipated energy in repeatedly reversing the magnetization as implied from the broad hysteresis loop. For a more detailed explanation of the effect of metal chloride layers on the functionality of MTJ device, FMR spectra of the Cl_2/H_2-

plasma treated samples were measured under the same plasma conditions used in Figure 3-14 while keeping the microwave source of X-band (9.78 GHz) constant. Figure 3-14c indicates in-plane anisotropy fields obtained from the resonance magnetic fields in Figure 3-14b and the saturation magnetizations. The FMR linewidth and resonance field show similar trend as the coercive fields in inset of Figure 3-12. However, FMR spectroscopy can be a more accurate probe to measure the anisotropy field.(Lee, Wang et al. 2009) The in-plane anisotropy field is calculated from the Kittel equation(Kittel 1948, Pettiford, Zeltser et al. 2006) $f_{FMR} = \gamma \cdot \sqrt{(H_k + H_{FMR}) \cdot 4\pi M_s}$ where gyromagnetic constant is $\gamma \cong 2.8\,\text{MHz/Oe}$, H_{FMR} is the resonance magnetic field from FMR measurements and M_s is the saturation magnetization obtained from SQUID experiments. For a fixed microwave frequency, H_k is inversely proportional to the saturation magnetization. On the other hand, the switching current density J_c in an MTJ is approximated by $J_c \propto \alpha\{H_k + (H_d - H_{k,per})/2\}$(Sun 2000), where α is the magnetic damping constant; $H_{k,per}$ is the free layer perpendicular anisotropy, which is induced from the interaction between the free and buffer layers(Ikeda, Miura et al. 2010); and H_d is the out-of-plane demagnetizing field. Since $H_{k,per}$ has not been applied in this work, J_c is inversely proportional to H_k and implies J_c must be reduced by increasing H_2 plasma treatment time up to the optimal time. In addition, the FMR linewidth is broader when the Cl_2 plasma exposure time on the pre-etched CoFe film increases. The broader FMR linewidth indicates higher switching current density because the FMR linewidth is proportional to the magnetic damping constant. (Liu, Zhang et al. 2011)
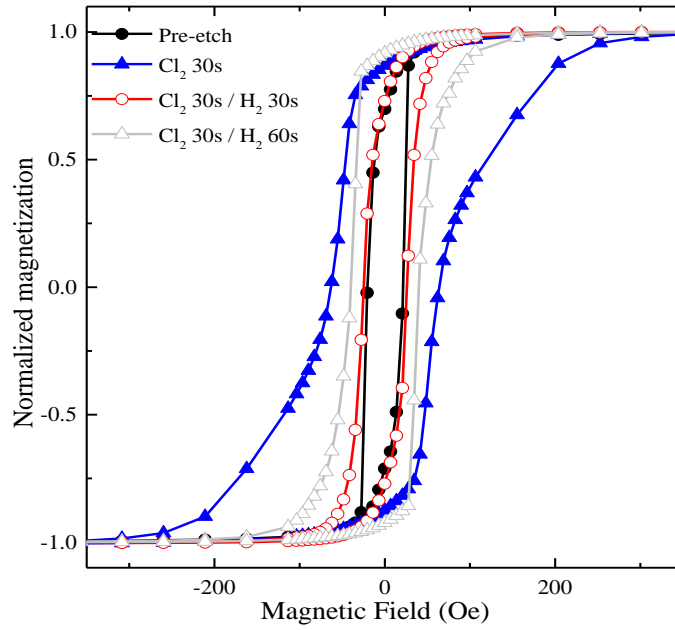
Figure 3-12 Magnetic hysteresis loop measured in CoFe films. Normalized magnetization (to saturation magnetization of pre-etch CoFe) vs. magnetic field under various etching conditions.
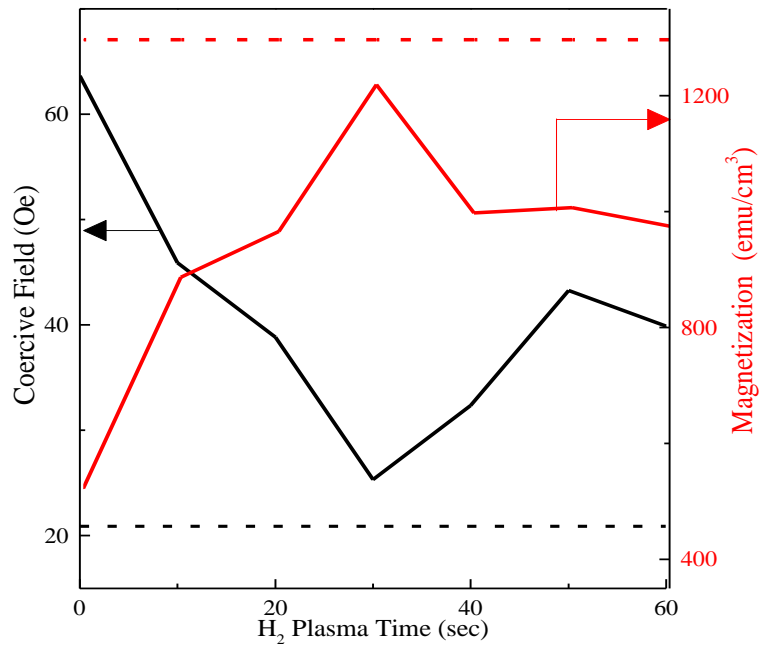
Figure 3-13 Coercive field and saturation magnetization as a function of H_2 plasma exposure time extracted from the magnetic hysteresis loop. The left and right y-axis indicate the coercive field and saturation magnetization from the pre-etched CoFe film, respectively.
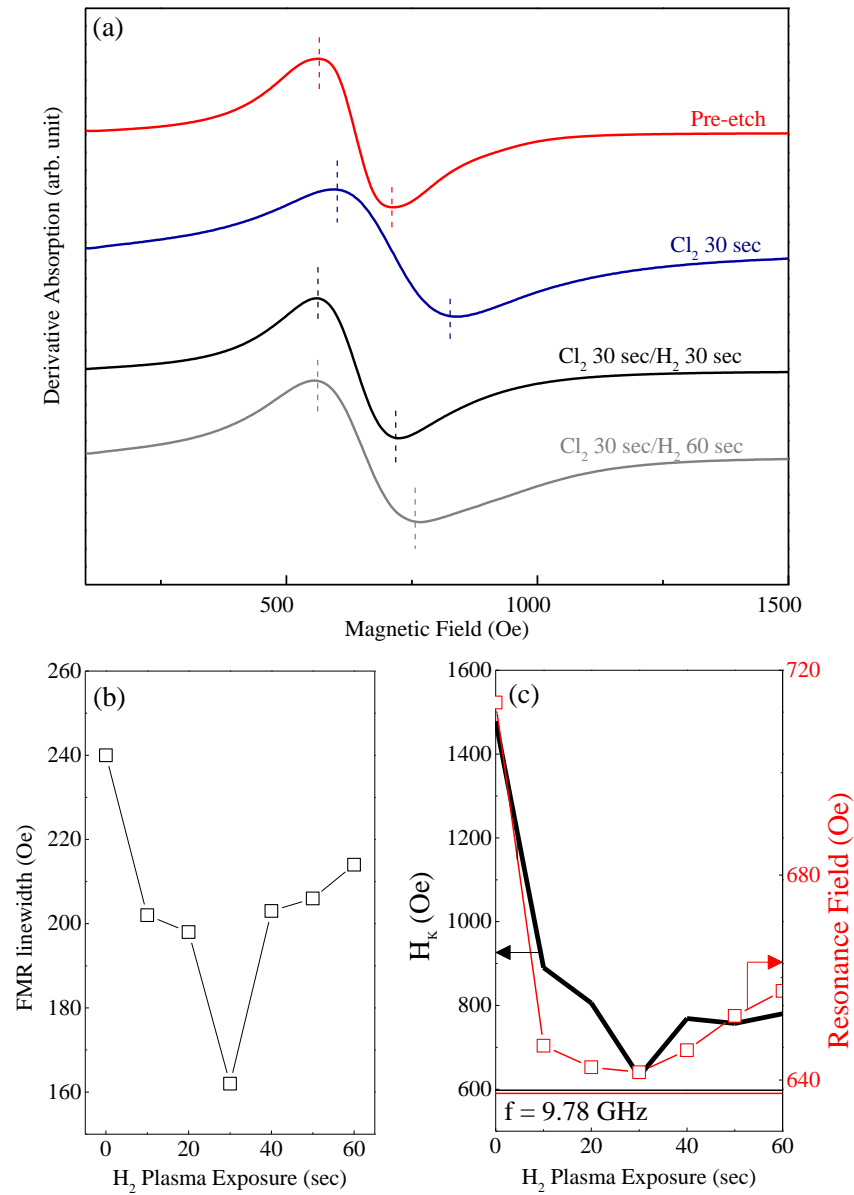
Figure 3-14 FMR spectra measured in CoFe films. (a) FMR spectra measured in pre-etched and post-etched CoFe films. Vertical dashed lines are the guide lines to represent the peak-to-peak line width deciding a damping coefficient. (b) FMR linewidth and resonance magnetic field obtained from FMR spectra with the values from the pre-etched film. (c) Resonance field and calculated anisotropy field as a function of H_2 plasma exposure time including the value from pre-etched CoFe film as denoted by the horizontal line.

3.4 Summary

The alternating exposure of Cl_2 and H_2 plasma is a viable etch chemistry for CoFe alloy film despite the fact that Cl_2 plasma alone is not an effective etch chemistry due to the generation of a metal chloride layer. According to the thermodynamic calculation, the atomic hydrogen addition to $CoCl_2$ and $FeCl_2$ film changes the equilibrium and leads to the formation of an etch product with a higher partial pressure. The measurements of an etch rate and a surface composition revealed that the alternating Cl_2/H_2 plasma exposure enhanced the etch rate by 20% compared to Cl_2 plasma showing the metal chloride removal from the surface. In addition, H_2 plasma could remove a metal chloride layer to yield a smooth etch profile. The development of a chemical etching process is required to fabricate high density integrated circuits. These results indicate that the alternating plasma approach is the first step toward fabricating high density MTJ-based RAM devices. Concerning the degradation of magnetic properties associated with halogen chemistry etch, the formation of metal chloride resulted in a significant change/increase in the coercive field which is not desirable. It was determined that the utilization of hydrogen led to a complete removal of the metal chloride, thus restoring the soft magnetic characteristics of CoFe. This confirms that the combination of Cl_2 and H_2 plasmas can not only etch CoFe at a reasonable rate but also preserve the magnetic property of CoFe. Since the thickness of the CoFe layer (3-5nm) is usually thicker than that of the tunnel oxide (~1nm), a double patterning process combining both chemical and physical etch processes may be necessary to successfully pattern both the magnetic layers as well as the tunnel oxide.

CHAPTER 4: ION BEAM ASSISTED ORGANIC CHEMICAL ETCH OF MAGNETIC

MATERIALS

An ion beam assisted organic chemical etch has been shown to chemically etch cobalt and iron which are major components in magetoresistive random access memory (MRAM). Acetylacetone (acac), hexafluoroacetylacetone (hfac) and 2,2,6,6-tetramethyl-3,5-heptanedionate (tmhd) have been first examined on etching cobalt and iron in solution. The etch rate of cobalt and iron in acac, hfac and tmhd solution were quantified by scanning electron microscopy (SEM). High selectivity of Co over Fe was observed in acac solution etch, which Co is 3.3 nm/min, and Fe is 0.9 nm/min. On the other hand, high selectivity of Fe over Co was also discovered in hfac, which Fe is 12.1 nm/min and Co is 0.3 nm/min. The electrospray ionization mass spectrometer (ESI-MS) has confirmed the formation of organometallic complex from metals and organics. Cobalt acetylacetonate ($Co(acac)_2$) and iron hexafluoroacetylacetonate ($Fe(hfac)_3$) were discovered in the post-etch solution of acac and hfac, respectively. To make organic chemical etch compatible with CMOS processing techniques and allow it to be integrated with other semiconductor processes, the thermodynamic analysis was applied to evaluate the dry etching efficacy. Although the organometallic product was calculated thermodynamically volatile, the merely no etch rate of cobalt in acac vapor suggested it was not kinetically favorable. Therefore, the argon ion beam was introduced to modify the surface prior vapor etch. An approximately ~180% enhancement of Co etch rate was observed with the alternating of argon ion beam and acac vapor, in comparison with only argon ion beam. This work suggests that a double patterning process combining ion beam assisted organic chemical etch may be necessary to successfully pattern the magnetic metals in MRAM device.

4.1 Thermodynamic Calculation of Etching Efficacy

This section documents the application of a previously developed, thermodynamic based methodology to explore the volatility of organometallic compounds. The thermodynamic calculation has proven to successfully predict the enhancement of Co and Fe etch rate by adding secondary H_2 plasma in traditional halogen-based plasma in chapter 3. However, the thermodynamic data for most of organometallic complex are not available, only selected organometallic complex such as metal acetylacetonates and metal hexafluoroacetylacetonates are found in the literature. (Fahlman and Barron 2000) Therefore, only cobalt and iron etched by acac and hfac are presented in the thermodynamic calculation.

Metal acetylacetonates, also known as pentanedionates, are synthesized by reacting metals and acetylacetone solution. Most of the common conventional precursors for the chemical vapor deposition (CVD) or atomic layer deposition (ALD) are metal acetylaceonates. Most of the metal acetylaceonates are stable in air and readily soluble in organic solvents such as acetonitrile or ethanol. Commercially available acetylacetonates organometallic compounds are shown in Table 4-1. (Pierson 1999) Halogen version metal acetylacetonate were increasingly synthesized recently due to its higher volatility compared to metal acetylacetonate. The fluorinated acetylacetonates such as $Cu(hfac)_2$, which has been proven to deposit high-purity copper films via thermally-induced CVD process. (Hampdensmith and Kodas 1995) Motivated by chapter 1, if an organo-metallic complex could facilitate the metal deposition with releasing the ligands, an excess of ligands on the metal surface may give rise to spontaneous etching based on Le Chatelier's principle (equilibrium law). This set of literature based on understanding the

thermodynamic property of organometallic compounds would be helpful on investigating metal etching efficacy by organic chemistry.

Table 4-1 Acetylacetonates organometallic compound (Pierson 1999).

Metal	Formula	Form	Melting point (^{o}C)
Barium	$Ba(C_5H_7O_2)_2$	Crystal	>320
Calcium	$Ca(C_5H_7O_2)_2$	White crystal	175
Cerium	$Ce(C_5H_7O_2)_3$	Yellow crystal	131
Chromium	$Cr(C_5H_7O_2)_3$	Violet crystal	214
Cobalt	$Co(C_5H_7O_2)_3$	Green powder	240
Copper	$Cu(C_5H_7O_2)_2$	Blue crystal	230
Dysprosium	$Dy(C_5H_7O_2)_3$	Powder	
Erbium	$Er(C_5H_7O_2)_3$	Powder	
Indium	$In(C_5H_7O_2)_3$	Cream powder	186
Iron	$Fe(C_5H_7O_2)_3$	Orange powder	179
Lanthanum	$La(C_5H_7O_2)_3$	Powder	
Lead	$Pb(C_5H_7O_2)_2$	Crystal	
Lithium	$LiC_5H_7O_2$	Crystal	250
Lutetium	$Lu(C_5H_7O_2)_3$	Powder	
Magnesium	$Mg(C_5H_7O_2)_2$	Powder	Decompose at room temp.
Manganese	$Mn(C_5H_7O_2)_2$	Buff crystal	180
Nickel	$Ni(C_5H_7O_2)_2$	Powder	
Palladium	$Pd(C_5H_7O_2)_2$	Orange needle	210
Platinum	$Pt(C_5H_7O_2)_2$	Yellow needle	
Silver	$AgC_5H_7O_2$	Crystal	
Strontium	$Sr(C_5H_7O_2)_2$	Crystal	220
Terbium	$Tb(C_5H_7O_2)_3$	Powder	
Vanadium	$V(C_5H_7O_2)_3$	Powder	
Ytterbium	$Yb(C_5H_7O_2)_3$	Powder	
Yttrium	$Y(C_5H_7O_2)_3$	Powder	
Zinc	$Zn(C_5H_7O_2)_2$	Needle	138
Zirconium	$Zr(C_5H_7O_2)_4$	White crystal	172

4.1.1 Volatility Diagram of Co and Fe in Acac and Hfac System

The potential reactions that were considered in the thermodynamic calculation for the system of Co and Fe etched by acac and hfac are listed in the Table 4-2. Reaction (1), (2) and (6)

are the sublimation of pure cobalt, reaction (3)-(5) are the sublimation of $Co(acac)_x$, reaction (7) is the sublimation of $Co(hfac)_3$. Reaction (8)-(12) are considered for iron which are very similar to those for cobalt, but less reactions were considered due to the lack of $Fe(acac)_2$, which According to literature, is readily transformed into $Fe(acac)_3$, based on the literature resulting in significant amounts of $Fe(acac)_3$ contaminated in $Fe(acac)_2$ commercial precursor. (Xue, Daran et al. 2011)

Table 4-2 Reactions utilized for plotting volatility diagrams in the M-acac & M-hfac systems (M = Co, Fe; acac = Acetylacetonate, hfac = Hexafluoroacetylacetonate) at 300K.

	Reaction	ΔG (kJ/mol)
(1)	$Co(c) \rightarrow Co(g)$	379.8
(2)	$Co(c)+ 2(acac)(g) \rightarrow Co(acac)_2(g)$	1053.0
(3)	$Co(acac)_2(c)+(acac)(g) \rightarrow Co(acac)_3(g)$	551.8
(4)	$Co(acac)_2(c) \rightarrow Co(acac)_2(g)$	50.6
(5)	$Co(acac)_3(c) \rightarrow Co(acac)_3(g)$	44.7
(6)	$Co(c)+ 3(hfac)(g) \rightarrow Co(hfac)_3(g)$	885.3
(7)	$Co(hfac)_3(c) \rightarrow Co(hfac)_3(g)$	13.0
(8)	$Fe(c) \rightarrow Fe(g)$	369.4
(9)	$Fe(c)+ 3(acac)(g) \rightarrow Fe(acac)_3(g)$	1537.9
(10)	$Fe(acac)_3(c) \rightarrow Fe(acac)_3(g)$	34.3
(11)	$Fe(c)+ 3(hfac)(g) \rightarrow Fe(hfac)_3(g)$	881.6
(12)	$Fe(hfac)_3(c) \rightarrow Fe(hfac)_3(g)$	9.3

The vapor pressures of organometallic compounds are plotted as function of partial pressure of acac and hfac in Figure 4-1. The horizontal dashed line at 10^{-8} atm referred to a reference point at which the weight loss of a material is detectable by a thermogravimetric analyzer and considered etchable. (Lou, Mitchell et al. 1985) The line (1) represents the reaction (1) and the sublimation of Co(c) to Co(g). The vapor pressure of Co(g) at 300K was lower than

10^{-66} atm. Line (2) represents the formation of Co(acac)$_2$(g) from Co(c), showing that the pressure of Co(acac)$_2$ increases dramatically as acac pressure increases in the reaction (2). The results suggest that the formation of Co(acac)$_2$(c) is much more favorable than Co(c). The vaporization of Co(acac)$_2$(c) to Co(acac)$_2$(g) is plotted by line (4). The pressure of Co(acac)$_2$(g) is much higher than that of Co(g), and it is very closed to the etchable reference line. While increasing the pressure of acac over10^{88} atm, the formation of Co(acac)$_3$(g) finally presented by line (5). From the Figure 4-1, the volatility of Co(acac)$_3$(g) is slightly higher than that of Co(acac)$_2$(g) and the etchable standard pressure, but the requirement of acac partial pressure is unreasonable high, which is not in the operational condition, 10-100 mtorr, ca. 10^{-4} atm. In the case of hfac chemistry for Co etch, the generation of Co(hfac)$_3$(g) takes place at 10^{67} atm, which is represented by line (11). Although the pressure of Co(hfac)$_3$(g) is much higher than that of Co(g), Co(acac)$_2$(g), and even Co(acac)$_3$(g), the requirement of acac partial pressure is too high to facilitate the reaction. In the conclusion, the thermodynamic calculation predicted that the acac would be relatively efficient in terms of etching efficacy compared to hfac.
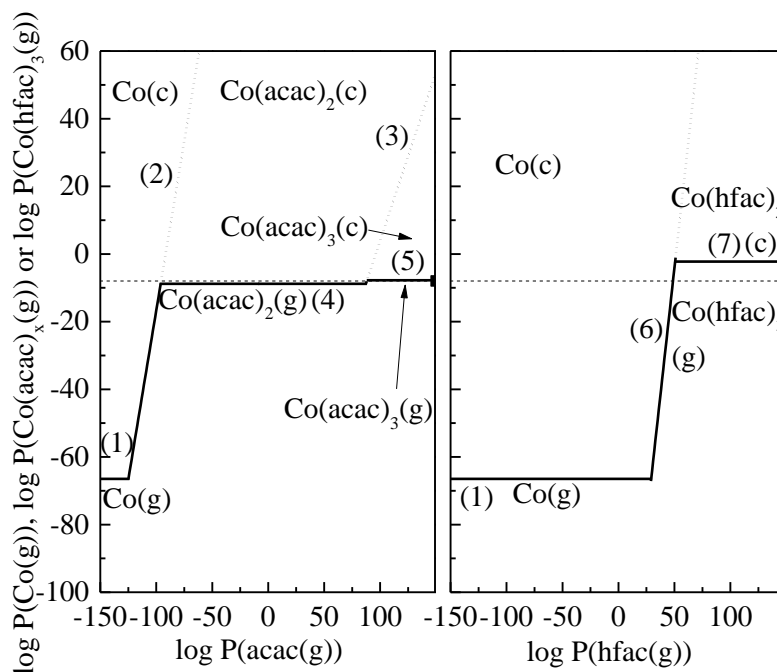
Figure 4-1 Volatility diagram for Co in acac and hfac at 300K. The reactions in the figure are presented in Table 4-2. The dashed line at 10^{-8} atm refers to the reactant volatility, corresponding to a weight loss that is detectable in a thermogravimetric analyzer.

The volatility diagram for iron is similar to that of cobalt (Figure 4-2), except the formation of Fe(acac)$_2$ is missing due to the nature of instability. (Xue, Daran et al. 2011) The sublimation of Fe(c) is presented by line (8), and the partial pressure of Fe (g) is as low as Co(g) in Figure 4-1. The generation of Fe(acac)$_3$(g) and Fe(hfac)$_3$(g) are presented by line (9) and (11), and they take place at 10^{75}, and 10^{50} atm of acac partial pressure, respectively. Line (10) and (12) represent the sublimation of Fe(acac)$_3$(c) and Fe(hfac)$_3$(c), and it is very similar to the case of Co that Fe(hfac)$_3$(g) has higher partial pressure than Fe(acac)$_3$(g). However, the formation of Fe(hfac)$_3$(g) requests lower partcial pressure of hfac than that of Fe(acac)$_3$(g), suggesting Fe(hfac)$_3$(g) would be more volatile than Fe(acac)$_3$(g). In the summary, hfac is relatively a promising chemistry compared to acac in etching Fe.

139
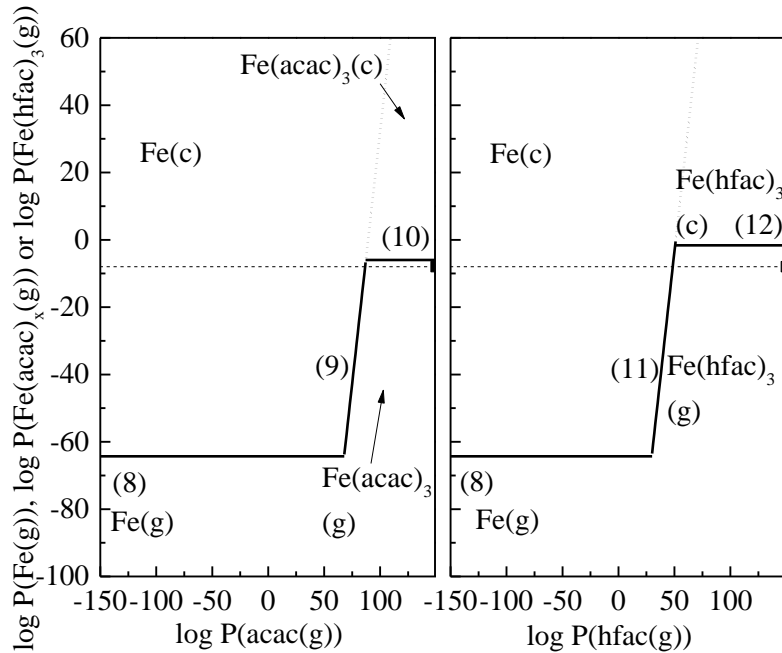
Figure 4-2 Volatility diagram for Fe in ACAC and HFAC at 300K. The reactions in the figure are presented in Table II. The dashed line at 10^{-8} atm refers to the reactant volatility, corresponding to a weight loss that is detectable in a thermogravimetric analyzer.

4.2 Organic Solution Etch of Co, Fe, Pt and Pd

4.2.1 Etch Rate Comparison

The etch rates of Co, Fe, Pd and Pt in 80°C acac solution were measured by SEM as shown in Figure 4-3a. The etch rate of Co (3.3 nm/min) is significantly higher than that of Fe (0.9 nm/min), Pd (0 nm/min), and Pt (0.0 nm/min). For the Co and Fe, the higher etch rates were observed in the first 40 min, but the etch rates were saturated after 80 min etch. The reason could be the concentration of organic on the metal surface decreased dramatically while etching due to the only driving force of mass transportation is concentration gradient. The colors of post etch solution are green for cobalt in acac, and light yellow for iron in acac, which are all consistent

with the literature, suggesting the formation of organometallic complex during the etch. (Pierson 1999) In the case of hfac solution etch, a high etch rate of Fe, 12.1 nm/min, is shown in the Figure 4-3b. Co is etched by hfac solution at merely 0.3 nm/min, and no etching is observed on Pd and Pt film. Figure 4-3c represents the etching of metal in tmhd, and no significant etching is observed. The experimental results follow the prediction of the thermodynamic calculation above. The reactivity between Co and acac is higher than that of Co and hfac; on the other hand, Fe shows a higher reactivity with hfac than that of acac.
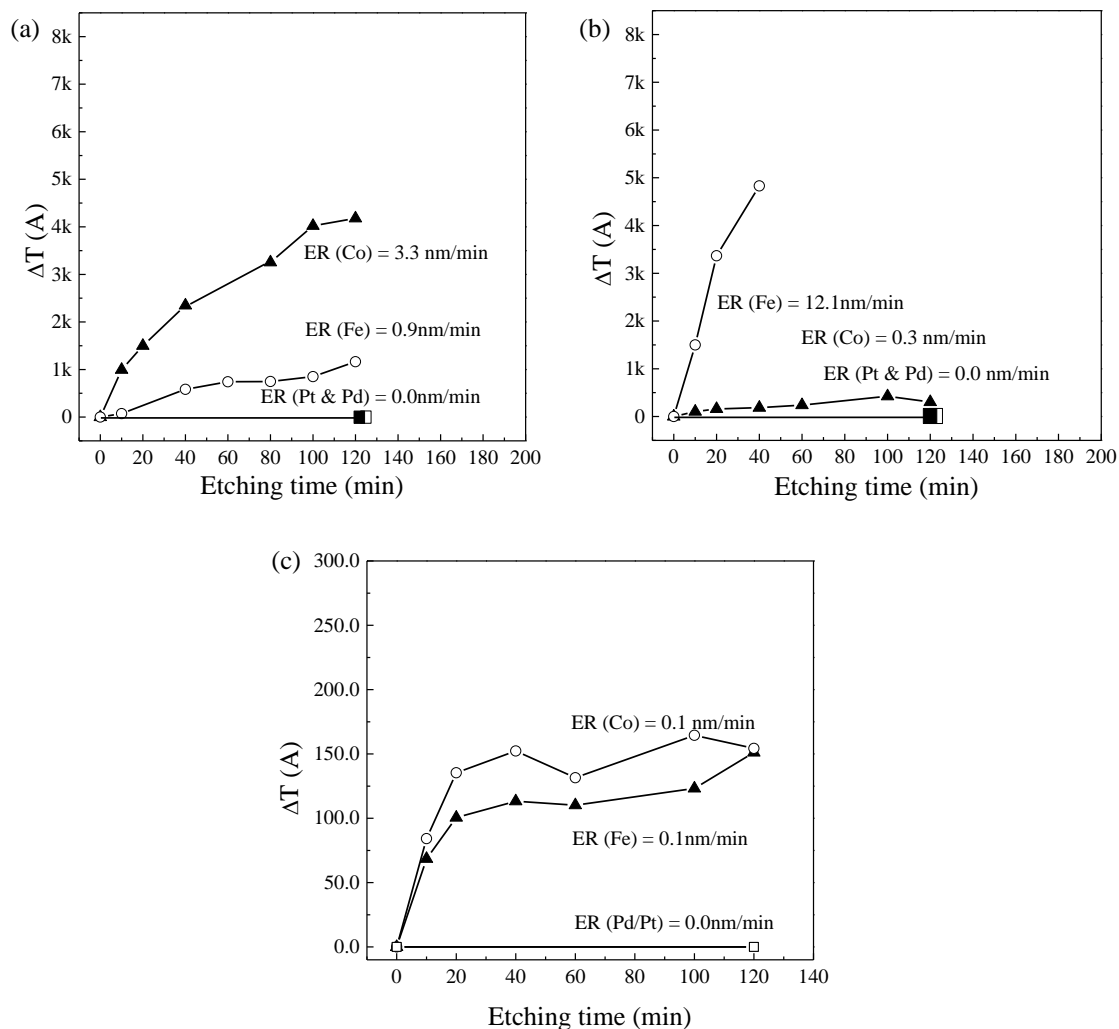
Figure 4-3 The etch rate of Co, Fe, Pd and Pt in (a) acetylacetone (acac) solution, (b) hexafluoroacetylacetone (hfac) and (c) 2,2,6,6-tetramethyl-3,5-heptanedione (tmhd) at 80°C was quantified by SEM. The triangle represents the etch of Co, the circle represents the etch of Fe, and the hollow square represents the etch of Pt and solid square represents the etch of Pd.

4.2.2 Etch Products Analysis

In order to confirm the formation of predicted etching products, the post-etch solutions were characterized by electrospray ionization mass spectrometry (ESI-MS). Figure 4-4(a) shows the mass spectra of Co and Fe etched in acac solution for 40 min. According to the mass to

charge ratio (m/z) and isotope patterns in the mass spectra, the isotopes of $Co(acac)_2$ (257amu) is found but not $Fe(acac)_3$ (353amu). Based on the theoretical calculation, the family of $Co(acac)_2$ isotopes would be 257 amu (100%), 258 amu (11.2%), 259 amu (1.3%), and 260 amu (0.1%). The experimental results follow the first two peaks with similar ratio of intensity but the rest of two are out of the detection range. In the case of Fe, almost no signal is found at $Fe(acac)_3$ (353amu), suggesting the low reactivity between Fe and acac. Figure 4-4(b) shows the mass spectra of Co and Fe etched in hfac solution for 40 min. The signal of $Co(hfac)_3$ (683 amu) in the post-etch solution would be too low to detect. The mass spectrum of Fe etched in hfac shows a strong set of signals, following that of calculated, 680 amu (100%), 681 amu (18.9%), 682 amu (3.1%), 683 amu (0.3%). Only the last peak is out of detection range, rest of them are matched the calculation results.
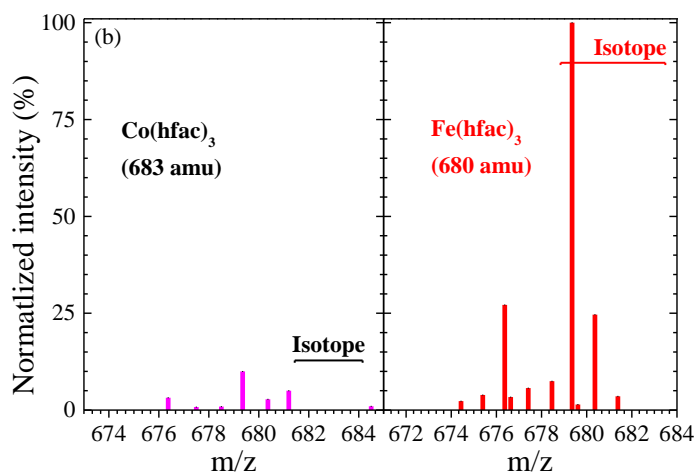
Figure 4-4 The mass spectrum of post-etch solution of (a) Co & Fe etched in acac solution, (b) Co & Fe etched in hfac solution. The isotope patterns of organometallic complex are shown on the right table.

4.2.3 Surface Chemical Characterization of Etched Surface

In order to better illustrate the specific chemical bonding changes as a result of organic exposure, CASA XPS software was used to deconvolute the spectra. This process thus allowed more detailed information to be extracted beyond overall composition fractions. For the study of

surface reactions, the thin films of Co and Fe were deposited as 20 nm, for observing the change in a short time. Figure 4-5 presents the surface chemical state of Co etched in acac solution at 80°C for 5 and 10 min. From the Figure 4-5a, the ratio of Co^{0+} to Co^{2+} increases significantly after 5 min acac solution etch. Similarly, the intensity of O-Co decreases after 5 min acac solution etch in O 1s spectrum, suggesting the preferential removal of cobalt oxide with acac. Ti 2p peaks show up after 10 min acac solution etch, indicating the end-point is achieved. From the Figure 4-6, similar phenomenon is observed on the Fe film etched in hfac. The ratio of Fe^{0+} to Fe^{2+} is slightly increased at Fe 2p$_{3/2}$ spectra, and the O-Fe peak dramatically decreases while reaching end-point. In conclusion, the organic chemicals tend to react with metal oxide, resulting in reducing of Co^{2+} and Fe^{2+} after 5 min etch in acac and hfac, respectively.
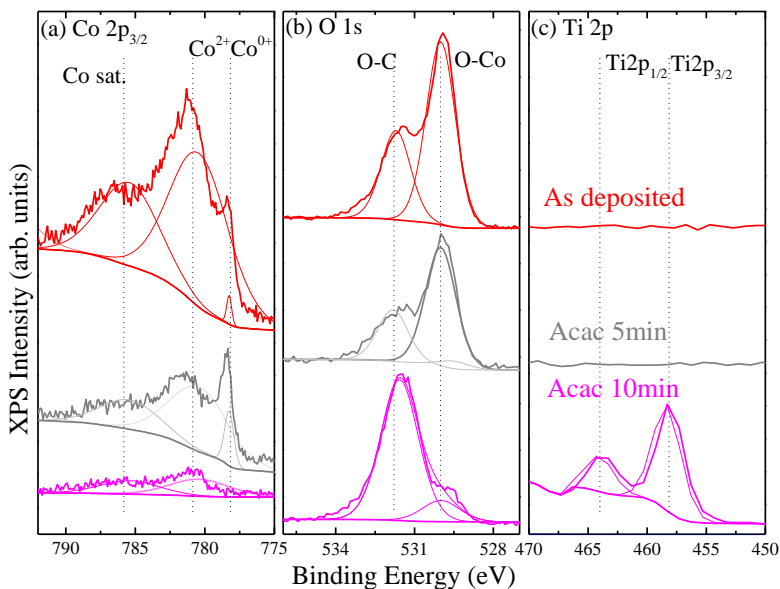
Figure 4-5 XPS spectra of (a) Co 2p3/2, (b) O 1s, and (c) Ti 2p. From the top, the spectra represents as deposited, acac solution etch 5 min, acac solution etch 10 min. For Co and Ti, each chemical state is represented by a spin-orbit split doublet, 2p3/2 and 2p1/2, which is constrained to have a 2:1 peak area ratio, equal full-width-at-half-maximum, and their energy separations are 15.0 eV, and 6.1 eV, for Co and Ti, respectively. For simplicity, only the 2p3/2 peak of Co is shown in the figure.
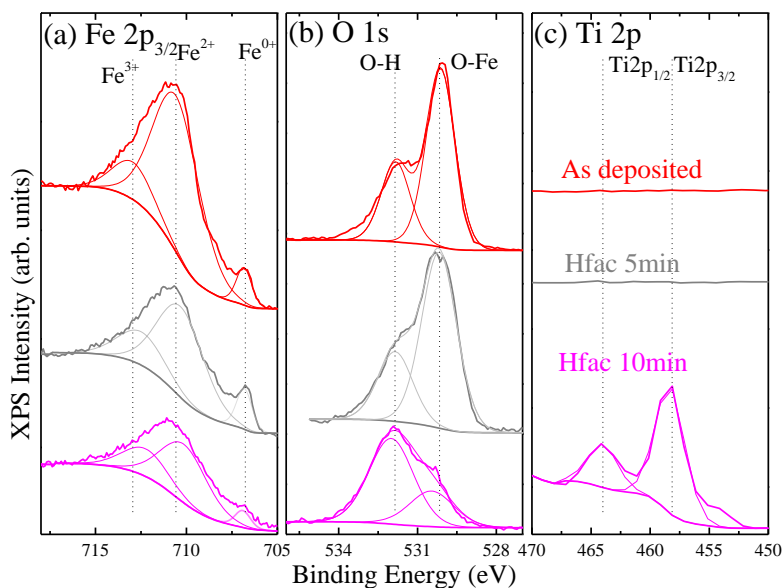
Figure 4-6 XPS spectra of (a) Fe $2p_{3/2}$, (b) O 1s, and (c) Ti 2p. From the top, the spectra represents as deposited, hfac solution etch 5 min, hfac solution etch 10 min. For Fe and Ti, each chemical state is represented by a spin-orbit split doublet, $2p_{3/2}$ and $2p_{1/2}$, which is constrained to have a 2:1 peak area ratio, equal full-width-at-half-maximum, and their energy separations are 12.9 eV, and 6.1 eV, for Fe and Ti, respectively. For simplicity, only the $2p_{3/2}$ peak of Co is shown in the figure.

4.3 Ion Beam Assisted Chemical Etch of Co

4.3.1 Acac Vapor Etch of Co

As motivated above, the etching process needs to be compatible with CMOS processing techniques and allowed to integrate with other semiconductor processes. Organic vapor etch is inevitable to the MRAM patterning. Before investigating the vapor etch, the acac solution is diluted by acetonitrile to perform the concentration dependent solution etch. In the Figure 4-7, the etch rate of Co decreases dramatically to zero when the concentration of acac decreases by the 4 order of magnitude. The etch rate of Co etched by acac vapor is labeled as a solid circle in

Figure 4-7. The density of acac molecule at 150°C and 0.5 mtorr is about 1.9×10^{-8} M (mol/L) and

the etch rate is only 0.004 nm/min.
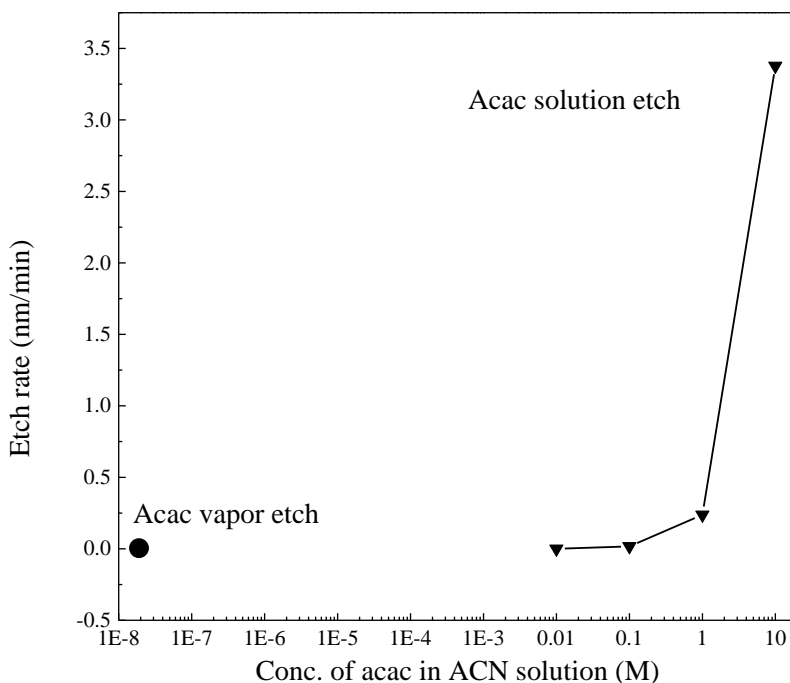
Figure 4-7 The etch rate of Co etched in several concentrations of acac diluted by
acetonitrile at 80°C for 60 min.

Figure 4-8 represents the XPS spectra of Co pre-etch and Co etched by acac vapor at

150°C for 8 hr. Due to the many peaks that had to be assigned in the case of carbon, Figure 4-8

shows the specific deconvolution of the C 1s region to better illustrate the bonding changes. The

same peak location values that were assigned in Chapter 2 were used to align the bonding states

in these spectra. As the C-Co, C-O, and C=O are appeared on the spectrum of Co etched in acac

vapor, suggesting the formation of organometallic compounds on the metal surface. Based on the

results above, the formation of the organometallic compounds is not the rate determining step but

the desorption of the organometallic compounds. Although the desorption process strongly

depends on the temperature of the surface, the operating temperature is not allowed to go over 300°C, which the magnetic susceptibility of the metal would decrease significantly and the magnetic property of MRAM device would be damaged. Therefore, Ar ion beam without heating up the metal surface was chosen to facilitate the desorption process of organometallic compounds.
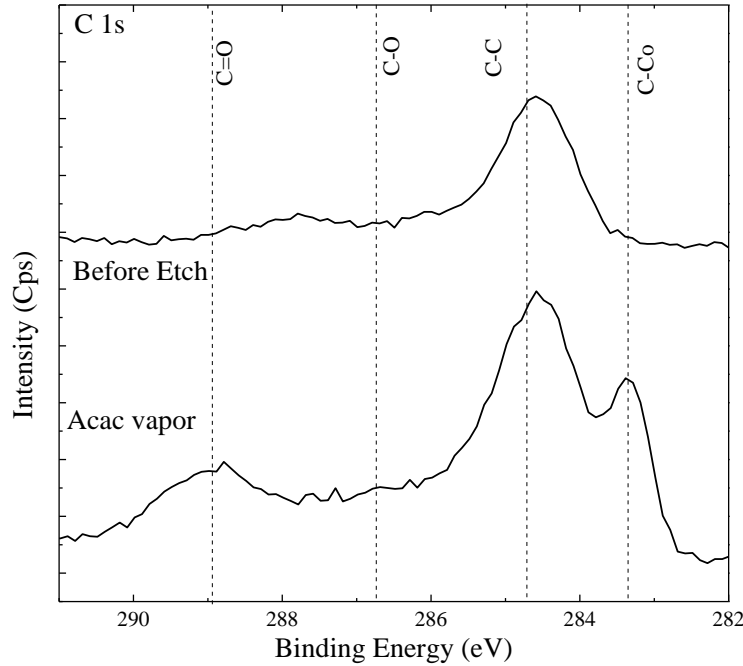
Figure 4-8 XPS spectra of C 1s. The top spectrum represents Co as deposited, and bottom spectrum represents Co etched by acac vapor for 8 hrs.

4.3.2 Ion Beam Etch of Co

Kaufman ion source with 3 cm beam size and defocused beam shape was selected to assist the chemical vapor etch of Co by acac. (Kaufman, Harper et al. 1979, Kaufman, Harper et al. 1979, Harper, Cuomo et al. 1982, Kaufman, Cuomo et al. 1982) The average number of atoms removed from a target per incident particle (atom or ion) is etching yield. It depends on

the target material, on the species of bombarding particles and their energy and the angle of incidence. Figure 4-9 shows the comparison of etching yield of Co as a function of Ar ion energy at a vertical incident angle from literature and the experimental results. (Laegreid and Wehner 1961, Stuart and Wehner 1962, Sletten and Knudsen 1972, Behrisch and Eckstein 2007) The range of ion energy on 3 cm Kaufman ion source is from 50 to 1000 eV. Thus, the etching yield is experimentally performed at 50, 100, 200, 300, 500, 1000 eV of Ar ion energy on Co 20 nm film. The experimental results follow the etching yield on literature, suggesting the controlling of ion beam energy is reliable. (Laegreid and Wehner 1961, Stuart and Wehner 1962, Sletten and Knudsen 1972, Behrisch and Eckstein 2007)
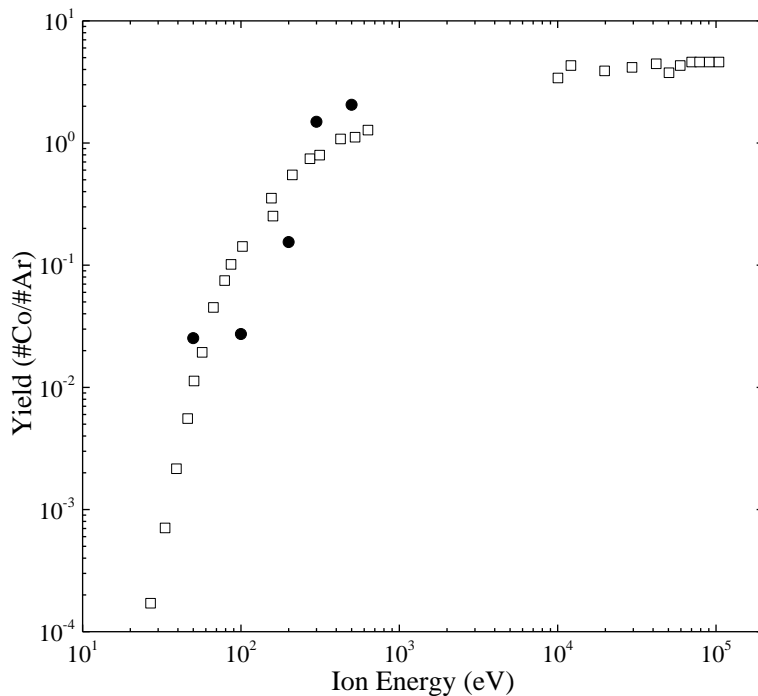
Figure 4-9 Etching yield of Co as a function of Ar ion energy. The Ar ion was vertical to the Co film. The hollow square represents the data from the literature (Laegreid and Wehner 1961, Stuart and Wehner 1962, Sletten and Knudsen 1972, Behrisch and Eckstein 2007), and the solid circle represents the data of ion beam in used.

Meanwhile, since the sample size of Co is about 15 mm in lateral dimension, the etch rate of Co is measured from -8 to 8 mm off of the beam center in lateral direction at 1 and 0.5 keV in Figure 4-10. The standard deviation are 0.32 and 0.24 nm at 1 and 0.5 keV, respectively, suggesting the Ar ion beam is uniform enough to neglect the deviation across the sample.
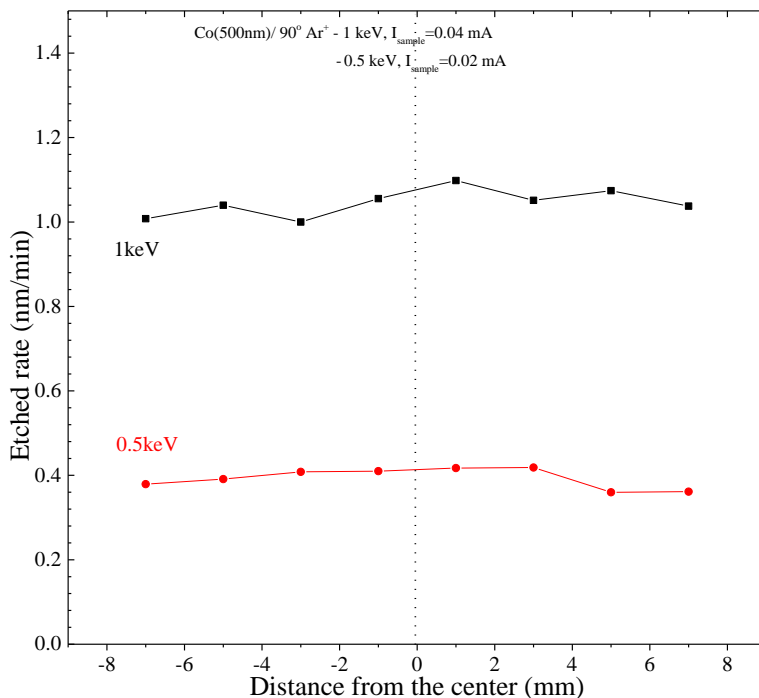
Figure 4-10 Uniformity of Co etch at 1 keV Ar ion beam. The etch rate was plotted as a function of distance from the center of Ar ion beam. The standard deviation is 0.32 nm at 1 keV, and 0.24 nm at 0.5 keV. The etched thickness was measured by SEM.

4.3.3 Ar Ion Beam Assisted Acac Vapor Etch of Co

An ion beam is used to assist the desorption of the organometallic compounds and subsequent etching process is performed by introducing acac vapor. Figure 4-11 represents the one cycle of alternating etch by following sequences: the surface cleaning performed by Ar ion

beam, 1) Ar ion beam is blocked by the shutter, and Co surface is exposed to the acac vapor, 2) acac ligands chemically bond to Co to form organometallic compounds, 3) Acac vapor is isolated from the valve, and Ar ion beam is exposed to the Co surface, 4) the desorption of organometallic compounds takes place on the Co surface. The process is simplified in Figure 4-12. It starts with a 5 sec Ar 1keV ion beam exposure, and followed by a 5 sec acac vapor exposure.
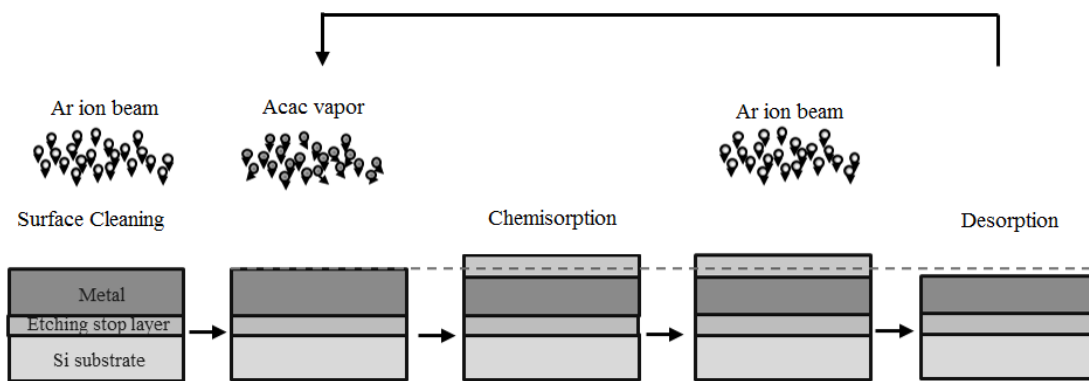
Figure 4-11 The process and mechanism proposed to facilitate the alternating etch, including the surface cleaning, acac vapor exposure, chemically bonding ligand and metal, Ar ion beam exposure, and the desorption of organometallic compounds.
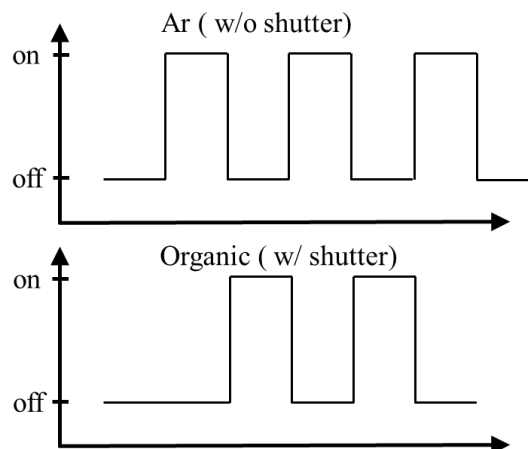
Figure 4-12 The detail of the process of alternating Ar and organic vapor exposure.

The design of the sample stage and shutter for the alternating etch system is shown in Figure 4-13. Top figure represents the three dimensional setup of the sample, shutter, and organic vapor doser. The figure at the bottom presents a side view of setup. When the shutter is closed, only right half of the sample is exposed to the acac vapor. But when the shutter is open, the entire sample is exposed to the Ar ion beam. Due to the pressure of acac is as low as 30 mtorr (4.0 Pascal), the mean free path can be calculated by following equation,

$$l = \frac{k_B T}{\sqrt{2}\pi d^2 p} \tag{4.1}$$

where, k_B is the Boltzmann constant in J/K, T is the temperature in K, p is pressure in Pascals, and d is the dimeter of the gas particles in meters. Since the mean free path of acac in the etching condition is about 8 mm, the 1 mm gap between film and shutter would not be visible to the acac molecular. Therefore, only the area directly exposed to doser is etched by acac vapor but not the area covered by shutter.
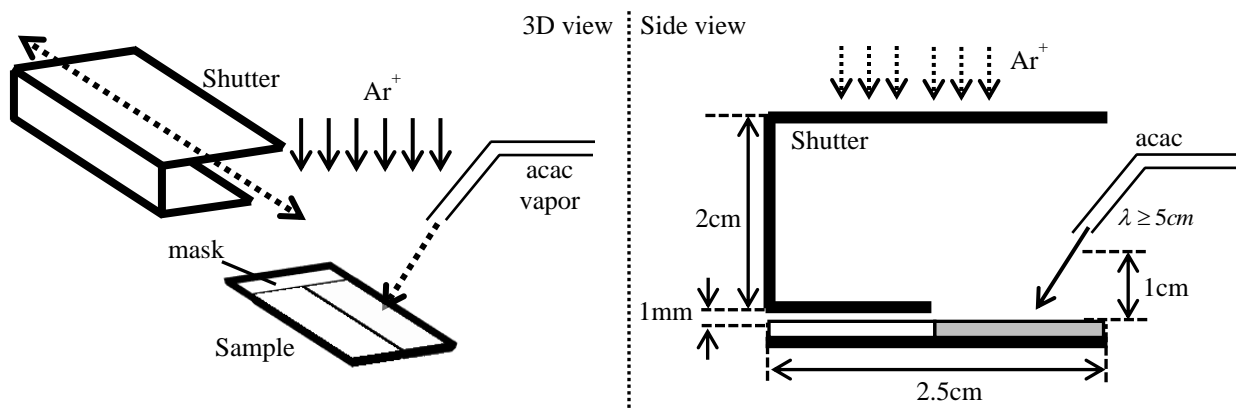
Figure 4-13 The design of the sample stage and shutter for the alternating etch system. Left figure presents the three dimensional setup of the sample, shutter, and organic vapor doser. The right figure shows a side view of setup that only 1 mm gap between shutter and sample would reduce the pressure of acac on the covered region dramatically.

During the acac dosing on right part of the sample, Ar ions were blocked by the shutter from sample. As shown in Figure 4-14, the SEM images are first aligned by a reference layer of 100 nm SiO_2, and the thickness of Co etched by alternating dosing is thinner than that of Co etched by Ar ion beam alone, suggesting an enhanced etch rate is achieved by additional organic chemical dosing. Figure 4-15 (a) presents the etch rate of Co etched by acac vapor, Ar ion beam, and sequential of Ar ion beam/acac vapor exposure were 0.004, 0.73, and 1.29 nm/min, respectively. The etch rate of Co is enhanced 176% by alternating Ar ion/acac vapor exposure compared to Ar ion only. Figure 4-15 (b) emphasizes the etch rate of the Ar ion beam and acac vapor combined beam is much greater than the sum of the two. The plot is learned from the Dr. Coburn and Dr. Winters when they first introduced the synergistic effect of chemical etching along with sputtering. (Coburn and Winters 1979)
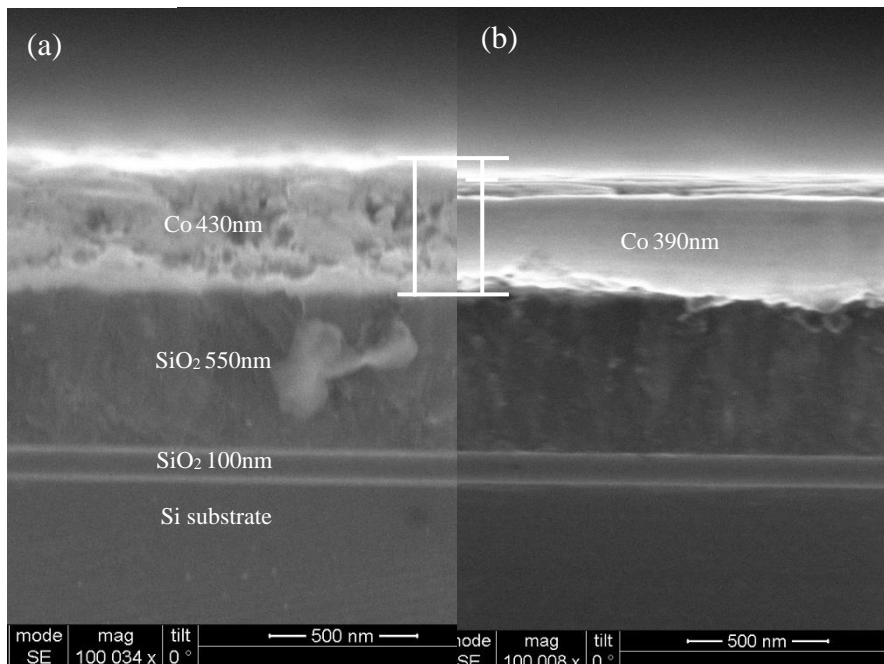
Figure 4-14 The SEM images of (a) Co etched by 1keV Ar ion beam for 75 min, and (b) Co etched by sequential dosing of 5 sec 1keV Ar ion beam and 5 sec acac vapor for 450 cycles, equivalent to 75 min.
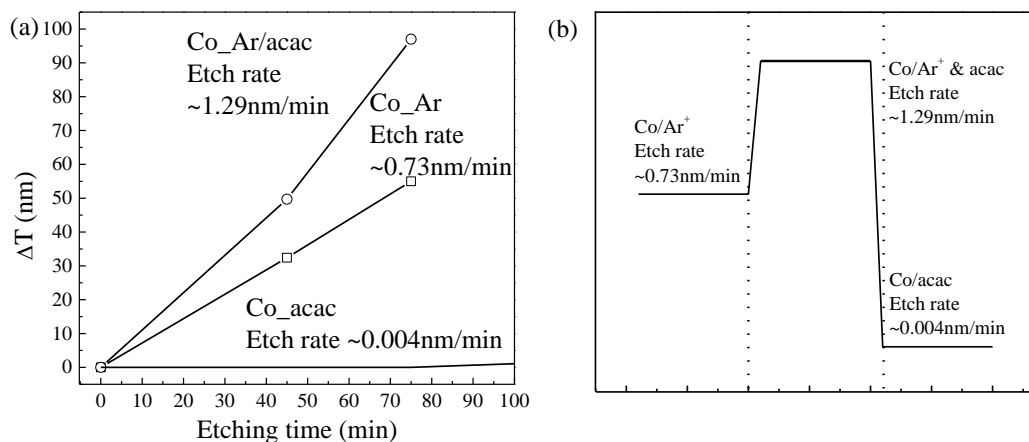
Figure 4-15 The etch rate of Co etched by acac vapor, Ar ion beam, and alternating exposure of Ar ion beam and acac vapor were 0.004, 0.73, and 1.29, respectively. The thickness was measured by SEM.

4.4 Summary

The etching of Co and Fe in acac and hfac are evaluated by the thermodynamic calculation and verified by experiments. The volatility diagram has predicted the selectivity of acac over hfac in etching Co, due to the higher partial pressure of $Co(acac)_2(g)$ than that of $Co(hfac)_3(g)$ at operating conditions. In the case of Fe, the high selectivity of hfac over acac is discovered, which the formation of $Fe(hfac)_3(g)$ requests lower partial pressure of hfac than that of acac to generate $Fe(acac)_3(g)$. The etch rates of Co and Fe by acac and hfac solution follow the prediction in thermodynamic calculation. The high selectivity of Co over Fe is observed in acac solution, and the even higher selectivity of Fe over Co is observed in hfac solution. However, when it comes to the concentration dependent etch, the etch rate of Co decreases to 0 nm/min when the concentration decreases by 4 orders of magnitude. The concentration of acac molecule in vapor phase is much lower than that in solution, which is about 8 order of magnitude

154

lower. Therefore, the etch rate of Co etched by acac vapor is extremely low, suggesting the modification in the etching process. Ar ion beam was introduced in order to facilitate the desorption process of organometallic compounds without degradation of the magnetic property of metals. The etching of Co by alternating Ar ion beam exposure and acac vapor exposure has the effect of significantly increasing the etch rate by approximately 180% compared to that of Ar ion beam only. The etch rate of Co by alternating Ar ion beam and acac vapor is much greater than the sum of the two, suggesting the synergistic effect of chemical etching along with sputtering is discovered in the ion beam assisted chemical etch process.

CHAPTER 5: ORGANIC CHEMICAL ETCH OF METALS WITH SURFACE

MODIFICATION

The approach to capturing the metal etching in organics discussed in Chapters 4 utilized a combination of thermodynamic calculation and experimental methods to verify its efficacy. Although an Ar ion beam has gained significantly improvement on patterning Co with organic vapor etch, the enhancement of the reactivity between metals and ligands is required to realize a sole chemical etch of metal. By modifying metal surface with plasma, the electron on the metal surface would be localized, resulting in a higher reactivity between organic ligands to metal. In this chapter, Pt is chosen as an example in terms of selecting the approach of surface modification and examining the etching efficacy of organic solution, because Pt is the most difficult-to-etch metal in the MRAM stack. Upon developing the optimized process for surface modification and the most efficient organic ligands in etching metals, the vapor etch is studied systematically with a vaporizer for delivering organic ligands and ICP O_2 plasma for surface modification. Furthermore, the sequential vapor etch was not only applied on Pt but extended to the other transition and noble metals such as Co, Fe, Cu, and Pd, demonstrating the capability of the generalized approach of metal etch. The etch of patterned samples with hard mask TiN on Co film and Ta on MTJ stack were performed by sequential vapor etch, and the selectivity of mask to metal, etching profile evolution, and magnetic property were realized to further understanding the atomic layer control of metal etch. Finally, the desired anisotropic etching profile was investigated in order to achieve a high density patterning of MRAM memory.

5.1 Surface Modification of Metals

The surface modification was originated from the chamber cleaning, which was a huge challenge in 1995. Very large scale integrated (VLSI) manufacturers applied a lot of efforts on removing the contamination from depositing the metal film through chemical vapor deposition. (Farkas, Chi et al. 1993, Kruck and Schober 1997, Lee, Ford et al. 1998, Nigg and Masel 1998, Nigg, Ford et al. 1999, Nigg and Masel 1999, Steger and Masel 1999) One of the most challenging contaminant was Ni, which drew a lot of attentions on chemical vapor cleaning. Some of the literature reported that pre-oxidized Ni shows higher reactivity to acac (acetylacetone) and hfac (hexafluoropentanedione) than metallic Ni. (Nigg and Masel 1998)

In early 1997, patterning of Cu was studied intensively due to its promising properties in repalcing Al alloy for circuit intenconnecting application. [need a literature]. However, it was very difficult in patterning Cu because there was no promising method in generating highly volatile products in dry etching process. (Kang, Kim et al. 1999) An approach involved the oxidation of Cu followed by hexafluoroacetylacetone (Hfac) vapor etch was investigated. (George, Hess et al. 1995, Jain, Kodas et al. 1995, Perry, Jain et al. 1995) While the metallic Cu exposed to hfac vapor, the fragments of decomposed hfac was found on the Cu surface. In contracts, the formation of organometallic compound, $Cu(hfac)_2$, was detected when Cu was oxidized prior hfac vapor etch. Therefore, the surface modification of metals are discussed in the following section.

157

5.1.1 Chemistry Selection for Metal Surface Modification

Several chemistries are selected to modify the metal surface, such as SO_2, Cl_2, CF_4, SF_6, O_2 plasma, and O_2 ion source. [Describe why we chose these chemistries] The metals of interest are hard-to-etch metals, such as Cu, and fundamental components in MRAM (Magnetoresistive random access memory) device such as Co, Fe, Pd, and Pt. In order to elucidate the generalize approach in patterning metal by surface modification, one of the most challenging metal, Pt, is selected as an example to show the surface chemical characterization. Pt is a noble metal, which is also the least reactive metal by nature. It has prominent resistance to corrosion even at high temperature, which makes it chemically stable on earth. (Weast 1988) Pt would be a great example in representing surface modification of metal.

Due to the availability of gas chemistry, several different plasma etcher were applied to study the surface modification of Pt. SO_2 and Cl_2 plasma treatments were supported by sponsor, Lam Research, with [etcher model] at source power of 500 W and bias power of 0 and 50 W. [waiting for Pressure and etcher model] The etcher of CF_4 and SF_6 plasma is Ulvac 550, and it is located at Integrated Systems Nanofabrication Cleanroom (ISNC) of California NanoSystems Institute (CNSI). The etch experiments were conducted at 500 W of source power, 5 mT, and 0 and 50 W bias power. O_2 plasma was conducted at custom-built inductively coupled plasma etcher in house. The operational condition was at 500 W of source power, 5 mT, and 0, -100, -150, and -200 V of bias voltage. Wafer pieces of the Pt films (~20 nm thick on Si substrates) approximately 2 cm^2 in area were loaded into the plasma chamber with several plasma conditions listed above. Samples were then analyzed via ex-situ XPS at a takeoff angle of 30° to

investigate the effects of plasma exposure. XPS spectra for the Pt 4f, Cl 2p and S 2p peaks of the pre-etched (1), SO$_2$ 500 W/0 W 1 min (2), SO$_2$ 500 W/50 W 1 min (3), Cl$_2$ 500 W/0 W 1 min (4), and Cl$_2$ 500 W/50 W 1 min (5) exposed Pt films are presented below in Figure 5-1. The FWHM of Pt peak was assessed for the pre-etched film and used to fit the etched spectra as well to provide an accurate measurement of the Cl 2p and S 2p area.
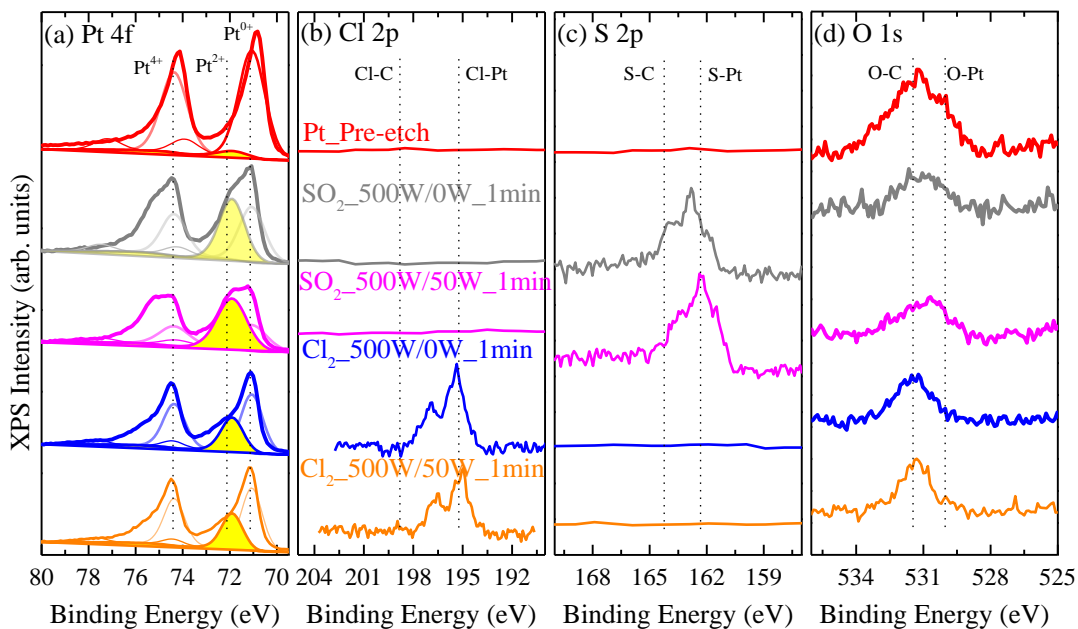
Figure 5-1 XPS spectra of (a) Pt 4f, (b) Cl 2p (c) S 2p, and (d) O 1s peaks for (1) pre-etch, 1 min surface treatment at (2) SO$_2$ in 500 W plasma source with 0W bias, (3) SO$_2$ in 500 W plasma source with 50W bias, (4) Cl$_2$ in 500 W plasma source with 0W bias, (5) Cl$_2$ in 500 W plasma source with 50W bias.

In order to better illustrate the specific chemical bonding changes as a result of plasma exposure, CasaXPS software was used to deconvolute the spectra of Pt. The process allowed more detailed information to be extracted beyond overall composition fractions. Due to three peaks that had to be assigned in the case of platinum, Figure 5-1 (a) shows the specific deconvolution of the Pt 4f region to better illustrate the bonding state changes. The bonding

energy of the peaks were assigned in Chapter 2, which can align the bonding states in these spectra.

Figure 5-1 (a) shows a deconvoluted Pt with Pt^{0+} (71.1 eV) and Pt^{2+} (71.9 eV). Since both sulphur and oxygen could potentially generate chemical bond of Pt(II)-S and Pt(II)-O, it would be complex in deconvoluting Pt 4f. Fortunately, the detail of O 1s in Figure 5-1 (d) suggests that the amount of oxygen on the platinum surface did not change significantly after SO_2 plasma treatment, implying the O 1s peak was basically C-O bond which formed in the atmosphere due to the ex situ XPS measurement. Furthermore, the peak of metal oxide located at 530.0 eV in Figure 5-1 (d) was relatively small compared to that of metal sulfide in S 2p spectra of Figure 5-1 (c). Therefore, the major bonding in Pt^{2+} peak is Pt(II)-S, suggesting Pt-S bond is relative easy to form compared to Pt-O. This observation is somewhat consistent with evidence in the literature that bond energy of Pt-O is 392 kJ/mol, which is 167% higher than that of Pt-S, ca. 234 kJ/mol. (Luo 2003) After 1min SO_2 plasma without bias exposure, the fraction of the Pt-S peak (Pt^{2+}) increased significantly compared to pre-etched spectra. Nevertheless, the fraction of Pt-S peak increased even higher at SO_2 plasma with 50 W bias, suggesting a higher degree of modification was achieved. On the other hand, it is relatively simpler in deconvoluting Pt 4f of the Pt treated by Cl_2 plasma, because there is no other element in competing with Cl for Pt^{2+} peak. Thus, the Pt^{2+} peak in Figure 5-1 (a) can be assigned to Pt-Cl bond. The fraction of Pt-Cl bond in Cl_2 plasma with and without bias increased slightly compared to pre-etched film, but they were not as significant as Pt-S peak in SO_2 plasma. Although the area under S 2p spectra is quite similar to that of Cl 2p, the atomic sensitivity factor (ASF) of S 2p is smaller than that of Cl 2p on XPS machine, suggesting the preference of bonding sulfur than chlorine to platinum.

After studying the surface modification by SO_2 and Cl_2 plasma, fluorine-contained compound plasma was investigated by XPS as well. Figure 5-2. shows the XPS spectra for the Pt 4f, F 1s and S 2p peaks of the pre-etched (1), CF_4 500 W/0 W 1 min (2), CF_4 500 W/50 W 1 min (3), SF_6 500 W/0 W 1 min (4), and SF_6 500 W/50 W 1 min (5) exposed Pt films.
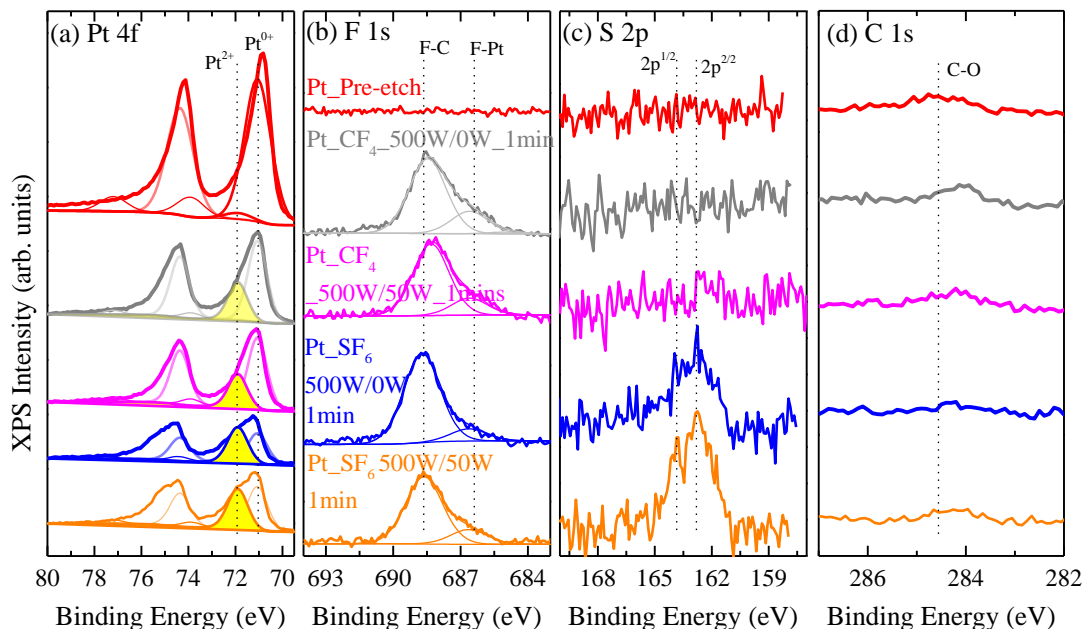
Figure 5-2 XPS spectra of (a) Pt 4f, (b) Cl 2p (c) S 2p, and (d) C 1s peaks for (1) pre-etch, 1 min surface treatment at (2) CF_4 in 500 W plasma source with 0W bias, (3) CF_4 in 500 W plasma source with 50W bias, (4) SF_6 in 500 W plasma source with 0W bias, (5) SF_6 in 500 W plasma source with 50W bias.

The deconvoluted Pt 4f with Pt^{0+} (71.1 eV) and Pt^{2+} (71.9 eV) is presented in Figure 5-2 (a). Similar to Pt treated by SO_2 plasma, a competing between F-Pt(II)-F and C-Pt(II)-C was found in Pt treated by CF_4 plasma. However, the detail of C 1s in Figure 5-2 (d) shows a very low amount of carbon on the film before and after CF_4 plasma treatment, suggesting the majority of Pt^{2+} is Pt-F bond. The increase of Pt-F peak (Pt^{2+}) were observed after CF_4 plasma treatment for 1 min compared to pre-etched Pt. But the amount of Pt-F did not increase with increasing

bias power, implying the difficulty in generating PtF_2 compound. The observation is confirmed by the literature that platinum fluoride is stable at solid PtF_6, instead of PtF_2. (Drews, Supel et al. 2006)

Therefore, it would be more complex in deconvoluting Pt 4f of Pt treated by SF_6 plasma, since sulphur and fluorine would possibly bond to platinum. However, Figure 5-2 (b) shows the amount of F-Pt (686.4 eV) is even lower than that in CF_4 plasma treatment. Meanwhile, Figure 5-2 (c) presents the S 2p peak that the atomic percentage of S-Pt is similar to that of Pt-S in Figure 5-2 (a), which has verified that the majority of Pt^{2+} is Pt-S bond. In contrast to CF_4 plasma treatment, the amount of Pt-S increased while increasing bias power, suggesting a higher degree of surface modification was achieved. The observation is perfectly matched the literature that Pt is easily poisoned by sulfur atom in catalyst application. (Argyle and Bartholomew 2015)

The surface modification by O_2 ion source is shown in Figure 5-3. The XPS spectra for the Pt 4f, O 1s and Pt $4p_{3/2}$ peaks of the pre-etched (1), 50 eV (2), 100 eV (3), 200 eV (4), and 500 eV (5) O_2 ion source exposed Pt films for 5 min.
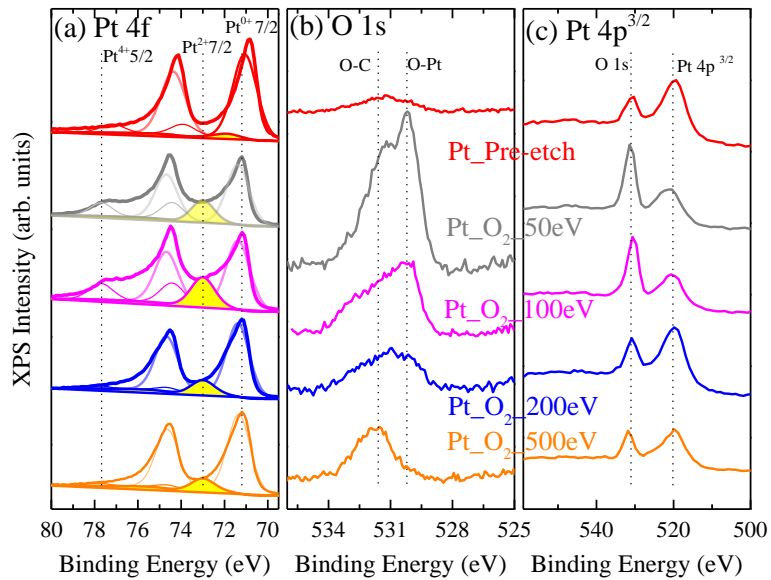
Figure 5-3 XPS spectra of (a) Pt 4f, (b) O 1s, and (c) Pt $4p^{3/2}$ peaks for (1) pre-etch, 5 min O_2 ion beam treatment at (2) 50 eV, (3) 100 eV, (4) 200 eV, and (5) 500 eV.

Unlike the studies of fluorine-, chlorine-, and sulfur-contained plasma, the Pt 4f of Pt treated by oxygen ion source is deconvoluted to Pt^{0+}, Pt^{2+}, and Pt^{4+} due to the formation of Pt(IV)O_2, which is much significant compared to others. Since there is only oxygen in the plasma, the only possibility of Pt^{2+} and Pt^{4+} peaks would be bonding of Pt-O and Pt-O_2, respectively. By considering the $Pt^{4+}_{5/2}$ peaks in Figure 5-3 (a), the 50 and 100 eV present a high amount of Pt-O_2 bond compared to 200 and 500 eV. In the O 1s spectra of Figure 5-3 (b), the O-Pt (530 eV) is distinct after 50 and 100 eV O_2 ion source treated. Figure 5-3 (c) of Pt $4p_{3/2}$ shows the peak of O 1s and Pt $4P_{3/2}$ together, which would allow to observe the ratio of O 1s to Pt $4p_{3/2}$. The peak of O 1s is stronger than Pt $4p_{3/2}$ in 50 and 100 eV, suggesting a higher degree of oxidation is achieved compared to pre-etched, 200, and 500 eV oxygen ion exposed Pt. This observation suggests that Pt is able to be oxidized by O_2 ion source, but it is also easily sputtered at high energy by O_2 ion source when ion energy is higher than 200 eV. In the Figure 5-4, the similar result was found in the literature that PtO$_2$ only formed at low sputtering power with O_2

gas. The PtO_2 tends to reduce to PtO and Pt while increasing sputtering energy from 40 to 100

W. (Mcbride, Graham et al. 1991) Although some of the literature suggests that PtO_2 tends to

decompose above 400 °C in ambient air, the maximum temperature of Pt surface was at 100 °C

based on thermocouple thermometer while conducting ion source experiments at all ion energies.

(Mosquera, Horwat et al. 2012) Therefore, the low energy of O_2 ion source is desired to generate

higher degree of platinum oxide.
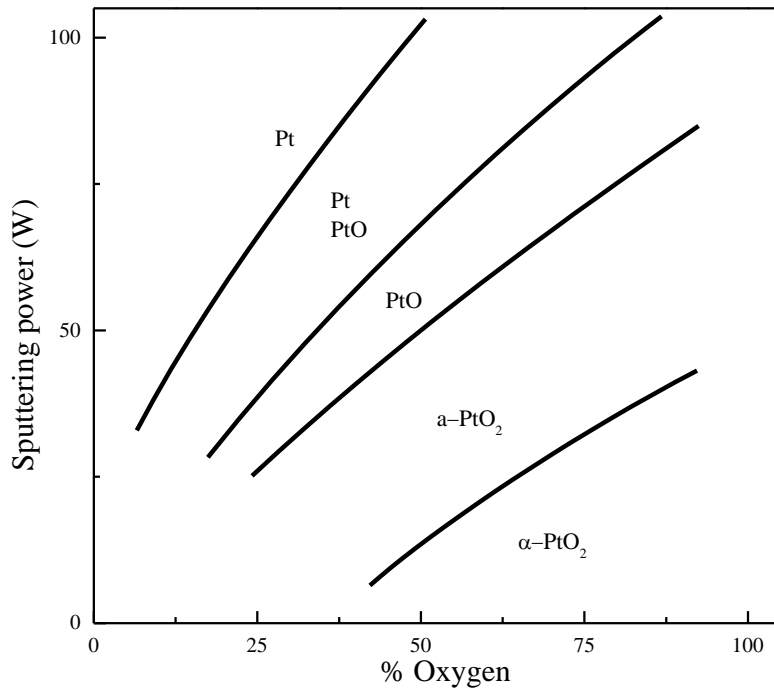
Figure 5-4 Schematic phase diagram for producing reactively sputtered platinum-oxygen films. Sputtering power is plotted against oxygen content for fixed sputtering pressure and substrate temperature (Mcbride, Graham et al. 1991).

Thus far, the XPS analysis suggests oxygen would be the most effective chemistry in

modifying platinum surface. Therefore, the surface modification by O_2 plasma is shown in

Figure 5-5. The XPS spectra for the Pt 4f, O 1s and Pt $4p_{3/2}$ peaks of the pre-etched (1), 0 V (2), -

100 V (3), -150 V (4), and -200 V (5) bias voltage with 500 W source power of O_2 plasma

exposed Pt films. Similar to deconvolution of Pt treated by O_2 ion source, Pt 4f in Figure 5-5 (a) is deconvoluted to Pt^{0+}, Pt^{2+}, and Pt^{4+} due to the formation of $Pt(IV)O_2$. The amount of $Pt\text{-}O_2$ bond is even higher than that generated in O_2 ion source, and it is quite constant across 0 to -200 V bias voltage compared to pre-etched Pt. O 1s spectra in Figure 5-5 (b) is deconvoluted to O-C and O-Pt bond, and the amount of O-Pt bond increased significantly with O_2 plasma with 0 V bias for 5min compared to pre-etched Pt. Also, the amount of O-Pt did not change while increasing bias voltage from 0 to -200 V. Figure 5-5 (c) presents the spectra of O 1s and Pt $4p_{3/2}$, the ratio of O 1s to Pt $4p_{3/2}$ increased significantly as well after O_2 plasma treatment, which is consistent with Pt 4f and O 1s spectra.
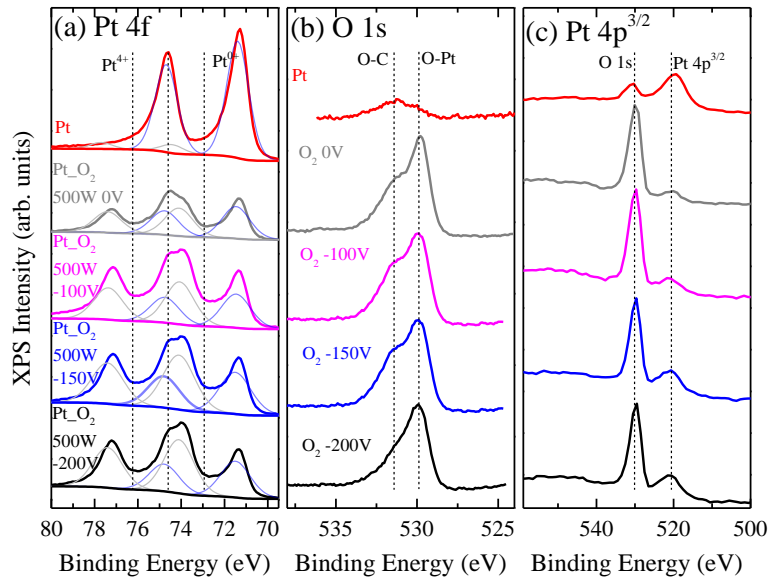
Figure 5-5 XPS spectra of (a) Pt 4f, (b) O 1s, and (c) Pt $4p^{3/2}$ peaks for (1) pre-etch, 5 min 500 W source power of O_2 plasma treatment with (2) 0 V, (3) -100 V, (4) -150 eV, and (5) -200 V bias.

In order to compare the surface modification of Pt in various chemical treatment, Figure 5-6 has summarized the percentage of Pt $^{0+}$, Pt $^{2+}$, and Pt $^{4+}$ from Pt 4f of XPS spectra. Figure 5-6 (a) presents the ratio of modified Pt to metallic Pt, i.e. $(Pt^{2+} + Pt^{4+})/Pt^{0+}$. The highest ratio of

modified Pt happened at O_2 plasma treated Pt, and the ratio increases with increasing bias voltage, indicating higher energy of oxygen ion could potentially diffuse deeper to form thicker oxide with higher oxidation state, Pt(IV). However, the higher the bias voltage, the more sputtering effect found on Pt surface. The thickness of Pt decreased significantly while increasing bias, for example, the Pt was etched 9 nm in 5 min at -200 V bias. The observation of physical sputtering at high bias voltage of O_2 plasma would damage the MRAM device as discussed in the Chapter 1, which short circuit may occur due to the sidewall re-deposition by generation of non-volatile etching products. Therefore, the O_2 plasma without bias voltage is selected due to the low sputtering effect and high degree of Pt surface modification.
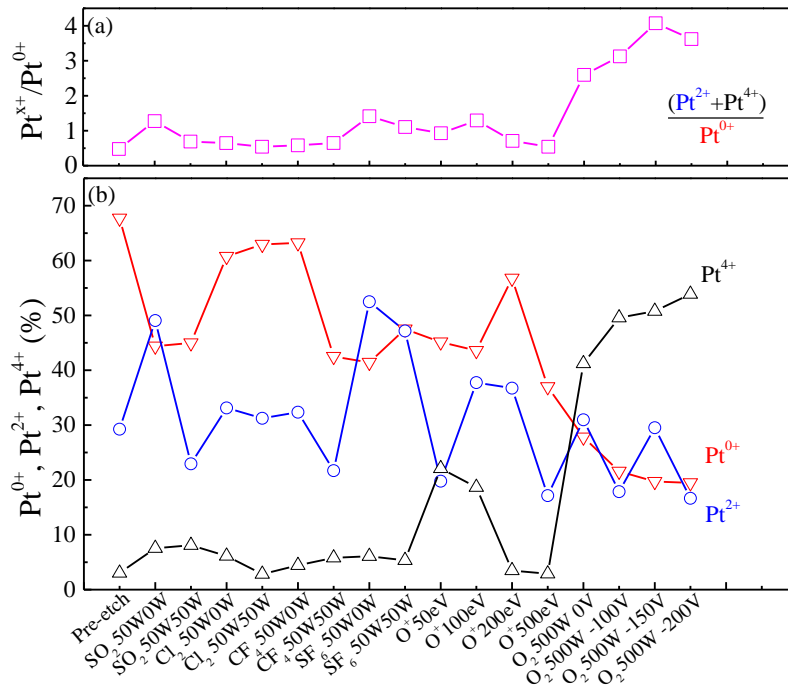
Figure 5-6 Degree of surface modification for pre-etch, SO_2, Cl_2, CF_4, SF_6, O_2 ion source, and O_2 plasma treated Pt. (a) The percentage of modified Pt to metallic Pt. (b) The composition of various chemical states in Pt 4f spectrum, including Pt^{0+}, Pt^{2+}, and Pt^{4+}.

166

5.2 Metal Oxidation

Since O_2 plasma has proven to be the most effective chemistry in modifying Pt surface and the thickness of thin oxide layer can be estimated by quantifying XPS results, other transition and noble metals such as Co, Fe, Cu, and Pd are examined under the same O_2 plasma condition. Figure 5-7 presents the Langmuir Probe measurement taken at the O_2 operating condition (500 W, 2.5 mT), T_e and n_i were calculated as 2.4 eV and 3.35×10^{10} #/cm^{-3} respectively, translating to an ion flux of 8.9×10^{15} cm^{-2} s^{-1}.by equation below.

$$J_{ion} = n_i \left(\frac{T_e}{M} \right)^{1/2}$$

While this is a higher value than expected, it should be noted that noise in the Langmuir Probe measurements could affect the estimate of the ion flux.
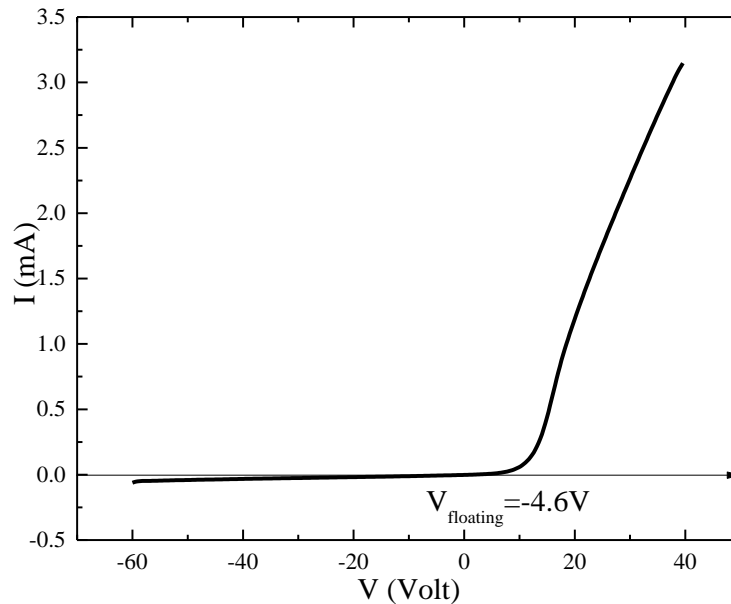
Figure 5-7 I-V curve measured by Langmuir probe at 500 W source power, 0 W bias power with 2.5 mtorr O_2 under ICP plasma.

Figure 5-8 presents the oxidation of metals as a function of O_2 plasma oxidation time. Apparently, the metal oxides increased immediately in the first few minutes, and the growth rate saturated at fifth min for all the metals. Various empirical kinetics for oxidation has been proposed at low temperature, parabolic, linear, and logarithmic. (Evans 1960) Most of them are suited for the presentation of experimental results but usually they cannot provide the interpretation of the mechanism. One of the traditional method to understand the mechanism is by curve fitting, although sometimes kinetics can be attributed to different reaction mechanisms, which is true if experiments are performed in the transition range between two mechanisms.
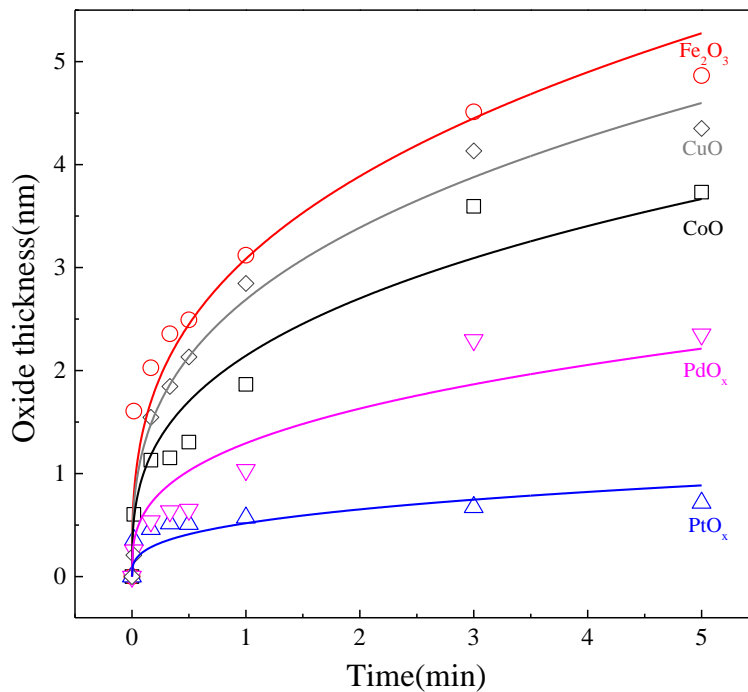
Figure 5-8 Oxide thickness of Fe, Cu, Co, Pd, and Pt as a function of the O_2 plasma oxidation time.

The basis of the parabolic law is the linear transport equation

$$j_{e,i} = -D_{e,i}\frac{\partial n_{e,i}}{\partial x} \pm E n_{e,i} v_{e,i} \tag{5.1}$$

where $j_{e,i}$ is the flux of the electron and ion in the oxide, $D_{e,i}$ present the diffusivity of electron and ion in the metal oxide, $\partial n_{e,i}/\partial x$ is the concentration gradient of electron and ion in a thin oxide layer, E is electrical field, $\nu_{e,i}$ is the charge mobility of the electron and ions. The first part of the equation represents the diffusion of oxygen ion, metal ion and electron due to the concentration gradient, and the second part is driven by the electrical field formed by the charge separation. The parabolic rate law, $l \propto \sqrt{t}$, is achieved after integration of the equation above. Diffusion control is the most common mechanism proposed in some theories, but the migration of cations is enhanced by an intrinsic electric field across the oxide layer produced by tunneling electrons was also proposed by Cabrera et al. (Cabrera and Mott 1948, Evans 1960, Hauffe 1965) Inverse logarithmic law was derived by Cabrera and Mott for the special case that incorporation of metal cations into interstitial sites of the oxide is rate determining. (Cabrera and Mott 1948) The oxide growth rate is proportional to the probability of surmounting the potential barrier between the sites of the atoms in the metal and interstitial sites in the oxide. The potential barrier is assumed to be potential dependent and integration of the rate law yields the Cabrera-Mott inverse logarithmic time law $l_0/l = const. - \log t$. (Cabrera and Mott 1948) Meanwhile, the logarithmic rate law was proposed by Mott for very thin oxide layers where electron tunneling prevails the electronic current depends on the tunneling probability. The oxide growth rate decreases exponentially with increasing layer thickness and a logarithmic time law $l \propto \log t$ is obtained by integration. (Mott 1940) For cubic rate law of oxidation, Cabrera and Mott used essentially the same assumptions as for n-type oxide, derived a theory for the growth of a thin p-type oxide such as copper oxide. It depends on the concentration of cation vacancies, which are assumed to be proportional to the number of adsorbed oxygen ions on the surface of the oxide. Wagner also suggested that the rate determining step for cubic rate law is the dissociation of

oxygen molecules at the oxide-oxygen interface, and the rate is proportional to the local concentration of excess electrons in the oxide next to the oxide-oxygen interface. (Cabrera and Mott 1948, Wagner 1969)

Figure 5-9 presents various curve fitting of the oxide thickness for Fe, Cu, Co, Pd, and Pt, and the goodness of curve fitting was calculated on Table 5-1. Fe and Co show the best of goodness of fitting are inverse logarithmic rate law which suggesting the rate determining step is incorporation of metal cations into interstitial site. In the case of Cu, a 98% fitting of cubic rate law suggests oxygen diffusion and dissolution are the rate determining step, which perfectly matched the results from the literature. (Wagner 1969) For Pd and Pt, the best fitting is parabolic rate law for oxidation, which means they are strongly controlled by diffusion of oxygen and migration of cations by the intrinsic electric field. The observation for Pd and Pt are also confirmed by Wang et al. and Schennach, respectively. (Wang, Yun et al. 2007, Schennach 2012)
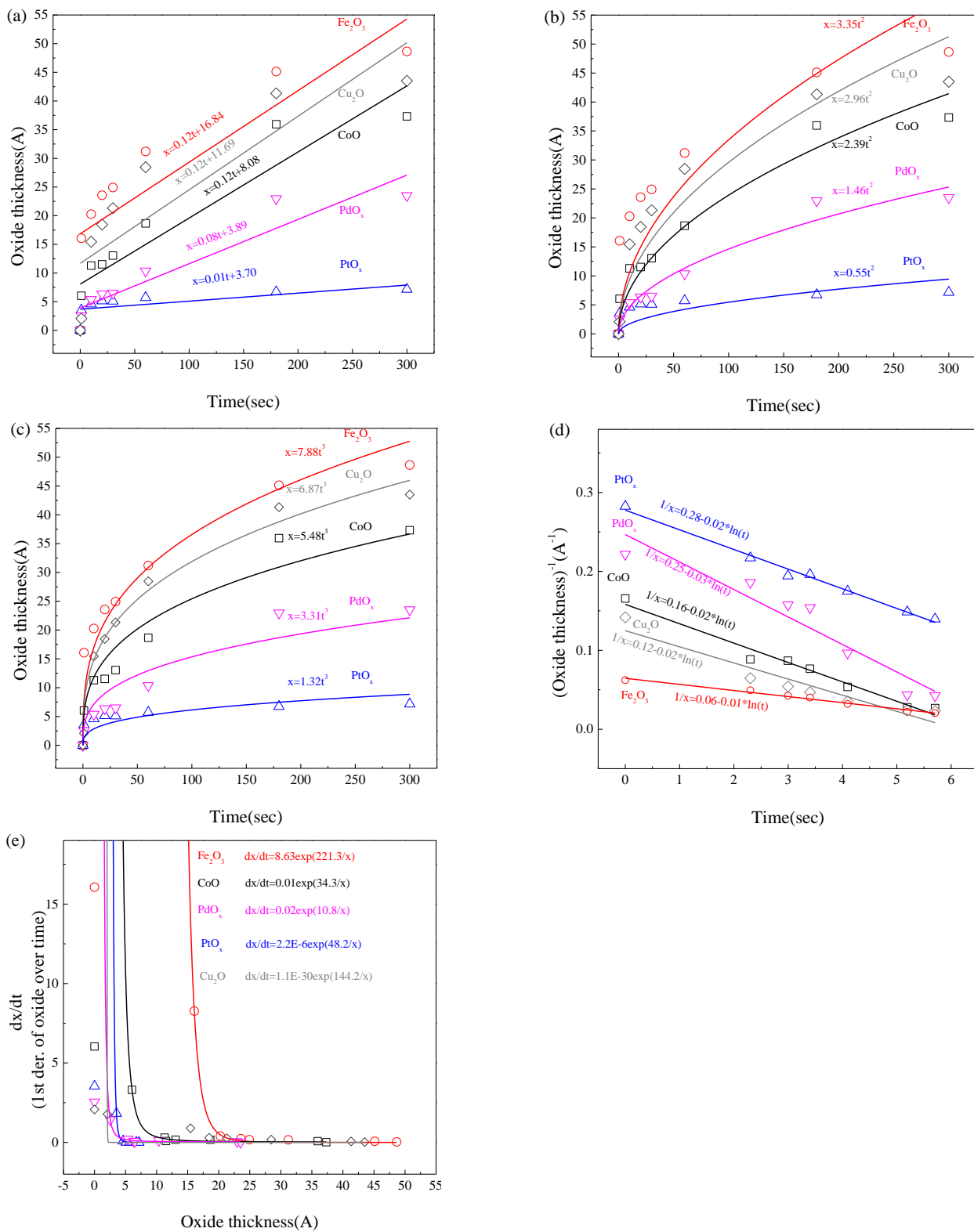
Figure 5-9 Curve fitting for oxidation of Fe, Cu, Co, Pd and Pt by O_2 plasma with (a) linear, (b) parabolic, (c) cubic, (d) inverse logarithmic, and (e) exponential.

171
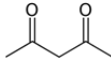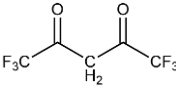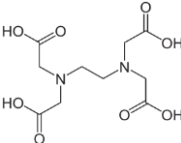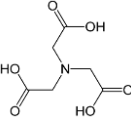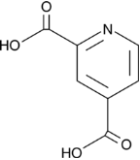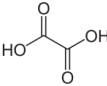
Table 5-1 Goodness of fitting for oxidation of Fe, Cu, Co, Pd and Pt by O_2 plasma with 500 W, 2.5mtorr O_2, Te~2.5eV and ion density:10^{15}#/cm^3.

Fitting approach	r-square	Fe	Cu	Co	Pd	Pt
Linear	x=At	70%	71%	84%	87%	37%
Parabolic	x^2=2Bt	72%	90%	95%	97%	95%
Cubic	x^3=3Ct	94%	98%	95%	91%	57%
Inverse log	1/x=D-E*ln(t)	98%	89%	97%	90%	94%
Logarithmic	dx/dt=F*exp(G/x)	78%	66%	77%	75%	79%

5.3 Organic Chemical Solution Etch

Since O_2 plasma is able to modify metal surface, the potential organic ligands for etching metals listed on Table 5-2 with boiling point and schematic structure have been investigated for patterning. Beta-diketone species such as acetylacetone (acac) and hexafluoroacetylacetone (hfac) have been utilized as common ligands for synthesizing metal precursors in atomic layer deposition (ALD) application. Metal acetylacetonates ($M(acac)_x$) are coordination complexes derived from the acetylacetonate anion and metal ions. A six-membered chelate ring stabilizes the organometallic compound when two oxygen atoms on the acac bind to the metal. (Braunstein 2004) Hfac presents the same structure as acac except the functional group on two ends are substituted by CF_3, exhibits the enhanced volatility and Lewis acidity relative to acac. (Henne, Newman et al. 1947) (Aygen and Vaneldik 1989) Ethylenediaminetetraacetic acid (Edta) is a hexadentate ligand which could bond to metal ions such as Ca^{2+} and Fe^{3+} efficiently. Similar to edta, Nitrilotriacetic acid (nta) presents three ligands, which could form coordination compounds with Ca^{2+}, Cu^{2+}, and Fe^{3+}. Pyridine-2,6-dicarboxylic acid (pdca) owns two carboxylic acid ligand which could be utilized in binding metal ions. Oxalic acid (oa) and formic acid have been using in removing iron oxide with formation of stable water-soluble salt. All the concentration of organic ligands was prepared at the maximum in order to rule out the concentration effect, but some of the organics were at low concentration such as edta, nta, and pdca due to the low saturated concentration.

Table 5-2 Potential organics in etching metals.

Organics	Acetyl-acetone	Hexafluoro-acetylacetone	Ethylene diamine tetraacetic acid	Nitrilo triacetic acid	Pyridine-2,6-dicarboxylic acid	Oxalic acid	Formic acid
Abbr.	ACAC	HFAC	EDTA	NTA	PDCA	OA	FA
Boiling point (^oC)	140	70	614	340	245	149	100
Concentr-ation (M)	9.7	7	0.5	0.5	0.5	1.2	13
Structure of organics							

Since platinum is the most challenging element in patterning due to its high stability, it was selected to examine the etching efficacy of the organic ligands. Usually the etch rate was determined by thickness change through scanning electron microcopy (SEM), transmission electron microcopy (TEM), or profilometer, but the thickness change on platinum was relatively small which could not measure by microcopy. Therefore, the surface characterization of chemical state on platinum via X-ray photoelectron spectroscopy (XPS) is chosen to screen the organic ligands in etching metal oxide.

After surface modification with 500 W oxygen plasma without bias for 5 min at 80 ^oC, Figure 5-10 presents Pt 4f and survey spectra of modified Pt film treated by various organic ligands. First of all, no contamination or carbon deposition was found in survey spectrum, suggesting the platinum surface remained intact. Later, the chemical state on Pt 4f spectra has revealed the etching efficacy of organic ligands. The strong Pt^{4+} peak was found on modified Pt after acac, hfac, edta, and nta treatment, suggesting no reaction took place with platinum oxide. Based on the decreasing of Pt^{4+} peak after pfca, oa, and formic acid treatment, the etching

efficacy with platinum oxide was proven. More chemical evidence has been provided in the case of CoPt etch in later paragraph.
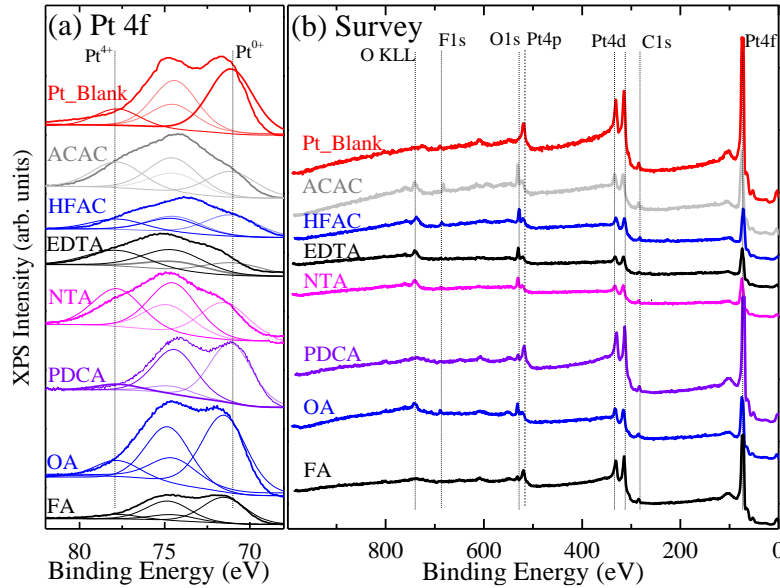
Figure 5-10 XPS spectra of (a) Pt 4f, (b) Survey for (1) pre-etch Pt, oxidized Pt treated by following organic solution for 20 min, (2) acac, (3) hfac, (4) edta, (5) nta, (6) pdca, (7) oxalic acid, and (8) formic acid.

As described in Chapter 1, the etching selectivity of metals to hard mask needs to be high enough to improve the fidelity in the vertical and horizontal direction. Tantalum as one of the most important hard mask material has been examined with all the ligands as well. Ta was first treated with same process of surface modification, 500 W oxygen plasma without bias for 5 minutes, and then etched by various organic solutions for 20 min at 80 °C. Figure 5-11 shows the Ta 4f and survey spectra of Ta before and after etched by acac, hfac, edta, nta, pdca, oa, and formic acid. According to the survey spectra, none of sample showed neither contamination nor carbon decomposition, suggesting clean Ta surfaces were sustained. The detailed scans of Ta 4f are presented in Figure 5-11 (a), the atomic ratio of oxidized Ta (Ta^{5+}) to metallic Ta (Ta^{0+})

remained the same after all the organic solutions etch, suggesting no reaction occurred between tantalum oxide and organic solutions. Since the thickness change also needs to be confirmed to verify the etch of Ta, Figure 5-12 presents the cross-sectional SEM images of Ta that no significant thickness change was observed after 4 hr etch by formic acid solution. Combing the results of XPS and SEM, Ta is verified as a potential candidate in patterning Pt as a hard mask due to the inert characteristic with selected organic ligands.
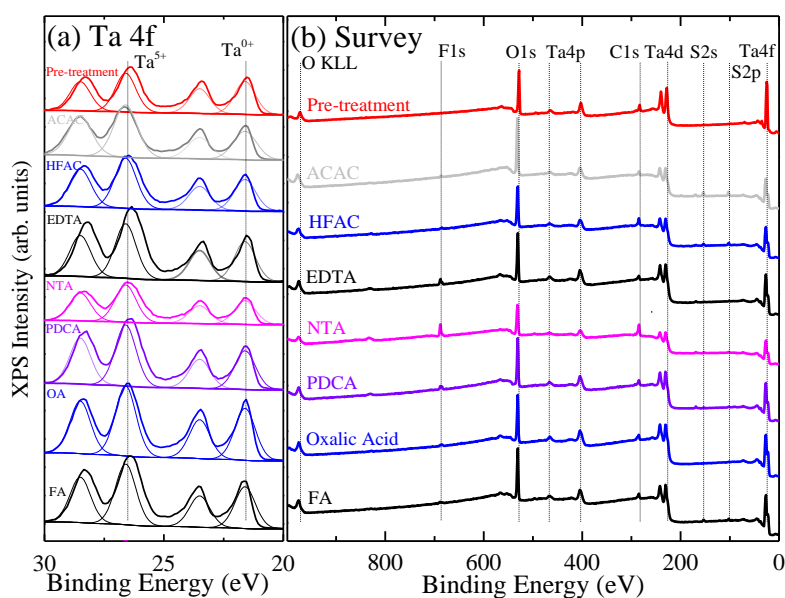
Figure 5-11 XPS spectra of (a) Ta 4f, (b) Survey for (1) pre-etch Ta, oxidized Ta treated by following organic solution for 20 min, (2) acac, (3) hfac, (4) edta, (5) nta, (6) pdca, (7) oxalic acid, and (8) formic acid.Ta etched by organics solution etch 20 min.
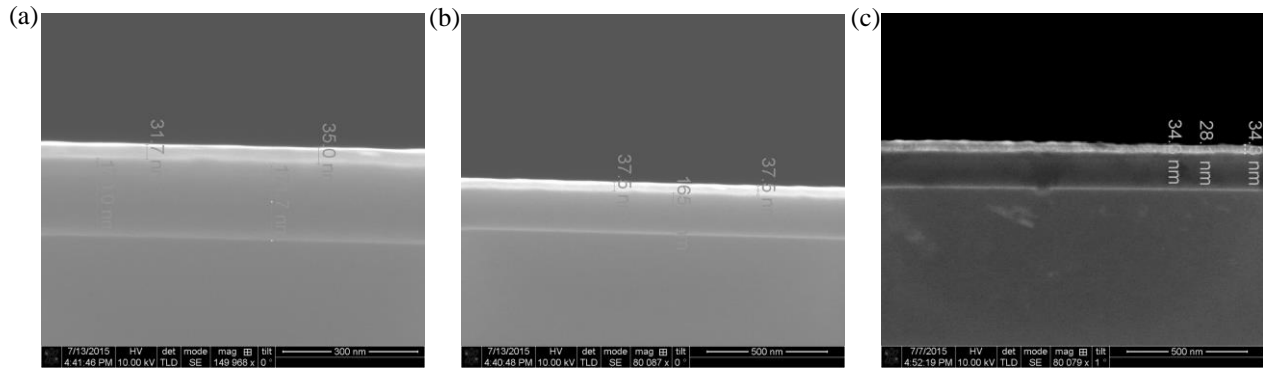
Figure 5-12 Cross-sectional SEM images of (a) Ta pre-etch, (b) Ta with surface modification of 500 W O₂ plasma without bias for 5 min, and (c) modified Ta etched by formic acid solution for 4 hr at 80 °C for 20 min.

Since several organic ligands presented promising results in etching single element Pt with surface modification, CoPt, an actual alloy being utilized in MRAM stack has been studied. Figure 5-13 shows Pt 4f, Co 2p, and O 1s spectra of CoPt alloy pre-etch and post-etch by surface modification of O₂ 500 W plasma without bias for 5 min prior to various organic solutions etch. Platinum 4f spectra of CoPt shown on Figure 5-13 (a) generally followed the trend in etching single element on Figure 5-10 (a), meaning the reactivity between platinum oxide and organic ligands do not change whether it is single metal or alloy. On the other hand, Co 2p spectra on Figure 5-13 (b) present two groups of spectra. First group are acac and hfac treated CoPt, presenting a fully oxidized Co (Co^{2+}), suggesting no or little reaction between cobalt oxide and organic ligands. For the rest of the spectra, the intensities of Co 2p significantly drop after organic solution etch, suggesting a high reactivity between cobalt oxide and organic ligands. Figure 5-13 (c) shows O 1s spectra of CoPt etched with various organics solutions. The oxygen-metal peak (O-M) remained strong after acac and hfac treatment, but rest of the spectra shift to oxygen-hydrogen peak, suggesting the removal of platinum oxide and cobalt oxide.

177
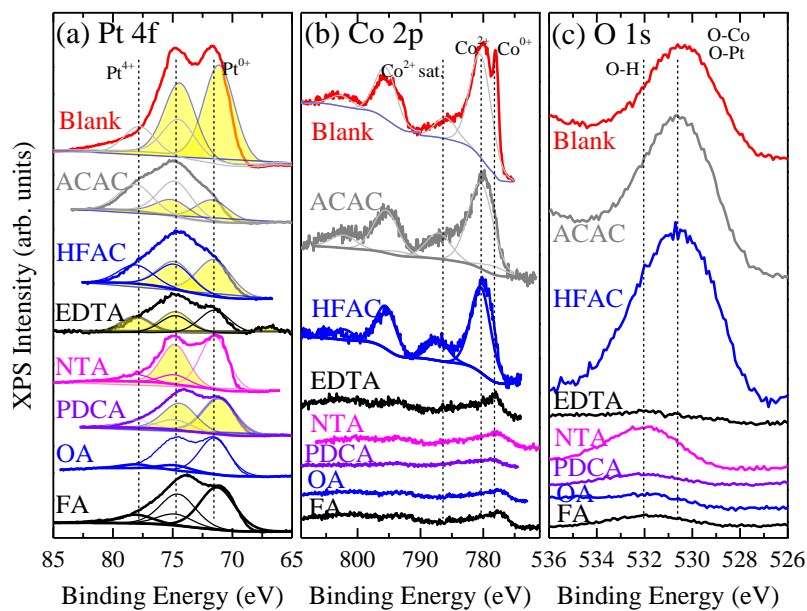
Figure 5-13 XPS spectra of (a) Pt 4f, (b) Co 2p, (c) O 1s for (1) pre-etch CoPt alloy, oxidized CoPt alloy treated by following organic solution for 20 min, (2) acac, (3) hfac, (4) edta, (5) nta, (6) pdca, (7) oxalic acid, and (8) formic acid.

To confirm the removal of Co and Pt after surface modification prior to organic solution etch, the post-etch solutions were analyzed by Inductively Coupled Plasma Mass Spectrometry (ICP-MS) in Figure 5-14. Firstly, the pure organic solutions were examined in short dotted line in Figure 5-14 as a background check, and neither Pt nor Co were detected by ICP-MS, suggesting a contamination-free sample preparation was designed. A control experiment for etching CoPt without surface modification prior organic solution etch is presented in dotted line. A negligible amount of Pt was found in edta and acac solution, it could be attributed to a small amount of native oxide remained on Pt surface. On the other hand, a significant high concentration of Co was detected in formic acid and edta, suggesting a relatively high etch rate with metallic cobalt. However, the amount of Co detected by ICP-MS increased dramatically after oxidation followed by organic solution etch, implying a relatively high reactivity between cobalt oxide and organic ligands. Among the organic chemicals, edta shows the highest

178

concentration of Co, suggesting one of the most stable organometallic complex contained hexadentate edta ligand bonded to centered Co(III). (Douglas, Brushmiller et al. 1963, Hidaka and Douglas 1964, Hidaka and Douglas 1964, Liu and Douglas 1964, Haines and Douglas 1965) Similar results have been observed for etching platinum with surface modification that high concentration of Pt was detected after oxidation prior to etch by formic acid, pdca, edta and nta. The highest concentration of Pt was found in the post-etch formic acid solution, suggesting a most effective chemical in etching platinum oxide.
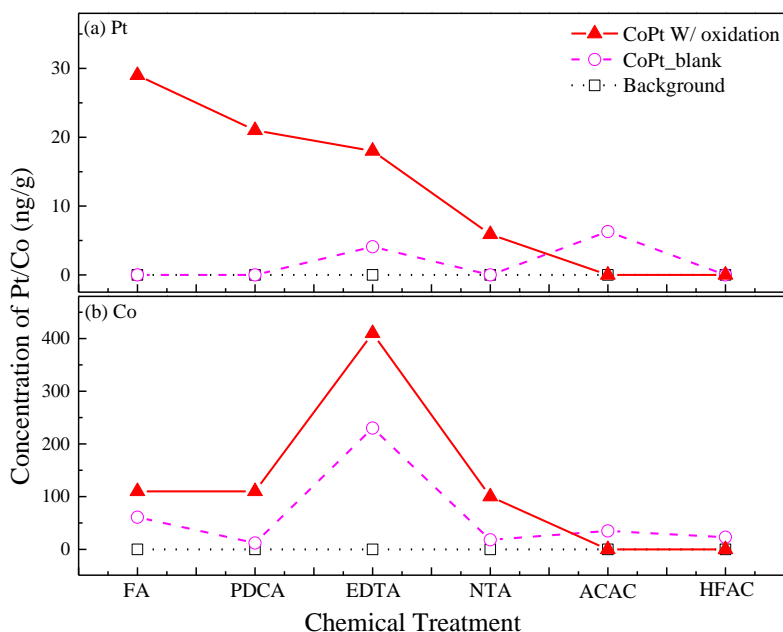
Figure 5-14 ICP-MS data of (a) Pt and (b) Co concentrations in the post-etch solution of formic acid, pdca, edta, nta, acac, and hfac. A control experiment with organic chemical solution only is shown in dotted line (square), etching of CoPt without surface oxidation is presented with long dotted line (circle), and the etch of CoPt with surface oxidation is labeled as solid line (triangle).

For platinum, similar trend is observed in the ratio of metal to oxide from XPS spectrum in Figure 5-15. By decoupling Pt 4f spectra, the atomic percentage of Pt^{0+} and Pt^{4+} can be retrieved. The ratio of 6.9 and 0.6 were found in metallic CoPt, and oxidized CoPt, respectively.

A ratio of Pt^{0+} to Pt^{4+} follows the order of pdca, formic acid, edta, nta, acac, and hfac, suggesting pdca is the most effective organic chemical in removing platinum oxide. The general trend follows the results from ICP-MS in Figure 5-14, except the discrepancy of the most effective chemical. Because the *ex situ* XPS was carried out for analyzing the chemical state of surface, CoPt treated by formic acid was exposed to the air relatively longer compared to pdca, resulting in lower ratio of Pt^{0+}/Pt^{4+} to pdca. Therefore, two conclusions can be drawn on the basis of the evidence that formic acid is the most effective organic chemical in etching platinum oxide, and the organic chemical ligands only react with Pt(IV) oxide, instead of Pt(II) oxide or metallic Pt.
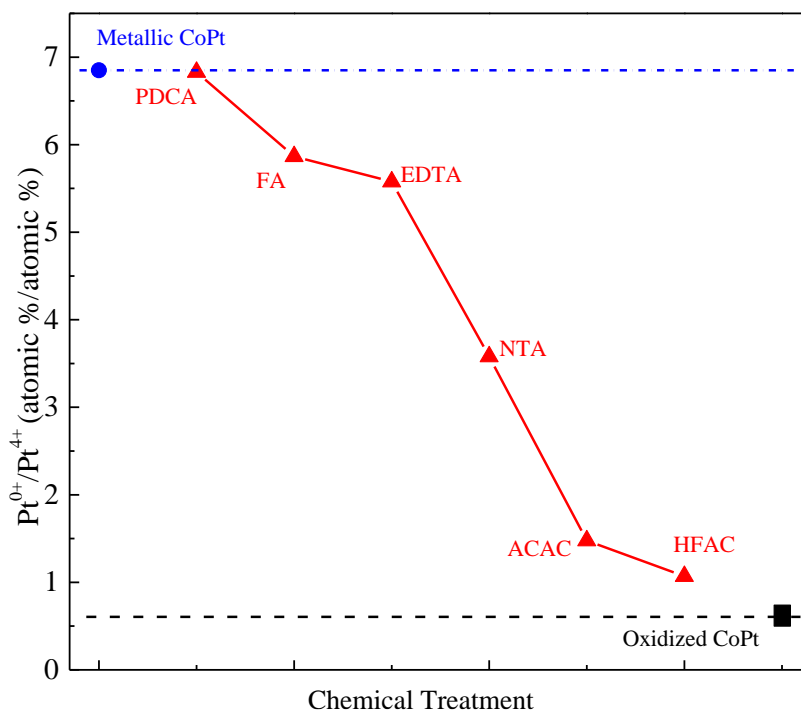
Figure 5-15 The ratio of Pt^{0+} to Pt^{4+} in atomic percentage decoupled from XPS results of CoPt etched by organics solution of pdca, formic acid, edta, nta, acac, and hfac for 20 min. (labeled by solid line with triangle) The ratio of Pt0+ to Pt4+ of metallic CoPt and oxidized CoPt are labeled as solid circle, and solid square, respectively.

Meanwhile, the etched thickness could be estimated by the amount of metal in the solution with known sample dimension, volume of organic solution, and the density of metal film. For example, all the samples were approximately 7 by 10 mm rectangles, the volume of organic solutions were about 2 mL, and the density of Co and Pt are approximately 8.9, and 21.5 g/cm³, respectively. (Lide 1995) The etched thickness was estimated in Figure 5-16 that greatest removal was only 0.8 Å for Pt etched by formic acid, but a removal of 28.0 Å was found for Co etched by edta. In order to keep the same composition of Co and Pt after patterning, formic acid is selected as a potential candidate due to the highest etch rate of platinum oxide but relatively low etch rate of cobalt oxide compared to other organic chemicals.
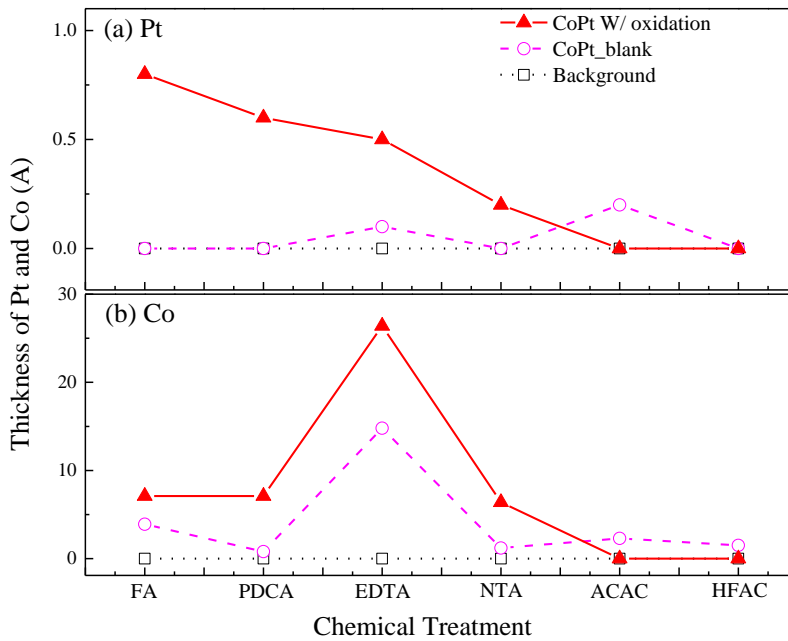
Figure 5-16 Estimated thickness of of Co and Pt etched by organic solution of formic acid, pdca, edta, nta, acac, and hfac for 20 min. The etched thickness is estimated by the results of ICP-MS by known dimension of sample, density of Co and Pt, and volume of organic solutions. A control experiment with organic chemical solution only is shown in dotted line (square), etching of CoPt without surface oxidation is presented with long dotted line (circle), and the etch of CoPt with surface oxidation is labeled as solid line (triangle).

Since formic acid is selected as an organic chemical etchant for CoPt, the time-dependent etch needs to be studied as well. Figure 5-17 presents the Pt 4f, Co 2p, O 1s, C 1s, and survey spectra of CoPt pre-etch, post-oxidation, oxidation prior to formic acid etch for 3, 5, 10, 20 min. Based on the result of survey in Figure 5-17 (e), no other elements were found, suggesting a contamination-free sample preparation is designed. Figure 5-17 (d) present C 1s spectra, and no carbon decomposition is observed from 3 to 20 min formic acid etch. O 1s spectra is presented in Figure 5-17 (c), an oxygen-metal peak in post-oxidation spectrum was totally removed in 3 min etch and left an oxygen-hydrogen peak alone. The result followed the trend in Pt 4f and Co 2p in Figure 5-17 (a) and (b) that Pt^{4+} and Co^{2+} peaks were entirely eliminated, suggesting the etch of metal oxide by formic acid was rapidly. Thus, the shorter etching time was examined in Figure 5-18. The removal of platinum (IV) oxide by formic acid solution was as rapid as in one second, which also confirmed the etching efficacy of organic chemical.
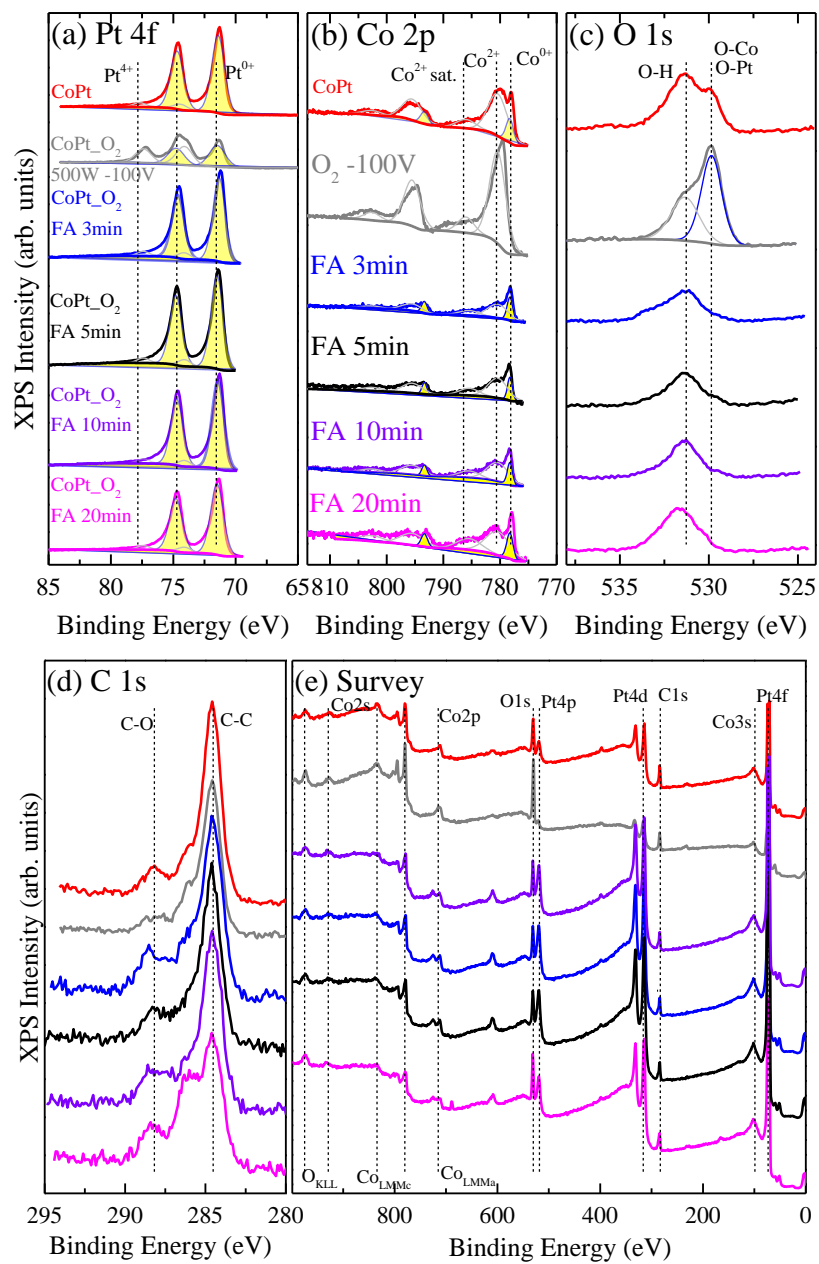
Figure 5-17 XPS spectra of (a) Pt 4f, (b) Co 2p, (c) O 1s, (d) C 1s, and (e) Survey for (1) pre-etch CoPt alloy, (2) oxidized CoPt alloy, oxidized CoPt treated by formic acid solution for (3) 3, (4) 5, (5) 10, (6) 20 min.
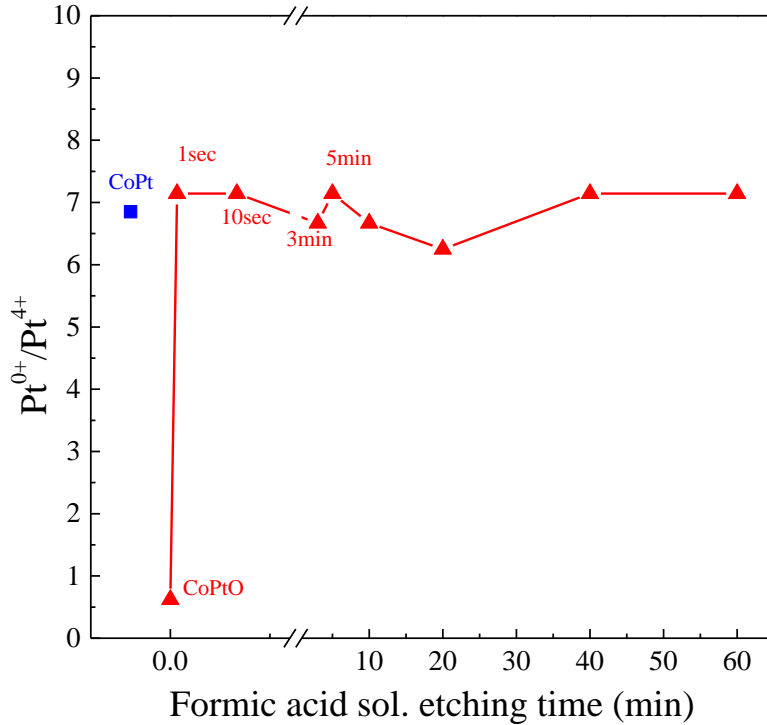
Figure 5-18 The ratio of Pt^{0+} to Pt^{4+} in atomic percentage decoupled from XPS results of CoPt etched by formic acid solution for 1 sec, 10 sec, 3min, 5 min, 10 min, 20 min, 40 min, and 60 min. The ratio of Pt^{0+} to Pt^{4+} of metallic CoPt is labeled as solid square.

A multiple etching cycles for CoPt alloy was conducted, and the thickness change as a function of etching cycle is shown in Figure 5-19. The thickness was measured by ellipsometer, and the calibration of ellipsometry model was confirmed by SEM with 10 and 20 nm CoPt films. A dotted line with circle presents a control experiment without surface modification of 500W O_2 plasma for 5 min. The thickness of CoPt decreased in the first two cycles due to the removal of native metal oxide which was approximately 1 nm. Because of the high selectivity of metal oxide to metal by formic acid solution, no thickness change was found after first two cycles. The solid line in Figure 5-19 represented an alternating etch with surface modification of 500 W O_2 plasma for 5 min followed by 30 sec organic solution etch. In the first half cycle, the decrease of CoPt thickness could be attributed to the removal of adventitious hydrocarbon layer by forming

184

volatile carbon dioxide and methane with O_2 plasma. Due to the etching of metal oxide by formic acid solution, the second half of the first cycle also showed the decrease of CoPt thickness. The volume expansion started at first half of second cycle, it is because the density of metal oxide formed by the O_2 plasma oxidation is relatively smaller than metal oxide. For example, the density of Co and CoO are 8.9 and 6.44 g/cm^3, respectively; the density of Pt and PtO_2 are 21.45 and 10.2 g/cm^3, respectively. (Lide 1995) As the density of CoO is only 2/3 of Co, the volume of oxide would be one and half times more than that of metal. After second cycle, the etched thickness gradually increased by cycles, and the average etch rate is 1.1 nm/cycle.
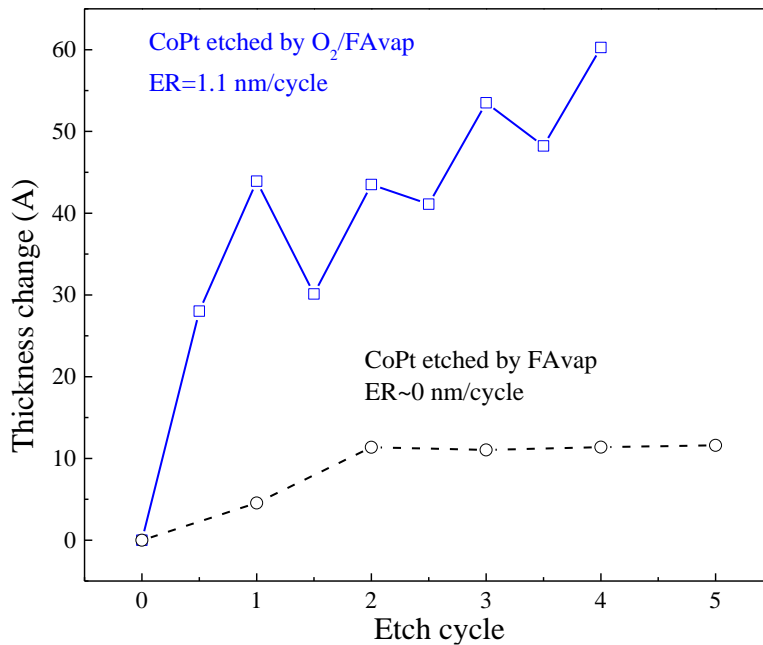
Figure 5-19 The thickness change of CoPt etched by surface modification of 500 W O_2 plasma for 5 min and formic acid solution for 30 sec alternatively. The dotted line with hollow circle represents CoPt etch without surface modification, and the solid line with hollow square stands for CoPt etch with surface modification prior to organic solution etch.

Not only physical measurement of thickness but also the chemical state of surface characterization through XPS was conducted for analyzing alternating etch by O_2 plasma and formic acid solution etch. Figure 5-20 shows Pt 4f, Co $2p^{3/2}$ and O 1s spectra from pre-etch, first, second, third, and fourth cycle of etching. For Pt 4f spectra, Pt^{4+} peak is shown periodically, which exactly the same as predicted, suggesting the removal of platinum oxide. Cobalt spectra are similar to that of platinum, the Co^{2+} peak presents periodically as well. The O 1s spectra is the most obvious that oxygen-metal peak appears at the first half of cycles, and disappear at the second half of cycles, suggesting the removal of metal oxide is completed.
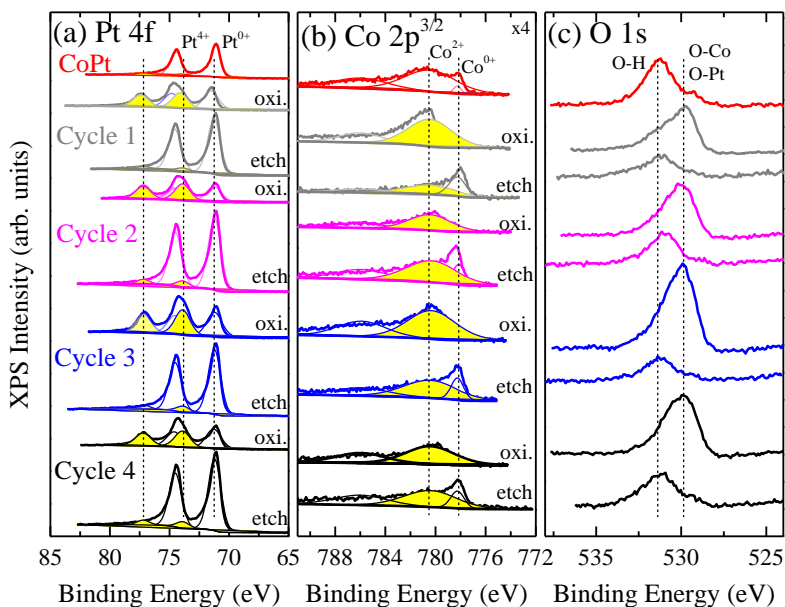
Figure 5-20 XPS spectra of (a) Pt 4f, (b) Co 2p3/2, and (c) O 1s, for (1) pre-etch CoPt alloy, (2) oxidized CoPt, and different cycles of surface oxidation and formic acid solution etch from (3) to (7).

However, as the cycles continued, the atomic percentage of Co to Pt on the CoPt alloy surface changed significantly. Table 5-3 shows the atomic percentage of Co and Pt at different cycle. In the beginning, the ratio of Co to Pt was about 3:7; however, the ratio became 1:9 at the

end of fourth cycle. It is attributed to the preferential removal of Co than Pt on CoPt surface. The

new organic chemical is necessary to develop for balancing the atomic ratio of alloy in the

future.

Table 5-3 Surface composition of Co and Pt in atomic percentage of CoPt etched by surface oxidation and formic acid solution etch sequentially from pre-etch, and cycle one to cycle four.

Cycle (#)	Pre-etch	1		2		3		4	
Atomic %	Blank	Oxi.	Etch	Oxi.	Etch	Oxi.	Etch	Oxi.	Etch
Co (%)	31	41	13	18	14	23	14	21	11
Pt (%)	69	59	87	82	86	77	86	79	89

5.4 Organic Chemical Vapor Etch

A vacuum-compatible etching process is needed in order to integrate it with other semiconductor processes, the study of the vapor etch is required. Since the formic acid solution etch of metal oxide was proven effective in the previous section, the etching efficacy of formic acid vapor was investigated by the setup of vapor etch chamber described in chapter two. Similar to solution etch, XPS was utilized to determine the removal of metal oxide by organic ligands. Figure 5-21 shows the XPS spectra of Pt thin film etched by formic acid vapor with surface modification of 500W O_2 plasma for 5 min. The survey in Figure 5-21 (b) shows clean platinum surfaces without contamination after one or two cycles of formic acid vapor etch with surface oxidation, excluding the decomposition of organic ligands on the surface. The detail scan of Pt 4f in Figure 5-21 (a) shows an increase of Pt^{4+} peak after O_2 plasma oxidation, and a significantly decrease of Pt^{4+} peak after formic acid vapor exposure, suggesting a similar etching efficacy of Pt in solution of formic acid etch.
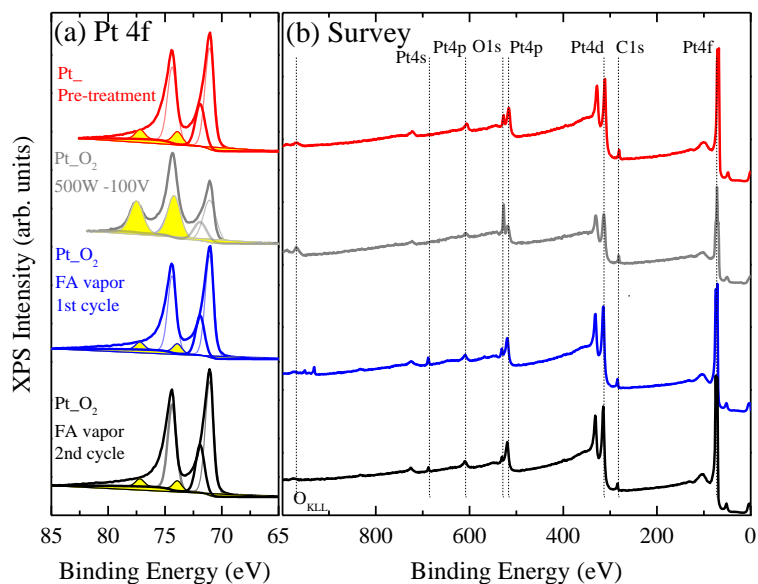
Figure 5-21 XPS spectra of (a) Pt 4f, and (b) Survey, for (1) pre-etch Pt, (2) oxidized Pt, (3) 1st cycle, and (4) 2nd cycle of sequential etch of surface oxidation and formic acid vapor exposure.

In order to confirm the etch efficacy, the thickness measurement of Co and Pt was performed by the ellipsometer in Figure 5-22. Etching of Co by formic acid vapor with surface modification is significant that a 25 nm Co film was totally removed in 3 cycles. The reason of etched thickness not being equal in each cycle was that the pressure of formic acid vapor in each cycle was not controlled well. Although a Baratron capacitance monometer is attached onto the vapor etch chamber to measure the pressure of formic acid vapor in the system, the pressure right on the sample surface is still not fully controlled, resulting in a fluctuated etching thickness of metal in each cycle. Due to a low reactivity of Pt by nature, a thickness change of 4 nm in 4 cycles for Pt is relatively lower than that of Co. But the etched thickness of Pt was equally distributed in each cycle, suggesting a saturation of removing platinum oxide by formic acid vapor was achieved in each cycle. Therefore, a same conclusion of preferential removal of Co to Pt found in solution etch is observed in vapor etch as well.

189
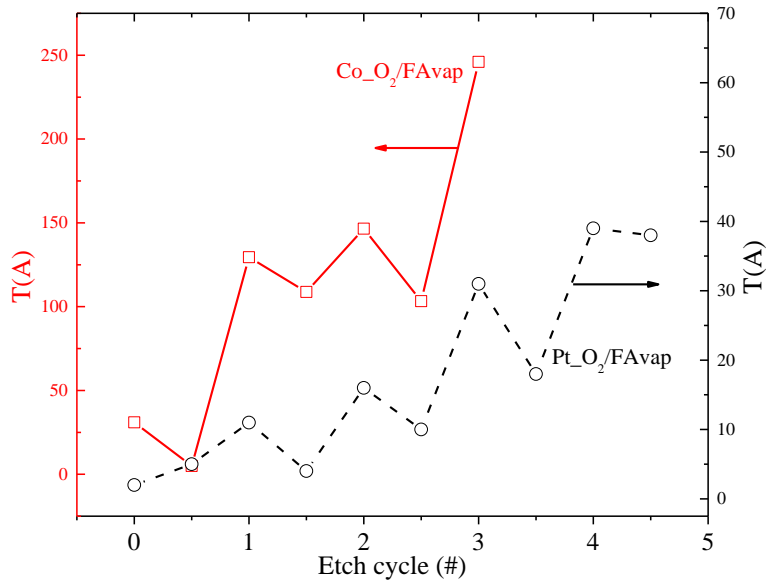
Figure 5-22 Etched thickness of Co and Pt etched by surface modification and exposure of formic acid vapor as a function of etching cycle. Hollow square represents etching of Co on left y-axis, and hollow circle represents etching of Pt on right y-axis.

Since the etching efficacy of Co and Pt by sequential surface oxidation and formic acid vapor exposure are confirmed separately, the etching of CoPt alloy is studied. A removal of 6-nm CoPt film was observed in 4 cycles in Figure 5-23, and a relatively large thickness change was found in the first cycle, ca. 4 nm. The reason could be the preferential removal of Co to Pt in the first cycle. Since the component of Co on the surface decreased significantly in the first cycle, the following cycles were mainly removal of Pt, resulting in a lower removal rate compared to first cycle.
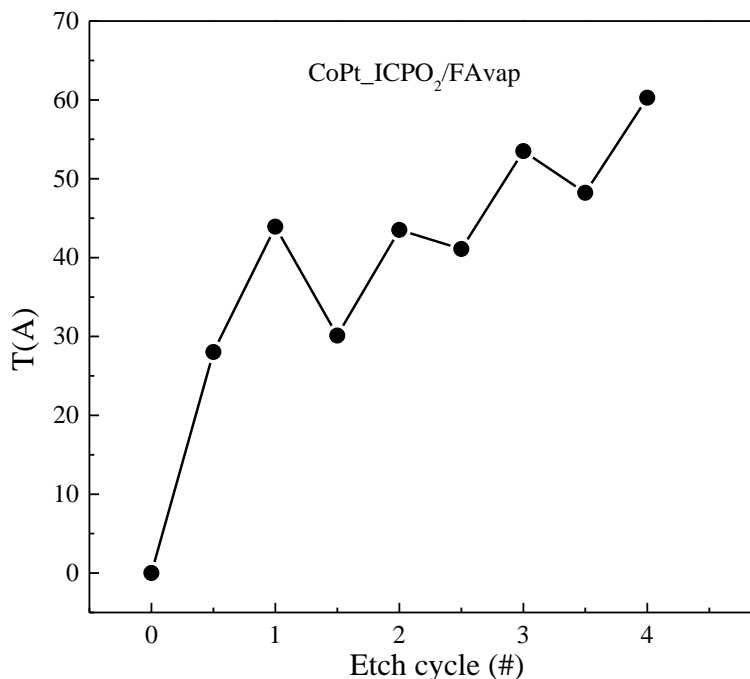
Figure 5-23 Etched thickness of CoPt alloy by surface modification and exposure of formic acid vapor as a function of etching cycle.

To further explore the etching efficacy of transition and noble metals with organic ligands, Fe, Cu, Co, Pd, and Pt have studied systematically. Figure 5-24 presents a growth of metal oxide as a function of O_2 plasma time. The thickness of metal oxide was estimated by XPS spectra as mentioned in Chapter 2. Apparently, the thickness of metal oxides increased immediately in the first few minutes, and the growth rate saturated at fifth min for most of the metals. Since there was no bias applied on the metals in the O_2 plasma treatment, the O_2 source were mainly oxygen radicals and neutrals. Thus, the principal mechanism of oxidation is the diffusion of oxygen radicals onto the metal surface. Iron oxide presents the highest growth rate followed by copper oxide, cobalt oxide, palladium oxide and platinum oxide, which follows the same trend in the literature that the self-diffusion coefficients of iron, copper, and cobalt ions in oxides are 1.18×10^{-1}, 4.36×10^{-2}, 2.15×10^{-3} cm^2/sec, respectively. (Hauffe 1965) Although,

the self-diffusion coefficients of noble metals, palladium and platinum, are not available, the

lower reactivity to oxygen radical compared to transition metals are as expected.
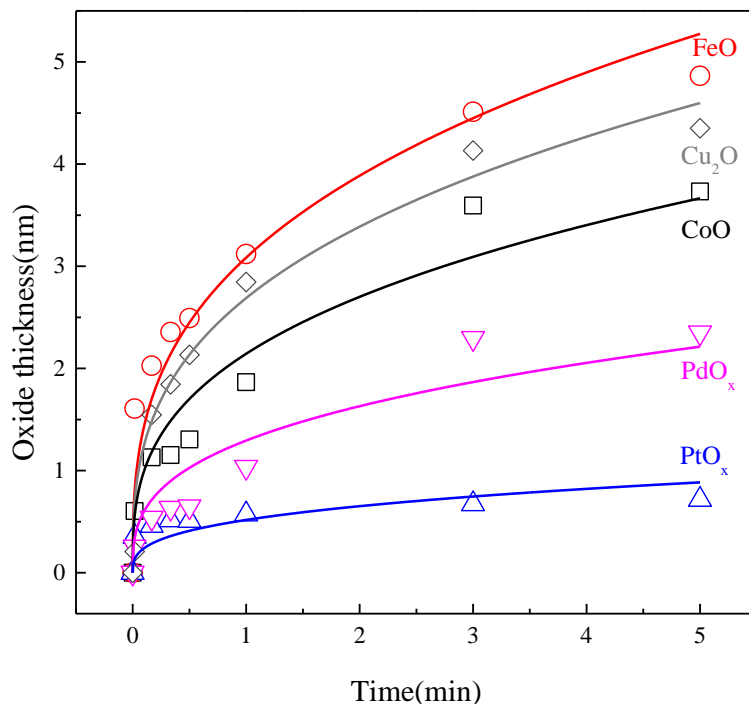
Figure 5-24 The growth of oxide thickness for Fe, Cu, Co, Pd, and Pt as a function of the oxidation time of 500 W O_2 plasma. The symbol of circle, diamond, square, inverted triangle, and triangle are represent FeO, Cu_2O, CoO, PdO_x, and PtO_x, respectively.

The etching of metals with formic acid vapor are conducted right after the surface

oxidation in Figure 5-25, and the thickness change were measured by ellipsometer. The etch rate

of iron, copper, cobalt, palladium, and platinum are 4.2, 3.7, 2.8, 1.2, and 0.5 nm/cycle,

respectively, the order of the etch rate follows the trend in the growth of metal oxide presented in

Figure 5-24. Therefore, the etch rate per cycle has compared to the growth rate of oxide in Figure

5-26, and a linear relationship between two components are shown. A high selectivity of metal

oxide to metal etched by formic acid vapor is achieved, suggesting one of the most important

requirement in atomic layer etch, self-limiting reaction, is fulfilled. By controlling the thickness of oxides with O_2 plasma oxidation, the etch rate of metals could be controlled even in atomic scale level.
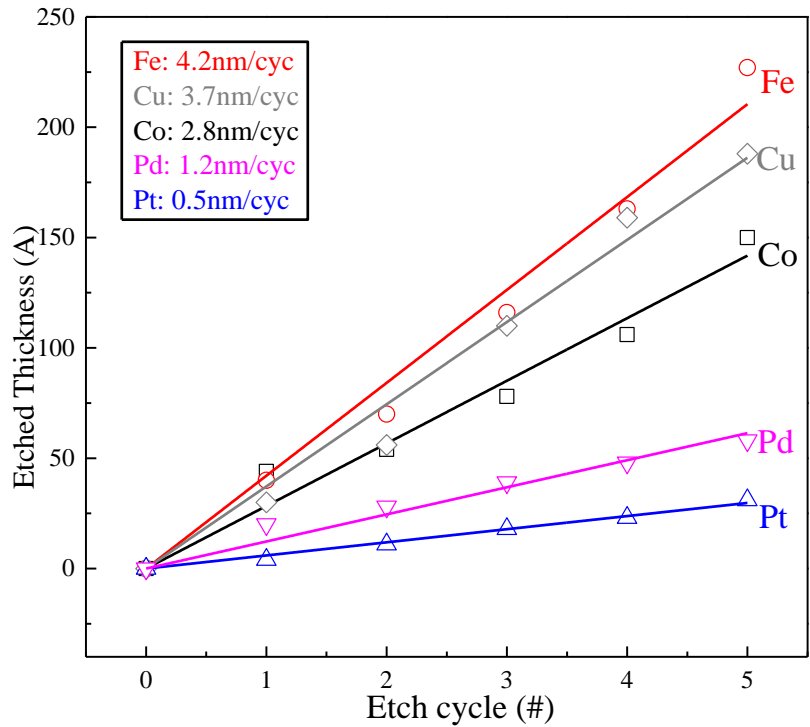
Figure 5-25 Etched thickness of Fe, Cu, Co, Pd, and Pt as a function of sequential etch cycle. The symbol of circle, diamond, square, inverted triangle, and triangle are represent FeO, Cu_2O, CoO, PdO_x, and PtO_x, respectively.
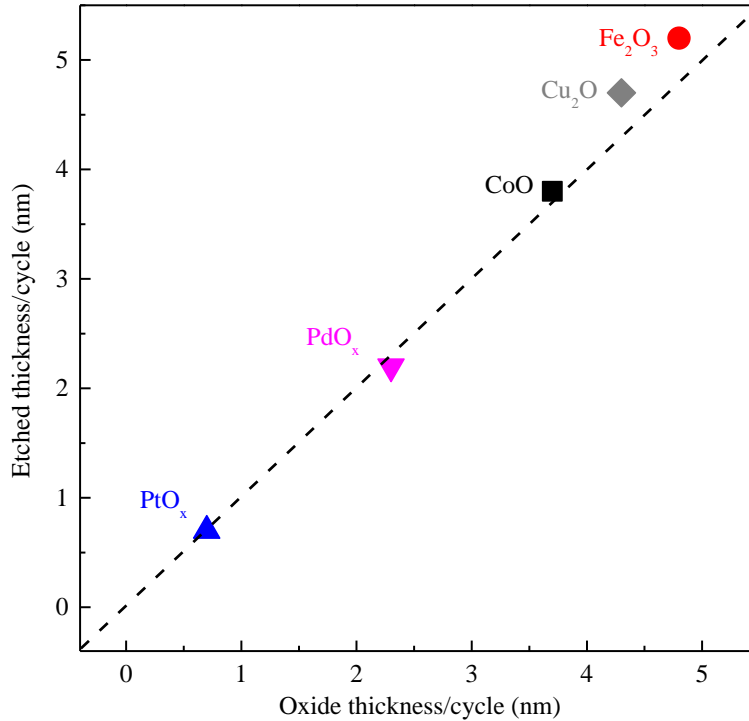
Figure 5-26 Etched thickness per cycle as a function of oxide thickness per cycle for Fe, Cu, Co, Pd, and Pt. The symbol of circle, diamond, square, inverted triangle, and triangle are represent FeO, Cu_2O, CoO, PdO_x, and PtO_x, respectively.

Although a chemical etch of blanket metal film is demonstrated, the patterning of metals with hard mask needs to be investigated as well in order to confirm the selectivity of hard mask to metals, which is one of the most severe issue in MRAM fabrication. In the Figure 5-27 (a), a Co 30 nm film was patterned by TiN hard mask 40 nm and SiN for 10 nm, and a 10-nm-barrier layer served as an etching stop layer under Co film. After 6 cycles sequential etch of 500W O_2 plasma 5 min and formic acid vapor 50 sec exposure, the etching profile is shown in Figure 5-27 (b). A significant undercut of cobalt is observed due to the isotropic characteristic of pure chemical etch. However, the hard mask is remained intact, which the thickness and sidewall profile are sustained due to the low reactivity of TiN to formic acid ligand. After 8 cycles of

194

sequential etch, a sever undercut of cobalt resulting in suspension of TiN hard masks shown in

Figure 5-27 (c). A series of cross-sectional SEM images with different tilted angle is shown in

Figure 5-28, several suspensions of TiN hard masks across a large area on sample is

observed, suggesting a uniform isotropic etch of Co by formic acid vapor.
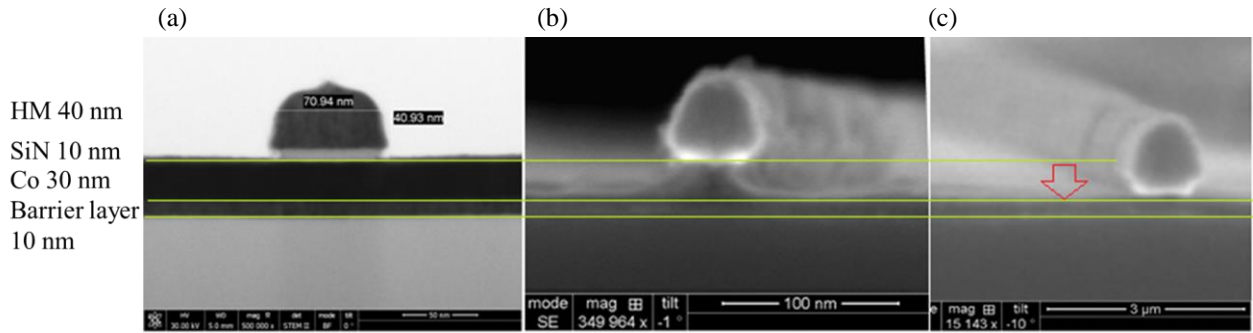
Figure 5-27 SEM images of patterned Co (a) pre-etch, (b) 6 cycles sequential etch, and (c) 8 cycles sequential etch.

(a) 10° (b) 8° (c) 6°

(d) 4° (e) 2° (f) 0°
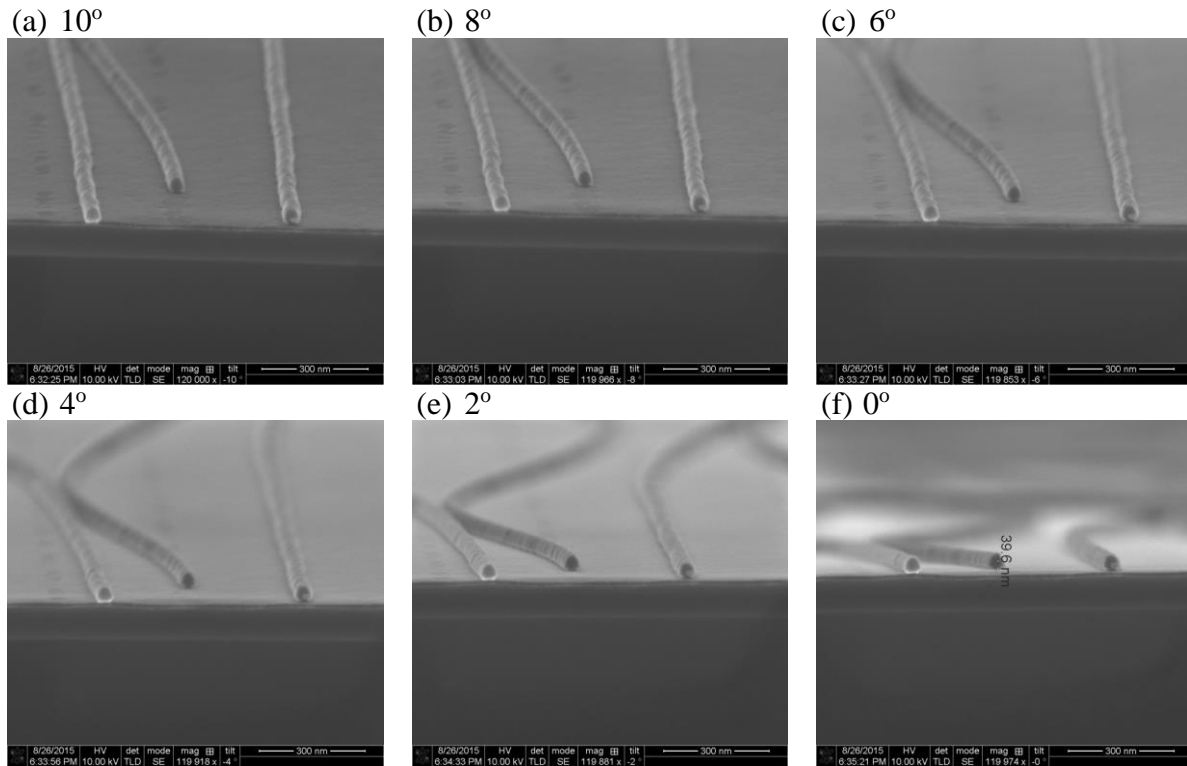
Figure 5-28 A series of cross-sectional SEM images of patterned Co etched by 8 cycles sequential etch with titled angle of (a) 10°, (b) 8°, (c) 6°, (d) 4°, (e) 2°, and (f) 0°.

In addition, the formic acid vapor etch with surface modification by O_2 plasma is closely related with the magnetic properties in the magnetic metallic film. The magnetic property of patterned sample was investigated by Superconducting Quantum Interference Device (SQUID) in Figure 5-29, which presents magnetic hysteresis loop for magnetization as a function of applied magnetic field of the pre-etched patterned Co, as a reference, and the patterned Co treated by O_2 plasma followed by formic acid vapor etch. The coercive field of 20 Oe and saturation magnetization of pre- and post-etch Co are approximately identical, which implying the magnetic property of Co is remained intact after the sequential etch. The change of remnant magnetization could be due to the adsorption of the formic acid molecules on the Co surface, but it was not enough to be detected by XPS as shown in Figure 5-21.
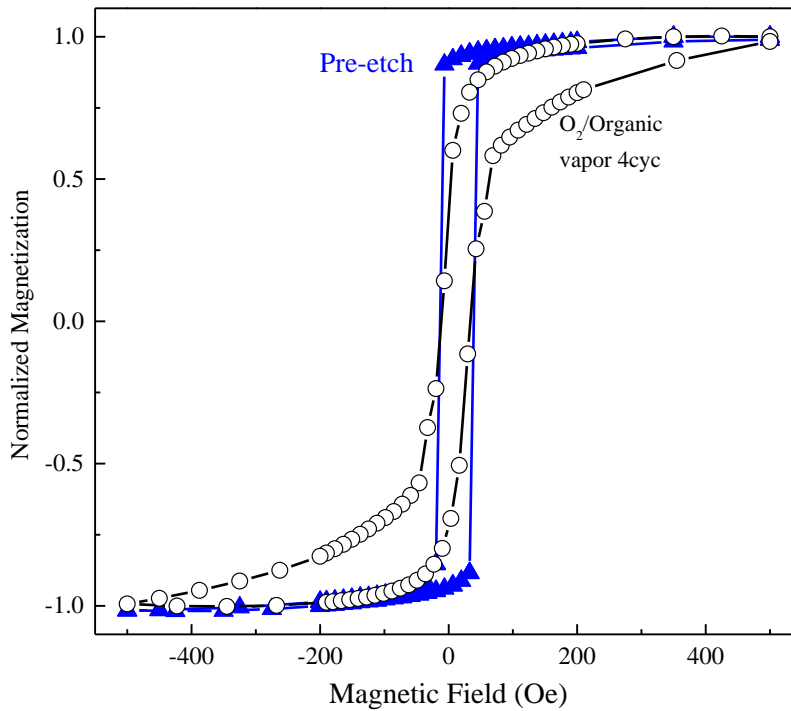
Figure 5-29 Magnetic hysteresis loop measured in patterned Co films. Normalized magnetization (to saturation magnetization of pre-etch patterned Co) vs magnetic field. The spectrum labeled by solid triangle represents pre-etch patterned Co, and the 4 cycles sequential etch of Co is labeled by hollow circle.

Besides the observation by SEM imaging, a surface chemical characterization through Energy-Dispersive X-Ray Spectroscopy (EDS) was also utilized to confirm the removal of Co by sequential etch of O_2 plasma oxidation followed by exposure of formic acid vapor in Figure 5-30. The spectra from bottom to top are pre-etch, 1, 2, 3, 5, 6, 7, 8 cycles of sequential etch. Two strong peaks of Si Kα (1.70 eV) and Al Kα (1.46 eV) are prenseted through all the spectra due to the silicon substrate and aluminum sample holder. The present of C Kα (0.28 eV) and O Kα (0.52 eV) peaks are from the exposure of atmosphere due to the ex-situ EDS measurement. Ti Kα (0.39 eV) peak, Co L3-M1 (0.66 eV), and Co L (0.77 eV) are from the Ti hard mask and Co film. Because of the low reactivity of Ti and formic acid ligand, the peak of Ti Kα is

remained the same throughout the etching. However, a gradual decreasing of the Co peak is found due to the slowly removal of Co by sequential etch. A 30-nm-Co film was totally removed in 8 cycles, suggesting an etch rate of 3.75 nm/cycle is achieved with O_2 plasma oxidation and formic acid vapor treatments.
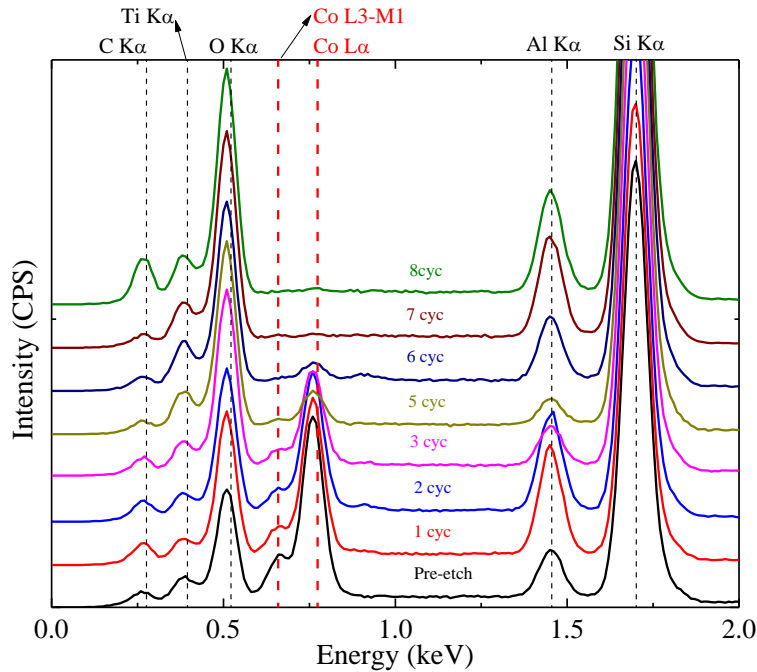
Figure 5-30 The EDS spectra of pre- and post- etched patterned Co with various cycles of sequential etch of surface oxidation and exposure of formic acid vapor.

Nonetheless, the anisotropic etching profile is still desired in pattering metals for MRAM fabrication. In order to obtain a directional oxygen ion to achieve higher degree of oxidation in vertical than lateral direction, a bias voltage of 200 V is chosen to apply onto Co sample. A control experiment of 500 W O_2 plasma with 200 V bias for 10 min is conducted, and a tapered etching profile is found in Figure 5-31 (b). Due to the physical sputtering of low-mass oxygen ion, TiN hard mask was sputtered faster than that of Co, resulting in re-deposition of Ti. The

sequential etch of patterned Co is shown in Figure 5-31 (c), which an anisotropic etching profile is observed and an acceptable recession of 5-nm TiN hard mask is found.

HM 40 nm
SiN 10 nm
Co 30 nm
Barrier layer
10 nm
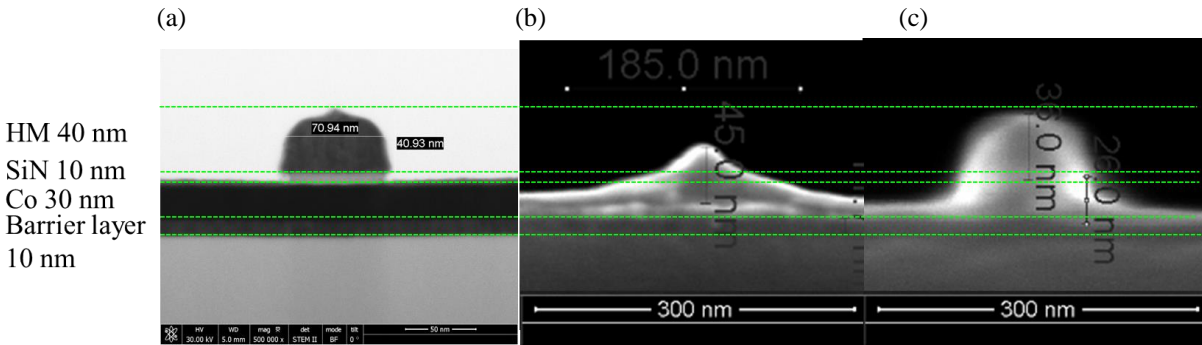
Figure 5-31 SEM images of patterned Co (a) pre-etch, (b) 500 W O_2 plasma with -200 V bias for 10 min, and (c) 4 cycles sequential etch with -200 V bias in 500W O_2 plasma.

5.5 Summary

A comprehensive framework for selecting viable chemistries in patterning magnetic metals has been developed, and the surface modification prior to organic chemical etch was realized to be necessary in chemically etching metals. The surface modification for metals were studied by XPS, and a process of O_2 plasma for converting metal to oxide was found to be the best among other plasma chemistries such as SO_2, Cl_2, CF_4, SF_6, and O_2 ion beam, and atomic percentage of Pt^{4+} was increased 5 times compared to pristine Pt. With the same technique of surface chemical analysis, the thickness of metal oxide was estimated by quantification of XPS with known inelastic mean free path (IMFP) of characteristic electron. By knowing the oxide thickness, the etch rate of each metals could be calculated and verified by ellipsometer and SEM. The mechanism of metal oxidation under mild O_2 plasma without bias was discussed by the

fitting of data and model, and Fe and Co follow inverse logarithmic rate law which suggested the rate determine step was incorporation of metal cations into interstitial site. In the case of Cu, a cubic rate law suggests oxygen diffusion and dissolution was the rate determining step. For noble metals Pd and Pt, the parabolic rate law points out a rate determining step of oxygen diffusion and migration of cations. Once the optimized process for surface modification was achieved, a study of organic solution etch of metal was performed with acac, hfac, edta, nta, podca, oxialic acid, and formic acid. Based on the results of XPS and ICP-MS, the relative high reactivity between platinum oxide to formic acid was observed among the organic chemicals. As a result, a sequential etch of Co, Pt and CoPt alloy with O_2 plasma followed by formic acid solution etch was studied. Due to the preferential removal of Co to Pt, a ratio of Co to Pt on the surface of CoPt alloy was decreased from 3:7 to 1:9, which the magnetic property would be changed. Thus, a new organic chemical is required to keep the same composition of surface in the future. Vapor etch of metals were performed after solution etch, and the etch rate of Fe, Cu, Co, Pd, and Pt were 4.2, 3.7, 2.8, 1.2, 0.5 nm/cycle, respectively. A high selectivity of metal oxide to metal by formic acid vapor was achieved, suggesting one of the most important requirement in atomic layer etch, self-limiting reaction, was fulfilled. By controlling the thickness of oxides with O_2 plasma oxidation, the etch rate of metals could be controlled in atomic scale level. The patterned samples of Co and MTJ stack were investigated with the optimized etching process, and an isotropic etching profile, high selectivity of mask to metals, and retaining of magnetic characteristic were observed, suggesting a process with solely chemical etch without physical sputtering was developed. In order to get a desired etching profile with anisotropic characteristic, directional oxygen ion for oxidation was successfully examined with applying bias onto the

patterned sample. Finally, an approach of successfully patterning metal was developed, and high

density of MRAM fabrication could be achieved based on the preliminary results.

CHAPTER 6: SUMMARY

As advanced memory devices begin to dictate the adoption of complex magnetic and multiferroic materials, overcoming the challenge of achieving high-fidelity patterning for these multifunctional films becomes imperative. Physics and chemistry-based modeling affords greater understanding of elementary reaction mechanisms in plasma patterning; however, the parameters necessary for kinetic modeling are sometimes difficult to obtain experimentally for novel multifunctional compounds. A comprehensive framework for selecting viable chemistries in plasma patterning of magnetic metals has been developed. In this work, a generalized methodology, combining thermodynamic assessment of various etching chemistries and kinetic verification of etching efficacy, is proposed. To screen various chemistries, reactions between the dominant vapor phase/condensed species at various partial pressures of reactants are first considered. The volatility of etch products is determined to aid the selection of viable etch chemistry. MTJ based MRAM was used as a case study to address the challenge of patterning multilayer constituent materials. Ar ion beam milling was a traditional method in patterning MRAM devices; however, sidewall re-deposition results in electrical shorts as the features become smaller with higher aspect ratios. Reactive ion beam etch has been investigated intensely to pattern magnetic metals, but degradation of magnetic properties was found due to residue of etching products with low volatility. In this work, three approaches have been developed and verified experimentally in the following order. First, the volatility of etching products was improved by introducing secondary chemistries to reactive ion etch. Second, the physical and chemical etch were combined into ion beam assisted organic chemical etch. Third, a solely chemical process was developed by introducing surface modification prior to organic vapor etch.

For the first approach, the attainable partial pressure of the major etch product was evaluated by thermodynamic calculations. The metal hydride was not volatile, but oxygen radical addition on MCl_x (M = Co, Fe, or Ni) could enhance the vapor pressure of the etch product. Hydrogen radical addition on chlorinated surfaces appears to be the most effective combination to etch metals, showing that the partial pressure of MH(g) can be higher than the reference value ($\sim 10^{-8}$ atm). According to the surface composition measurements, hydrogen plasma could etch a MCl_x layer but not pure metals. As a result, the etch rates of Co, Fe, and Ni by alternating Cl_2/H_2 plasmas were enhanced by 17, 6, and 20%, respectively, compared to those measured in a continuous Cl_2 plasma. The thermodynamic expectation was consistent with the experimental result. First, Co and Ni etch rate by a Cl_2 plasma was similar, while Fe etch rate was higher than those metals. Second, atomic hydrogen addition could etch a metal chloride layer at an enhanced rate. A reactive hydrogen atom and the stable byproduct such as HCl acted as driving forces for increasing the attainable partial pressure. These results indicate that the alternating plasma approach is the first step toward fabricating high density MTJ-based RAM devices. Concerning the degradation of magnetic properties associated with halogen chemistry etch, the formation of metal chloride resulted in a significant change/increase in the coercive field which is not desirable. It was determined that the utilization of hydrogen led to a complete removal of the metal chloride, thus restoring the soft magnetic characteristics of CoFe. This confirms that the combination of Cl_2 and H_2 plasmas can not only etch CoFe at a reasonable rate but also preserve the magnetic property of CoFe. Since the thickness of the CoFe layer (3-5nm) is usually thicker than that of the tunnel oxide ($\sim$1nm), a double patterning process combining both chemical and physical etch processes may be necessary to successfully pattern both the magnetic layers as well as the tunnel oxide.

Although the reactive ion etch has been verified to achieve reasonable etch rates with preservation of magnetic properties of metals, the low selectivity of the hard mask to metals due to the sputtering effect is still not acceptable. From the second approach, the organic chemical etch of generating highly volatile etching products is desired. Two traditional β-diketonate precursors for CVD have been selected to perform the reverse engineering of ALD. Thermodynamic calculations were first utilized to screen the organic chemistries in etching Co and Fe. A preferential etch of Co by acac through formation of $Co(acac)_2$ and the generation of by $Fe(hfac)_3$ etched with hfac were predicted to be the most thermodynamically favorable products. Similarly, experiments were conducted to verify the theoretical prediction. The etch rates of Co and Fe by acac and hfac solutions have been quantified by profilometer, etching products have been analyzed and verified by ESI-MS, and the selectivity predicted by thermodynamics was verified. The volatility diagram has predicted the selectivity of acac over hfac in etching Co, due to the higher partial pressure of $Co(acac)_2(g)$ than that of $Co(hfac)_3(g)$ at operational condition. In the case of Fe, the high selectivity of hfac over acac was discovered, wherein the formation of $Fe(hfac)_3(g)$ requires lower partial pressure of hfac than that of acac to generate $Fe(acac)_3(g)$. However, a significant drop of etch rate was found while decreasing the concentration of organic in solution, suggesting a lower reactivity of metal with organic vapor. A surface modification with Ar ion beam was introduced in order to facilitate the activation of surface and desorption of organometallic compounds without degrading the magnetic property of metals. The etching of Co by alternating Ar ion beam exposure and acac vapor exposure has a strong effect in improving the etch rate by approximately 180% compared to that of Ar ion beam alone. The etch rate of Co by alternating Ar ion beam and acac vapor is much greater than the

sum of the two, suggesting a synergistic effect of chemical etch along with sputtering has discovered in the ion beam assisted chemical etch.

Nevertheless, Ar ion beam is a limiting factor in patterning high density MRAM device due to the high aspect ratio of features, requiring development of an etching process using only chemical reaction. Thus, a surface modification prior to organic chemical etch was realized to be necessary in chemically etching metals. The surface modification for metals were studied by XPS, and a process of O_2 plasma for converting metal to oxide was found to be the most effective. The mechanism of metal oxidation under mild O_2 plasma without bias was discussed by the fitting of data and model for Co, Fe, Cu, Pd and Pt. Once the optimized process for surface modification is achieved, a study of organic solution etch of metal is performed with several solutions. Based on the results of XPS and ICP-MS, the relative high reactivity between metal oxide and formic acid was observed among the organic etchants. As a result, a sequential etch of metal with O_2 plasma followed by formic acid solution etch was studied. Vapor etch of metals was performed after solution etch, and the etch rate of Fe, Cu, Co, Pd, and Pt were 4.2, 3.7, 2.8, 1.2, 0.5 nm/cycle, respectively. A high selectivity of metal oxide to metal by formic acid vapor is achieved, suggesting one of the most important requirements in atomic layer etch, self-limiting reaction, is satisfied. By controlling the thickness of oxides with O_2 plasma oxidation, the etch rate of metals could be controlled at the atomic level. Patterned Co and MTJ stack samples were investigated with the optimized etching process, and an isotropic etching profile, high selectivity of mask to metals, and retention of magnetic characteristics were observed, suggesting a process of solely chemical etch without physical sputtering was developed. In order to get a desired etching profile with anisotropic characteristic, directional oxygen ion for oxidation was successfully examined with applying bias onto the patterned sample. Finally, an

approach of successfully patterning metal is developed, and high density of MRAM fabrication would be achieved based on the preliminary results.

This work has developed a generalized approach for plasma patterning with a case study of magnetic metal etch, and this methodology could be applied to additional fields. For example, as critical dimensions of gate-length approach 7 nm in 2016, the industrial need for an etching method capable of atomic resolution has led to the pursuit of atomic layer etch. Although the atomic layer etch (ALE) of silicon has been realized recently, controlling of threshold energy in the ALE window is extremely challenging and it requires stringent control of system cleanliness. The ALE process developed in this work does not require the controlling of ion energy, because it depends on the generation of highly volatile products with bulky organic ligand. Finally, anisotropic and selective etching with atomic scale control could be achieved by the generalized approach proposed in this work. Atomic layer etch has been realized by reversing atomic layer deposition (ALD), which required a self-limiting reaction to achieve atomic scale control. However, the isotropic characteristic of ALD is not desired in atomic layer etch, which necessitates anisotropic etching profile. Based on the outcome of generalized approach above, it could potentially facilitate anisotropic etch for selected metals with directional oxygen ion while surface modification. All of this work is a great challenge and opportunity to keep up with Moore's law, and an opportunity for academia to fully understand the truth inside the black box.

TABLE OF CONTENTS

A. Inductively Coupled Plasma Reactor

A.1. Emergency Shutdown Procedures
I. In case of Cl_2 is smelled
    1. Close tank valve.
    2. Close others valve if possible. The diaphragm valve D4, located directly behind chamber, and the regulator R1 on Cl_2 cylinder located in gas cabinet to the right of the MFC cabinet.
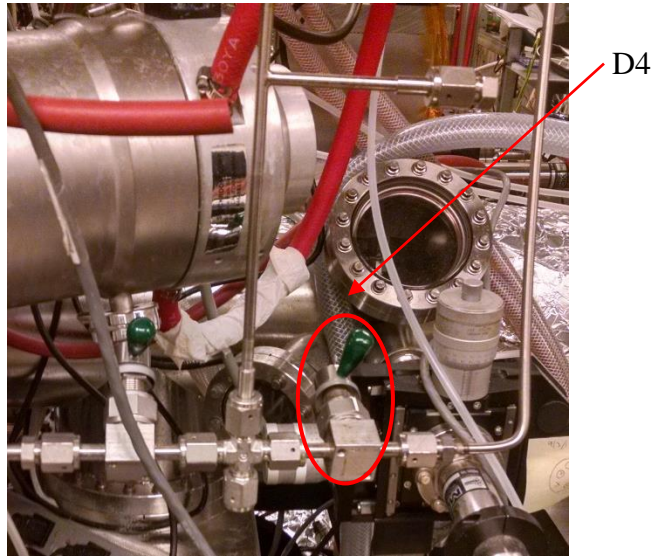
Figure A-6-1 D4 valve directly behind chamber.
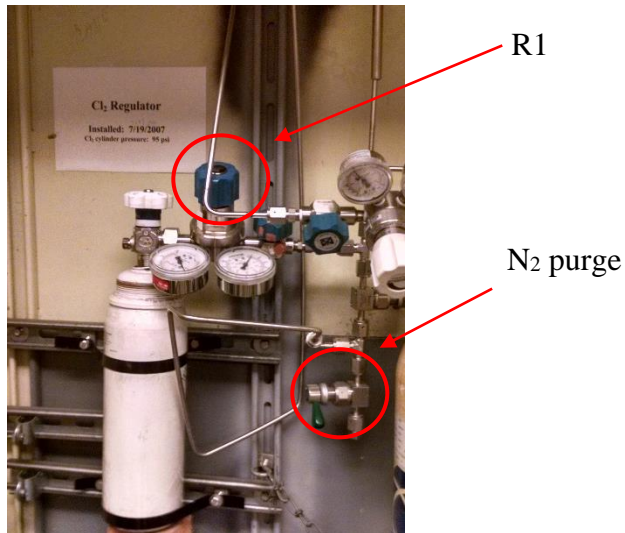
Figure A-6-2 R1 regulator located in chlorine gas cabinet.

    3. Evacuate.

4. Contact EH&S as needed.
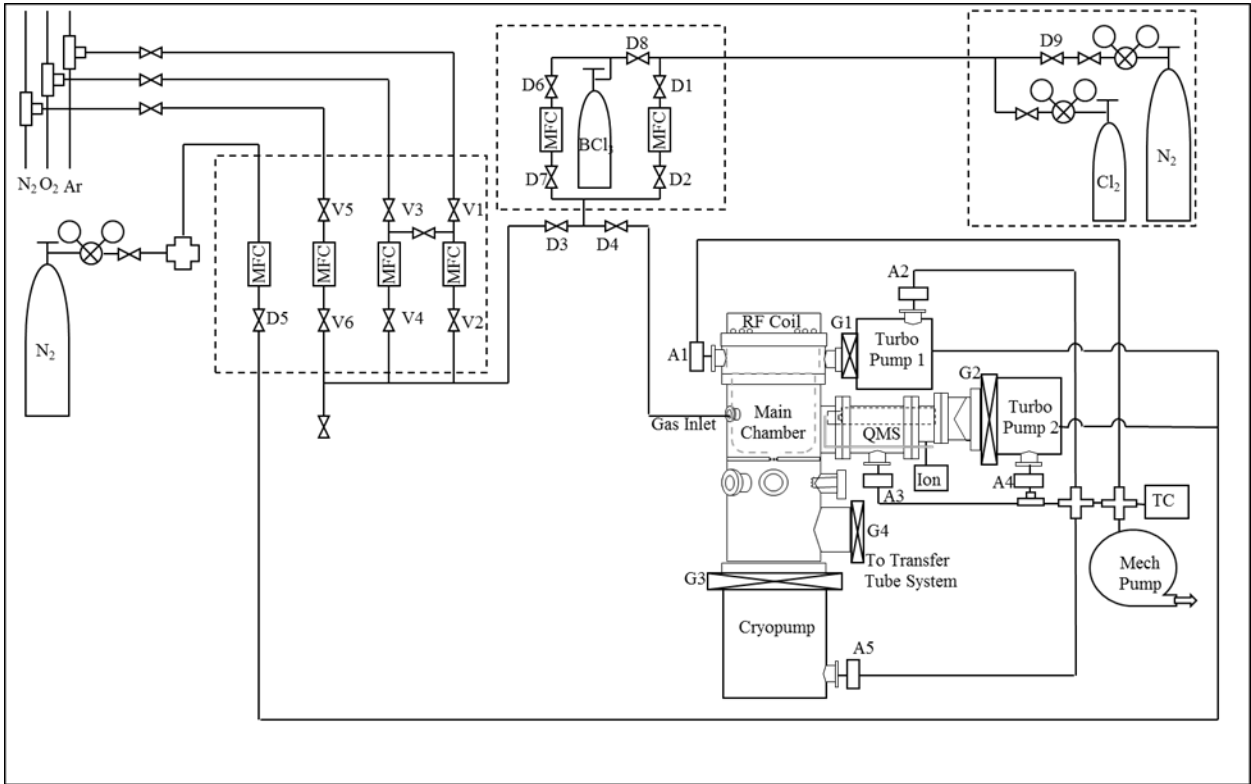
Figure A-6-3 Gas line system for ICP system including corrosive gases Cl_2 and BCl_3, inert gases Ar, N_2, and O_2.

The ICP system including corrosive and inert gas line, molecular turbo pump, cryopump and mechanical pump. V1 and V2 are the valves for Ar, V3 and V4 are the valves for O_2. Since the control flow rate of Ar MFC is small which only has 10 sccm, the one for O2 can go to 50 sccm, the bridge from Ar to O_2 gas line enable high flow rate for Ar gas. V5 and V6 are the valves for high purity of N_2 and D5 is a valve for industrial N_2 which go to the back of TMP to dilute the corrosive gas into mechanical pump. In the corrosive gas aspect, Cl_2 is accompanied with purge N_2 gas, and share with the double wall corrosive gas line with BCl_3. D1 and D2 are the valves for Cl_2 and purge N_2 gas, and D6 and D7 are the valves for BCl_3. D3 is the inert valve and D4 is the corrosive valve control the flow rate into chamber. A1 and A3 are the valves pumping down the chamber by mechanical pump, and A2 and A4 are the valves for MTP back side to the mechanical pump.

II. In case a noise is heard from turbo molecular pump on Main Chamber
  1. Close manual gate valve between turbo pump and chamber.

Gate
Valve
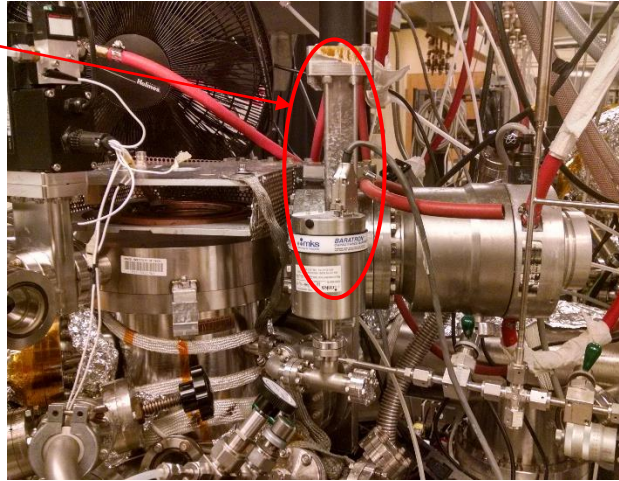
Figure A-6-4 Gate Valve for Main Chamber Turbo Pump.

  2. Turn off the turbo molecular pump by pushing the "stop" button on the controller.

Stop button
(read label to
confirm)

Figure A-6-5. Turbo Pump Controller for Chamber.

  3. Isolate mechanical pump by closing manual valve between turbo and MP.
III. In case a noise is heard from mechanical pump on Chamber
  1. Close manual gate valve between turbo pump and chamber. (See Figure 3)
  2. Turn off the turbo molecular pump by pushing the "stop" button on the controller. (See
      Figure 4) And close the roughing from turbo pump to mechanical pump.
  3. Switch off the mechanical pump by turning off the breaker.
IV. In case a ratcheting is heard from Cryopump on Chamber
  1. Close the pneumatic gate valve between ICP and Cryopump by pressing the corresponding
      switch on the control box (trace the cable if unsure). (See Figure 5)

Gate
Valve

Control
Box
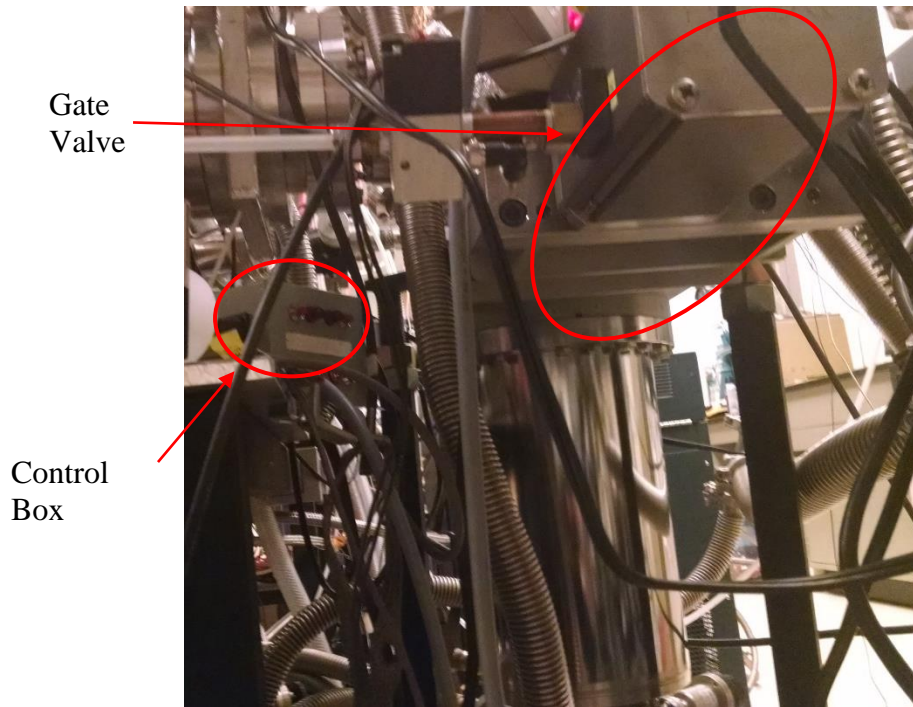
Figure A-6-6 Gate Valve between Cryopump and ICP.

2. Ensure that the roughing valve between the cryopump and the chamber mechanical pump is closed.
3. Turn off the cryopump by flipping the white circuit breaker on the compressor (See Figure 6 - in the event of pump failure this may turn off automatically – check to see if the unit is operating).
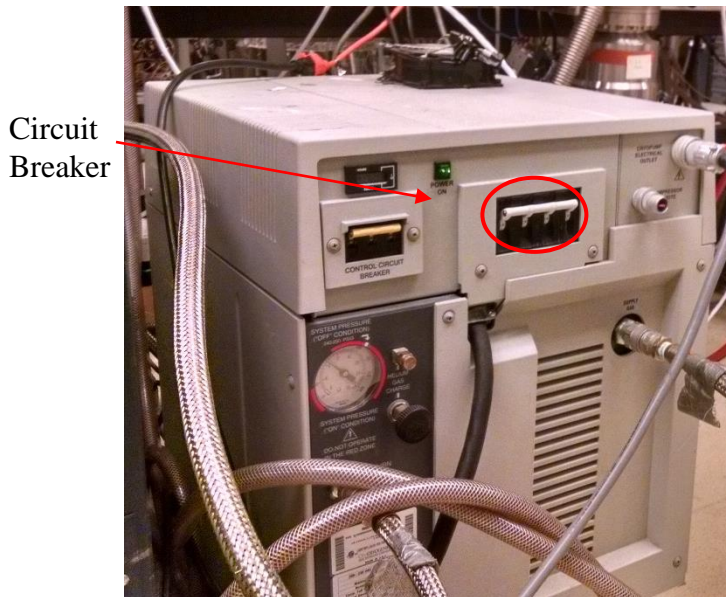
Circuit
Breaker

Figure A-6-7 Compressor and Circuit Breaker Switch.

V. In case noises are heard from any of the electronics

1. If units have power switches, turn them off and unplug all units (see pictures below).
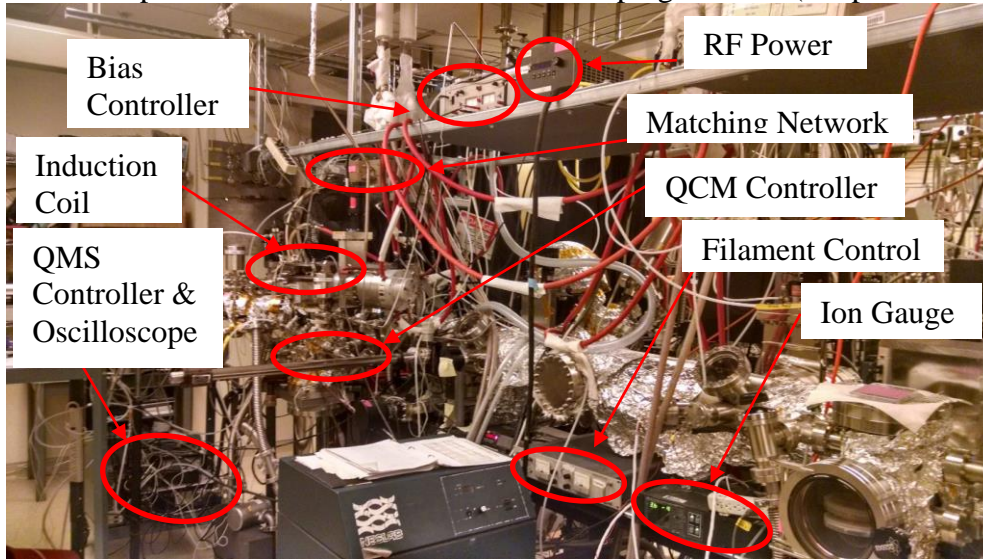
Figure A-6-8 The components of ICP system.

VI. In case the vapor etch system needs to be shut down
    1. Turn off vaporizer heater.
    2. Close valve to 1.
    3. Unplug vaporizer heater, LFC controller, and MFC controller.

A.2. Schematics

ICP reactor
Main chamber – Side view

University of California, Los Angeles, Department of Chemical and Biomolecular Engineering							
Part		Material	Stainless steel				
Filename		Scale	Yes	Units	inch	Quantity	1
Designer	Yunpeng Yin(MIT)	Date	6/11/2003				
Revised by		Date					
Contractor	Applied Vacuum Technologies	Date	6/11/2003				
Comments		Tolerance			+/- .0001		

ICP reactor

Main chamber – Isometric view

O-ring groove
see detail
Drawing #1-2 front view

10" OD flange, without holes
Nonrotatable

Port 9

Port 8

Port 6

Port 5

Port 7 (view port)

Port 1

Port 4

Port 2

10" OD flange, clearance holes,
nonrotatable, with 4 steel brackets
welded at 45, 135, 225, 315 degree,
looking at drawing #1-7 bottom
view for the detail dimentions

Reference plane

Port 3
(Viewport)

University of California, Los Angeles, Department of Chemical and Biomolecular Engineering							
Part		Material	Stainless steel				
Filename		Scale	Yes	Filename		Scale	Yes
Designer	Yunpeng Yin(MIT)	Date	6/11/2003				
Revised by		Date					
Contractor	Applied Vacuum Technologies	Date	6/11/2003				
Comments		Tolerance	+/- .0001				

ICP reactor

Main chamber – Front view

University of California, Los Angeles, Department of Chemical and Biomolecular Engineering							
Part		Material	Stainless steel				
Filename		Scale	Yes	Filename		Scale	Yes
Designer	Yunpeng Yin(MIT)	Date	6/11/2003				
Revised by		Date					
Contractor	Applied Vacuum Technologies	Date	6/11/2003				
Comments			Tolerance		+/- .0001		

ICP reactor

Main chamber – Top view

University of California, Los Angeles, Department of Chemical and Biomolecular Engineering							
Part		Material	Stainless steel				
Filename		Scale	Yes	Filename		Scale	Yes
Designer	Yunpeng Yin(MIT)	Date	6/11/2003				
Revised by		Date					
Contractor	Applied Vacuum Technologies	Date	6/11/2003				
Comments		Tolerance	+/- .0001				

217

ICP reactor

Main chamber – Button view

University of California, Los Angeles, Department of Chemical and Biomolecular Engineering							
Part		Material	Stainless steel				
Filename		Scale	Yes	Filename		Scale	Yes
Designer	Yunpeng Yin(MIT)	Date	6/11/2003				
Revised by		Date					
Contractor	Applied Vacuum Technologies	Date	6/11/2003				
Comments				Tolerance		+/- .0001	

ICP reactor

Main chamber – QMS chamber

3.9800

0.4533

All Leak-Check slots are vertical
unless otherwise indicated

90°

1.5467

4.1233

Axis 1

4.1333

6.0"OD Flange, 4.0"OD tube, CF
Nonrotatable, tapped
Leak-Check slots are parellel
to axis 1

4.1333

3.9800

6.0"OD Flange,CF
4.0"OD tube
Nonrotatable
Tapped

6.0"OD Flange,CF
4.0"OD tube
Nonrotatable
Tapped

University of California, Los Angeles, Department of Chemical and Biomolecular Engineering							
Part		Material	Stainless steel				
Filename		Scale	Yes	Filename		Scale	Yes
Designer	Yunpeng Yin(MIT)	Date	6/11/2003				
Revised by		Date					
Contractor	Applied Vacuum Technologies	Date	6/11/2003				
Comments			Tolerance		+/- .0001		

219

ICP reactor

Sample stage

University of California, Los Angeles, Department of Chemical and Biomolecular Engineering						
Part		Material	Stainless steel			
Filename		Scale	Yes	Filename	Scale	Yes
Designer	Yunpeng Yin(MIT)	Date	6/11/2003			
Revised by		Date				
Contractor	Applied Vacuum Technologies	Date	6/11/2003			
Comments			Tolerance		+/- .0001	

ICP reactor

Quartz in the ICP chamber

(10.0)

1

(0.5)

(0.5)

(0.71)

University of California, Los Angeles, Department of Chemical and Biomolecular Engineering							
Part		Material	Stainless steel				
Filename		Scale	Yes	Filename		Scale	Yes
Designer	Yunpeng Yin (MIT)	Date	6/11/2003				
Revised by		Date					
Contractor	Applied Vacuum Technologies	Date	6/11/2003				
Comments			Tolerance		+/- .0001		

ICP reactor

Transfer Tube

University of California, Los Angeles, Department of Chemical and Biomolecular Engineering							
Part		Material	Stainless steel				
Filename		Scale	Yes	Filename		Scale	Yes
Designer	Jane Chang (MIT)	Date	1994				
Revised by		Date					
Contractor	Applied Vacuum Technologies	Date	1994				
Comments				Tolerance		+/- .0001	
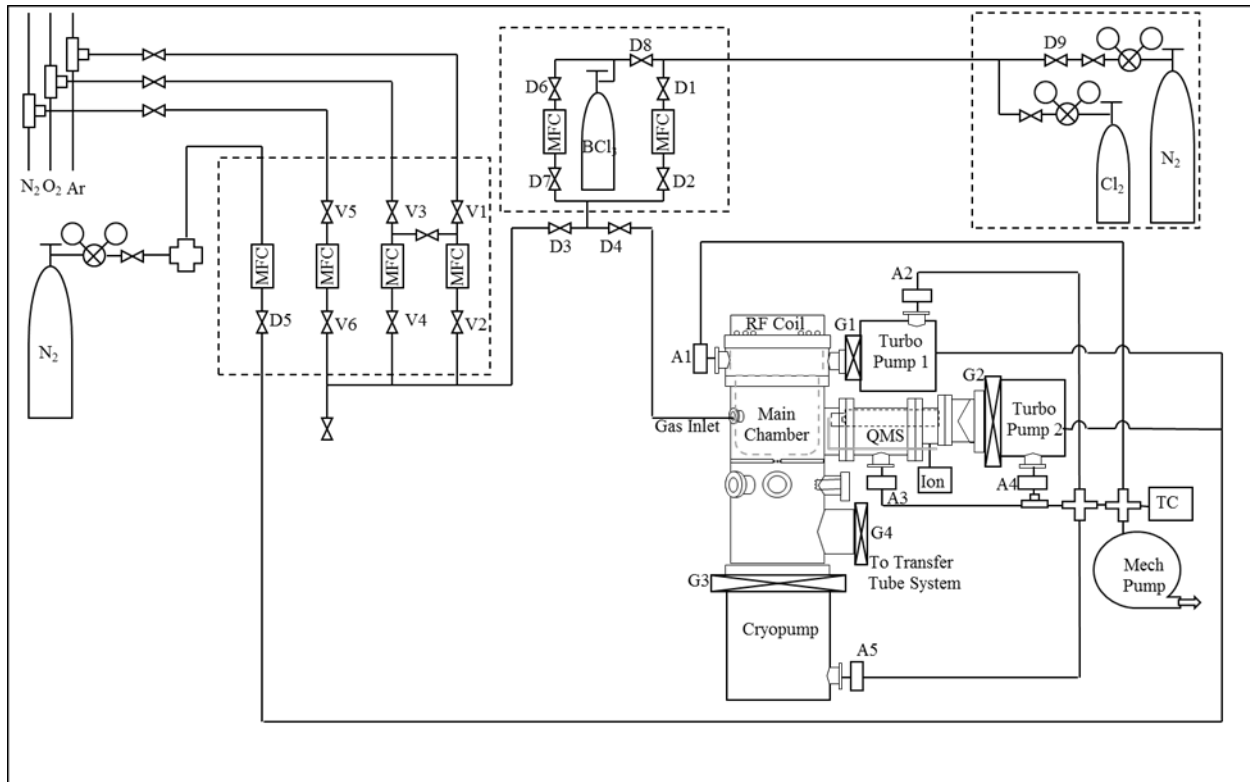
Figure A-6-9 Gas line system for ICP system including corrosive gases Cl_2 and BCl_3, inert gases Ar and N_2, and O_2.

The ICP system including corrosive and inert gas line, molecular turbo pump, cryopump and mechanical pump. V1 and V2 are the valves for Ar, V3 and V4 are the valves for O_2. Since the control flow rate of Ar MFC is small which only has 10 sccm, the one for O_2 can go to 50 sccm, the bridge from Ar to O_2 gas line enable high flow rate for Ar gas. V5 and V6 are the valves for high purity of N_2 and D5 is a valve for industrial N_2 which go to the back of TMP to dilute the corrosive gas into mechanical pump. In the corrosive gas aspect, Cl_2 is accompanied with purge N_2 gas, and share with the double wall corrosive gas line with BCl_3. D1 and D2 are the valves for Cl_2 and purge N_2 gas, and D6 and D7 are the valves for BCl_3. D3 is the inert valve and D4 is the corrosive valve control the flow rate into chamber. A1 and A3 are the valves pumping down the chamber by mechanical pump, and A2 and A4 are the valves for MTP back side to the mechanical pump.

A.3. Operating Procedures
1. Pump down the main chamber (Note: The chamber's default state should be pumped down, check the pressure reading on the ion gauge to verify. The following steps should only be taken if you aware that the chamber has been vented and not pumped back down).
   a. The following interlocks for the pump down procedure must be met to begin pumping:
      I. cooling water for main chamber turbo molecular pump(TMP) must be on
      II. cooling water flow to compressor should be between 2.3 and 3.5 gpm.
   b. Check that all the flanges are tightened and all the valves are in the closed position.
   c. Check all the cables are correctly connected.

d. Check the oil level in the mechanical pump(MP), which should be 2/3 full in view window.
e. Check MP and its exhaust for liquid leaks. (oil, condensation, exhaust fluid)
f. Turn on MP by turning on the breaker. The thermocouple(TC) gauge reading should start going down within 20 seconds. If not, turn off the pump and check connections to chamber, turbopump and cryopump for vacuum leaks.
g. Wait until MP reaches the base pressure ~60 mTorr. This process may take several minutes if system was shut down for some time.
h. If the gas lines have been exposed to ambient conditions, diaphragm valve D3 and D4 should be open so that the gas lines could be pumped down as well. Rough pump the chamber using MP until a base pressure of ~75-85 mTorr is achieved.
i. After the TC gauge reaches the base pressure, close roughing valve between chamber and MP and gradually open roughing valve between TMP and MP.

2. Before TMP is turned on, check:
a. The cooling water is running
b. The roughing valve between the chamber and TMP should be always CLOSED while the TMP is on.
c. If TMP is running, the base pressure should be achieved right away. (This would occur only if MP was turned off for less than approximately 10 minutes and TMP was isolated prior to shut off of MP)
d. If pumping down after TMP has been off for a few hours it may be safer to purge TMP with N_2 using the N_2 MFC for 30 seconds. Then gradually open the roughing valve and wait until base pressure is reached in MP.
e. Open the gate valve between TMP and chamber. At this stage, the TC gauge readout should NOT vary at all.
f. Turn on TMP by pushing the start button on the Leybold controller, unless already on. The green acceleration indicator should be on.
g. Within 5 minutes, the turbo molecular pump should reach full speed and the yellow indicator should be on normal.
   1.If any strange noise is heard from TMP, turn it off right away by pushing the off button on the controller.
   2.If corrosive gas is anticipated to be used, 36 sccm industrial level nitrogen (corresponding to ~50 mTorr rise in TC pressure) should be provided through the purging port on the bottom of the pump by opening valve D5 and switching on the MFC "N_2 ind." on the control panel once the pump has reached full rotation, which is indicated by the normal light being lit on the TMP controller. (Refer to Leybold 361C Turbo Molecular Pump manual.)
h. Wait until the chamber reaches the base pressure 6.0×10^{-7}. This process may take up to couple of days depending on how long the chamber has been under atmosphere.
   • If the chamber has been exposed to ambient or pumping system has been off for more than a day, baking the chamber is necessary to achieve base pressure and remove any build up on the sidewalls of the chamber. Two heating tapes are used to bake the chamber. Do NOT turn on the power over 20% of the full range on the variable transformer to prevent over heating. At this point the chamber pump down procedure is complete. If no processing is to be performed system should be left in this idle state.

After base pressure in the chamber is achieved, plasma processing can begin using the following procedure. If a sample is to be processed the following procedure must be followed to load the sample in to the chamber. However, it is better to warm up the plasma before processing a sample, in which case skip to steps 3-6, and then return to step 2 and repeat the following steps.

3. Transfer the sample from transfer tube to the chamber:
    a. See instructions for loading a sample from the loadlock in the Transfer Tube SOP.
    b. Move the cart into position for transfer to the ICP.
    c. Before opening the gate valve between the ICP and the TT check that their pressures are roughly equivalent. If the ICP pressure is over 10^{-7} torr which is 2 order higher than TT pressure, 10^{-9} torr, then the gate valve between the TT and its cryopump/turbo pump should be closed. Ensure that no gas is flowing into the ICP.
    d. Open the gate valve (G4) using the controller box (trace the cable to ensure). Check the ion gauge controllers on both the ICP and TT to ensure that the pressure has not changed significantly.
    e. Secure the sample by sliding the holding fork attached to the end of the transfer arm around the upper groove of the sample holder.
    f. Using the manipulator, lift the sample off the cart. Verify that the arm has cleared the cart (a setting of about 4-5 on the Y-axis manipulator is sufficient).
    g. Slowly slide the transfer arm forward to move the sample into the ICP chamber.
    h. Visually confirm the location of the sample in relation to the sample stage pin by checking through the viewport on the lower section of the ICP chamber.
    i. Lower the sample holder onto the protruding pin. Visually confirm.
    j. Slowly begin sliding the transfer arm out. The holder should stay on the stage.
    k. When re-entering the transfer tube ensure the height of the transfer arm is readjusted so as not to hit the cart or holding pin in front of the ICP chamber.
    l. Fully withdraw the transfer arm into the tube so that it has cleared the gate valve.
    m. Close the gate valve (G4) between the ICP and TT.
    With the sample loaded, if necessary, plasma processing can begin. Processing gases must be introduced into the reactor prior to striking plasma by performing the following procedure. Proceed to step 3, 4, or 5 depending on plasma chemistry.

4. Feed in process gas for plasma for inert gas only:
    a. Check that the chamber is at the base pressure of 1.0×10^{-7} torr.
    b. Check regulators for all the desired gases (N_2, Ar, O_2) by opening the gas tank.
    c. Check the cylinders are filled with enough gas to obtain required flow rate.
    d. Open the pneumatic valves for gases to be used before the Mass Flow Controller (MFC), which are V1, V3, and V5.
    e. Gradually open the corresponding valve after the MFC, which are V2, V4, and V6, to prevent a large pressure difference to the MFCs.
    f. Adjust the set point on the MFC control unit to desired flow rate for each gas.
    g. Open Diaphragm valve D3 and then gradually open D4. The chamber pressure should go slightly higher; wait until it goes back to the base pressure. This will pump down the gases which have been sitting in the line.
    h. Turn off the ion gauge, which cannot go above 1×10^{-3} torr.
    i. Turn on the MFCs for the gases to be used. Wait until a steady flow is achieved. Do fine adjustments if needed.

j. Record pressure achieved in chamber after steady flow is reached

5. Feed in corrosive process gas (Cl_2 and/or BCl_3) only:

   The following interlock for corrosive gas use must be met to begin: n_2 purge to main chamber and QMS turbo pumps must be on.

   a. Check that the chamber is at the base pressure of 1.0×10^{-7} torr.
   b. Check there is enough Cl_2 gas in the cylinder and the tank and regulator should be CLOSED. (This regulator should always be closed while Cl_2 gas is not in use.)
   c. Check that 36 SCCM nitrogen is supplied to the purging ports of TMP1 and 2 by MFC.
   d. Gradually open Diaphragm valve D4. The chamber pressure should go slightly higher; wait until it goes back to the base pressure.
   e. Adjust the set point on MFC control unit, which is channel 1, to desired flow rate for Cl_2 gas.
   f. Turn off the ion gauge.
   g. Open the valve on Cl_2 cylinder and the isolation valve after the regulator. Adjust the regulator to get 12 Torr outlet pressure. Then close gas cabinet door.
   h. Gradually open the Diaphragm valve D1 and then D2 for Cl_2 and/or D6 and D7 for BCl_3. Close the gas cabinet door.
   i. Turn on the MFC. Wait until the steady flow is achieved.
   j. Record pressure in chamber once steady flow is achieved.

6. For corrosive gas and inert gas mixture (Cl_2, BCl_3, Ar, O_2, N_2):

   The following interlock for corrosive gas use must be met to begin: n_2 purge to main chamber and qms turbo pumps must be on.

   a. Check that the chamber is at the base pressure of 1.0×10^{-7} torr.
   b. Check there is enough Cl_2 and or BCl_3 gas in the cylinder.
   c. The regulators should be CLOSED. (This regulator should always be closed while Cl_2 gas is not in use.)
   d. Check 36 SCCM nitrogen is supplied to the purging ports of Turbopumps 1 and 2.
   e. Gradually open Diaphragm valve D3 and D4. The chamber pressure should go slightly higher; wait until it goes back to the base pressure.
   f. Adjust the set points on MFC control unit to desired flow rates for gases.
   g. Turn off the ion gauge.
   h. Open the regulator on Cl_2 cylinder and/or BCl_3 at their respective gas tanks.
   i. Open the pneumatic valves, for the inert gas, before the MFC (V1, V3, and V5) first, and then open the corresponding valve after the MFC (V2, V4, and V6).
   j. Turn on the MFCs for the inert gases.
   k. Gradually open the Diaphragm valve D1 and then D2 for Cl_2 and/or D6 and D7 BCl_3.
   l. Close the gas cabinet doors.
   m. Turn on the Cl_2 and/or the BCl_3 MFC. Wait until the steady flow is achieved.
   n. Record chamber pressure once flows have stabilized.

7. Turning on the plasma

   The following interlock for plasma generation must be met to begin:

   1. Induction coil fan on.
   a. Ensure the fan on the induction coil is plugged in and operating.
   b. Turn on the main power of the RF generator (Seren R1000) by flipping the main power switch.

c. Turn on the main power of the matching network tuning controller (RFPP 761 Unit) and ensure its operation mode is set to "Auto".

d. If bias is desired, turn on the main power and bipolar voltage control of the DC bias controller (Kepco BOP 500M).

e. If etching in the lower chamber is desired, turn on the filament power supply (Harrison Labs 6263A). Let all the electronics units warm up for 30 - 45 minutes.

f. Flow the process gases (pressures should be adjusted in steps 2-4).

g. Set the RF generator to the desired source power and press the "RF on" button. A red light should indicate RF power is being supplied.

h. If plasma does not strike, check that the reflected power as indicated on the generator display is not higher than 70 W, or that no warnings are displayed. If the reflected power is low, consider increasing the gas flow using the appropriate MFC. If the power is high or if warnings are displayed, turn off the RF supply by pressing the "RF on" button again and check the connections between the generator, matching network and source coil.

i. If bias is desired, set the DC bias to the appropriate voltage.

j. If etching in the lower chamber is desired, set the filament power supply to ~2 Amps. Usually this should be done a minute or two before the experiment to ensure the filament is receiving current (indicated by a reddish glow).

k. After the process is finished, turn off the RF power by pushing the "RF on" button on the front panel of the Seren R1000. Processes should not exceed 15 minutes so as to not over heat system.

l. Turn off the corrosive process gases first on the MFC.

m. Leave the inert gases running for about 5 minutes.

n. Turn off the MFCs, close the corresponding pneumatic valves and the Diaphragm valve D4 and D3 for Cl_2 and/or D6 and D7. BCl_3.

o. Turn off TMP1 purging nitrogen.

8. Troubleshooting

This section details major problems occurring on ICP chamber and the steps taken to fix them.
3/2012:
Problem: Unable to strike the plasma such as $O_{2(g)}$ and $N_{2(g)}$.
Solution:
    1. Check the connection of cable on the top of chamber.
    2. Shine the light into chamber while turning on the RF generator.
    3. Flow the Ar gas with O_2 or N_2 to strike the plasma, once the plasma been ignited then Ar could be slowly decreased to 0.

7/2012:
Problem: The wire connected from voltage supplier to bias ring was burn out.
Solution:
    1. Order stainless steel wire from McMaster Carr.
    2. Clean up the stainless steel wire by IPA and alcohol, cut into a suitable length and then replace old one.
    3. Check by the multimeter for connection between voltage supplier and bias ring.

8/2012:
Problem: The turbo pump started making a high pitch noise.
Solution:

1. Check the turbo pump controller is in normal condition.
2. Isolated the turbo pump. First, close gate valve to chamber, and then switch off the turbo pump by controller. Wait 20 mins to pump out the turbo pump by mechanical pump, and close the roughing valve to mechanical pump.

8/2012:

Problem: The bias beam couldn't be observed during the plasma etching process.

Solution:
1. Check the mesh at the center of upper chamber is clean and grounded.
2. If mesh is covered by green species or other contamination, the mesh need to be cleaned.
   a. Flip up the plate in the upper chamber, undo the filament connection carefully.
   b. Take out the plate and undo the screws at the center mesh. Be careful that there are three small of stainless steel piece between the plate and mesh which can make the mesh grounded.
   c. Sonicate the mesh with IPA for 10 mins two times.
   d. Reinstall the mesh and plate into the chamber, and connect the filament wire.
   e. Use multimeter to check the mesh is grounded.

9. Cryopump Regeneration
   a. Isolate cryopump by closing gate valve and closing backing valve.
   b. Turn off compressor. Leave cryopump for 2-3 hours, expect to see condensation.
   c. After condensation evaporates, apply heating jacket and plug it in.
   d. Let the cryopump heat for 8 hours.
   e. Close backing of transfer tube (TT) and load lock (LL) turbo pumps, set timer to 5 min.
   f. Look at TT mechanical pump thermocouple (TC) gauge, slowly open cryopump backing. You should see a pressure spike.
   g. Let cryopump pump out until timer runs out, then close cryopump backing. Let TC gauge bottom out, then reopen TT and LL backing.
   h. Repeat steps e-g until TC gauge no longer spikes when cryopump backing is opened. Close cryo backing.
   i. Unplug heating jacket, let it cool then remove it.

B. Quadrupole Mass Spectrometer Operational Guidelines

B.1. Emergency Shutdown Procedures

1. Turn off the UTI100C Electronics Controller by following the sequence labeled below in the order indicated.

1

Rotate the Emission Control fully counter-clockwise until it clicks off.

2

Depress the Off Switch
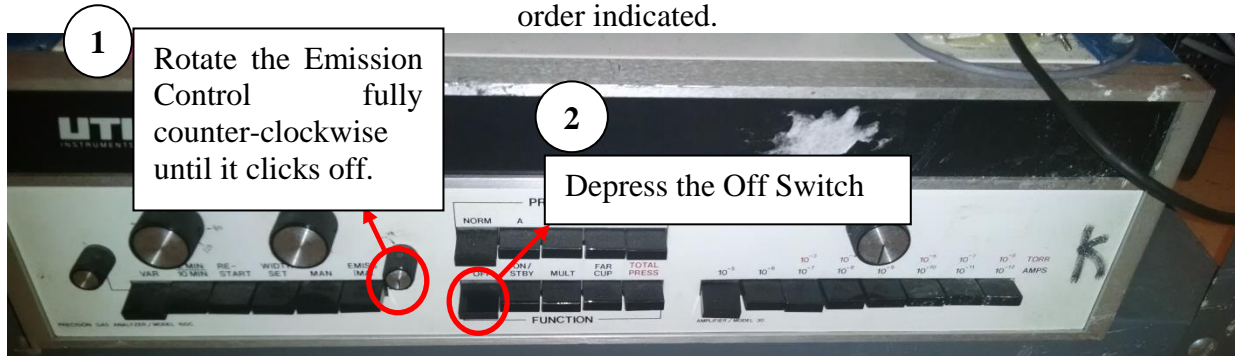
Figure B-1 QCM panel.

2. Turn off the oscilloscope by pressing the power button:

Power Button
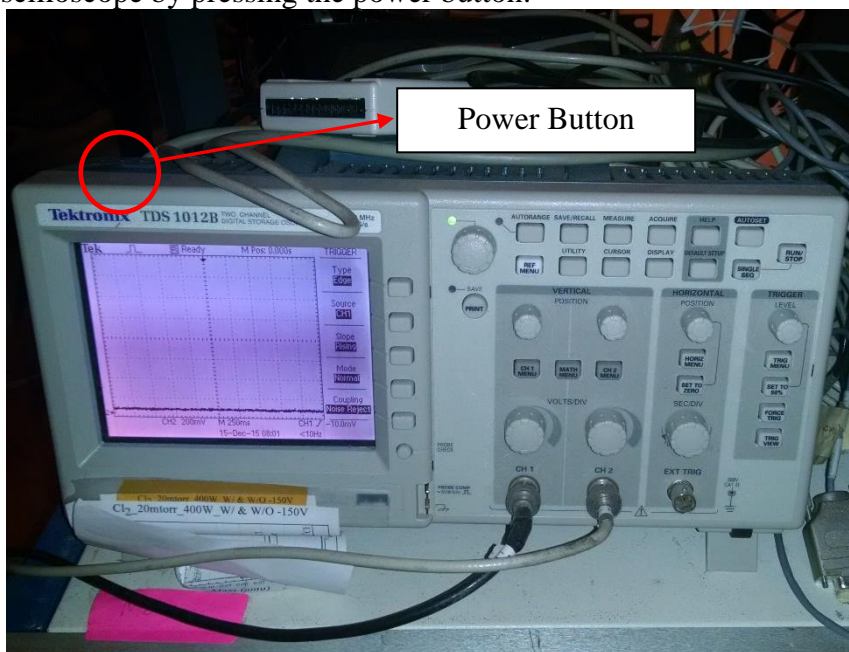
Figure B-2 Oscilloscope panel.

B.2. Schematics
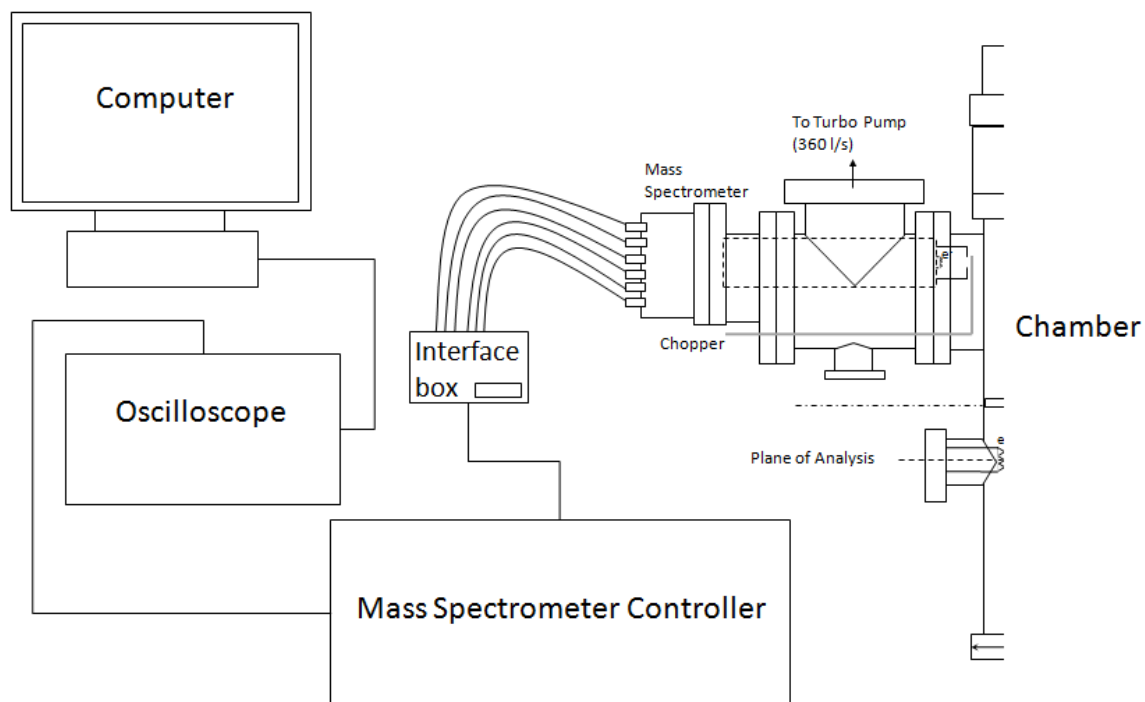
Figure B-3 QMS schematics.

B.3. Operation Procedures

1. Check the base pressure of the system, which should be about $2.8*10^{-8}$ Torr. Write the base pressure in the logbook.
2. Check the connections between the Spectrometer and the Interface Box, the Interface Box and the Spectrometer Control Unit (SCU), the SCU and the Oscilloscope, and the Oscilloscope and the Computer (Illustrated below). Turn on the computer.
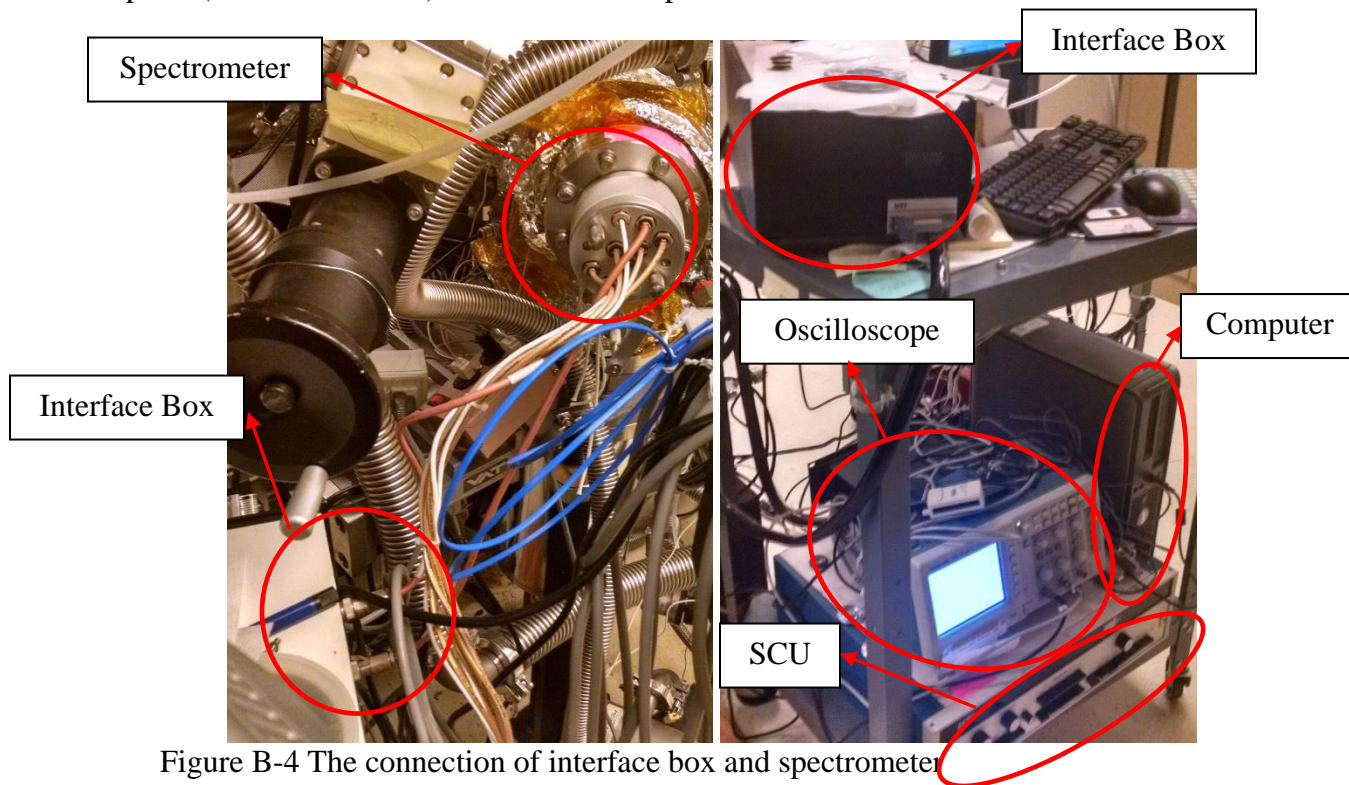
Figure B-4 The connection of interface box and spectrometer

3. Ensure that the power cable into the SCU is plugged in. Check that the follow switches are depressed (labeled below): "Var" and "Man" in the Scan section, "Norm" in the Program Section, "Off" in the Function Section and "10^{-5}" in the Damper Section. Also make sure the emission control is off (rotated fully counter-clockwise).
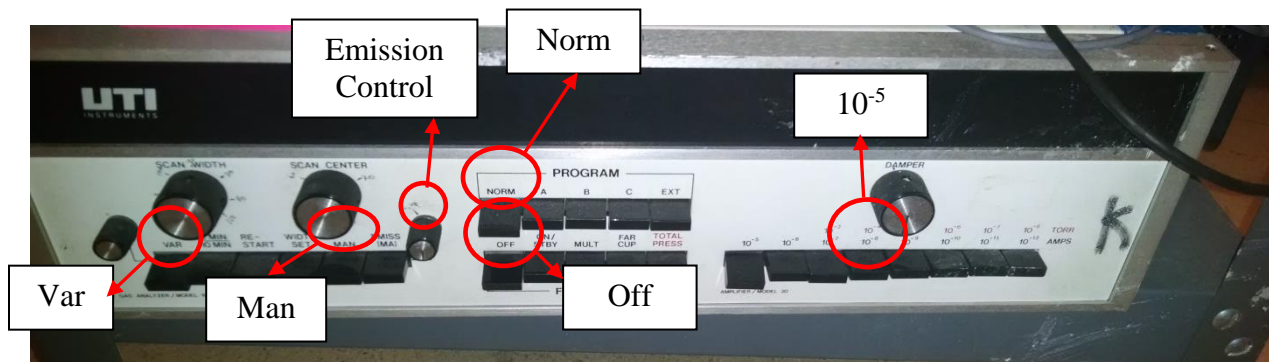
Figure B-5 QCM panel.

4. Depress the "On/Stby" switch on the SCU directly to the right of the "Off" switch. Let the electronics warm up for 30 minutes. Power on the oscilloscope by pressing its power button. Windows should indicate that new USB device has been plugged in and you need to select the software option to view the device.
5. Select TekDesktopAcquisition (the TDS 1012B should be selected as device by default).
6. After the electronics have warmed up set the scan center and width using the Scan Control section of the SCU. To set the center "Man" has to be depressed. To set the width, "Width Set" has to be depressed and "Man" should be released. Both of these values are set by using the corresponding rotary controls above the switches (can be seen in the preceding image).
7. Flow gas and strike plasma as required by your experiment.
8. Monitor the QMS pressure. The maximum operating pressure for QMS is $5*10^{-6}$ Torr.
9. Start the QMS scan by releasing the "Man" switch, and depressing "Emiss (mA) and "Mult" switches at the same time. Adjust the emission current using the rotary control (max = 0.5 mA). If no signal is seen adjust the Damper (max = 10^{-9}).
10. Monitor the scan on the oscilloscope and adjust the visual as necessary using the controls for the y- and x-axis. A visual can be captured using the Tektronic software "Data Capture" button.
11. After finishing all the experiments, close the software and transfer all the data files to the server.
12. Turn off the power to the SCU by using the steps outlined below:
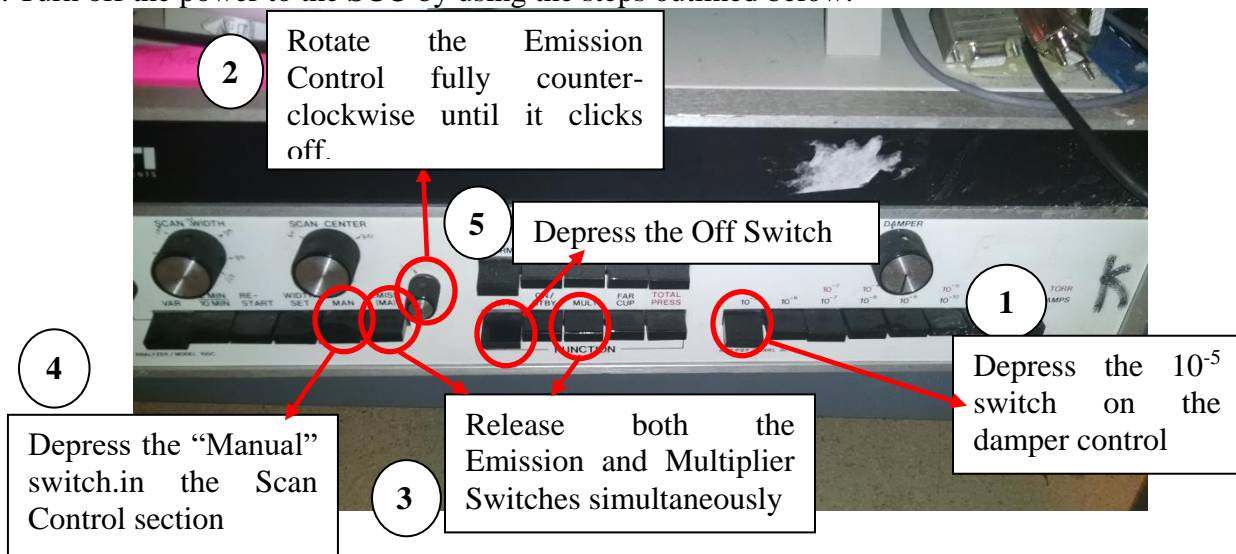
Figure B-6 QCM panel.

13. Turn off the oscilloscope by pressing its power switch.
14. Finish the logbook.

C. Langmuir Probe Operation Procedure

C.1. Emergency Shutdown Procedures

I. In case of an emergency overpressure situation in the plasma etcher

1. Stop any current scans using the Hiden ESPsoft software: STOP SCAN
2. If necessary, pull the probe tip out of the etcher main chamber and back it's housing unit by homing the z-stage: Probe → Home ZStage.
3. Exit the Hiden ESPsoft program: File → Exit.
4. Turn off the Langmuir probe electronics by pressing the "OFF" switches on the front panels of both electronics units.

II. In case probe has been driven into the closed gate valve

1. Immediately stop the motor of the z-stage by pressing "Cancel" on the "Probe Positioning" window of the ESPsoft software.
2. Home the z-stage.
3. At this point, the Langmuir probe housing will need to be disassembled off the etcher system in order to assess damage to the probe.

C.2. Schematics

The Hiden Analytical Langmuir Probe system consists of the following components:
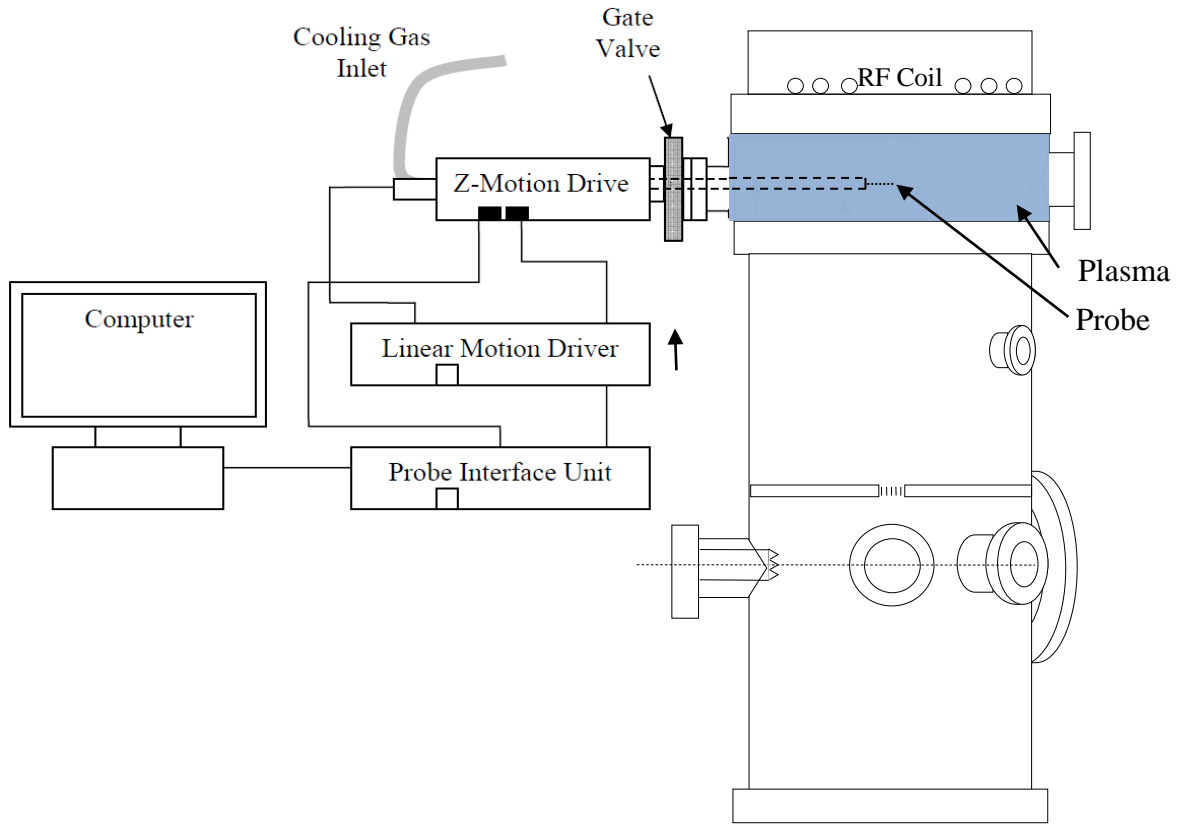
Figure C-1 Schematic of Langmuir Probe System and ICP chamber connection.

C.3. Operating Procedures

I. Install Langmuir probe into upper ICP chamber

This section details how to install probe into chamber.

1. Replace the window in upper chamber with Langmuir Probe:

   Prepare the adaptor, gate valve, Cu gasket, nuts, bolts and screws beforehand, calculate the length of the bolt for each adaptor and valve. The following is the necessary component for the connection:

Component	Quantity	Component	Quantity	Component	Quantity
Adaptor 4 5/8"	1	Nuts 2 3/4"	6	Cu gasket 2 3/4"	3
Extension 2 3/4"	1	Nuts 1 5/8"	10	Cu gasket 4 5/8"	1
Gate Valve	1	Nuts 2"	6		
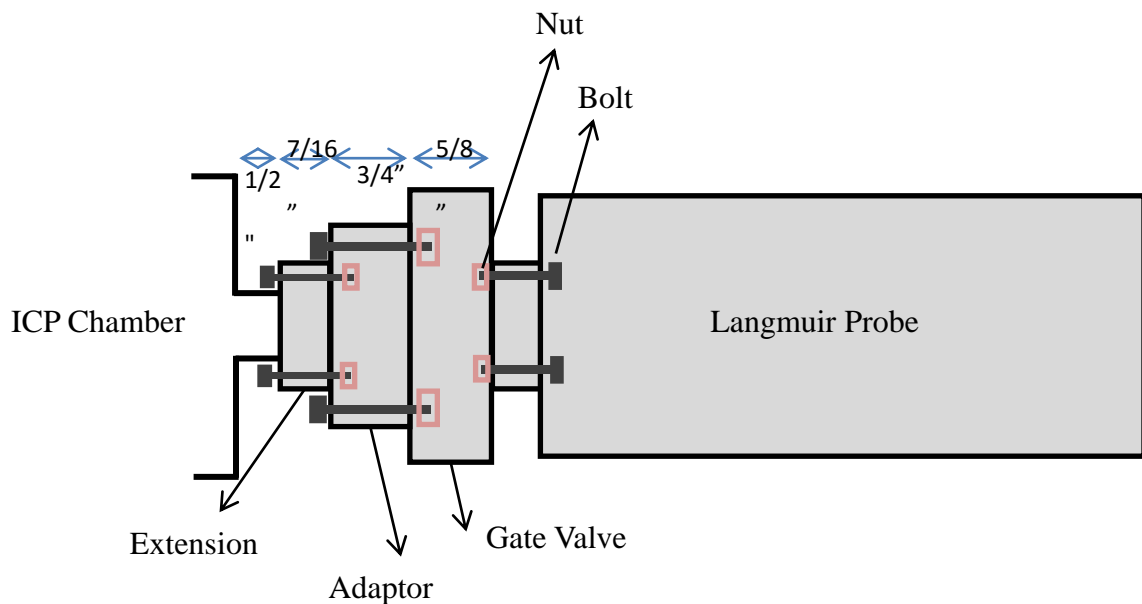
Figure C-2 Schematic of Langmuir Probe System showing connection of components.

2. Find a stand to support the Langmuir probe main body.

II. Probe Operation and Data Collection

This section details how to set up and perform scans for plasma analysis.

1. Check that the etcher system is at base pressure. Then slowly open the Langmuir probe gate valve. If the Langmuir probe housing has been isolated for a long time, a significant amount of gas may have accumulated in the Langmuir probe bellow and the pressure in the chamber will rise once the gate valve seal has been cracked open. Slowly opening the valve will help protect the etcher main chamber turbo pump.

2. Turn on the Langmuir probe and z-drive electronics units and warm up for 30 minutes before acquiring data.

3. Open the ESP soft program on the diagnostics computer.
4. With the gate valve is open, advance the probe into the main chamber by selecting Probe → Z-Stage, then entering the desired insertion distance (in cm) in the Park position prompt, then selecting "Move Now" and "Ok". (parking the probe tip at the center of the main chamber requires a position of 26-27 cm)
5. Set the desired parameters for acquisition by selecting Probe → Edit, and then inputting all desired parameters.
6. Once a plasma is struck, data can be acquired by selecting Probe → Run, then entering the amount of acquisitions, naming the file, and selecting "Start".

III. Probe Tip Replacement

This section details how to uninstall the Langmuir probe from the vacuum chamber and replace the probe tip

1. Home the z-drive and close the manual gate valve connecting the Langmuir probe house from the main chamber.
2. Remove screws holding the outer housing to the z-drive chassis, then take off the outer housing.
3. Disconnect the cables connecting the back end of the 2 ¾" CF flange (the end that the probe is attached to on the inside), then, while holding the flange (and probe) in place, remove the bolts connecting the CF flange to the bellow valve.
4. While *carefully* and *firmly* holding the bellow valve in place with one hand, and holding the CF flange/probe in the other, advance the z-drive forward in small (~2 cm) increments until the probe can be safely removed from the bellow. It is *very important* to secure the bellow valve while doing this as when it is compressed it   want to spring out sideways! Allowing this to happen could damage the fragile bellow weldings and cause a leak.
5. Replace the probe tip using gloves and clean tongs.
6. To replace the probe, follow this procedure in reverse order, making sure to hold the probe steady while retracting the z-stage. Colliding the probe tip with the bellow while retracting could damage the new tip!
7. Once the probe CF flange is reattached to the bellow and the housing cover is replaced, the bellow volume will have to be opened to the etcher while it is isolated from all turbopumps in order to protect them (remember the bellow volume will be at atmospheric pressure!).
8. Rough pump the chamber and then pump down with the turbopump, as instructed in the etcher system operation procedures.

IV. Troubleshooting

This section details major problems occurring on the Langmuir probe and the steps taken to fix them.

Spring 2007:

It was found that some plasma conditions (e.g. BCl3-containing chemistries) lead to rapid degradation of the collected current. This is due to deposition on the probe tip while it is idle. In order to avoid deposition on the tip and prolong the lifetime of each probe tip, the following procedures are suggested:

a. Always keep the Langmuir probe retracted into the housing with the gate valve closed for any experiments that do not require data acquisition using the Langmuir probe.
b. Keep experiments as short as possible whenever the Langmuir probe is in use(this applies to all plasma conditions!)
c. If a potentially depositing plasma chemistry will be in use, always set the "Idle Park Potential" of probe (in the Probe → Edit menu) to a high negative voltage (~-80 V) right before striking

plasma, and return the idle park potential to 0 V once the plasma has been turned off. This will induce ion bombardment of the probe with the plasma on which will prevent a deposition layer from developing.

d. In addition, in the Probe → Edit menu, turn on the automatic cleaning during for data acquisition in depositing plasmas by selecting the checkbox next to "Automatic Cleaning On" as well as "20 ms clean/5 ms data acq.", and set the "Cleaning *Potential" to a high negative voltage (~ -80 V).*

D. Optical Emission Spectrometer Operation Procedures

D.1 Emergency Shutdown Procedures

    1. Stop the program, and no further shutdown procedure is required.

    2. The modules needed to be moved are optical fibers and the S2000 module where the fibers are attached.

    3. The ADC1000-USB module is used for the computer on the ECR etcher (or other computers with the software properly installed if needed).

From within the software, selecting File → Exit will shutdown the program.
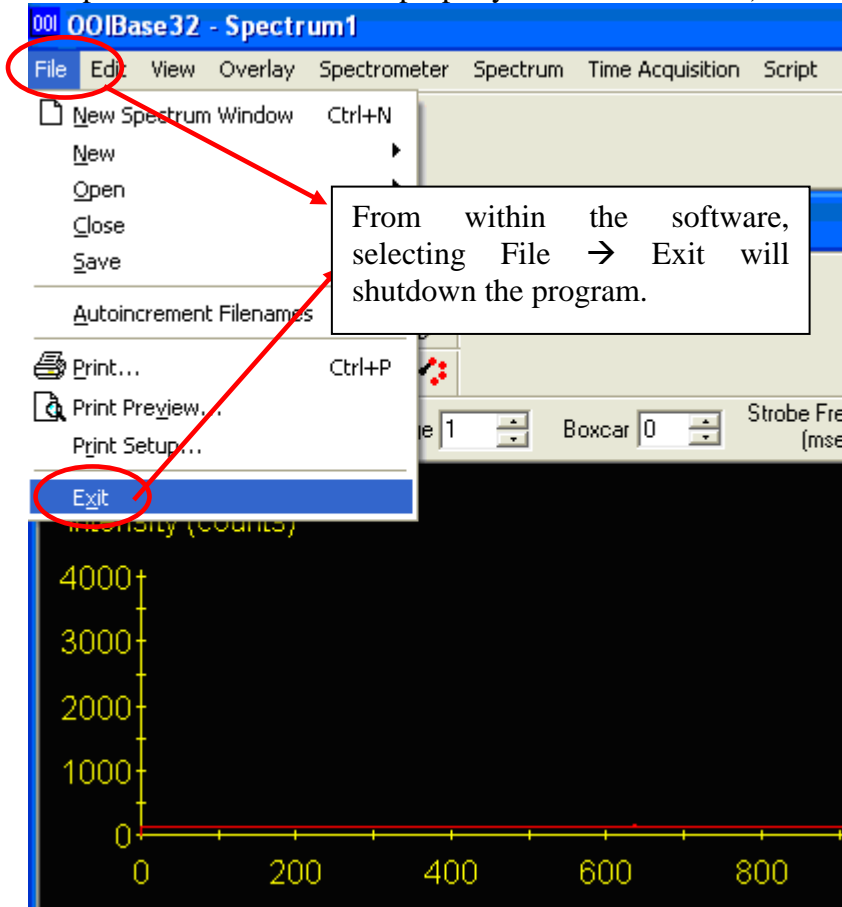
Figure D-1 OES operating software.

D.2. Schematic

The Ocean Optics S2000 System consists of 5 fiber optic cables (Labeled Master, Slave 1-4) connected to an analyzer which interfaces with a computer workstation so that data can be collected. The fiber optic cables are attached to a viewport in the ECR reactor through a machined cover held in place by screws
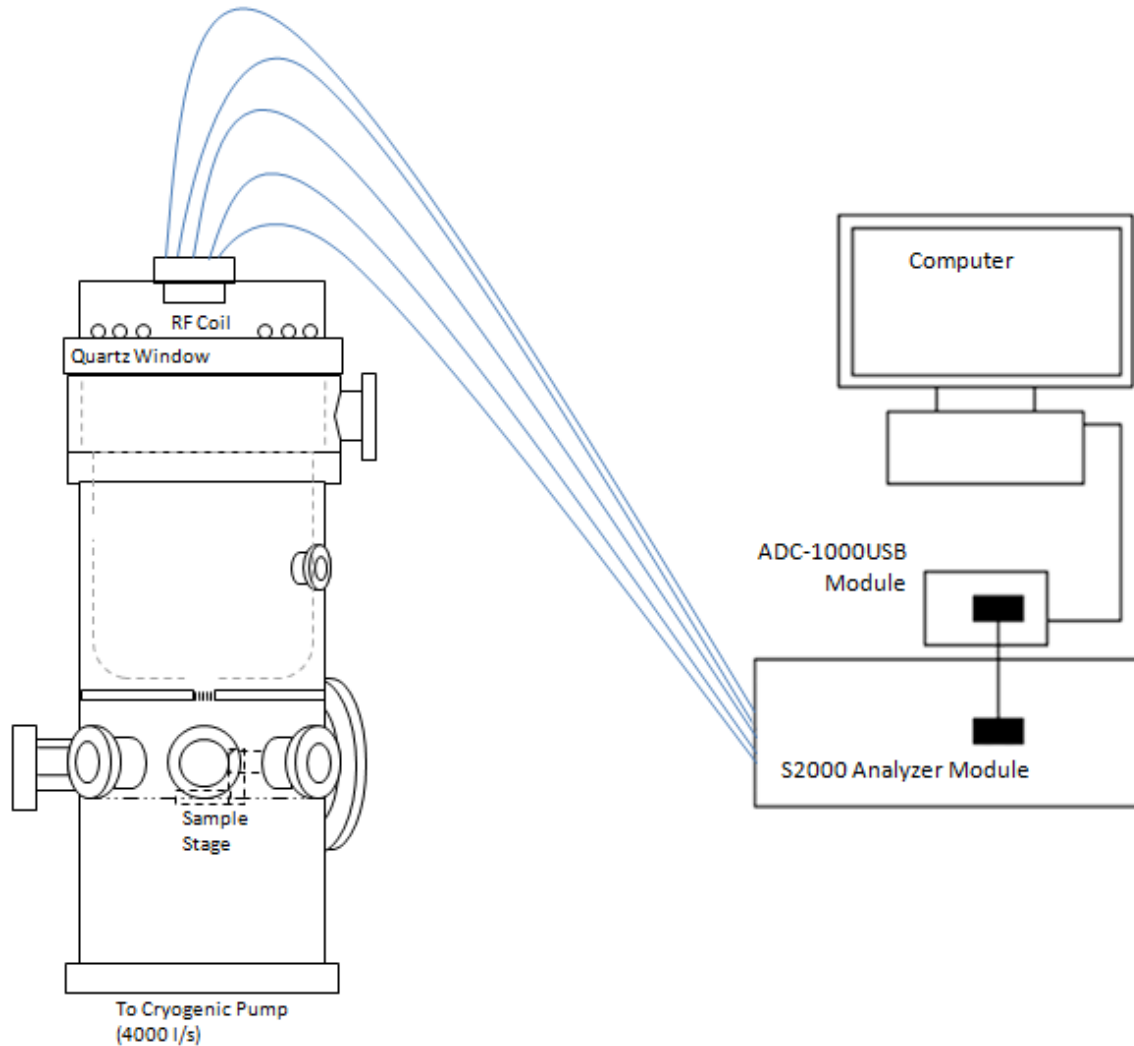
Figure D-2 Schematic of Optical Emission Spectrometer showing connection of components.

D.3. Safety and Operating Procedures

1. Have Optical fiber and cable connections ready
      i. One end of the fiber points to the light source (plasma)
      ii. The other side of the fiber plugged into the S2000 module.
      iii. S2000 module connects to ADC1000-USB (S/N ADUD6666) converter
      iv. USB cable goes from ADC1000-USB to the computer USB port
2. Start the OOIBase 32 program
3. Load the configuration file:
      a.   Go to Spectrometer → Open Configuration
      b.   Load c:\Program Files\Ocean Optics\OOIBase32\Default.spec
4. Enable channels:
      a. Go to Spectrometer → Configure
      b. Select Wavelength Calibration → Spectrometer Channel
      c.   For Master, Slave 1, Slave 2, Slave 3, and Slave 4: check Channel Enabled Box.
      d.   Click OK

5. Set proper integration time and time of average required.

D.4. Wavelength Calibration Settings:

These calibrations are set in the *.spec, the file that currently loads properly is located in Jerry's directory in the main Ocean Optics\OES folder.
Settings for Each Channels

Channel	Coefficient	
Master	First Coefficient	0.09149
	Second Codfficient	-6.95276e-6
	Third Coefficient	8.21743e-11
	Intercept	195.774872
Slave 1	First Coefficient	0.08122
	Second Codfficient	-6.12735e-6
	Third Coefficient	-4.10603e-10
	Intercept	327.208588
Slave 2	First Coefficient	0.10891
	Second Codfficient	-9.05373e-6
	Third Coefficient	-3.54458e-10
	Intercept	437.932098
Slave 3	First Coefficient	0.16705
	Second Codfficient	-1.29450e-5
	Third Coefficient	-5.23387e-10
	Intercept	585.628601
Slave 4	First Coefficient	-015435
	Second Codfficient	-1.47189e-5
	Third Coefficient	-1.54958e-10
	Intercept	786.201172

E. X-ray Photoelectron Spectroscopy Operational Guidelines

E.1 Emergency Shutdown Procedures

1.   Make sure the transfer loading arm from the tube is all the way out of the XPS chamber and then close the gate valve to the transfer tube.
2.   Turn off X-ray source by pressing HV button (should be lit, light will turn off when pressed) and then STANDBY button (should be unlit, will light when pressed and OPER button to the right should become unlit). If there is time, wait for water to flow to cool the anode for ~ 1 minute and press COOLING ON button. Then, turn off the main power and chiller power.
3.   Turn off energy analyzer by turning off ESCA kV and power switches on boxes from bottom to top (lens, detector, control and display)
4.   Turn off software by pressing the Stop Expt/Kill Data switch until experiment stops.
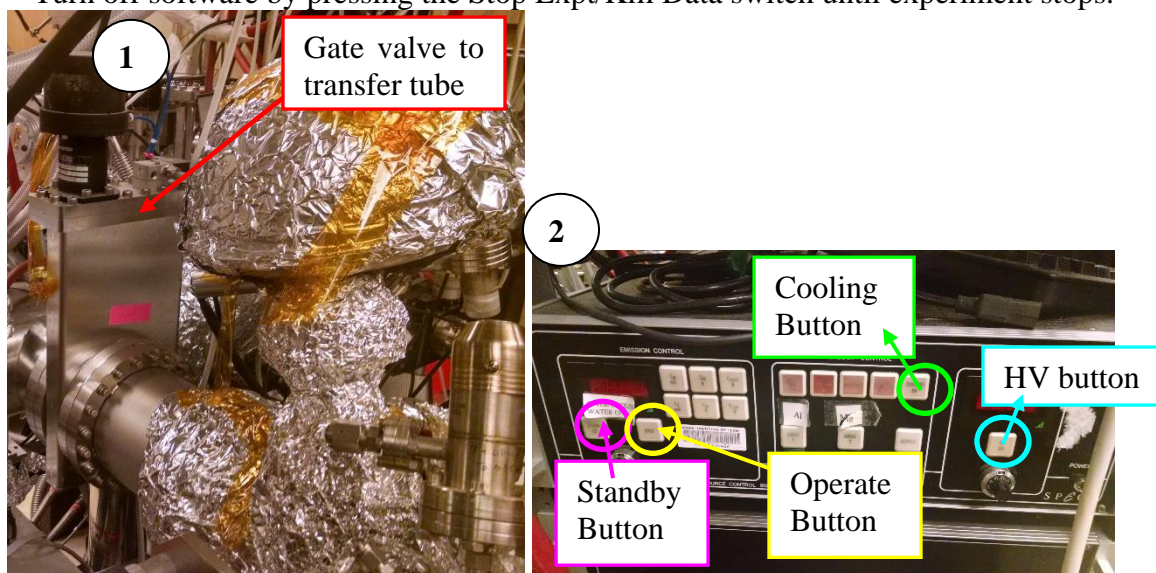
Figure E-1 XPS apparatus and control panel.
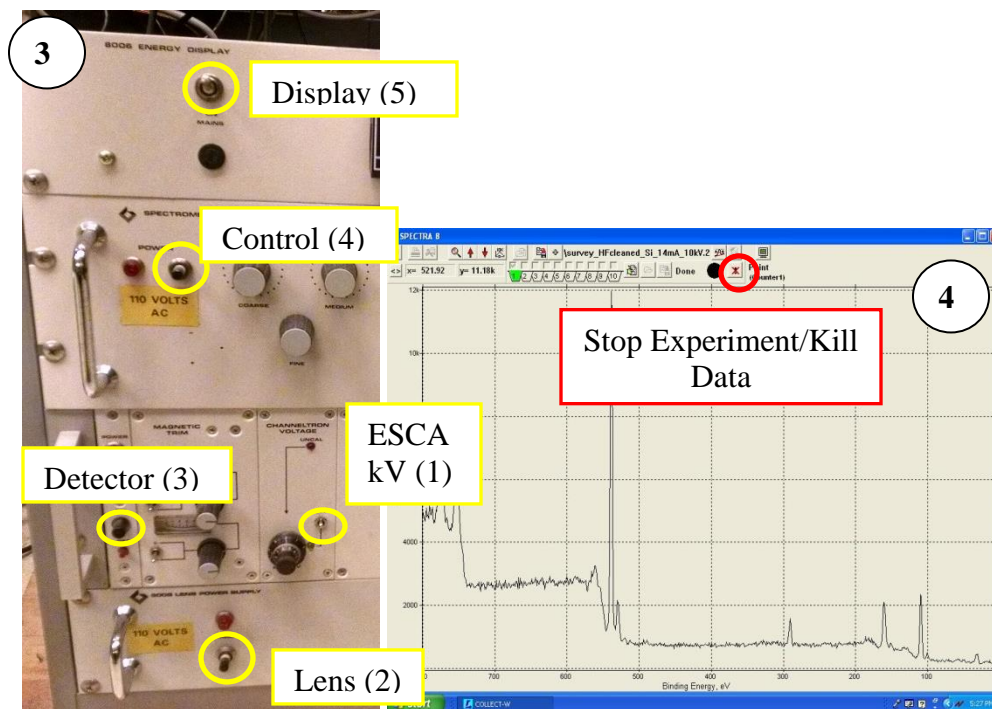
Figure E-2.

E.2. Safety and Operating Procedures

1. Before transferring the sample, make sure the x-ray gun is backed out to a setting of about 1.5 mm on the motion manipulator (~1 cm from the Teflon spacer). Move the sample stage towards the gate valve to a setting of 1-2 on the corresponding manipulator). Lower the stage to a setting of ~4 on the corresponding manipulator. Ensure the stage is vertical. Be careful as the stage rotates easily.
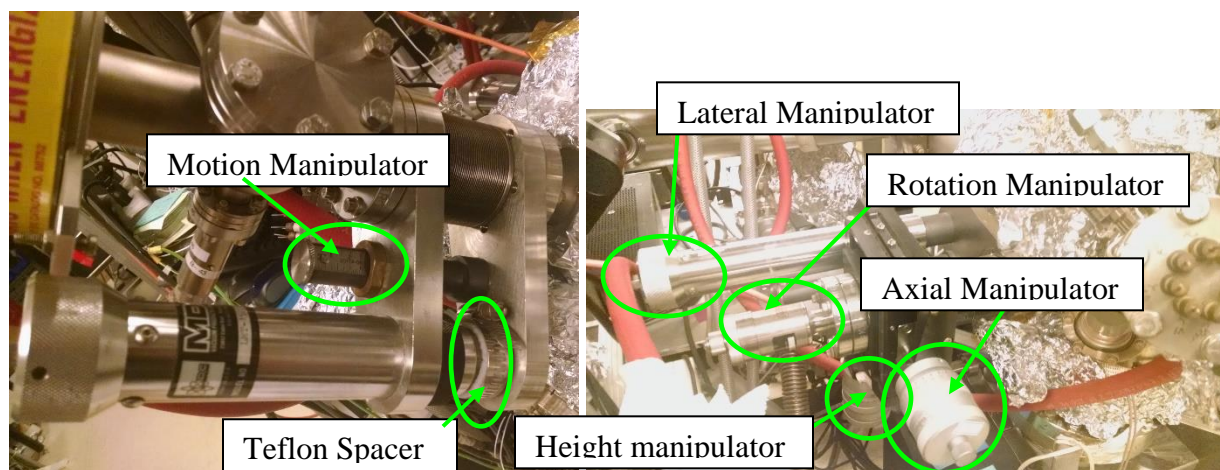
Figure E-3 Sample stage manipulator.

2. Check the pressure on the XPS using the ion gauge controller (base is ~1 x 10^{-9} Torr, but anything below 3 x 10^{-9} Torr is acceptable. If the pressure is above the 10^{-9} Torr range check the ion pump controller for current reading – should read ~$10^5 – 10^6$ A). Check the pressure on the TT using its ion gauge controller, pressure should be ~4 x 10^{-9} Torr (if it

242

is higher check that the gate valve between the cryo and the TT is open, if it is not, then open it using the controller box (trace the cable to be sure)). Once both pressures are in the requisite range open the gate valve between the TT and XPS using the corresponding controller box (trace the cable if unsure).

3.
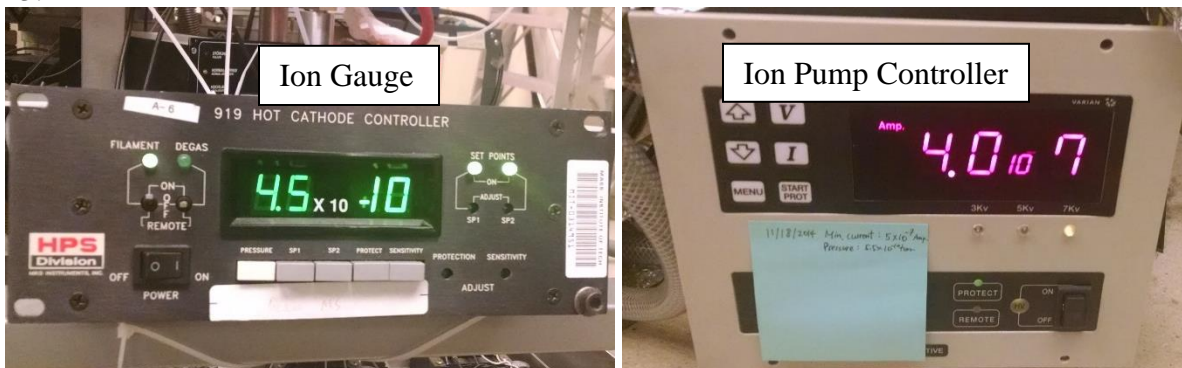
Figure E-4 XPS pressure gauge.

4. Slide the transfer arm into the tube slowly, checking the viewport occasionally to make sure that you do not collide with the stage or x-ray source. The manipulator settings on the arm should be X-setting = 5.5 (black) and Y-setting = 5 (black). Make sure the stage is aligned with the sample using the lateral manipulator (pictured in Step 1 on previous page). At this point you may have to raise the sample or lower the stage to provide the necessary vertical clearance. Lower the sample onto the stage. You may have to lower the loading arm to a Y-setting of 3-4 in order to remove the fork from the sample – slowly pull out the fork and after each small movement, increase the Y-setting slightly to avoid excessive straining. Retract the fork completely, being cautious to clear the transfer cart, and close the gate valve between the tube and the XPS.

5. Move the sample stage closer to the source and move source in until it is about 0.25 cm away from the Teflon spacer. Select the angle theta, which is the angle between the sample surface and the detector axis, using the rotational control - 240° corresponds to a 90° take off angle and 270° to a 60° take-off angle.

6. Move x-ray source closer if desired and adjust the stage position using the various manipulators until you are satisfied that the beam will illuminate the sample. Check the pressure in the XPS chamber – it should be at or below 3×10^{-9} Torr. Turn on the analyzer by turning on the switches labeled in the left picture below – from top to bottom: Display, Control, Detector, Lens, then ESCA kV. Turn on the x-ray source by pressing the power switch on the Control Unit. Press "Cooling On" (this should result in the button beginning to blink with a green light) and then turn on the NESLAB HX-75 Chiller (This should result in the green light becoming steady). Select an anode by pressing the corresponding button (selection will result in the button being illuminated by a green light). At this point none of the Interlock Buttons should be lit red. If they are seek assistance from a senior lab member or cautiously check all connections from electronics to the unit.
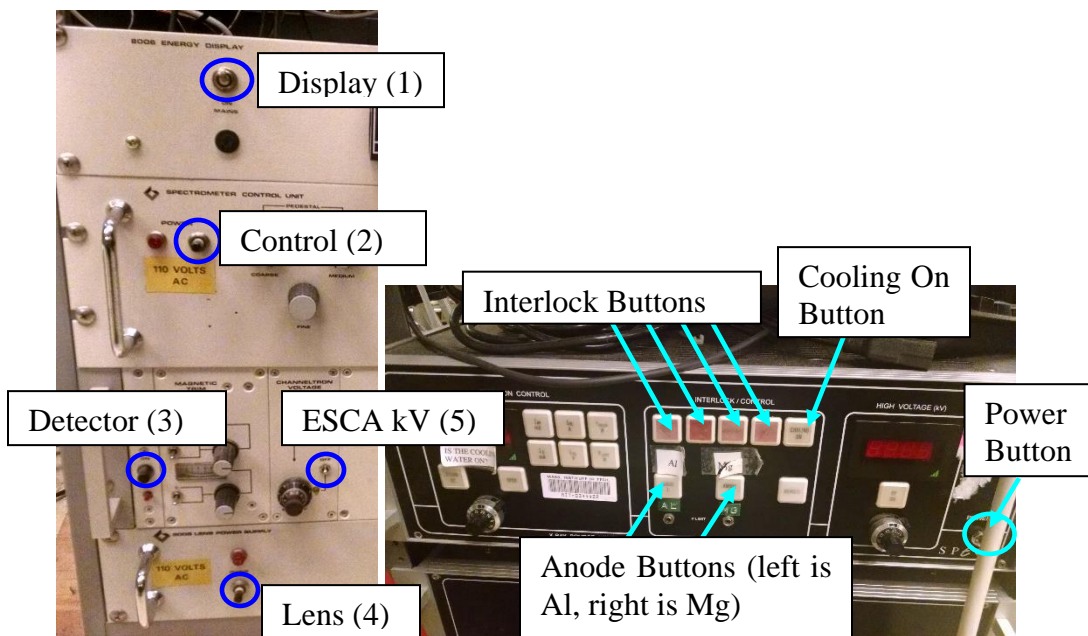
Figure E-5 XPS control panel.
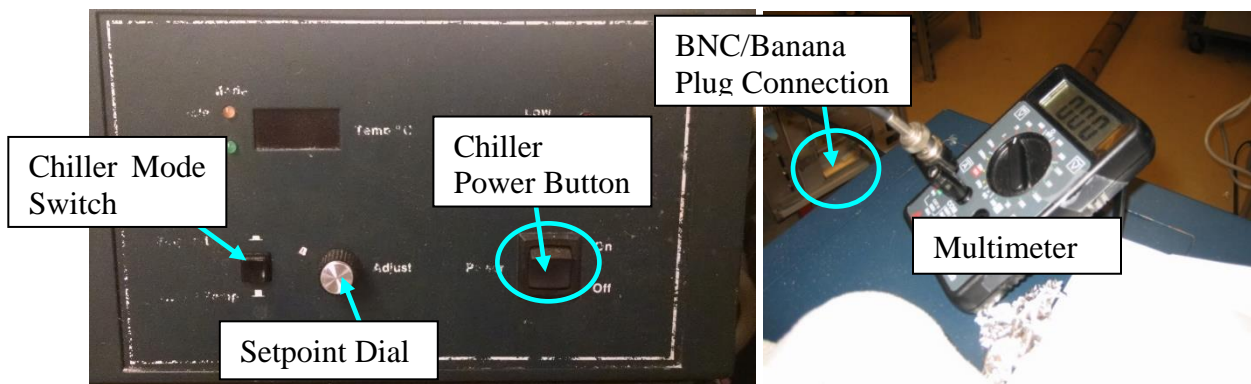
Figure E-6 XPS chiller control panel and grounding test by multimeter.

Check the chiller setpoint by pushing in the chiller mode switch. This should read 17 degrees. If it has changed adjust the setpoint dial while keeping the mode switch depressed. Check the flow rate by plugging in the BNC/Banana Plug connection to the multimeter. When set to measure DC Voltage the multimeter should give a reading of over 3.4 V. All the electronics to warm up for 10 minutes before running an experiment.

7. Launch the software program SPECTRA by double clicking the icon labeled SPECTRA in the center of the desktop. To save time before the experiment begins you can define your regions (survey, detailed, etc) by clicking the Edit Region Info Button. Also confirm that the software is configured for the anode you selected in Step 5, by clicking the Tools Button, then clicking "Setup Card" in the menu that pops up. In the dialogue box that

pops up you can select either Mg (1253.6 eV) or Al (1486.6 eV) in the Excitation field.
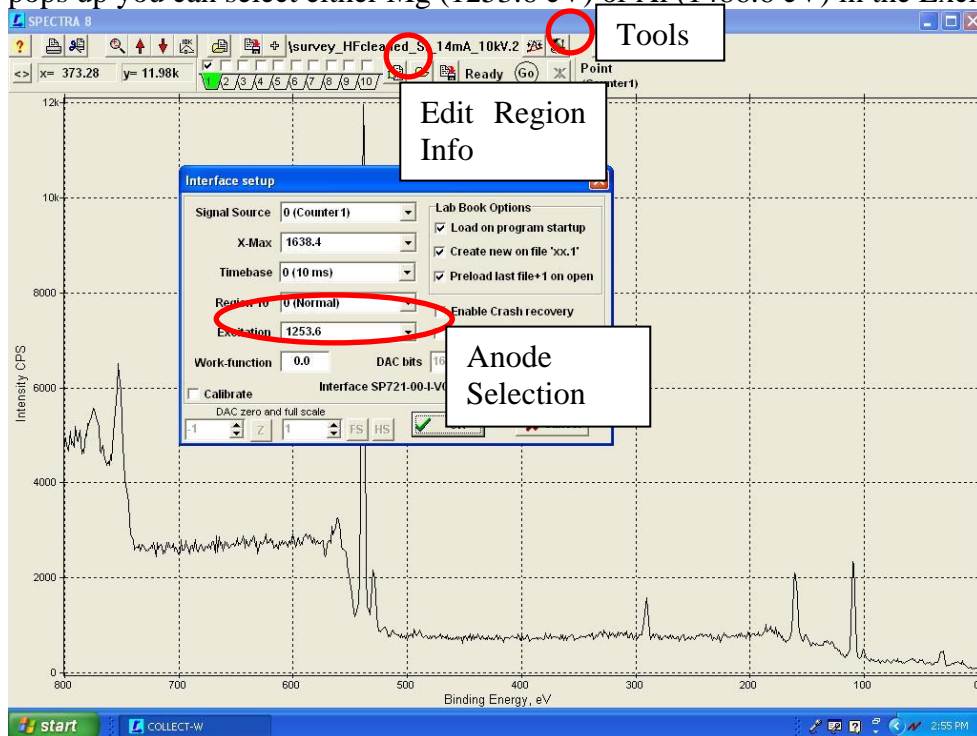
Figure E-8 Set up in the XPS software.

8. Once the electronics have warmed up, check that the Spectrometer Control Unit is set to COMP mode and that the Energy Selector corresponds to the Binding Energy (BE) of the anode you selected earlier in Step 5.

Figure E-9 XPS control panel.

9. Press the "I$_{FIL}$" button on the X-Ray Souce Control Unit, which should light up green. Press the "Stand By" button (display should change to 2.91 A) and monitor the pressure in the chamber, which will rise to as high as 2 x 10^{-8} Torr, but should decrease quickly. When it has returned to 10^{-9} Torr, press the "HV on" button and adjust the dial so that the display reads ~4.00 – 5.00 kV. Monitor the pressure, which should still be in the 10^{-9} range (Note: These values are for Mg anode, Al may be higher). Press the "Oper" button,

245

the value of I_{FIL} should rise to ~ 3.6 A and the light should blink briefly before becoming steady again. Press the "I_E" button (should light up green) and use the left and right dials to gradually increase the I_E and HV values to the desired reading (14 mA for I_E and 10 kV for HV are standard, 18 mA for I_E and 12 kV are maximum for Mg anode, 14 kV can be used for Al anode). In the SPECTRA window press the circular button marked "Go" to the right of the Edit Regions Button.
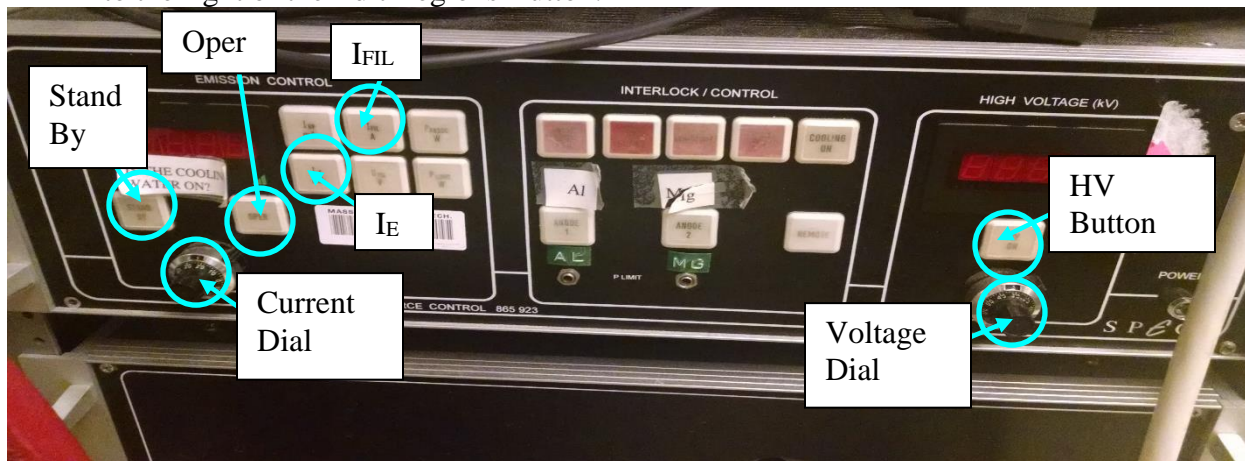
Figure E-10 XPS control panel.

10. Once the scans are finished, ramp down the HV and I_E values by turning down the dials slowly until they are at about 4 kV and 5 mA respectively, then Press "Oper" (the light should go off and the "Standby" button should light up. Press "HV" (the light should go off), then press "Standby" (the light should go off. If you are going to do more scans but the pressure has increased significantly over the course of your run, the system can be left in this state while it pumps down. If the pressure has not increased significantly, you can adjust the region info and then run more scans at your discretion without having to turn off the HV/I_E switches.

If you will not run anymore scans, leave the "Cooling On" button on to let the anode cool down for ~5-10 minutes. Press "Cooling On", then press the power switch. Turn off the chiller. Turn off the analyzer electronics by turning off ESCA kV first, then the boxes from bottom to top (in reverse order from Step 5). Remove your sample from the chamber if desired.

246

F. Spectroscopic Ellipsometer Operational Guidelines

F.1 Emergency Shutdown Procedures
1. Turn off the power of LPS-400 light source.
2. Shut off the circuit breaker of the power controller.

LPS-400 lamp housing/power supply

Light source power and ignition buttons

Circuit breaker of the power controller

Power button of the ellipsometer power supply
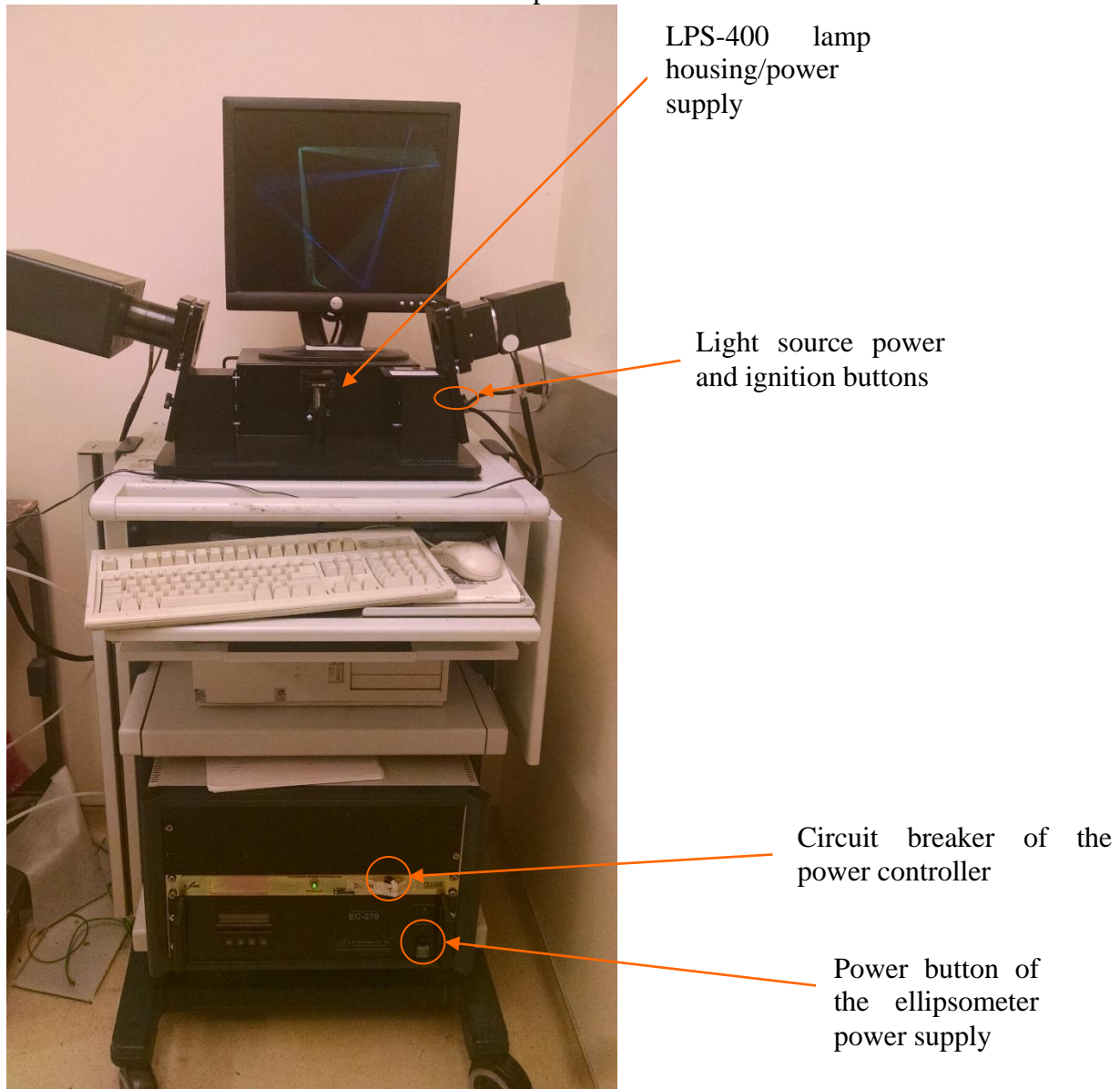
Figure F-1 Ellipsometer apparatus.

F.2. Safety and Operating Procedures

Turn-on procedure
1. Turn on the circuit breaker of the power controller.
2. Turn on the power of the ellipsometer power supply (Electronics Control Module EC-270).
3. Turn on the light source (LPS-400). Press "power" button, and wait a few seconds, then press "ignition" button.
4. Flip on the sign that reads "Lamp ON!"

Turn-off procedure
<For short time off>
1. Turn off the light source (LPS-400).
2. Flip on the sign that reads "Lamp OFF but Power ON!"

<For system off at the end of the day>
1. Turn off the light source (LPS-400).
2. Turn off the circuit breaker of the power controller.
3. Flip on the sign that reads "Power OFF!"

Do not leave the light source on for extended time periods.

F.3. Software Operation
1. Load the software (WVASE32).
2. Press "Window" on the menu bar, and select "Hardware".

   The "Hardware" window pops up, showing a message "Status:Hardware NOT Initialized"
3. Press "Initialize".

   You will hear motor-running sound from the ellipsometer.
4. Place your sample on the stage. Make sure the beam is hitting the area you want to probe.
5. Press "Align". The window for alignment will pop up. Your goal is to align the red cross to the center of the reference frame.
6. Adjust two tuning knobs underneath the sample stage until the red cross appears on the center of the reference frame.
7. Once alignment is done, press "Esc" key on the keyboard to exit the window.
8. Press "Ellipsometric data". A new window of "In-situ real-time scan" will appear.
9. Press "Acquire Single Scan". Data will be collected. It takes only a second.
10. To see the graphical results, press "Window" to select "Graph".

   It will show Ψ and Δ.

   You can see other parameters (such as $\varepsilon_1,\ \varepsilon_2$, $n,\ k,$ etc.) by pressing "Type" and selecting the parameter you want to see.

To estimate layer thickness (Sequence: choose a model → fit the data)
1. Choose a model
   1) Press "Window" and select "Model".
   2) Press "Addlayer" and select a proper material file (*.mat) for substrate.

      You can set substrate thickness to 1 mm. Contact Woolam if the material you are interested in is not in the data base.
   3) Press "Addlayer" and select a proper material file (*.mat) for each layer.

248

1. For files containing *n* and *k* data (tabulated-layer file), the initial layer thickness should be reasonably close to the actual thickness. Check the "Fit" box, and press "OK".
2. For functional files, you can fit other coefficients as well as layer thickness by checking the "Fit" boxes.

Recommended material-data file (*.mat):   Files are located in C:\wvase32\mat\ Examples:

- Si: SI_JELL.mat (*n,k* data)
- SiO$_2$: Sio2.mat (*n,k* data)
- HfO$_2$: \mat\dielectr\Hfo2.mat (*n,k* data) or Hfo2_c.mat (Cauchy fit)
- ZrO$_2$: \ mat\dielectr\ Zro2_c.mat (Cauchy fit)
- Y$_2$O$_3$: \mat\dielectr\y2o3.mat (*n,k* data)
- SiC: \mat\semicond\sic.mat (*n,k* data)
- AlN: aln_final_nk.mat (*n,k* data) or aln_cauchy_final.mat (Cauchy fit)

2. Fit
   1) Press "Window" and select "Fit".
   2) Press "Normal fit" several time until the result value conversed.
3. Save the data
1)   Press "Experimental Data" window and go to "file" to save the data.
2)   Press "Generated Data" window and go to "file" to save the data.

F.4. Hardware Calibration Procedure

1. Place a sample on the stage and align it.
2. Load the software (WVASE32).
3. window → hardware → calibrate
4. You will see a dialog box "Calibration Mode" with five selections, which are;
   a. Normal
   b. Coarse
   c. Detector electronics (off sample)
   d. Detector system (straight-through configuration)
   e. Detector system (with calibration sample)
- "Normal" or "coarse" calibration can be performed every time the system is turned on and the data acquisition is to be carried out. However, it is not necessary to perform it unless you suspect the system is not working correctly.
- "Detector system (straight-through configuration)" calibration must be performed only once, when the instrument is first set up, and does not need to be performed every time the instrument is turned on. To perform it, please see the manufacturer's manual.
5. For routine calibration, choose "normal" or 'coarse" calibration, and press "OK"
6. To see the graph: window → graph

F.5. Installation of Compensator

Follow the manual for the JA Woollam Manual Retarder to remove the input module and install compensator in between the base and the input.

Figure F-2 Sample stage, light source and compensator of ellipsometer .

A Si wafer with a medium thickness SiO_2 film ~260 Å should be used for calibration.
9/7/04

After the Retarder is set to "IN", be careful not to turn X and Y screws too far or they will come out and the compensator must be reassembled.

The screws should be adjusted so Psi lines up exactly and the Delta model should be shifted lower than the experimental value by 40-90deg.

Problems: On Step 10 in the manual for the JA Woollam Manual Retarder, when doing the Detector System Calibration (Calibration Sample), it finished acquiring the data. Then at Channel #87 an Error Message appeared "Error bars on calibration parameters exceed suggested limits. Verify instrument is operating properly and then repeat the straight through calibration procedure."

Solution: Increased error tolerances in the "mmx-cal.cnf" file in the WVASE32 folder. Repeated Step 10. The calibration finished. Entered delta offsets in the "hardware.cnf" file according to the manual.In "Ellipsometric Data", the High Accuracy Mode option needs to be checked.Took data on several SiC and Si samples. Much cleaner data. Better fit. Delta is much smoother, near 90deg. Unsure if it is still very accurate for SiC…

9/29/04

Problem: Tried to measure SiC samples. Delta for the model was extremely noisy for all samples and would not fit the data.

Solution: Tried to repeat Steps 10,11. No Change.

Repeating entire calibration procedure.

Performed normal calibration (out)
Acquired dynamic data (in) and aligned psi and offset delta.
Guessed delta offset parameters in Model Options
Performed Detector System Calibration (with Calibration Sample)

$$DelOff1 = 78.014$$
$$DelOff2 = -1.9517e-2$$

F.6. Replacement of Protection Device

On March 11, 2005 the WVASE 32 program would not load. When clicking on the WVASE 32 icon on the desktop, the message "Protection Device Not Found!" was given. After contacting J.A. Woollam (phone # (402) 477-7501) and speaking to Ping He, it was determined that the protection device plugged into one of the parallel ports in the back of the computer was no longer working. J.A. Woollam sent us a replacement protection device, and the WVASE 32 program is now working.

G. Transfer Tube

G.1 Emergency Shutdown Procedures

1. Ensure that all transfer arms are in the fully withdrawn position (i.e. they are not extended into any reactor chambers).
2. Close all electrically operated gate valves on the system using the control boxes located on the transfer tube table. (In the event of a power outage, this should automatically happen). Visually inspect that this has taken place whenever possible by looking through the appropriate windows on the transfer tube. In the event that a manual gate valve is present, close it by hand.

Gate valves can be seen through these viewports

This switch closes the gate valve (trace power cable to gate valve to confirm).

Example of a manual gate valve
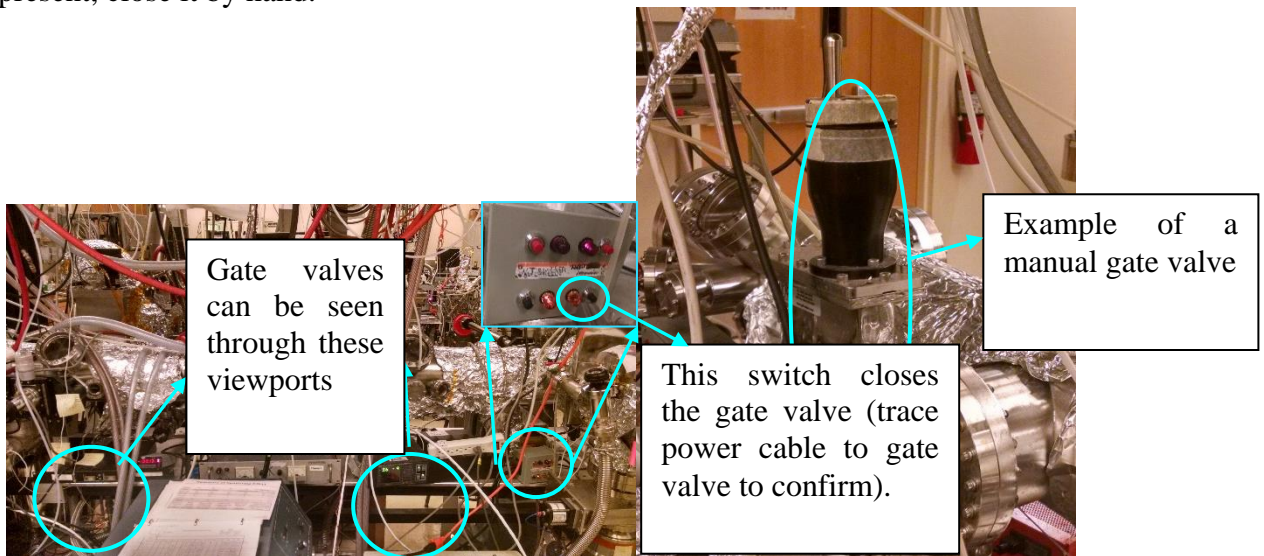
Figure G-1 Windows, gate valve and gate valve controller of transfer tube.

3. Press the stop button on all the turbo pump controllers (in the event of the power outage the controllers should all turn off).

Stop button (read label to confirm)

Figure G-2 Controller of TMP.

4. If power is still available, allow the turbo pumps 10-15 minutes to wind down and then close all the roughing valves between the turbo pumps and their backing mechanical pumps. In the event of power loss close these valves immediately.

Roughing valves between turbo (and cryo) pump and mechanical pump (trace flexible hoses to confirm)
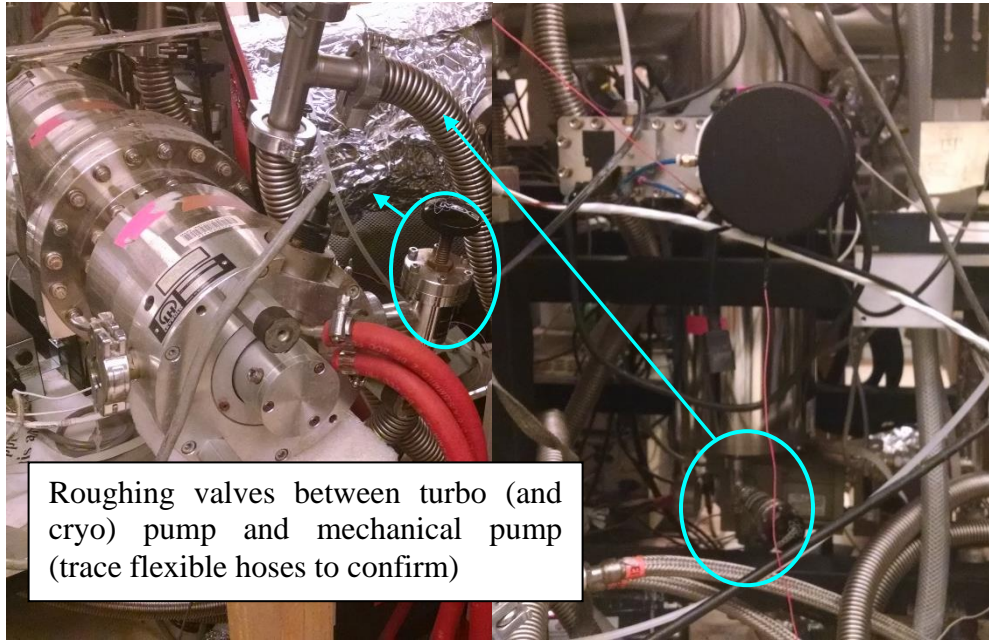
Figure G-3 Roughing valve of TMP and cryopump.

5. Use your discretion to turn off the mechanical pump on the tube, situated under the table.

Power switch for the pump is located on the pump itself, near the front.
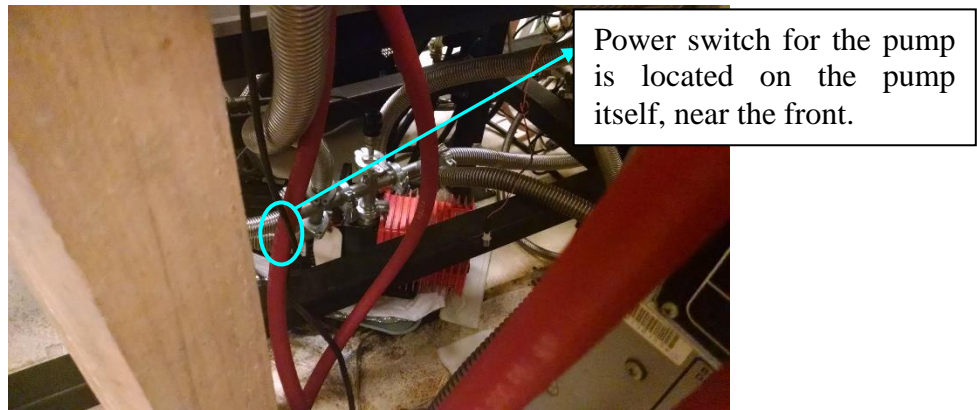
Figure G-4. Mechanical pump of TMP.

6. The pressure of the transfer tube is displayed on a readout/controller located on the tube table next to the loadlock (this controller monitors the loadlock and transfer tube pressure), facing the north side of the room. Monitor the pressure regularly.
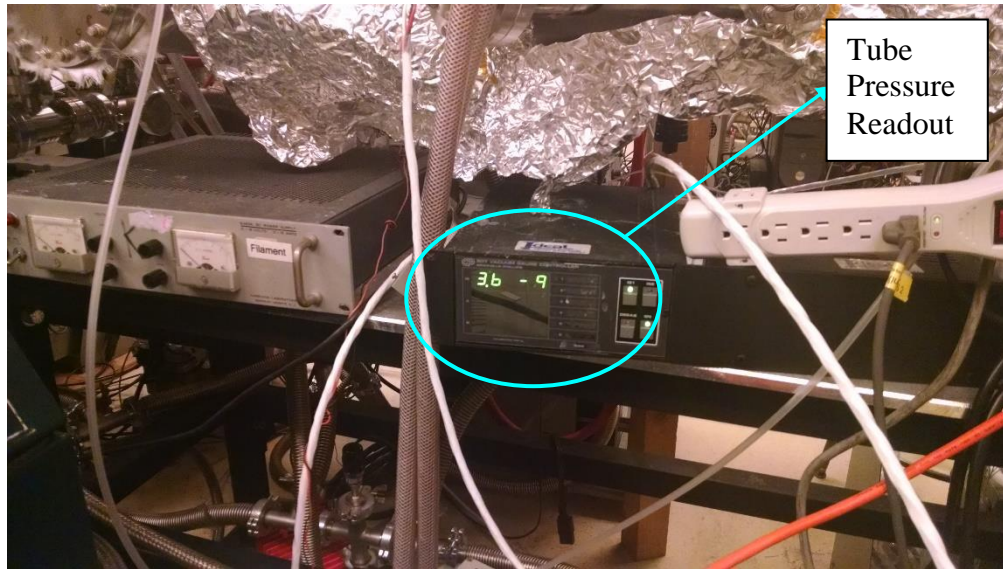
Figure G-5. Ion gauge of transfer tube system.

7. Double check that the gate valve above the cryopump is shut and the rough valve between the cryopump and the mechanical pump is closed (this should have been done in the previous steps). Turn off the CTI 9600 Compressor connected to the cryopump by flipping the white circuit breaker to the "off" position.
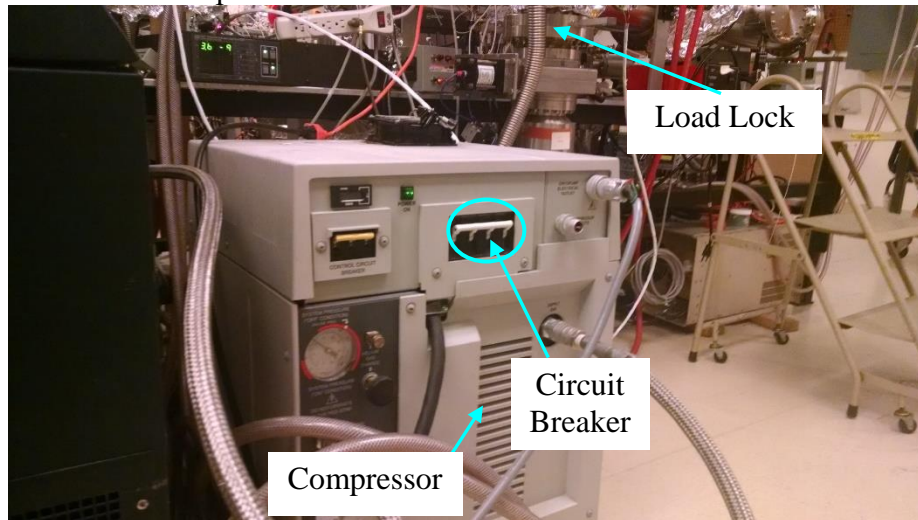
Figure G-6 Compressor of cryopumps.

G.2. Safety and Operating Procedures

Please refer to the following labeled picture when performing Steps 1 and 2.
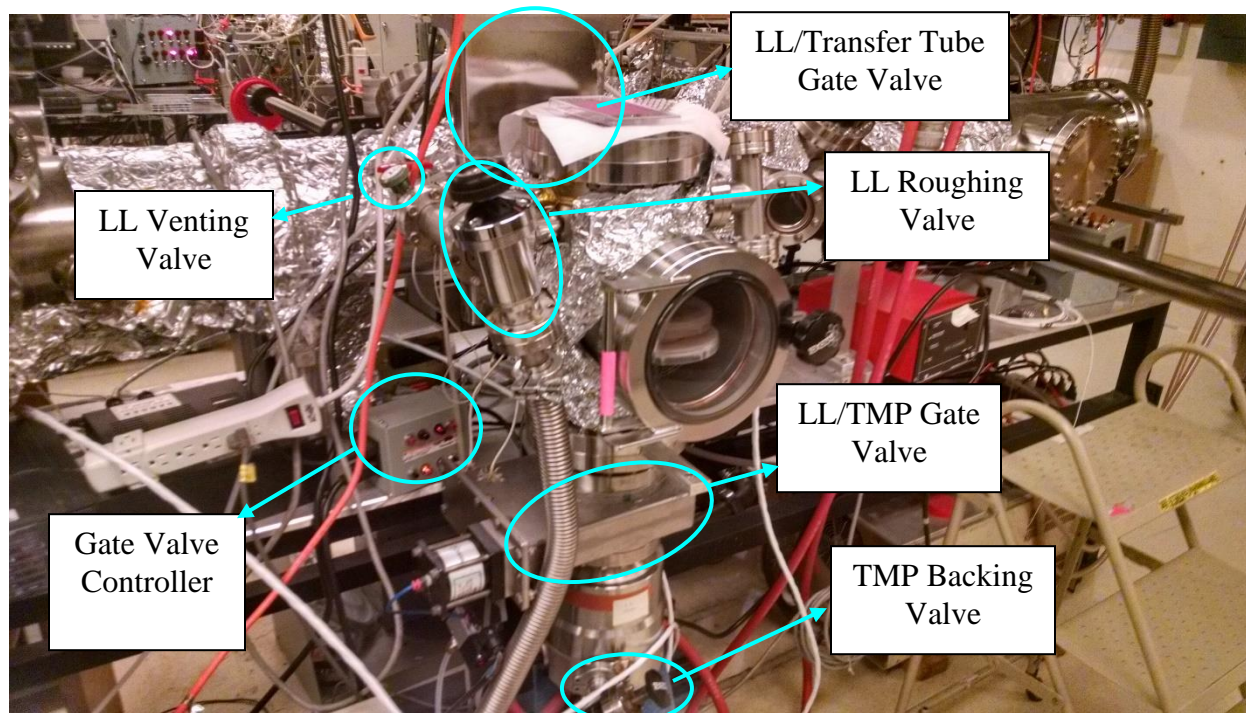
Figure G-7 Components of load lock.

1. To load a sample, the loadlock must first be vented. Ensure that the gate valve between the load lock and the transfer tube is CLOSED. Close the gate valve between the LL turbo and the LL. Ensure that the roughing valve between the LL and its mechanical pump is also closed. Vent the load lock by SLOWLY opening the green venting valve. Within a short time period the load lock door should open easily. Close the green venting valve. DO NOT UNDER ANY CIRCUMSTANCES OPEN THE GATE VALVE BETWEEN THE LL AND ITS TURBO WHILE THE LOAD LOCK IS VENTED! Place your sample holder on the pin holder inside of the load lock. If you used screws to secure your sample, ensure that the screws are facing you.

2. Close the LL door and slightly tighten the handle. Isolate the LL turbo pump and the TT turbo pump by closing the roughing valve between these pumps and their backing mechanical pump (trace the flexible hoses to confirm the pump identity). Open the roughing valve between the load lock and the mechanical pump while pressing in the door. Readjust the tightness of the screw handle, but do not overtighten. Verify that the LL is pumping down by checking the pressure on the thermocouple gauge attached to the mechanical pump. Note that the turbopumps can only be isolated for ~5 minutes. When the pressure has dropped to ~60 mTorr, close the roughing valve to the LL, unisolate the LL and TT turbo pumps and open the gate valve to the LL turbo. Monitor the pressure using the LL ion gauge.

3. When the pressure in the LL is ~5 x 10^{-6} Torr, sample transfer is possible. In this case the pressure in the tube should be ~10^{-8} Torr. (If the loadlock pressure is ~5 x 10^{-7} Torr, then the pressure in the tube can be ~10^{-9} Torr). Accomplish this by closing the TT/Cryopump gate valve, then monitoring the pressure using the ion gauge. When the pressures are at the requisite levels open the gate valve between the LL and the transfer tube. Check for pressure spikes using the TT ion gauge. If you are uncomfortable about transferring by yourself you may close the gate valve between the LL and its turbo pump to prevent samples from hitting the TMP if they fall.

4. Use the transfer arm to place the sample holder onto the cart (recommended settings are on the transfer arm, but exercise caution when carrying out this operation). Try to ensure that the tines

of the loading fork extend past the edge of the sample holder nearest to you. Also remember that the arm cannot be lifted to its maximum value if it is near the limit of its lateral extension. Make adjustment in small increments, consistently checking to ensure that nothing is strained. Retract the transfer arm completely and close the LL/TT gate valve.
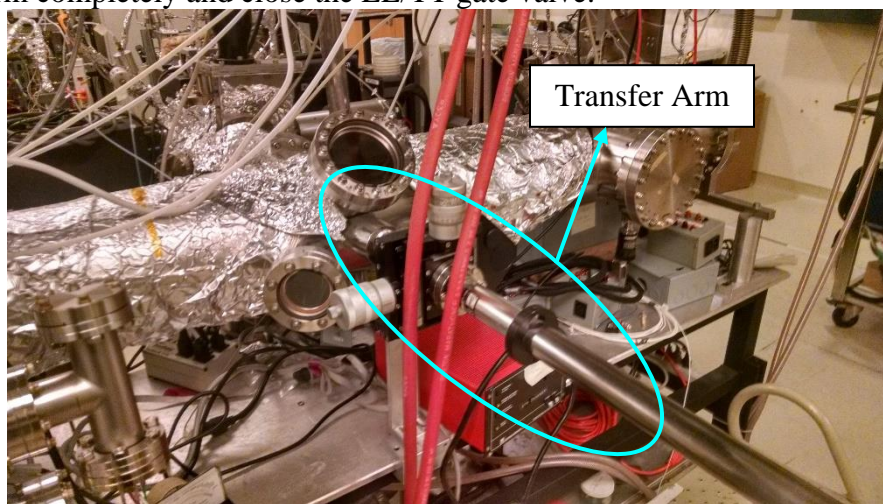
Figure G-8 Transfer arm on the transfer tube.

5. Use the motor control situated at the eastern end of the tube to move the cart to the desired chamber. If the cart is having problems moving, closing the gate valve between the tube and its turbo pump often rectifies this situation, as well as the gate valve between the tube and its cryopump. However, remember to reopen the valves after moving the cart into place. Once in place, close the gate valve between the transfer tube and its cryo pump, then open the gate valve to the transfer tube. Use the transfer arm to lift the sample holder off the cart and place it into the chamber. Retract the arm completely and then close the chamber/TT gate valve before reopening the TT/Cryopump gate valve.
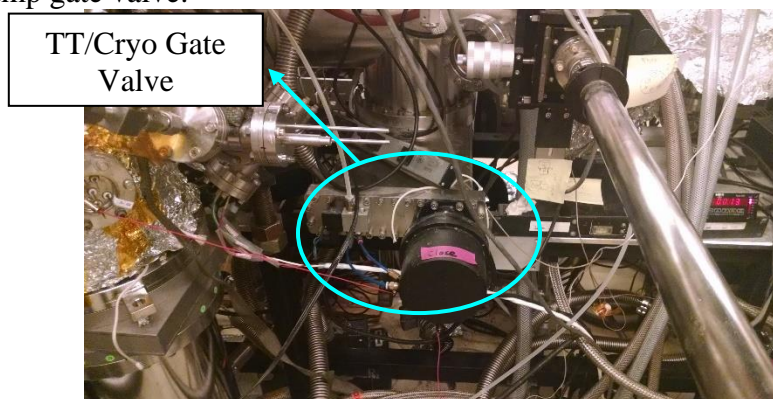
Figure G-9 Gate valve of cryopump to transfer tube.

6. To transfer samples from chambers to the transfer tube, first make sure the experiment has been fully halted (i.e. there is no gas flow, plasma, etc.) and that the chamber has been pumped down to its base pressure for ~15-30 minutes. Close the TT/Cryo gate valve first, then open the chamber/TT gate valve. Use the transfer arm to remove the sample from the chamber and place it into the transfer cart. Retract the transfer arm completely, close the chamber/TT gate valve and then reopen the TT/Cryo gate valve.

H. Vapor Etch Chamber
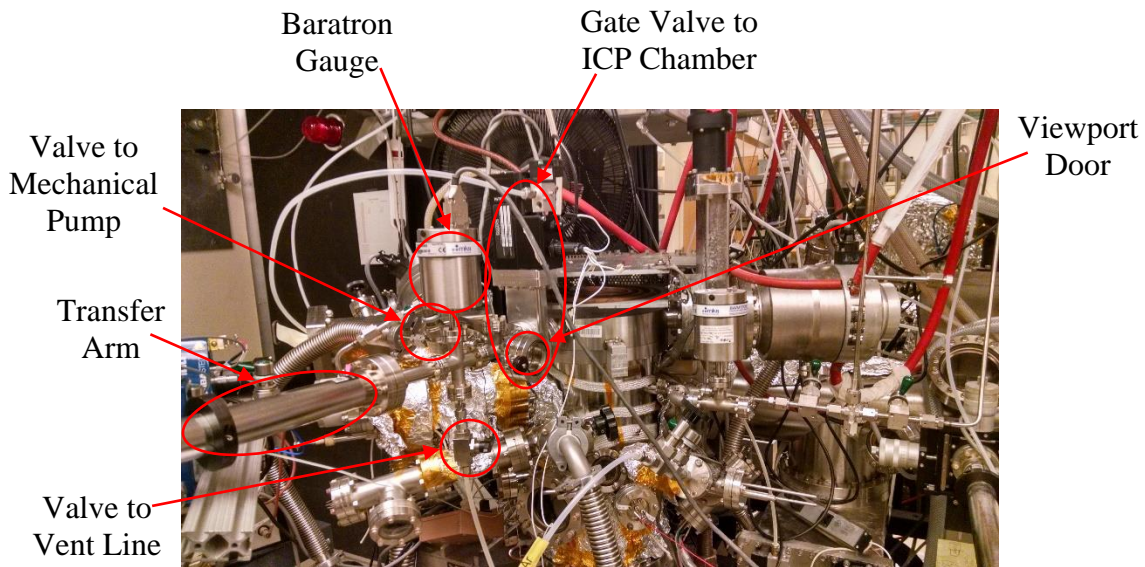
Figure H-1 Vapor Etch Chamber Components

Labels (Figure H-1):
- Baratron Gauge
- Gate Valve to ICP Chamber
- Valve to Mechanical Pump
- Viewport Door
- Transfer Arm
- Valve to Vent Line
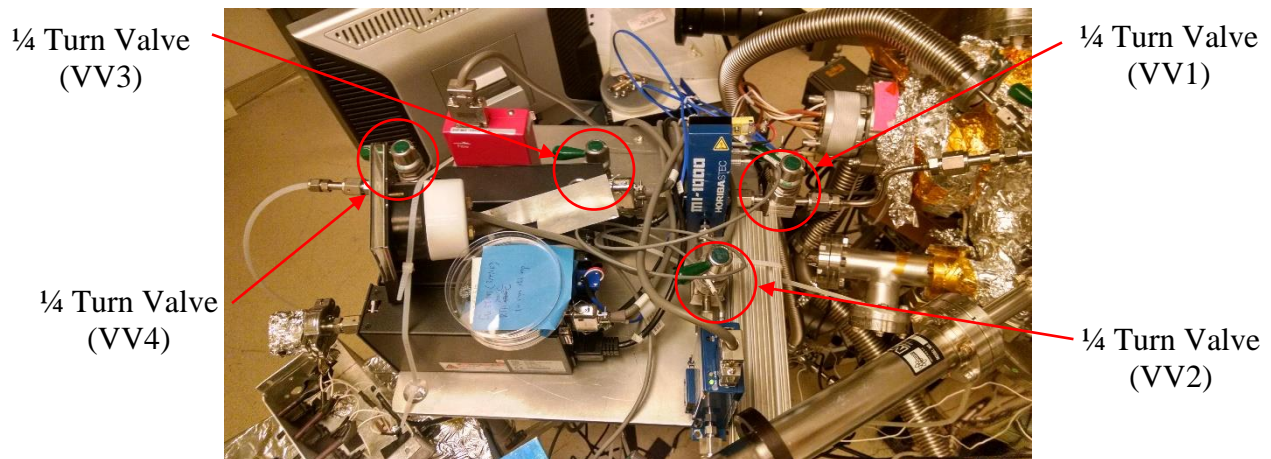
Figure H-2 Valve Layout for Vapor Delivery.

Labels (Figure H-2):
- ¼ Turn Valve (VV3)
- ¼ Turn Valve (VV1)
- ¼ Turn Valve (VV4)
- ¼ Turn Valve (VV2)

H.1. Emergency Shutdown Procedures

1. To Shut off the chamber in the event of an emergency:
   a. Turn off vaporizer heater.
   b. Close VV1.
   c. Unplug vaporizer heater, LFC controller, and MFC controller.

H.2. Operating Procedures

1. To load sample into vapor etch chamber:
   a. Check that gate valve to ICP chamber is in the closed position.
   b. Check that valve to mechanical pump is in the closed position.
   c. Loosen viewport door lock.

d. Open vent line valve until viewport door opens. Pressure gauge should read approx. 750 torr.
e. Attach sample to transfer arm with carbon tape.
f. Close viewport door.
b. To pump down vapor etch chamber:
a. Check that vent line valve is in the closed position.
b. Check that viewport door is closed and secured.
c. Open valve to mechanical pump slowly. Pressure should drop at approx. 10 mtorr/sec. until gauge reads approx. 30 torr.
c. To operate vapor delivery system
a. Check that VV2 is closed, allow LFC to fill.
b. Check that VV3 and VV4 are open. Thermocouple gauge should show a slight increase in pressure. Set MFC and check that it is holding at setpoint correctly.
c. Once MFC is flowing, open VV2 slowly. Set LFC and check that it is holding at setpoint correctly.
d. Check that flow is correct and vaporizer heater is set correctly. When ready, open VV1 slowly to expose sample to vapor.
d. To stop vapor delivery system
a. Close VV1.
b. Close MFC and LFC and turn off vaporizer heater.
e. To load sample from vapor chamber to ICP chamber
a. Open pneumatic gate valve and close mechanical pump valve immediately after. Pressure should read approx. 0.5 mtorr.
b. Insert arm into ICP chamber with sample facing vapor chamber viewport door.
c. Once the sample has reached the desired position within the ICP chamber, rotate the transfer arm such that the sample is facing down.
d. If the transfer arm is having clearance issues, the height of the transfer arm can be adjusted to compensate.

H.3. Schematics

Vapor Etch Chamber + ICP Chamber							
(a) Front View							
University of California, Los Angeles, Department of Chemical and Biomolecular Engineering							
Part		Material	Stainless steel				
Filename		Scale	Yes	Units	inch	Quantity	1
Designer	Jack Chen (UCLA)	Date	1/1/2015				
Revised by		Date					
Contractor		Date					
Comments			Tolerance			+/- .0001	

Vapor Etch Chamber + ICP Chamber

(b)

Side View

University of California, Los Angeles, Department of Chemical and Biomolecular Engineering							
Part		Material	Stainless steel				
Filename		Scale	Yes	Units	inch	Quantity	1
Designer	Jack Chen (UCLA)	Date	1/1/2015				
Revised by		Date					
Contractor		Date					
Comments			Tolerance			+/- .0001	

Vapor Etch Chamber + ICP Chamber

(c)

Side View

University of California, Los Angeles, Department of Chemical and Biomolecular Engineering							
Part		Material	Stainless steel				
Filename		Scale	Yes	Units	inch	Quantity	1
Designer	Jack Chen (UCLA)	Date	1/1/2015				
Revised by		Date					
Contractor		Date					
Comments			Tolerance			+/- .0001	

(d)	Vapor Etch Chamber + ICP Chamber						
	Isometric View						

University of California, Los Angeles, Department of Chemical and Biomolecular Engineering							
Part		Material	Stainless steel				
Filename		Scale	Yes	Units	inch	Quantity	1
Designer	Jack Chen (UCLA)	Date	1/1/2015				
Revised by		Date					
Contractor		Date					
Comments			Tolerance			+/- .0001	

Figure H-3 Schematics of Vapor Etch System Attached to ICP Chamber (a-d).

H.4. Vaporizer Info

Liquid phase etchant is first stored in a round bottom glass vial, ¾" in diameter which is attached to a 1.33" to ¼" VCR adapter for incorporation into the feed line. A metal tube protrudes into the glass vial as a channel for delivering the liquid phase etchant under reduced pressures to the liquid mass flow controller, a Horiba[TM] LF-F20M-A model fitted with 1/8" stainless steel Swagelok (capable of handling most corrosive chemicals except HCl and HF,

generally) and 1/8" Swagelok to ¼" VCR fittings for vacuum compatibility. This allows for metered feeding up to mass flow rates of 0.1 g/min of the liquid phase etchant at temperatures varying from 5-50°C into the vaporizing unit.
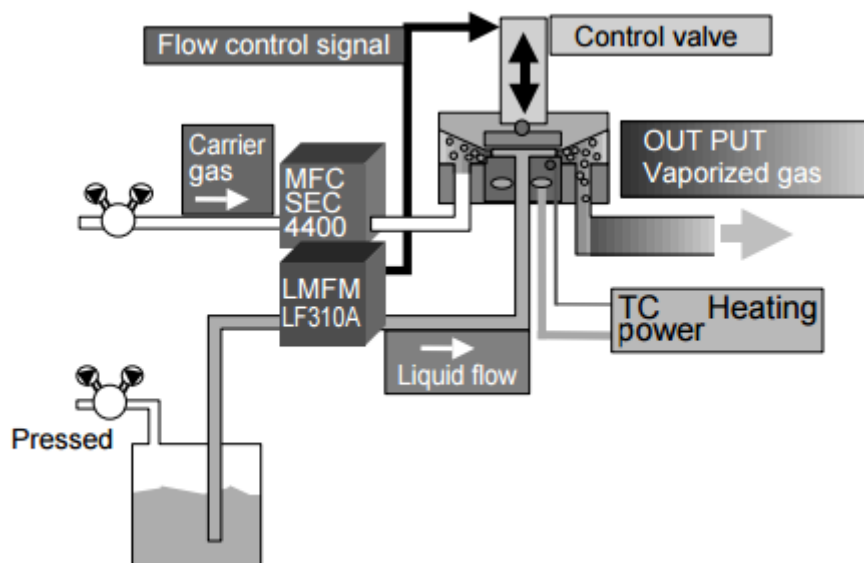
Figure H-4 Liquid injection method utilizing heating element to vaporize liquid flow and introduce to vacuum chamber (Image courtesy of STEC Inc)

To aid in the delivery of the vaporized gas output, an inert gas input is recommended as a secondary input to the vaporizer unit. For these studies, ultra-high purity N_2 will be used at flowrates controlled via a Horiba^{TM} SEC-E40 gas MFC with maximum flowrates of 100 sccm. This MFC contains two 1/4" VCR connections, eliminating any need for adapters between the N_2 MFC and vaporizer. With both of these MFC units connected to the M1-1141-PN, resulting vapor can be delivered at flowrates of up to 3cm^3/min (rated with ispropanol) at temperatures of up to 140°C. This delivery temperature is sufficient for complete vaporization of the organic chemicals of interest to the study.

I. Ion Source Chamber

PLEASE SEE ATTACHED DIAGRAM AT THE END OF THE EMERGENCY SHUT DOWN FOR LOCATION OF VALVES, GAS AND PUMPS, IF PICTURE IS NOT PROVIDED!

I.1 Troubleshooting

1. In case a noise is heard from turbo molecular pumps on Main Chamber
    a. Close manual gate valves between turbo pumps and chamber and the pneumatic gate valve between top turbo pump and ion gun.
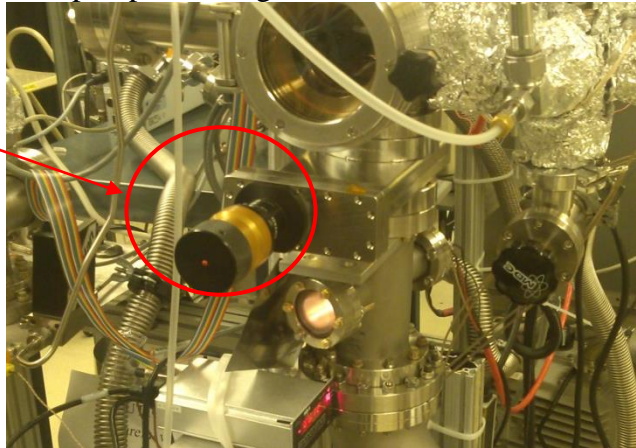
Manual Gate Valve
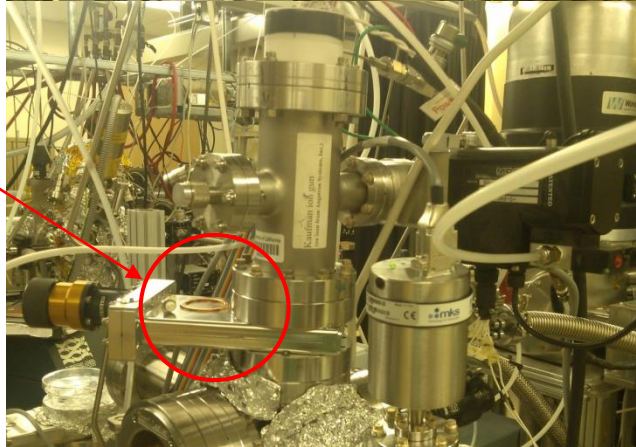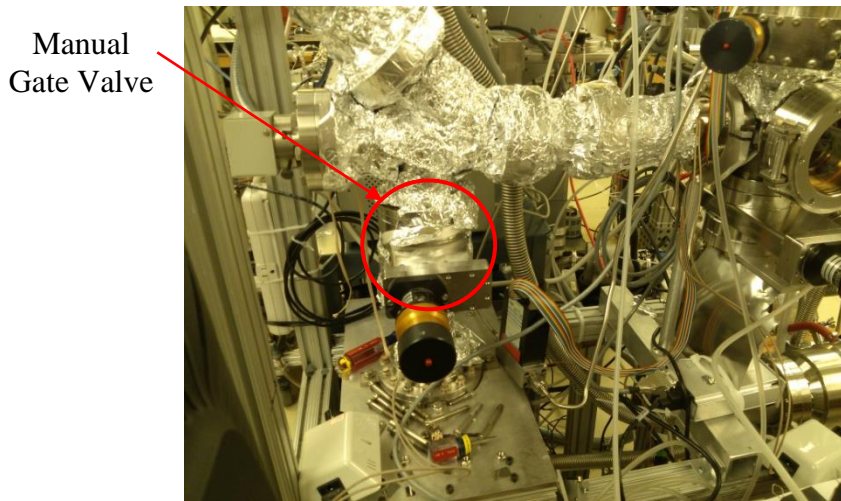
Figure I-1 Gate valves for turbo pumps.

b. Turn off the turbo molecular pumps by pushing the "stop" button on the two Leybold controllers and the "stand by" button on the Pfeiffer controller.

Stand By

Stop
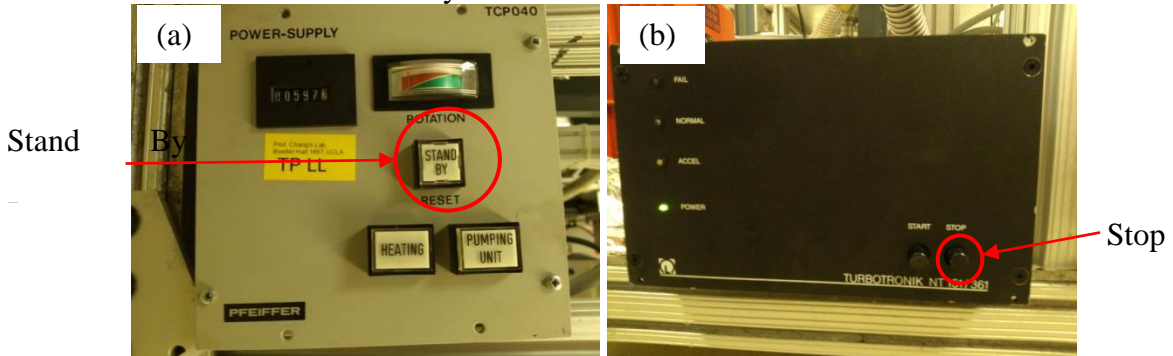
Figure I-2 (a) Leybold controller for bottom turbo pump and mass spectrometer turbo pump. (b) Pfeiffer controller for top turbo pump.

c. Isolate the turbo pumps by closing the three roughing valves between the TMPs and MP.
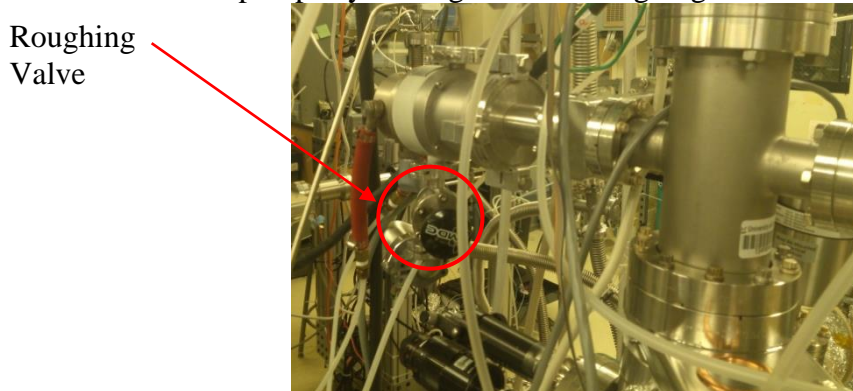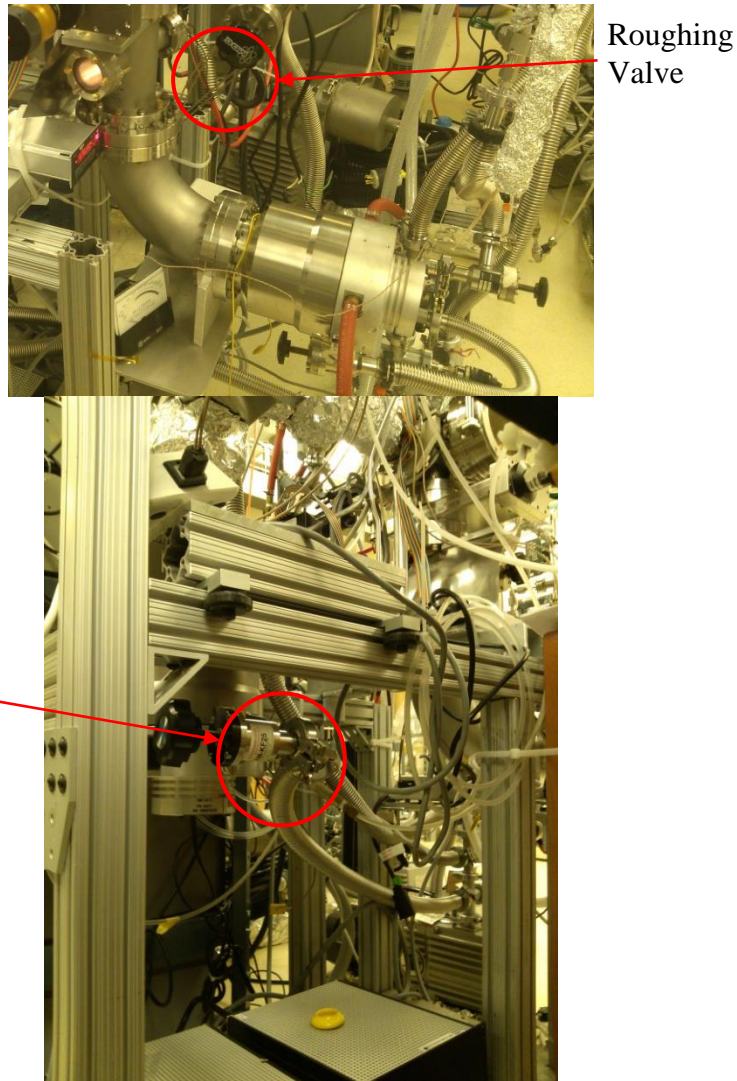
Roughing Valve

Figure I-3 Roughing valves between turbo pumps and mechanical pump.

2. In case a noise is heard from mechanical pump on chamber
    a. Close the three manual gate valves between the TMPs and the chamber and the pneumatic
       gate valve between the ion gun and the TMP.
    b. Turn off the turbo molecular pumps by pushing the "stop" button on the Leybold controller
       and the "stand by" button on the Pfeiffer controller.
    c. Switch off the mechanical pump by turning off the breaker switch on the power strip.
3. In case noises are heard from any of the electronics
    a. If units have power switches turn them off, and unplug all units.

I.2. Operation Procedures for Ion Source Chamber

1. Pumping down the entire system (Note: The chamber's default state should be pumped down;
    check the pressure reading on the ion gauge to verify. The following steps should only be
    taken if you aware that the chamber has been vented and not pumped back down).
    a. THE FOLLOWING INTERLOCKS FOR THE PUMP DOWN PROCEDURE MUST BE
       MET TO BEGIN PUMPING: COOLING WATER FOR MAIN CHAMBER TURBO

PUMP AND ION GUN TURBO PUMP MUST BE ON, COOLING WATER FLOW TO COMPRESSOR SHOULD BE BETWEEN 2.3 AND 3.5 GPM).

b. Check that all the flanges are tightened and all the valves are in the closed position.
c. Check all the cables are correctly connected.
d. Check the oil level in the mechanical pump, which should be 2/3 full in view window.
e. Check MP and its exhaust for liquid leaks. (oil, condensation, exhaust fluid).
f. Check that the Baratron and thermocouple gauges are on and that the ion gauges are off.
g. Turn on MP by turning on the switch on the power strip. The thermocouple gauge reading should start going down within 20 seconds. If not, turn off the pump and check connections to chamber and turbopumps for vacuum leaks.
h. Slowly open the three roughing valves between the turbo pumps and mechanical pump. Wait until Baratron gauge reaches ~10 mTorr.
i. Slowly open the two roughing valves between the chamber and the MP and between the mass spectrometer and the MP.
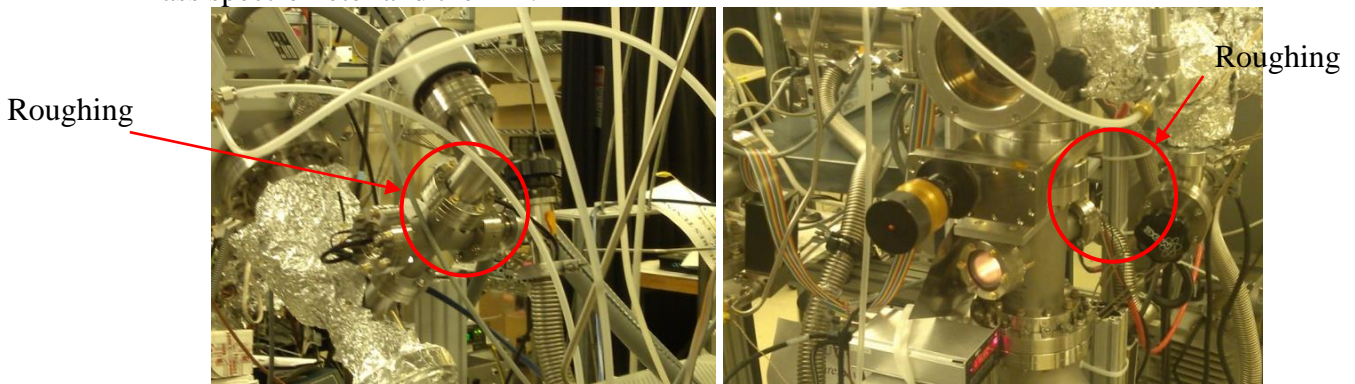
Figure I-4 Roughing valves between the chamber and mechanical pump.

j. Wait until Baratron gauge reaches the base pressure ~10 mTorr. This process may take several minutes if system was shut down for some time.
k. Slowly open manual gate valve between ion gun and main chamber.
l. Slowly open Ar gas line valve to purge the gas line.
m. After the Baratron gauge reads less than 10 mTorr, close the two roughing valves between the chamber and the MP and between the mass spectrometer and the MP.
    a. Before TMPs are turned on, check:
        i. The cooling water is running.
        ii. TC gauge reads less than 10 mTorr.
        iii. Either the roughing valve between the chamber and MP *or* the roughing valves between the TMPs and MP and gate valves between TMPs and main chamber should be always CLOSED while the TMPs are on.
n. Turn on TMPs by pushing the start button on the Leybold controllers and the pumping unit button on the Pfeiffer controller, unless already on. The green acceleration indicator on the Leybold controllers should be on, and the rotation gauge on the Pfeiffer controller should shift from red to green.
    a. Within 5 minutes, the turbo molecular pumps should reach full speed. The yellow indicator on the Leybold controllers should be on normal, and the rotation gauge on the Pfeiffer controller should be in the solid green area.

i. If any strange noise is heard from TMPs, close the gate valves between the TMPs and the chamber. Then turn off the TMPs right away by pushing the off button on the Leybold controllers and the stand by button on the Pfeiffer controller. Close the roughing valves between the TMPs and the MP.

b. Turn on the ion gauges by pressing the IG1 and IG2 buttons on the ion gauge controller. If the pressure reads above 5.0×10^{-5} Torr, shut off ion gauge by pressing the IG1 or IG2 button and wait several minutes before turning the gauge back on.

c. Open the pneumatic gate valve between the ion gun and the TMP by flipping the switch labeled LL/TMP. The gate valve is open when the red light above the switch is on.

o. Gradually open the two manual gate valves between the bottom TMP and the chamber and between the mass spectrometer and the chamber. Do not let ion gauge read above 5.0×10^{-5} Torr.

p. Wait until the chamber reaches the base pressure $\sim 2.0 \times 10^{-7}$ Torr.

a. If chamber was vented for more than one day, close Ar gas line valve and wait until chamber reaches 10^{-8} Torr.

Pneumatic Gate Valve Switch

Figure I-5 Pneumatic gate valve control for gate valve between ion gun and top turbo pump.

Ion Gauge Button "IG1"
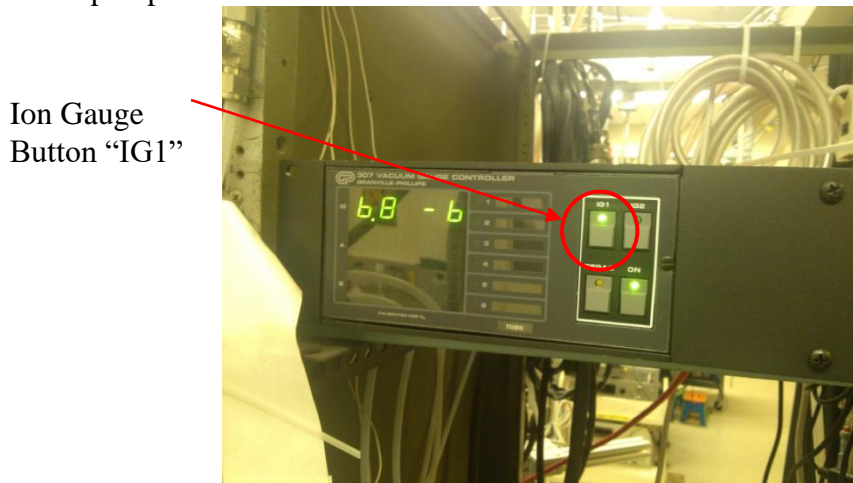
Figure I-6 MFC with Ar gas line switch.

2. Loading Sample (Note: this assumes chamber has already been pumped down. If chamber is exposed to ambient pressure, load sample and then follow instructions in section 1 for pumping down the entire chamber).

a. Close the three manual gate valves between chamber and TMPs and the pneumatic gate valve between the ion gun and the TMP by flipping the switch labeled LL/TMP.

b. Loosen black knob on loading door. The knob will be damaged if it is not loosened before pressurizing the chamber.

c. Slowly open air inlet valve to chamber. Watch ion gauge reading to make sure the manual gate valves are completely closed.

d. Wait until the loading door pops open. The chamber is now at ambient pressure.

e. Close air inlet valve to chamber.

f. Open loading door and load the sample.

g. Close loading door and hand tighten black knob.

h. Close the three roughing valves between the TMPs and the MP.

i. Gradually open the two roughing valves between chamber and MP and between mass spectrometer and MP. Wait until Baratron gauge reads below 10 mTorr.

j. Gradually open manual gate valve between ion gun and main chamber.

k. Close the two roughing valves between chamber and MP and between mass spectrometer and MP.

l. Open the three roughing valves between the TMPs and the MP.

m. Open gate valve between ion gun and TMP by flipping switch labeled LL/TMP.

n. Gradually open the two manual gate valves between chamber and TMP and between mass spectrometer and TMP. Do not let ion gauge read above 5.0×10^{-5} Torr.

o. Wait until chamber reaches base pressure 10^{-7} Torr.

3. Turning on the ion source controller (Note: the sample must already be loaded and the chamber must be already pumped down).

a. Ensure the Ar gas line valve is open.

b. Turn off the ion gauges by pressing the IG1 and IG2 buttons on the ion gauge controller if they are on.

c. Turn on the Ar gas switch on the MFC. The Baratron gauge should read ~0.30 mTorr.

d. Turn on power switch on ion source controller.

e. Turn on left source beam switch. Do not turn on the right source beam switch yet.

f. Hold down discharge switch to the voltage setting and adjust the discharge dial until the monitor reads 40.0 V.

g. Hold up discharge switch to the current setting and adjust the cathode dial until the monitor reads 0.25 mA.

h. Turn on right source beam switch.

i. Hold neutralizer switch to the emission setting and adjust the neutralizer dial until the monitor reads a value close to the value displayed on the beam display. This value should be about 5 mA.

Ar Gas Line
Switch

Figure I-7 MFC with Ar gas line switch.

4. Turning off the ion source controller.
    a. Turn the neutralizer, cathode, and discharge dials counter-clockwise until they stop.
    b. Turn off the right source beam switch, then the left source beam switch.
    c. Turn off the power switch.
    d. Turn off Ar gas switch on MFC.
    e. Turn on ion gauges by pressing the IG1 and IG2 buttons on the ion gauge controller.
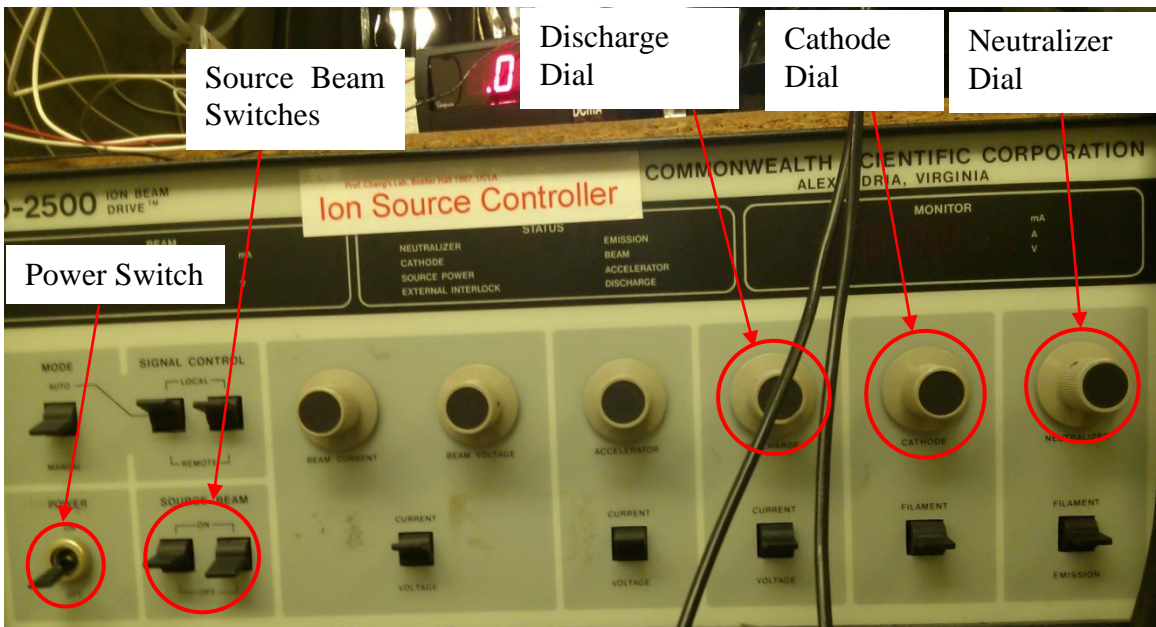
Figure I-8 Ion source controller.

I.3. Operating Procedure for Analysis (#6) in Professor Chang's Lab

EQP QMS

Emergency Shutdown

1. Turn off the filament and stop data acquisition from the software: In the MASsoft Software Window, click the red button icon on the primary row of buttons, or select "Shutdown" from the System Menu.

Shutdown Button

System → Shutdown
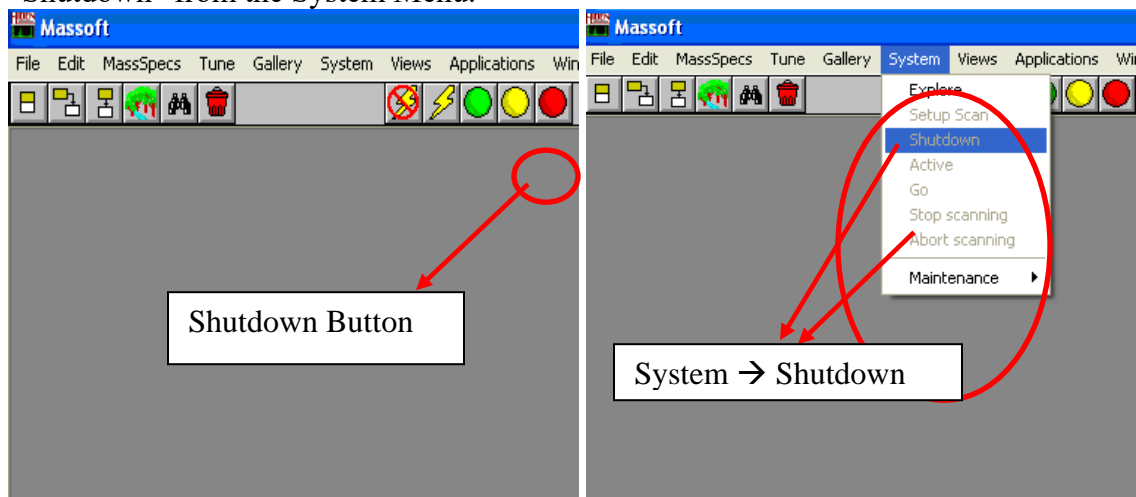
2. Switch off the power switches on the electronics (Green power button on the MSIU, large middle button on cold cathode gauge controller – see picture below).

Cold Cathode Gauge Power Switch (Note:

MSIU Power
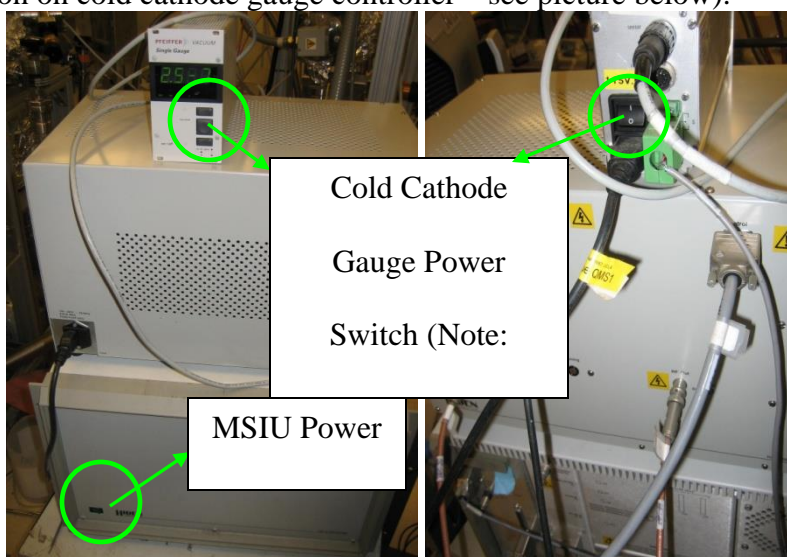
Operating Procedures

1. Check the QMS logbook for the previous scan and check the base pressure of the system, which should be about $9*10^{-8}$ Torr. Write the base pressure in the logbook.
2. Plug the power cable into the RF generator (the electronic box next to the computer monitor) and turn on the power switch of the MSIU unit on the bottom level of the cart. The switch should be lighted green and a beep sound should be heard. Allow 30 min warm up before doing any analysis. If the beep sound is continuous (longer than 1 s), turn the unit off and check for errors.
3. Open the operating software MASsoft.

271

4. Degas the filament (as necessary) by choosing the "system", "maintenance", and "degas". The desired the degas filaments and time can be chosen.
5. Set up the operation file. The new operation file can be generated by choose "file", and "new". However, because the EQP parameters need to be consistent, it is suggested that one "open" an existing file and "save as" to another filename. For neutral scan, double check the electron energy and emission current, and make sure electron energy is not very low.
6. Start the experiment, for example, turn on and tune the plasma. It is very important to turn on the plasma before turn on the filament for neutral scan. Otherwise, the filament will be broken.
7. Monitor the QMS pressure. The maximum operating pressure for QMS is $5*10^{-6}$ Torr.
8. Start the QMS scan by clicking the green circle in the top section of the window. A promotion will ask you if you want to overwrite the current file or save to another filename. If the "open and save as" procedure was followed in step 5, you may choose "overwrite".
9. Monitor the scan and make sure the signal intensity is not too high (close to $1*10^7$).
10. The scan can be terminated automatically or manually. To terminate the scan automatically, the proper scan cycle can be set in the operation file. To terminate the scan manually, click the yellow circle next to the starting green circle. The scan will stop after the current cycle is finished. The scan can also be terminated immediately by clicking the red circle next to the yellow circle. However, the data will not be saved in this way.
11. After finishing all the experiments, close MASsoft and transfer all the data files to the server.
12. Turn off the power to the electronics following the reversed procedure in step 2.
13. Check the base pressure of QMS and bake it as necessary.
14. Finish the logbook.

I.4. Install and Test EQP QMS System

Make sure the EXP pressure is ALWAYS $< 5 \times 10^{-6}$ Torr
Make sure the count rates are $< 5 \times 10^6$ cts/s
Make sure the electron energy is tuned so that the filament current is not too high
Need to connect CCG to the trig connector on MSIU (trig pressure $< 5 \times 10^{-6}$ Torr)

Problems

(1) H_2O dominates the RGA spectra after striking a plasma (mass peak splits due to saturation)
(2) $Ar^+(40)$ dominates the +ion SIMS spectra (energy peak splits due to saturation --> de-tune the system)
  − Use isotope whenever possible to AutoTune (Ar36)
  − Extl.actor energy should not be changed
  − Use Lens 1 and Lens 2 energies to de-tune the signal as they won't affect the IED (Multiplier voltage is also effective)
  − Focus 2 energy can also be adjusted
(3) Mass peaks of O_2 and O splits in 900 W plasma (tune Lens 2, set Vert, Horiz, and DC Quad to 0)
(4) S/N: Use ms rather than % in Dwell Time to better control the S/N ratio, Use "Accumulation" and "Mean"
(5) Computer crash "Error Detected in MemFreePtr[117F:0032]", "Error at or near addresses 117F:0000"
  a. Obtain base pressure $< 6 \times 10^{-5}$ Torr
  b. (Aug. 31). Check Base Pressure, EQP:2.5-6×10^{-7} Torr; PECVD: 3.8×10^{-6} Torr
  c. Cold cathode gauge failed
  d. Turbo pump failed
  e. Switched the PECVD turbo pump with the EQP turbo pump
  f. Connect all cables (some were labeled incorrectly, now corrected.)
  g. The computer need to be > 200 MHz
  h. Connect the computer with the EQP using RS232 cable

Installation

1. Install software: MASSoft (one CD and one System disk) –
  − MASSoft\wr11029\ 5 Tune files
  − (Master, NegTune, nRGATune, PosiTune, and RGATune)
2. Read ReadMe and Initialization file
3. Program
  a. INI file editor --If re-setup computer with the 10-base T connection, change NoOfAddresses in Initialization file from "0" to" 1 "
  b. 3b. Terminal (Hyper Terminal) --Need to turn on MSIU first to establish the connection
    − type "help [return]" (to get all information about Interface Unit)
    − Important parameters: AutoTuneWindow, AutoTuneThreshold, and AutoTuneMinimum
    − type "pget AutoTuneWindow [return]" to get the value for AutoTuneWindow

- type "pget AutoTuneThreshold [return]" to get the value for AutoTuneThreshold
- type" pget AutoTuneMinimum [return]" to et the value for AutoTuneMinimum

	Hiden tested setting	Default
AutoTuneWindow	2	7
AutoTuneThreshold	50	500
AutoTuneMinimum	50	0
AutoTuneMaximum	?	500

- type "pset AutoTuneMinimum [return]" to set the value for AutoTuneMinimum

4. The system does not have Suppressor, and the source focus is connected to DAC (pp. 210-211)
5. Scan:

   BAR
   PROFILE
   MID
   LEAK DETECT

MAP

   SURFACE

6. Red-LED in RF Generator indicating tuning is needed
7. Tune the RF Generator
   1) Open the cover of RFG
   2) Using multimeter to measure the voltage(DC) between TP25 (or TP24) and TP36(GND), V=O0
   3) Go to Hyper Terminal
      - type "Iget mass 5.50"
      - type "Iset mass 0.4 "
      - Adjust the turning screw head on the front panel of the RFG
      - type "Iset mass 0.4", measure V =0.05v
      - type "Iset mass I ", V= 0.05v
      - type "Iset mass 2", V= 0.05v
      - type "Iset mass 3", v= 0.05v
      - type "Iset mass 4", V= 0.05v
      - type "Iset mass 3", v= 0.05v
      - type "lset mass 3.5", v= 0.05v
      - V doesn't change!
   4) Suspect the electronics inside the RFG or the EQP Head have faults
   5) Remove the Amplifier from the EQP Head
   6) Open the cover of the EQP Head
   7) Check the Quadropole, measure the resistance between the top 4 connectors inside the head
      - make sure none of the poles shorts to the ground
   8) Quadrupole is OK
   9) Open the RFG again, take out the circuit boards together with the coil
   10) The wires connecting with the Coil are both BROKEN!
   11) Weld the broken wires
   12) Connect the RFG and the EQP Head again

13) Tune the RFG again
14) Go to Hyber Terminal
15) "lget mass" 3.0

Iset mass	Voltage TP25 ←→ TP36
0.4 (min mass)	? (10 mV)
1	0.004v
5	?
10	?
50	?
100	?
200	?
500	0.344v
1000 (max mass)	0.714v (~700mV)

16) Now the RFG tuning is done

8. Run MASsoft application
1) Scan: mass 0.4 → 50
2) There are peaks appearing. But the peaks do not correspond the correct masses
3) Tune the RFG again.
   – Open the cover of RFG
   – Adjust the RV 1 potentiometer on the circuit board (3 next to a red wire) ????
   – By adjusting the screws, the peaks can shift.
   – Scan mass: 0.4 --> 10, check the peaks
   – Scan mass: 13 --> 23, refer the peak around m=18.0, adjust the screw, make the peak shift to m=18
   – Scan mass: 144 --> 154, check the peaks
   – Scan mass: 164 --> 174, check the peaks
   – m = l47 and m= 167 are filament material peaks, but they will disappear eventually ???
4) Tune the RGA mode ? Need to check with Byeong and Alex
5) Test RGA mode with air only; OK
6) Test RGA mode with Ar flowing in, pressure = 3.0mT; OK
7) Test RGA mode with Ar + O2, pressure = 5 .0mT , OK
8) Test to get the appearance potential, OK
9) *Tune the +ion SIMS mode ? ? ?* Need to check with Byeong and Alex
10) Test +ion SIMS mode with Ar + O2 plasma, pressure = 7.8mT, OK
11) Test the function of NEUTRAL analysis in plasma
    – In RGA mode
    – Set Extractor = +50V
    – Set Len 1 = -10 ~ -20V
    – Other parameters keep the same
    – * The m = 18 peak is too high, ~1.4×10^7 c/s
    – Turn off the plasma in PECVD, the peak is still high
    – * Suspect the filament is covered by some material
    – -Degas the filament. (How???)
    – * Suspect there is too much H2O inside the EQP chamber

275

– Keep scanning and monitoring the m =18 peak, for ~1 hr, the intensity 1.4×10^7 → 1.8×10^6

*** The procedure of testing, refer to the MASsoft manual

9. AutoTune
 – 3 scans or so
 – System --> Maintanence --> AutoTune
 – Select Mass, Select Mode to be Tuned
 – Ex: +ion Mass (save to PSIMSTUN.exp on 09/03/2001)
     a. Energy: 0 to 30, it is important to do the energy scan for different conditions to maximize the signal intensity as the IEDF changes significantly with conditions (chemistry, power, bias, etc.)
     b. Lens 1: -370 to 0 (once the scan starts, can reduce the range, for example to -140 in one case)
     c. Lens 2: -200 to -50 (can not be set to ZERO!)
   (once the scan starts, can reduce the range, for example to -140 in one case)
     d. Focus 2: -360 to 0 (once the scan starts, can reduce the range, for example to -300 in one case)
 – Use Lens I, Focus2, Lens 2 to de-tune the signal, as they won't affect the IED

10. Manual Tune --> Chang save option to "Manual Selection" to avoid software crashing during manual tuning
 (This should not be done if the system is tuned.
 This was done when we didn't realize the peak splitting was due to signal saturation)
 – Fine Tune (Plates, Lens 2, Vert, Horiz, Axis, Energy, DC Quad)
 – +- 2V for DC Quad (correspond to 100% to -100%)
 – +- 4V for Vertical and Horizontal (correspond to 100% to -100%)
 – Change a few % on DC Quad, Vert, and Horiz
 – Chang Horiz from 0% to -16% affected the IED significantly
 – Generate a co-variance plot (Horiz -16 to 0 and energy 0 to 25) cycle=l, l00 ms, FineTunl.exp

11. Electron attachment for 0 (high pressure at 400 mtorr , e- ~ 10 e V) ?

12. Integrate the mass over the energy

Control Schemes

| Shutdown | | Events |
| Global: RGA/SIMS |
| SEM (detector) | | Scan 1: mass/f(x) |
| Stop (Continuous, cycles, shutdown after scan) |
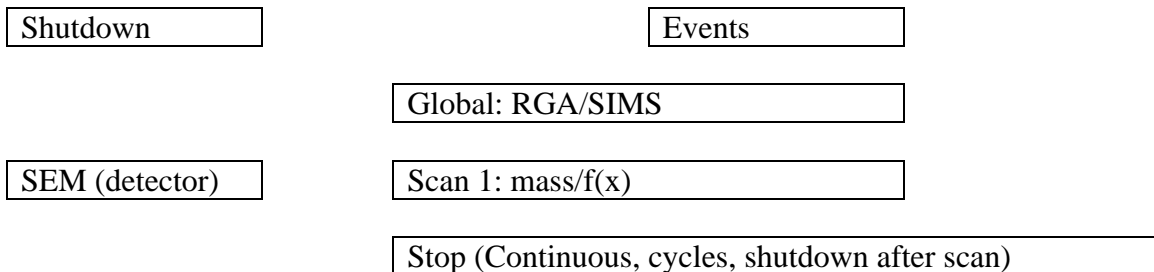
Global Environment (Before Dec, 2005)

RGA	Min	Max	Current Setpoint		Note
Multiplier	0	3000	1800	V	→ increase up to 2200 V
1st dynode	-1200	1200	-1200	V	
Resolution	-100	100	0	%	→ for > 100 amu
Delta-M	-100	100	0	amu	→ for < 100 amu
Discriminator	-100	100	-10	%	
Mass	0.4	1000	18	amu	→ sit on a mass for energy analysis
Rate_selection	0	1	0	c/s	
Reference	-1000	1000	0	V	→ see pp. 211, ref. Voltage adjustment
Emission	0.2	2000	100	microA	→ de-sensitize the instrument
Electron Energy	0	150	70	V	→ set to very small for electron attachment
Cage (ion collector)	-10	10	3	V	→ set to –25 V at the end of the scan
Source focus	-370	370	-340	V	
Focus 2	-360	360	-356	V	
Extractor	-370	370	0	V	
Lens 1	-370	370	0	V	
Plates	-20	20	7.27	V	→ 45º energy filter (see pp. 213)
Lens 2	-360	360	-104	V	
Vertical	-100	100	12	%	
Horizontal	-100	100	5	%	
Axis	-90	90	-40	V	
Energy	-100	100	3.85	V	
D. C. Quad	-100	100	2	%	
Transit energy	-10	10	3	V	
Mode-change delay	0	2.1E+09	1000	ms	→ switch between modes, eg. SIMS and RGA

+ ion SIMS	Min	Max	Current Setpoint		Note
Multiplier	0	3000	1800	V	
1st dynode	-1200	1200	-1200	V	
Resolution	-100	100	0	%	→ for > 100 amu
Delta-M	-100	100	0	amu	→ for < 100 amu
Discriminator	-100	100	-10	%	
Mass	0.4	1000	18	amu	→ sit on a mass for energy analysis
Rate_selection	0	1	0	c/s	
Reference	-1000	1000	0	V	→ see pp. 211, ref. Voltage adjustment
Emission	0.2	2000	100	microA	→ de-sensitize the instrument
Electron Energy	0	150	70	V	→ set to very small for electron attachment
Cage (ion collector)	-10	10	0	V	→ set to –25 V at the end of the scan

Source focus	-370	370	0	V	
Focus 2	-360	360	-264	V	
Extractor	-370	370	-2	V	
Lens 1	-370	370	-76	V	
Plates	-20	20	7.27	V	→ 45º energy filter (see pp. 213)
Lens 2	-360	360	-95	V	
Vertical	-100	100	0	%	
Horizontal	-100	100	0	%	
Axis	-90	90	-40	V	
Energy	-100	100	14	V	
D. C. Quad	-100	100	0	%	
Transit energy	-10	10	3	V	
Mode-change delay	0	2.1E+09	1000	ms	→ switch between modes, eg. SIMS and RGA

-ion SIMS	Min	Max	Current Setpoint		Note
Multiplier	0	3000	1800	V	
1st dynode	-1200	1200	800	V	
Resolution	-100	100	0	%	→ for > 100 amu
Delta-M	-100	100	0	amu	→ for < 100 amu
Discriminator	-100	100	-10	%	
Mass	0.4	1000	18	amu	→ sit on a mass for energy analysis
Rate_selection	0	1	0	c/s	
Reference	-1000	1000	0	V	→ see pp. 211, ref. Voltage adjustment
Emission	0.2	2000	100	microA	→ de-sensitize the instrument
Electron Energy	0	150	70	V	→ set to very small for electron attachment
Cage (ion collector)	-10	10	0	V	→ set to –25 V at the end of the scan
Source focus	-370	370	0	V	
Focus 2	-360	360	340	V	
Extractor	-370	370	50	V	
Lens 1	-370	370	201	V	
Plates	-20	20	-7.27	V	→ 45º energy filter (see pp. 213)
Lens 2	-360	360	119	V	
Vertical	-100	100	0	%	
Horizontal	-100	100	0	%	
Axis	-90	90	40	V	
Energy	-100	100	-16.6	V	
D. C. Quad	-100	100	0	%	
Transit energy	-10	10	-3	V	
Mode-change delay	0	2.1E+09	1000	ms	→ switch between modes, eg. SIMS and RGA

-ion RGA	Min	Max	Current Setpoint		Note
Multiplier	0	3000	1800	V	
1st dynode	-1200	1200	800	V	
Resolution	-100	100	0	%	→ for > 100 amu
Delta-M	-100	100	0	amu	→ for < 100 amu
Discriminator	-100	100	-10	%	
Mass	0.4	1000	18	amu	→ sit on a mass for energy analysis
Rate_selection	0	1	0	c/s	
Reference	-1000	1000	0	V	→ see pp. 211, ref. Voltage adjustment
Emission	0.2	2000	20	microA	→ de-sensitize the instrument
Electron Energy	0	150	1.9	V	→ set to very small for electron attachment
Cage (ion collector)	-10	10	-3	V	→ set to –25 V at the end of the scan
Source focus	-370	370	367	V	
Focus 2	-360	360	353	V	
Extractor	-370	370	0	V	
Lens 1	-370	370	0	V	
Plates	-20	20	-7.27	V	→ 45º energy filter (see pp. 213)
Lens 2	-360	360	108	V	
Vertical	-100	100	0	%	
Horizontal	-100	100	0	%	
Axis	-90	90	40	V	
Energy	-100	100	-3.7	V	
D. C. Quad	-100	100	0	%	
Transit energy	-10	10	-3	V	
Mode-change delay	0	2.1E+09	1000	ms	→ switch between modes, eg. SIMS and RGA

Global Environment (Oct 10, 2006)
RGA, tuned for mass 70 in a Cl2/BCl3 plasma(Oct 10, 2006)

RGA	Min	Max	Current Setpoint		Note
Multiplier	0	3000	3000	V	(→ increase up to 2200 V)
1st dynode	-1200	1200	-1200	V	
Resolution	-100	100	0	%	→ for > 100 amu
Delta-M	-100	100	0	amu	→ for < 100 amu
Discriminator	-100	100	-10	%	
Mass	0.4	1000	70	amu	→ sit on a mass for energy analysis
Rate_selection	0	1	0	c/s	
Reference	-1000	1000	0	V	→ see pp. 211, ref. Voltage adjustment
Emission	0.2	2000	100	microA	→ de-sensitize the instrument
Electron Energy	0	150	70	V	→ set to very small for electron attachment

Cage (ion collector)	-10	10	3	V	→ set to –25 V at the end of the scan
Source focus	-370	370	-295	V	Parameter tuned
Focus 2	-360	360	-138	V	Parameter tuned
Extractor	-370	370	50	V	Not Tuned
Lens 1	-370	370	-15	V	Not Tuned
Plates	-20	20	7.27	V	→ 45º energy filter (see pp. 213)
Lens 2	-360	360	-89	V	Parameter tuned
Vertical	-100	100	8	%	Parameter tuned
Horizontal	-100	100	2	%	Parameter tuned
Axis	-90	90	-40	V	
Energy	-100	100	-3.05	V	Parameter tuned
D. C. Quad	-100	100	20	%	Parameter tuned
Transit energy	-10	10	3	V	
Mode-change delay	0	2.1E+09	1000	ms	→ switch between modes, eg. SIMS and RGA

Ion SIMS: Tuned for Mass 40 aum (Oct 10, 2006)

+ ion SIMS	Min	Max	Current Setpoint		Note
Multiplier	0	3000	3000	V	
1st dynode	-1200	1200	-1200	V	
Resolution	-100	100	0	%	→ for > 100 amu
Delta-M	-100	100	0	amu	→ for < 100 amu
Discriminator	-100	100	-10	%	
Mass	0.4	1000	18	amu	→ sit on a mass for energy analysis
Rate_selection	0	1	0	c/s	
Reference	-1000	1000	0	V	→ see pp. 211, ref. Voltage adjustment
Emission	0.2	2000	100	microA	→ de-sensitize the instrument
Electron Energy	0	150	70	V	→ set to very small for electron attachment
Cage (ion collector)	-10	10	0	V	→ set to –25 V at the end of the scan
Source focus	-370	370	-352	V	Parameter tuned
Focus 2	-360	360	-307	V	Parameter tuned
Extractor	-370	370	-20	V	Parameter tuned
Lens 1	-370	370	-237	V	Parameter tuned
Plates	-20	20	7.27	V	→ 45º energy filter (see pp. 213)
Lens 2	-360	360	-141	V	
Vertical	-100	100	77	%	Parameter tuned
Horizontal	-100	100	3	%	Parameter tuned
Axis	-90	90	-40	V	
Energy	-100	100		V	Parameter tuned
D. C. Quad	-100	100	-88	%	Parameter tuned
Transit energy	-10	10	3	V	

Mode-change delay	0	2.1E+09	1000	ms	→ switch between modes, eg. SIMS and RGA

Ion SIMS: Tuned for Mass 320 aum (Oct 10, 2006)

+ ion SIMS	Min	Max	Current Setpoint		Note
Multiplier	0	3000	3000	V	
1st dynode	-1200	1200	-1200	V	
Resolution	-100	100	0	%	→ for > 100 amu
Delta-M	-100	100	0	amu	→ for < 100 amu
Discriminator	-100	100	-10	%	
Mass	0.4	1000	320	amu	→ sit on a mass for energy analysis
Rate_selection	0	1	0	c/s	
Reference	-1000	1000	0	V	→ see pp. 211, ref. Voltage adjustment
Emission	0.2	2000	100	microA	→ de-sensitize the instrument
Electron Energy	0	150	70	V	→ set to very small for electron attachment
Cage (ion collector)	-10	10	0	V	→ set to –25 V at the end of the scan
Source focus	-370	370	-225	V	Parameter tuned
Focus 2	-360	360	-302	V	Parameter tuned
Extractor	-370	370	-16	V	Parameter tuned
Lens 1	-370	370	-240	V	Parameter tuned
Plates	-20	20	7.27	V	→ 45º energy filter (see pp. 213)
Lens 2	-360	360	-141	V	
Vertical	-100	100	37	%	Parameter tuned
Horizontal	-100	100	7	%	Parameter tuned
Axis	-90	90	-40	V	
Energy	-100	100		V	Parameter tuned
D. C. Quad	-100	100	-69	%	Parameter tuned
Transit energy	-10	10	3	V	
Mode-change delay	0	2.1E+09	1000	ms	→ switch between modes, eg. SIMS and RGA

Scan Editor

Scan Mode	Global (RGA)	
	RGA	
	+ion SIMS	
	-ion SIMS	
	- ion RGA	

Scan legend	mass	
	f(x)	
	electron-energy	
	Source focus	
	focus 2	
	Extractor	
	Lens1	
	Lens2	
	Axis	
	Energy	
	(Can also create new terms, such as scanning multiplier)	

Start Stop
Stop
Increment
Step

Advance	Option	RestartAutoRange
		NoDeferAutoRange
		SaveScanDevice --> Reset after each scan
		BeamOnBefore --> Turn on the beam before each scan
		BeamOffAfter --> Turn off the beam after each scan
		YieldToEvents
		Accumulate --> Useful for low intensity ions (e.g. neg. ion)
		Mean --> Useful for low intensity ions (e.g. neg. ion)
	ScanRest	None
		Align
		AutoTune
		Max
		Sum
		Top
		XvalAtMaxY

<u>Input Selection</u>

SEM $\rightarrow$ Start   c/s
raw-counts Highest c/s
auxiliary I Lowest c/s
auxiliary 2 Dwell Time   % or ms --> Time spent at each point
f (x)   Settle Time   % or ms --> Time between two sets of scans

<u>Discussions with Peter Hatton</u>

  CC gauge
  RFG
  Filament material
  IED
  H_2O dominates the spectra
<u>Heat the EQP Head</u>

Tech Support: Allen Reese, Claire Greenwood
Improve the S/N: Use ms rather than %

I.5. Schematics

Ion Source Chamber

(a)

Isometric View

University of California, Los Angeles, Department of Chemical and Biomolecular Engineering							
Part		Material	Stainless steel				
Filename		Scale	Yes	Units	inch	Quantity	1
Designer	Jack Chen (UCLA)	Date	1/1/2015				
Revised by		Date					
Contractor		Date					
Comments			Tolerance			+/- .0001	

Ion Source Chamber

(b)

Side View

University of California, Los Angeles, Department of Chemical and Biomolecular Engineering							
Part		Material	Stainless steel				
Filename		Scale	Yes	Units	inch	Quantity	1
Designer	Jack Chen (UCLA)	Date	1/1/2015				
Revised by		Date					
Contractor		Date					
Comments			Tolerance		+/- .0001		

Ion Source Chamber							
(c)							
Front View							
University of California, Los Angeles, Department of Chemical and Biomolecular Engineering							
Part		Material	Stainless steel				
Filename		Scale	Yes	Units	inch	Quantity	1
Designer	Jack Chen (UCLA)	Date	1/1/2015				
Revised by		Date					
Contractor		Date					
Comments			Tolerance		+/- .0001		

Figure I-10 Ion Source Chamber Schematics (a-c).

J. Superconducting quantum interference device (SQUID)

J.1. Introduction
Superconducting quantum interference device (SQUID) is a magnetometer that measures magnetization (M) as a function of the applied field (H). A hysteresis loop can be plotted to extract information regarding the magnetic properties of the film. For example, coercivity, H_c, is the horizontal intercept of the hysteresis curve. It is the applied field necessary to change the direction of magnetization within the domains of the material. It indicates the stability of magnetization in the material. The saturation magnetization, M_s, is the maximum magnetization of a material dM/dH=0. It indicates the magnetic strength a material. The enabling phenomenon behind SQUID is the Josephson junction.
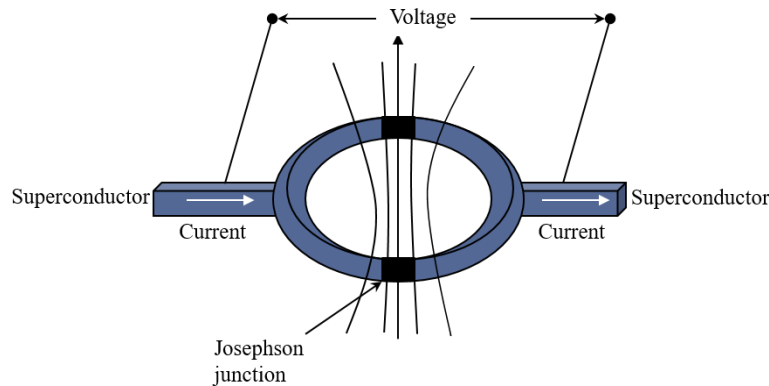
Figure J-1 Diagram of Josephson junction utilizing a superconducting loop with two parallel non-superconducting sections.

The Josephson junction is a superconducting loop separated by two parallel pieces of non-superconducting material (Figure 1). Electrons tunnel through the non-superconducting material in the form of Cooper pairs, electrons that are bound together in a very low energy state that allows for long range interaction over hundreds of nanometers (Allender, Bray et al. 1973). This interaction is very weak, on the order of 0.001 eV, and requires reduced temperatures since small amounts of thermal energy can break it.

An applied current, I, is split equally across the two parallel branches. If a magnetic field is applied, a screening current, I_s, is circulates the loop resulting in a magnetic flux equal but opposite of the external magnetic flux (Bardeen, Cooper et al. 1957). This induced current travels in the same direction as current in one branch, and opposite in the other, causing two different currents across the parallel non-superconducters Equations 1 and 2.

$$I_1 = \frac{I}{2} + I_S \tag{1}$$

and

$$I_2 = \frac{I}{2} - I_S \tag{2}$$

Once a threshold current is reached, a measurable voltage appears across the junction. If the magnetic flux exceeds $\varphi_0/2$, or half of the magnetic flux quantum, the system will

energetically favor an increase in this value to an integer of φ_0, which results in the current flipping direction. This phenomenon causes the current to oscillate as a function of the applied magnetic flux. Equation 3 represents the magnetic flux quantum, where h is Planck's constant and e is the elementary charge.

$$\varphi_0 = \frac{h}{2e} = 2.067833 \times 10^{-15} \text{ tesla-m}^2 \tag{3}$$

The SQUID device has two Josephson junctions, at either end of the device. By maintaining a constant current within the SQUID, the measurable voltage will fluctuate at each of the two Josephson junctions, allowing for the oscillation to be correlated to the amount of magnetic flux through the sample. Equation 4 is the resulting voltage change, which is dependent on the resistance, R, and the loop's inductance, L, as well as the change in the magnetic flux quantum, $\Delta\varphi$.

$$\Delta V = \frac{R}{L}\Delta\varphi \tag{4}$$

To measure the magnetic properties via SQUID, the sample is first moved up and down between two electromagnets to change the applied field. A pair of sensory coils around the sample measures the voltage. For these measurements, a Quantum Design Magnetic Property Measurement System (MPMS) XL was used. This tool only measures the total magnetization, so data must be normalized by the volume of magnetic material, excluding the substrate. Due to the diamagnetic influence of air within the sample holder as well as the response generated from the silicon substrate, it is necessary to first perform a linear fit of the raw data at either very high or very low fields. The diamagnetic response can be subtracted from raw data to obtain the magnetic measurement of the sample.

J.2. SQUID Operating Procedure
Sample preparation
1. Put on clean pair of gloves. Obtain drinking straw, remove wrapper.
2. Using diamond scribe, cleave sample of interest into a 5mm x 5mm square
3. Record dimension of sample using digital calipers
4. Calculate and make a note of the volume of magnetic film in cm^3 by taking product of calculated sample area and film thickness
5. Obtain a pill capsule, pull apart the two halves, and insert the sample into the inner half of the capsule. It may be necessary to gently squeeze the capsule to accommodate larger samples.
6. Once the sample has been placed inside, releasing the capsule should hold the sample upright by tension of the capsule wall. Rejoin the two halves and insert the capsule into the straw
7. Using a metal rod, gently push the capsule into an eye-balled center of the straw.
8. Using a fine-tipped permanent marker, label the very top of the straw with the date and sample information
   Sample loading

1. Check the MPMS MultiVu Application window at the bottom to determine the current state of the SQUID machine.
2. If the temperature is below 298 K, left-click System (see photo, outlined in red)

3. The "Temperature Parameters" window will appear.
4. Under "Control" change "Set Point" value to 298. Change "Rate" to 10 K/min. Left-click "Set" button.
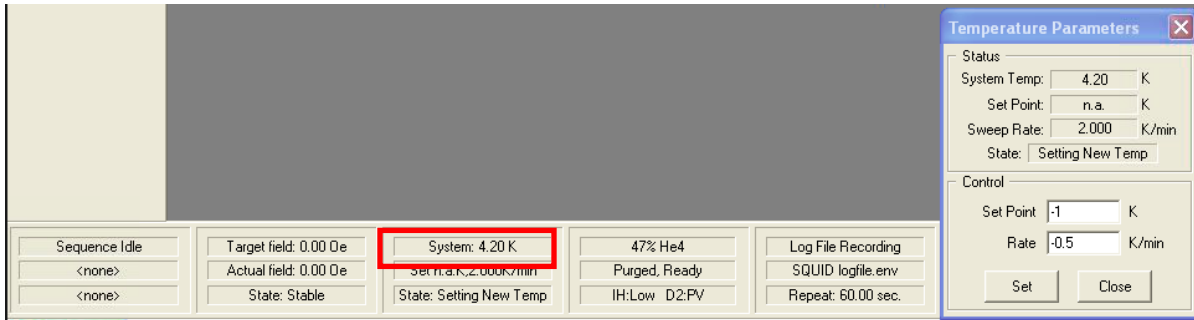
Figure J-2 Example SQUID MPMS MultiVu Application window. Outlined in red is the System temperature. Left-clicking here will bring up the Temperature Parameter window.

5. The temperature must reach a minimum 100K before the sample can be loaded. Otherwise a "Remove Servo Sample" window will display saying that "The sample space is too cold to be safely opened."
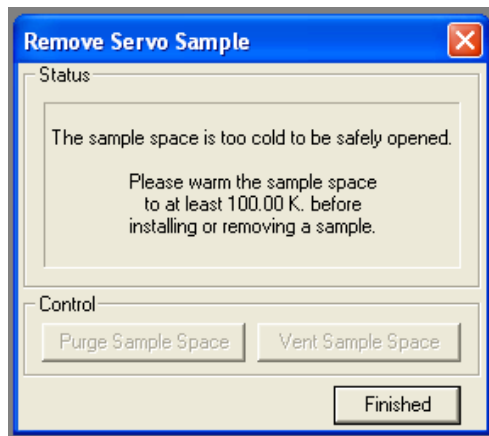
Figure J-3 Remove Servo Sample window will appear when the system temperature is below 100K while trying to remove a sample.

6. The SQUID machine will make a clicking noise and while observing the loading port, the top of the sample insertion rod should become visible—generally the top consists of a small blue cylindrical piece at the top. This can be seen through the clear plastic housing.
7. Remove the top piece sealing the loading port and turn it over.
8. Screw the threaded white plastic portion into the top of the sample loading rod and carefully remove the rod from the SQUID chamber. If a sample was previously in the chamber, it will appear mounted to the end of the loading rod. Carefully remove it from the bottom of the rod and place it on the SQUID machine housing next to the computer.
9. Before mounting on the rod, carefully pierce the straw, making three of holes radially around the sample. Do this two more times, each time making the set about 1.5 cm from the last.
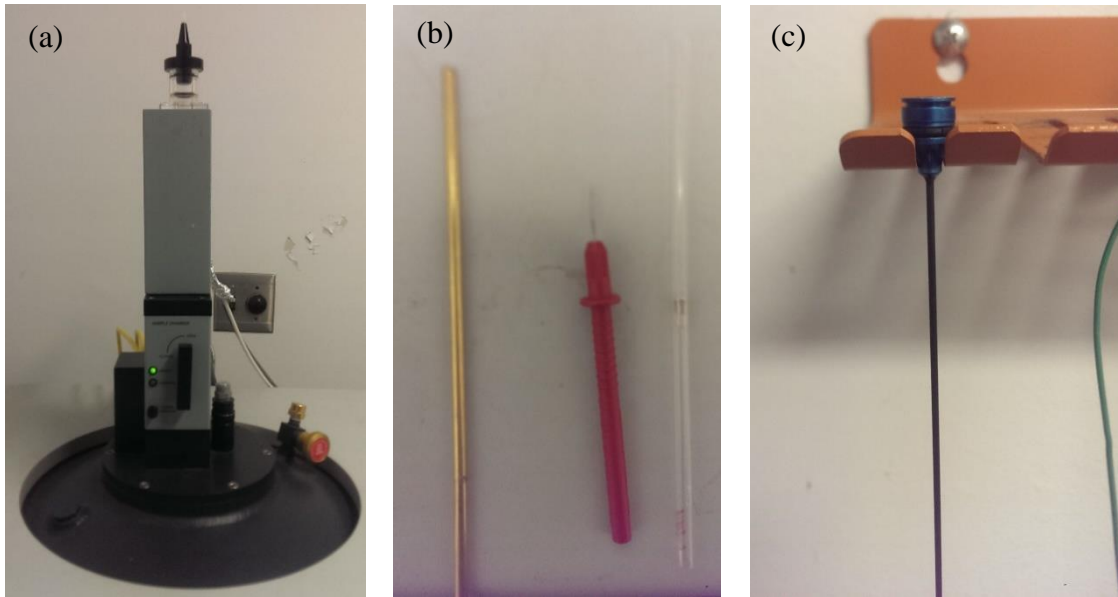
Figure J-4 (a) SQUID loading chamber with sealing top piece, (b) centering rod, piercing tool, and straw with inserted pill capsule and sample, and (c) loading rod with blue cylindrical top piece.

10. Avoid piercing the capsule as it can crack and break, releasing the sample and causing it to fall out of the straw.
11. Taking the sample to be scanned, gently push the top of the straw onto the peg at the bottom of the loading rod.
12. Insert the second plug on the bottom of the sample straw.
13. Re-insert the loading rod into the SQUID loading chamber until it is just barely visible, the exact same position was when it was unloaded.
14. Replace the sealing topper, ensuring that the o-ring makes good contact with the port.
15. Press the black button labeled "Purge". The SQUID will cycle through purging the chamber with helium until a green light is illuminated indicating that the port has been purge and is ready to load.
16. Left-click "Center" → "RSO…" → "Initialize Transport" to load the sample. The sample loading rod can be observed descending into the chamber.
17. Next the sample must be centered. Left-click "Center" to perform the centering scan. A window will appear showing both a fitted regression (blue) and the measured data (red). The key is to have the blue fit overlapping with red data in a Gaussian shaped peak at the ideal centered distance (x-axis).
18. Adjust the position manually to 3.5 and scan, this will seek out the more sensitive bottom coil and establish a lower limit to the position
19. Ensure that the box is checked, adjust the position manually again to 3.5 and scan
20. At this point, the program should have lined up the maximum or minimum from the scan.
21. Using the value automatically populated in the field, click Adjust position (without inputting 3.5)
22. The result should be that the fit and data should overlap and the sample will be sufficiently centered in between the coils.

K. Copper Volatility Diagram Construction

K.1. Introduction

A volatility diagram is a suitable method for studying the dry etching of solid materials, and it can be constructed from knowledge of the reaction thermodynamics of a particular system. For the etching of copper by chlorine, the relevant reactions can be found in Table K-1.

The relationship between the pressure of each gas phase Cu-Cl compound and the pressure of Cl_2 can be determined from expressions for the equilibrium constant of each reaction. Examples of this for each reaction listed in Table K-1 can be found below.

Table K-1 Table of relevant reaction for Cu-Cl systems, reproduced from (Kulkarni, et al., 2002).

Reaction		$\Delta H°$ (kj/mol)			
		50C	*100C*	*150C*	*200C*
(1)	$Cu(c) + 1/2\ Cl_2(g) \rightarrow CuCl(c)$	-137.01	-136.62	-136.17	-135.66
(2)	$CuCl(c) + 1/2\ Cl_2(g) \rightarrow CuCl_2(c)$	-80.63	-80.30	-79.98	-79.70
(3)	$Cu(c) \rightarrow Cu(g)$	337.50	337.30	337.05	336.80
(4)	$CuCl(c) \rightarrow Cu(g) + 1/2\ Cl_2(g)$	474.52	473.91	473.22	472.46
(5)	$CuCl_2(c) \rightarrow Cu(g) + Cl_2(g)$	555.15	554.20	553.20	552.16
(6)	$Cu(c) + 1/2\ Cl_2(g) \rightarrow CuCl(g)$	91.06	90.72	90.37	90.01
(7)	$CuCl(c) \rightarrow CuCl(g)$	228.07	227.34	226.54	225.67
(8)	$CuCl_2(c) \rightarrow CuCl(g) + 1/2\ Cl_2(g)$	308.70	307.64	306.52	305.37
(9)	$Cu(c) + Cl_2(g) \rightarrow CuCl_2(g)$	-43.31	-43.39	-43.49	-43.59
(10)	$CuCl(c) + 1/2\ Cl_2(g) \rightarrow CuCl_2(g)$	93.22	93.22	92.68	92.07
(11)	$CuCl_2(c) \rightarrow CuCl_2(g)$	173.52	173.52	172.66	171.77
(12)	$3\ Cu(c) + 3/2\ Cl_2(g) \rightarrow Cu_3Cl_3(g)$	-246.47	-246.47	-246.55	-246.66
(13)	$3\ CuCl(c) \rightarrow Cu_3Cl_3(g)$	163.38	163.38	161.95	160.32
(14)	$3\ CuCl_2(c) \rightarrow Cu_3Cl_3(g) + 3/2\ Cl_2(g)$	404.27	404.27	401.90	399.41

K.2. Example Calculations
For Cu(g) only:

$$Cu(c) + \frac{1}{2}Cl_2(g) \rightleftharpoons CuCl(c) \rightarrow \log(K_1) = \log\left(\frac{a_{CuCl}}{a_{Cu}P_{Cl_2}^{\frac{1}{2}}}\right) \rightarrow \log(P_{Cl_2}) = -2\log(K_1) \tag{1}$$

$$CuCl(c) + \frac{1}{2}Cl_2(g) \rightleftharpoons CuCl_2(c) \rightarrow \log(K_2) = \log\left(\frac{a_{CuCl_2}}{a_{CuCl}P_{Cl_2}^{\frac{1}{2}}}\right) \rightarrow \log(P_{Cl_2}) = -2\log(K_2) \tag{2}$$

$$Cu(c) \rightleftharpoons Cu(g) \rightarrow \log(K_3) = \log\left(\frac{P_{Cu}}{a_{Cu}}\right) \rightarrow \log(P_{Cu}) = \log(K_3) \tag{3}$$

$$CuCl(c) \rightleftharpoons Cu(g) + \frac{1}{2}Cl_2(g) \rightarrow \log(K_4) = \log\left(\frac{P_{Cu}P_{Cl_2}^{\frac{1}{2}}}{a_{CuCl}}\right) \rightarrow \log(P_{Cu}) = \log(K_4) - \frac{1}{2}\log(P_{Cl_2}) \tag{4}$$

$$CuCl_2(c) \rightleftharpoons Cu(g) + Cl_2(g) \rightarrow \log(K_5) = \log\left(\frac{P_{Cu}P_{Cl_2}}{a_{CuCl}}\right) \rightarrow \log(P_{Cu}) = \log(K_4) - \log(P_{Cl_2}) \tag{5}$$

For CuCl₂(g) only:
Eq. 1 and 2.

$$Cu(c) + \frac{1}{2}Cl_2(g) \rightleftharpoons CuCl(g) \rightarrow \log(K_6) = \log\left(\frac{P_{CuCl}}{a_{Cu}P_{Cl_2}^{\frac{1}{2}}}\right) \rightarrow \log(P_{CuCl}) = \log(K_6) + \frac{1}{2}\log(P_{Cl_2}) \tag{6}$$

$$CuCl(c) \rightleftharpoons CuCl(g) \rightarrow \log(K_7) = \log\left(\frac{P_{CuCl}}{a_{CuCl}}\right) \rightarrow \log(P_{CuCl}) = \log(K_7) \tag{7}$$

$$CuCl_2(c) \rightleftharpoons CuCl(g) + \frac{1}{2}Cl_2(g) \rightarrow \log(K_8) = \log\left(\frac{P_{CuCl}P_{Cl_2}^{\frac{1}{2}}}{a_{CuCl}}\right) \rightarrow \log(P_{CuCl}) = \log(K_8) - \tag{8}$$

$$\frac{1}{2}\log(P_{Cl_2})$$

For CuCl₂(g) only:Eq. 1 and 2.

$$Cu(c) + Cl_2(g) \rightleftharpoons CuCl_2(g) \rightarrow \log(K_9) = \log\left(\frac{P_{CuCl_2}}{a_{Cu}P_{Cl_2}}\right) \rightarrow \log(P_{CuCl_2}) = \log(K_9) + \log(P_{Cl_2}) \tag{9}$$

$$CuCl(c) + \frac{1}{2}Cl_2(g) \rightleftharpoons CuCl_2(g) \rightarrow \log(K_{10}) = \log\left(\frac{P_{CuCl_2}}{a_{CuCl}P_{Cl_2}^{\frac{1}{2}}}\right) \rightarrow \log(P_{CuCl_2}) = \log(K_{10}) + \tag{10}$$

$$\frac{1}{2}\log(P_{Cl_2})$$

$$CuCl_2(c) \rightleftharpoons CuCl_2(g) \rightarrow \log(K_{11}) = \log\left(\frac{P_{CuCl_2}}{a_{CuCl_2}}\right) \rightarrow \log(P_{CuCl_2}) = \log(K_{11}) \tag{11}$$

For Cu₃Cl₃(g) only:Eq. 1 and 2.

$$3\text{Cu(c)} + \frac{3}{2}\text{Cl}_2\,(\text{g}) \rightleftharpoons \text{Cu}_3\text{Cl}_3\,(\text{g}) \rightarrow \log(K_{12}) = \log\left(\frac{P_{\text{Cu}_3\text{Cl}_3}}{a_{\text{Cu}}^3 P_{\text{Cl}_2}^{\frac{3}{2}}}\right) \rightarrow \log\left(P_{\text{Cu}_3\text{Cl}_3}\right) = \log(K_{12}) +$$

(12)

$$\frac{3}{2}\log\left(P_{\text{Cl}_2}\right)$$

$$3\text{CuCl(c)} \rightleftharpoons \text{Cu}_3\text{Cl}_3\,(\text{g}) \rightarrow \log(K_{13}) = \log\left(\frac{P_{\text{Cu}_3\text{Cl}_3}}{a_{\text{CuCl}}^3}\right) \rightarrow \log\left(P_{\text{Cu}_3\text{Cl}_3}\right) = \log(K_{13})$$

(13)

$$3\text{CuCl}_2\,(\text{c}) \rightleftharpoons \text{Cu}_3\text{Cl}_3\,(\text{g}) + \frac{3}{2}\text{Cl}_2\,(\text{g}) \rightarrow \log(K_{14}) = \log\left(\frac{P_{\text{Cu}_3\text{Cl}_3}\,P_{\text{Cl}_2}^{\frac{3}{2}}}{a_{\text{CuCl}_2}^3}\right) \rightarrow \log\left(P_{\text{CuCl}_2}\right) =$$

(14)

$$\log(K_{14}) - \frac{3}{2}\log\left(P_{\text{Cl}_2}\right)$$

Each of these equations can be plotted together to produce a volatility diagram for the system of Cu and the species in question. Volatility diagrams for each gas can be found below in Fig. K-1-K-4. A volatility diagram for all species can be found in Fig. K-5. MATLAB code for calculating and producing these plots can be found following Fig. K-5.

K.3. Volatility Diagrams

Figure K-1. Volatility diagram for Cu(g) only.
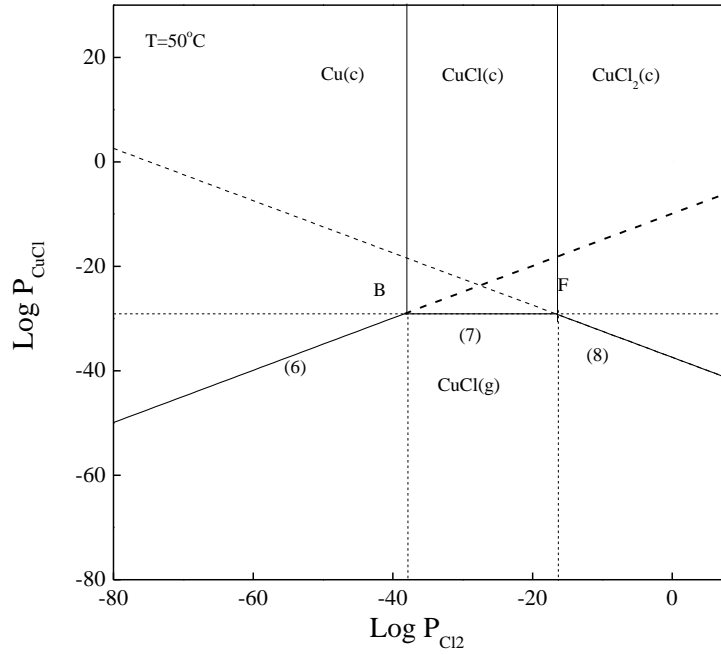
Figure K-2. Volatility Diagram for CuCl(g) only.
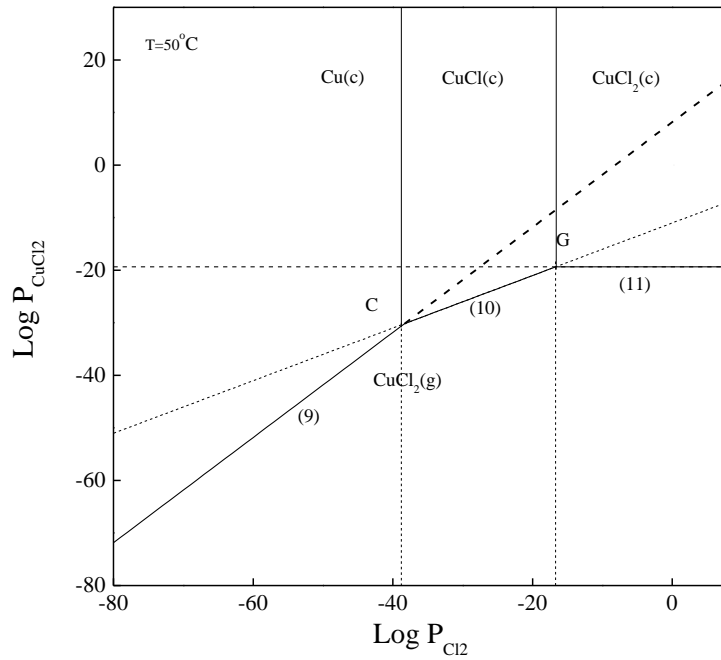
Figure K-3 Volatility diagram for $CuCl_2(g)$ only.
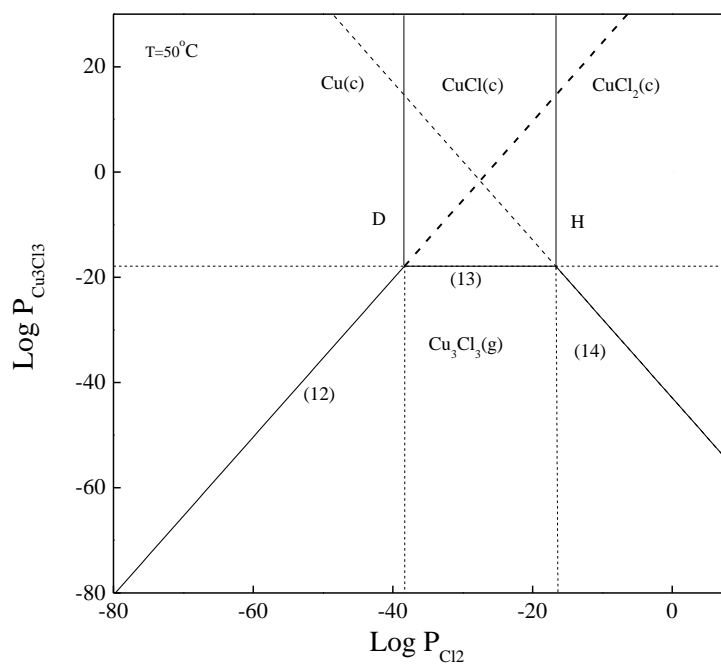
Figure K-4 Volatility diagram for $Cu_3Cl_3(g)$ only.
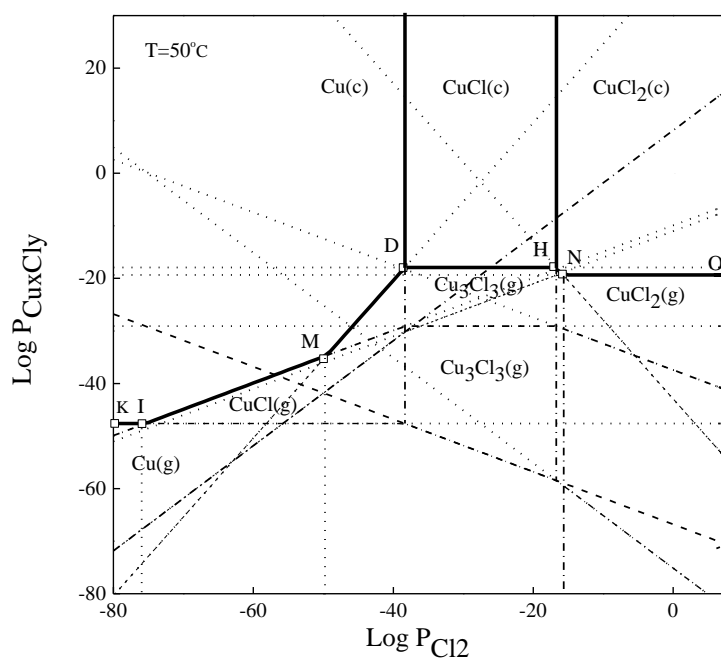
Figure K-5 Volatility diagram for entire Cu_xCl_y system.

295

K.4. Matlab Code

Matlab code for constructing these diagrams at T = 50ºC can be found below:

```matlab
%% Set up log(P_Cl2), log(K), and log(P_gas_species) (rxn)
logPCl2 = linspace(10,-80,1000);
logK = [19.17 8.34 -47.63 -66.80 -75.13 -9.91 -29.09 -37.43 8.16 -11.02 -
19.36 39.61 -17.91 -42.93];
rxn = {-2*logK(1); -2*logK(2); logK(3); logK(4)-0.5*logPCl2;
    logK(5)-logPCl2; logK(6)+0.5*logPCl2; logK(7); logK(8)-0.5*logPCl2;
    logK(9)+logPCl2; logK(10)+0.5*logPCl2; logK(11); logK(12)+1.5*logPCl2;
    logK(13); logK(14)-1.5*logPCl2};

%% For Cu(g) only
xmin = -80;
xmax = 10;
ymin = -80;
ymax = 30;

rxn1 = ones(1,2).*cell2mat(rxn(1));
rxn2 = ones(1,2).*cell2mat(rxn(2));
rxn3 = ones(1,length(logPCl2)).*cell2mat(rxn(3));
rxn4 = cell2mat(rxn(4));
rxn5 = cell2mat(rxn(5));

[L1] = InterX([rxn1; [ymin ymax]],[logPCl2; rxn3]);
[L2] = InterX([rxn2; [ymin ymax]],[logPCl2; rxn4]);

l1x = [L1(1) L1(1)];
l1y = [L1(2) ymax];
l2x = [L2(1) L2(1)];
l2y = [L2(2) ymax];
l3x = [xmin L1(1)];
l3y = [L1(2) L1(2)];
l4x = [L1(1) L2(1)];
l4y = [L1(2) L2(2)];
l5x = [L2(1) xmax];
l5y = [L2(2) ymin];

plot(l1x,l1y,l2x,l2y,l3x,l3y,l4x,l4y,l5x,l5y);

axis([xmin xmax ymin ymax]);
xlabel('Log P_{Cl_2}99 (atm)');
ylabel('Log P_(Amorim, Maciel et al.) (atm)');
legend('Reaction   1','Reaction   2','Reaction   3','Reaction   4','Reaction
5','Location','NorthWest');

%% For CuCl(g) only
xmin = -80;
xmax = 10;
ymin = -80;
ymax = 30;

rxn1 = ones(1,2).*cell2mat(rxn(1));
rxn2 = ones(1,2).*cell2mat(rxn(2));
rxn6 = cell2mat(rxn(6));
```

```matlab
rxn7 = ones(1,length(logPCl2)).*cell2mat(rxn(7));
rxn8 = cell2mat(rxn(8));

[L1] = InterX([rxn1; [ymin ymax]],[logPCl2; rxn6]);
[L2] = InterX([rxn2; [ymin ymax]],[logPCl2; rxn7]);

l1x = [L1(1) L1(1)];
l1y = [L1(2) ymax];
l2x = [L2(1) L2(1)];
l2y = [L2(2) ymax];
l3x = [xmin L1(1)];
l3y = [rxn6(length(rxn6)) L1(2)];
l4x = [L1(1) L2(1)];
l4y = [L1(2) L2(2)];
l5x = [L2(1) xmax];
l5y = [L2(2) rxn8(1)];

plot(l1x,l1y,l2x,l2y,l3x,l3y,l4x,l4y,l5x,l5y);

axis([xmin xmax ymin ymax]);
xlabel('Log P_{Cl_2} (atm)');
ylabel('Log P_{CuCl} (atm)');
legend('Reaction   1','Reaction   2','Reaction   6','Reaction   7','Reaction
8','Location','NorthWest');

%% For CuCl2(g) only
xmin = -80;
xmax = 10;
ymin = -80;
ymax = 30;

rxn1 = ones(1,2).*cell2mat(rxn(1));
rxn2 = ones(1,2).*cell2mat(rxn(2));
rxn9 = cell2mat(rxn(9));
rxn10 = cell2mat(rxn(10));
rxn11 = ones(1,length(logPCl2)).*cell2mat(rxn(11));

[L1] = InterX([rxn1; [ymin ymax]],[logPCl2; rxn9]);
[L2] = InterX([rxn2; [ymin ymax]],[logPCl2; rxn10]);

l1x = [L1(1) L1(1)];
l1y = [L1(2) ymax];
l2x = [L2(1) L2(1)];
l2y = [L2(2) ymax];
l3x = [xmin L1(1)];
l3y = [rxn9(length(rxn9)) L1(2)];
l4x = [L1(1) L2(1)];
l4y = [L1(2) L2(2)];
l5x = [L2(1) xmax];
l5y = [L2(2) rxn11(1)];

plot(l1x,l1y,l2x,l2y,l3x,l3y,l4x,l4y,l5x,l5y);

axis([xmin xmax ymin ymax]);
xlabel('Log P_{Cl_2} (atm)');
```

297

```matlab
ylabel('Log P_{CuCl_2} (atm)');
legend('Reaction   1','Reaction   2','Reaction   9','Reaction   10','Reaction
11','Location','NorthWest');

%% For Cu3Cl3(g) only
xmin = -80;
xmax = 10;
ymin = -80;
ymax = 30;

rxn1 = ones(1,2).*cell2mat(rxn(1));
rxn2 = ones(1,2).*cell2mat(rxn(2));
rxn12 = cell2mat(rxn(12));
rxn13 = ones(1,length(logPCl2)).*cell2mat(rxn(13));
rxn14 = cell2mat(rxn(14));

[L1] = InterX([rxn1; [ymin ymax]],[logPCl2; rxn12]);
[L2] = InterX([rxn2; [ymin ymax]],[logPCl2; rxn13]);

l1x = [L1(1) L1(1)];
l1y = [L1(2) ymax];
l2x = [L2(1) L2(1)];
l2y = [L2(2) ymax];
l3x = [xmin L1(1)];
l3y = [rxn9(length(rxn12)) L1(2)];
l4x = [L1(1) L2(1)];
l4y = [L1(2) L2(2)];
l5x = [L2(1) xmax];
l5y = [L2(2) rxn14(1)];

plot(l1x,l1y,l2x,l2y,l3x,l3y,l4x,l4y,l5x,l5y);

axis([xmin xmax ymin ymax]);
xlabel('Log P_{Cl_2} (atm)');
ylabel('Log P_{Cu_3Cl_3} (atm)');
legend('Reaction   1','Reaction   2','Reaction   12','Reaction   13','Reaction
14','Location','NorthWest');

%% Total volatility diagram for Cu(g), CuCl(g), CuCl2(g), and Cu3Cl3(g)
xmin = -80;
xmax = 10;
ymin = -80;
ymax = 30;

[L1] = InterX([logPCl2; rxn3],[logPCl2; rxn6]);
l1x = [xmin L1(1)];
l1y = [L1(2) L1(2)];
[L2] = InterX([logPCl2; rxn12],[logPCl2; rxn6]);
l2x = [L1(1) L2(1)];
l2y = [L1(2) L2(2)];
[L3] = InterX([logPCl2; rxn12],[logPCl2; rxn13]);
l3x = [L2(1) L3(1)];
l3y = [L2(2) L3(2)];
[L4] = InterX([logPCl2; rxn13],[logPCl2; rxn14]);
l4x = [L3(1) L4(1)];
```

```
l4y = [L3(2) L4(2)];
[L5] = InterX([logPCl2; rxn14],[logPCl2; rxn11]);
l5x = [L4(1) L5(1)];
l5y = [L4(2) L5(2)];
l6x = [L5(1) xmax];
l6y = [L5(2) L5(2)];
l7x = [L3(1) L3(1)];
l7y = [L3(2) ymax];
l8x = [L4(1) L4(1)];
l8y = [L4(2) ymax];

plot(l1x,l1y,l2x,l2y,l3x,l3y,l4x,l4y,l5x,l5y,l6x,l6y,l7x,l7y,l8x,l8y);
axis([xmin xmax ymin ymax]);
xlabel('Log P_{Cl_2} (atm)');
ylabel('Log P_{Cu or CuCl or CuCl_2 or Cu_3Cl_3} (atm)');
legend('Reaction    3','Reaction    6','Reaction   12','Reaction   13','Reaction
14','Reaction 11','Reaction 1','Reaction 2','Location','NorthWest');
```

The function InterX is used to calculate the intersection and self-intersections between two curves within a particular range. It is authored by NS and is available online at the Matlab File Exchange (File ID #22441).

L. Gibbs Free Energy Minimization

L.1. Introduction
Total Gibbs free energy for a system is defined as:

$$G_{total}\left(T, P, \{n_j\}_{j=1}^k\right) = \sum_p \sum_j n_{pj}\mu_{pj}$$

Where n_{pj} defined as mols of species j in phase p, and μ_{pj} is defined as the chemical potential of species j in phase p. Chemical potential is defined by:

$$\mu_j = \left(\frac{\partial\left(nG(T, P, \{n_i\}_{i=1}^k)\right)}{\partial n_j}\right)_{T,P,N_{i\neq j}} = G_j^o(T) + RT\ln\frac{\hat{f}_j}{f_j^o}$$

Where G^o is the heat of formation, R is the universal gas constant, T is temperature, f hat is the species fugacity, and f0 is the reference fugacity.
For gasses:

$$\hat{f}_j = \hat{\phi}_j y_j P$$

Where ϕ is the fugacity coefficient, $y_j P$ is the partial pressure of j.

$$f_j^o = P_0$$

$$\mu_j = \Delta G_{fj}^o(T) + RT\ln\left(\frac{P}{P_0}\frac{n_j}{\Sigma n_j}\right) = \Delta G_{fj}^o(T) + RT\ln\left(\frac{P}{P_0}y_j\right)$$

For Solids:

$$\mu_j = G_j^o(T) + RT\ln\frac{f_j}{f_j^{sat}}$$

Where f^{sat} is the fugacity at P^{sat}

$$f_j = \phi_j^{sat}P_j^{sat}\exp\left(\frac{\left(V_j^{sat}(P - P_j^{sat})\right)}{RT}\right)$$

$$f_j^{sat} = P_j^{sat}$$

Where ϕ^{sat} is the fugacity coefficient at P^{sat}.

$$\phi_j^{sat} = \exp\left(\frac{B_{ii}P_j^{sat}}{RT}\right)$$

Where B_{jj} is the virial coefficient corresponding to volume occupied by molecules.

$$\mu_j = \Delta G^o_{fj}(T) + RTln\left(exp\left(\frac{B_{jj}P^{sat}_j + \left(V^{sat}_j(P - P^{sat}_j)\right)}{RT}\right)\right)$$

$$\mu_j = \Delta G^o_{fj}(T) + B_{jj}P^{sat}_j + \left(V^{sat}_j(P - P^{sat}_j)\right) = \Delta G^o_{fj}(T) + \left(V^{sat}_j(P - P^{sat}_j)\right)$$

The B_{jj} term goes to zero if it is assumed that gas molecules have negligible volume. For a system at equilibrium:

$$\sum_j \frac{\partial(nG)}{\partial n_j} = \sum_j \mu_j = 0$$

A generic atom balance is given as:

$$N_a - \sum_j v_{a,j}n_j = 0$$

Where N_a is the total number of atom a, n_j are mols of species j, and v_{aj} is the atoms of a in species j. Mols can be constrained to only positive values

$$n_j \geq 0 \ \forall j = 1, 2, \ldots, k$$

The most energetically favorable distribution of products at equilibrium is the product distribution that has minimum total Gibbs energy while satisfying mass balance and equilibrium constraints.

$$\left\{\begin{array}{c} \left(\min_{\{n_j\}^k_{j=1}} \left(G_{total}\left(T, P, \{n_j\}^k_{j=1}\right)\right)\right) \\ j = 1, 2, \ldots, k \\ s.t. \\ \sum_j \frac{\partial(nG)}{\partial n_j} = \sum_j \mu_j = 0 \\ N_a - \sum_j v_{a,j}n_j = 0 \\ n_j \geq 0 \ \forall j = 1, 2, \ldots, k \end{array}\right\}$$

L.2. Examples

Example: 1 kmol SiOCH$_2$ and 6 kmol CF$_4$ at P = 10^{-5}atm

1. Linear constraint of atomic mass conservation

$$\begin{pmatrix} n_{Si,SiOCH_2} & n_{Si,SiO_2} & n_{Si,CF_4} & n_{Si,SiF_4} & n_{Si,CO_2} & n_{Si,H_2} \\ n_{O,SiOCH_2} & n_{O,SiO_2} & n_{O,CF_4} & n_{O,SiF_4} & n_{O,CO_2} & n_{O,H_2} \\ n_{C,SiOCH_2} & n_{C,SiO_2} & n_{C,CF_4} & n_{C,SiF_4} & n_{C,CO_2} & n_{C,H_2} \\ n_{F,SiOCH_2} & n_{F,SiO_2} & n_{F,CF_4} & n_{F,SiF_4} & n_{F,CO_2} & n_{F,H_2} \\ n_{H,SiOCH_2} & n_{H,SiO_2} & n_{H,CF_4} & n_{H,SiF_4} & n_{H,CO_2} & n_{H,H_2} \end{pmatrix} \begin{pmatrix} n_{SiOCH_2} \\ n_{SiO_2} \\ n_{CF_4} \\ n_{SiF_4} \\ n_{CO_2} \\ n_{H_2} \end{pmatrix} = \begin{pmatrix} n_{Si,in} \\ n_{O,in} \\ n_{C,in} \\ n_{F,in} \\ n_{H,in} \end{pmatrix}$$

2. Define feed (1 kmol SiOCH$_2$, 6 kmol CF$_4$)

$$\begin{pmatrix} 1 & 1 & 0 & 1 & 0 & 0 \\ 1 & 2 & 0 & 0 & 2 & 0 \\ 1 & 0 & 1 & 0 & 1 & 0 \\ 0 & 0 & 4 & 4 & 0 & 0 \\ 2 & 0 & 0 & 0 & 0 & 2 \end{pmatrix} \begin{pmatrix} 1 \\ 0 \\ 6 \\ 0 \\ 0 \\ 0 \end{pmatrix} = \begin{pmatrix} 1 \\ 1 \\ 7 \\ 24 \\ 2 \end{pmatrix}$$

3. Minimize total Gibbs free energy function

$$\min_{n_j} \left\{ \frac{G_{Total}}{RT} = \sum_{phase} \sum_{j} \frac{n_{p,j}\mu_{p,j}}{RT} \right\}$$

The Gibbs free energy minimization scheme utilizes three separate MATLAB files "createSpeciesHSC.m", "gibbsminsolve_Cr_phasecorrected.m", and "gibbsInterface_solve.m". "createSpeciesHSC.m" is a list of possible species that can form in the system at equilibrium. The list is sorted into gas and solid phase components using the specs.gas and specs.solid tags. Each gas phase component has 3 variables:

`specs.gas(n).name` : gives the name in the form of the molecular formula
`specs.gas(n).bal` : elemental composition of each compound `[Si O C F H N I]`
`specs.gas(n).Gf` : Gibbs free energies of formation at temperatures defined in the temperature array contained in "gibbsInterface_solve.m".

The data for these Gibbs free energies of formation can be taken in the form of ΔG_f° reported in the NIST-JANAF databases or in the HSC software. Solid phase components, generally in the form of the thin film material of interest, contains an added variable:

`specs.solid(n).molvol` : this is the molar volume (i.e. inverse of the molar density) of the material of interest. These values can be calculated based off of the reported density of the material.

"gibbsminsolve_Cr_phasecorrected.m" is the portion of the MATLAB code which does the actual calculations for minimizing the objective function in the form of the total Gibbs free energy of the system. This file contains the gas constant (R), standard state pressure (Po), array of temperatures wherein the calculation is done at each element (T= [...], and the operating pressure (P). The conditions used for the simulations done in this work are provided below.

```
R = 0.008314;
Po = 0.986923267;
T = [1 100 200 298.15 300 400 500…2000];
P = 1e-5;
```

Due to the numerical nature of the algorithm used in calculating the minimum, initial guesses must be provided in the form of an array (x0). Generally these values are held at unity for each species:

```
x0 = [1 1 1 1 1 1 1 1 1 1 1 1 1 1 1 1 1 1 1 1 1 1];
```

Additionally, a lower boundary must be established such as that seen in the solving criteria, depicting that one cannot have less than zero moles of any component, thus the lower bound is set to zero in the following array (LB = zeros…)

```
LB = zeros(1,lenGas+lenSol).
```
Finally, the "gibbsInterface_solve.m" file contains the vital information of the names of the gases and solids, for example:
```
gases = {'CO2(g)'  'SiF4(g)'  'COF2(g)'  'SiF3(g)'  'CO(g)'  'CF4(g)'  'SiF2(g)'
'N2(g)'  'CH4(g)'  'CHF3(g)'  'CH2F2(g)'  'CH3F(g)'  'CH2O(g)'  'CIF3(g)'  'H2(g)'
'HF(g)'  'HCN(g)'  'H2O(g)'  'NH3(g)'  'SiF(g)'};
```

```
solids = {'SiOCH2(s)'};
```
as well as the input feed of each mol of each atom. For this example a feed of 1 kmol of $SiOCH_2(s)$ and 6 kmol of $CF_4(g)$ was simulated. Converting this into a column vector of Si, O, C, F, H, N, and I atoms in kmol results in:
```
    input = [1          % mol Si fed
             1          % mol O fed
             7          % mol C fed
             24         % mol F fed
             2          % mol H fed
             0          % mol N fed
             0];        % mol I fed
```
This is then handed as input into the aforementioned "gibbsminsolve_Cr_phasecorrected.m" file, which in turn matches each component name with the specific Gibbs free energy data contained in "createSpeciesHSC.m" and minimizes the total Gibbs free energy function.

The output can then be graphed to visualize the product distribution of components predicted to be present at equilibrium as a function of temperature—since the calculation was done at each temperature predefined in the T = […] array previously shown.
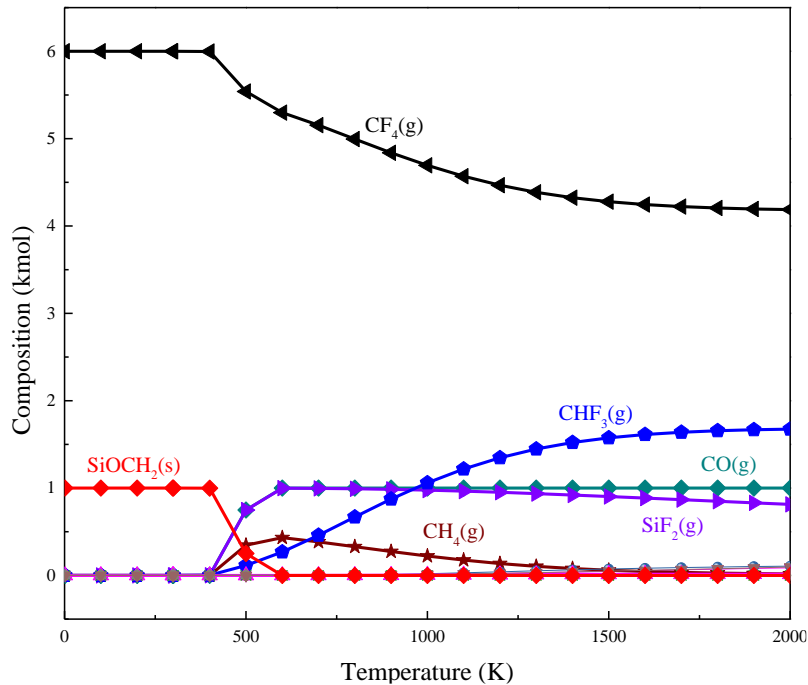
Figure L-1 The plot of composition as a function of temperature for the system of 1 kmol $SiOCH_2$ and 6 kmol CF_4 at P = 10^{-5}atm based on the Gibbs free energy minimization.

L.3. Matlab Code

The full code for the "createSpeciesHSC.m" of this example is shown below:

```
function specs = createSpeciesHSC()
%Gases
specs.gas(1).name = 'CO2(g)';
specs.gas(1).bal = [0 2 1 0 0 0 0]';   %element composition of each compound
[Si O C F H N I]
specs.gas(1).Gf = [-393.151
-393.683
-394.085
-394.389
-394.394
-394.675
-394.939
-395.182
-395.398
-395.586
-395.748
-395.886
-396.001
-396.098
-396.177
-396.24
-396.288
-396.323
-396.344
-396.353
-396.349
-396.333]';
```

304

```
specs.gas(2).name = 'SiF4(g)';
specs.gas(2).bal = [1 0 0 4 0 0 0]';
specs.gas(2).Gf = [-1609.428
-1599.596
-1586.418
-1572.711
-1572.449
-1558.165
-1543.75
-1529.287
-1514.816
-1500.354
-1485.91
-1471.484
-1457.077
-1442.686
-1428.308
-1413.941
-1399.58
-1385.222
-1370.418
-1353.088
-1335.767
-1318.454]';
specs.gas(3).name = 'COF2(g)';
specs.gas(3).bal = [1 1 0 2 0 0 0]';
specs.gas(3).Gf = [-635.798
-632.823
-628.302
-623.329
-623.232
-617.909
-612.454
-606.918
-601.329
-595.701
-590.046
-584.369
-578.676
-572.968
-567.247
-561.516
-555.774
-550.021
-544.258
-538.485
-532.7
-526.905]';
specs.gas(4).name = 'SiF3(g)';
specs.gas(4).bal = [1 0 0 3 0 0 0]';
specs.gas(4).Gf = [-1082.273
-1080.471
-1077.058
-1073.218
-1073.143
-1068.976
-1064.673
```

```
-1060.29
-1055.855
-1051.384
-1046.883
-1042.354
-1037.8
-1033.221
-1028.615
-1023.983
-1019.323
-1014.634
-1009.467
-1001.745
-994.005
-986.247]';
specs.gas(5).name = 'CO(g)';
specs.gas(5).bal = [0 1 1 0 0 0 0]';
specs.gas(5).Gf = [-113.805
-120.239
-128.526
-137.163
-137.328
-146.338
-155.414
-164.486
-173.518
-182.497
-191.416
-200.275
-209.075
-217.819
-226.509
-235.149
-243.74
-252.284
-260.784
-269.242
-277.658
-286.034]';
specs.gas(6).name = 'CF4(g)';
specs.gas(6).bal = [0 0 1 4 0 0 0]';
specs.gas(6).Gf = [-927.229
-916.822
-902.995
-888.507
-888.229
-873.107
-857.841
-842.523
-827.197
-811.884
-796.596
-781.337
-766.108
-750.909
-735.739
-720.597
```

```
-705.479
-690.383
-675.308
-660.251
-645.21
-630.184]';
specs.gas(7).name = 'SiF2(g)';
specs.gas(7).bal = [1 0 0 2 0 0 0]';
specs.gas(7).Gf = [-587.013
-590.839
-594.726
-598.278
-598.343
-601.733
-604.955
-608.046
-611.029
-613.918
-616.723
-619.449
-622.103
-624.685
-627.201
-629.651
-632.036
-634.359
-636.173
-635.401
-634.583
-633.72]';
specs.gas(8).name = 'N2(g)';
specs.gas(8).bal = [0 0 0 0 0 2 0]';
specs.gas(8).Gf = [0
0
0
0
0
0
0
0
0
0
0
0
0
0
0
0
0
0
0
0
0
0]';
specs.gas(9).name = 'CH4(g)';
specs.gas(9).bal = [0 0 1 0 4 0 0]';
specs.gas(9).Gf = [-66.911
```

```
-64.353
-58.161
-50.768
-50.618
-42.054
-32.741
-22.887
-12.643
-2.115
8.616
19.492
30.472
41.524
52.626
63.761
74.918
86.088
97.265
108.445
119.624
130.802]';
specs.gas(10).name = 'CHF3(g)';
specs.gas(10).bal = [0 0 1 3 1 0 0]';
specs.gas(10).Gf = [-690.096
-683.593
-673.566
-662.586
-662.372
-650.535
-638.317
-625.867
-613.274
-600.593
-587.861
-575.1
-562.325
-549.546
-536.77
-524
-511.239
-498.488
-485.747
-473.016
-460.296
-447.585]';
specs.gas(11).name = 'CH2F2(g)';
specs.gas(11).bal = [0 0 1 2 2 0 0]';
specs.gas(11).Gf = [-443.005
-439.137
-431.68
-423.076
-422.905
-413.261
-403.037
-392.424
-381.549
-370.494
```

```
-359.319
-348.062
-336.752
-325.407
-314.042
-302.665
-291.282
-279.9
-268.519
-257.142
-245.77
-234.404]';
specs.gas(12).name = 'CH3F(g)';
specs.gas(12).bal = [0 0 1 1 3 0 0]';
specs.gas(12).Gf = [-226.275
-223.802
-217.703
-210.359
-210.21
-201.716
-192.515
-182.822
-172.783
-162.5
-152.045
-141.47
-130.81
-120.093
-109.338
-98.557
-87.761
-76.956
-66.147
-55.338
-44.53
-33.725]';
specs.gas(13).name = 'CH2O(g)';
specs.gas(13).bal = [0 1 1 0 2 0 0]';        %element composition of each
compound [Si O C F H N I]
specs.gas(13).Gf = [-112.057
-112.63
-111.598
-109.921
-109.884
-107.615
-104.923
-101.917
-98.675
-95.259
-91.712
-88.068
-84.351
-80.578
-76.763
-72.914
-69.039
-65.141
```

```
-61.225
-57.292
-53.345
-49.385]';
specs.gas(14).name = 'CIF3(g)';
specs.gas(14).bal = [0 0 1 3 0 0 1]';
specs.gas(14).Gf = [-583.227
-581.659
-576.793
-571.109
-570.997
-564.51
-553.952
-540.717
-527.541
-514.427
-501.372
-488.371
-475.421
-462.516
-449.651
-436.822
-424.023
-411.25
-398.499
-385.766
-373.046
-360.336]';
specs.gas(15).name = 'H2(g)';
specs.gas(15).bal = [0 0 0 0 2 0 0]';
specs.gas(15).Gf = [0
0
0
0
0
0
0
0
0
0
0
0
0
0
0
0
0
0
0
0
0]';
specs.gas(16).name = 'HF(g)';
specs.gas(16).bal = [0 0 0 1 1 0 0]';
specs.gas(16).Gf = [-272.499
-273.266
-273.947
```

310

```
-274.646
-274.659
-275.344
-275.981
-276.566
-277.102
-277.59
-278.036
-278.443
-278.816
-279.157
-279.471
-279.76
-280.027
-280.273
-280.502
-280.714
-280.911
-281.093]';
specs.gas(17).name = 'HCN(g)';
specs.gas(17).bal = [0 0 1 0 1 1 0]';
specs.gas(17).Gf = [135.529
131.784
128.187
124.725
124.66
121.192
117.769
114.393
111.063
107.775
104.525
101.308
98.12
94.955
91.812
88.687
85.579
82.484
79.403
76.333
73.274
70.226]';
specs.gas(18).name = 'H2O(g)';
specs.gas(18).bal = [0 1 0 0 2 0 0]';
specs.gas(18).Gf = [-238.921
-236.584
-232.766
-228.582
-228.5
-223.901
-219.051
-214.007
-208.812
-203.496
-198.083
-192.59
```

```
-187.033
-181.425
-175.774
-170.089
-164.376
-158.639
-152.883
-147.111
-141.325
-135.528]';
specs.gas(19).name = 'NH3(g)';
specs.gas(19).bal = [0 0 0 0 3 1 0]';
specs.gas(19).Gf = [-38.907
-34.034
-25.679
-16.367
-16.183
-5.941
4.8
15.879
27.19
38.662
50.247
61.91
73.625
85.373
97.141
108.918
120.696
132.469
144.234
155.986
167.725
179.447]';
specs.gas(20).name = 'SiF(g)';
specs.gas(20).bal = [1 0 0 1 0 0 0]';
specs.gas(20).Gf = [-21.912
-30.708
-41.165
-51.559
-51.755
-62.254
-72.636
-82.905
-93.071
-103.142
-113.123
-123.02
-132.837
-142.578
-152.246
-161.844
-171.372
-180.834
-189.783
-196.144
-202.456
```

```
-208.722]';
specs.solid(1).name = 'SiOCH2(s)';
specs.solid(1).bal = [1 1 1 0 2 0 0]';
specs.solid(1).molvol = 0.0000226888218;
specs.solid(1).Gf = [-556.4131
-538.8001
-521.1871
-503.89994
-503.5741
-485.9611
-468.3481
-450.7351
-433.1221
-415.5091
-397.8961
-380.2831
-362.6701
-345.0571
-327.4441
-309.8311
-292.2181
-274.6051
-256.9921
-239.3791
-221.7661
-204.1531]';
end  %creates structure "specs" that contains name, Gibbs energy of formation
(from HSC data)
```

The full code for the "gibbsInterface_solve.m" of this example is shown below:

```matlab
clear;
gases = {'CO2(g)' 'SiF4(g)' 'COF2(g)' 'SiF3(g)' 'CO(g)' 'CF4(g)' 'SiF2(g)'
'N2(g)' 'CH4(g)' 'CHF3(g)' 'CH2F2(g)' 'CH3F(g)' 'CH2O(g)' 'CIF3(g)' 'H2(g)'
'HF(g)' 'HCN(g)' 'H2O(g)' 'NH3(g)' 'SiF(g)'};
solids = {'SiOCH2(s)'};

    n = 0;
    % initial feed of 1 kmol SiOCH2(s), 6 kmol CF4(g)
    input = [1          % mol Si fed
             1          % mol O fed
             7          % mol C fed
             24         % mol F fed
             2          % mol H fed
             0          % mol N fed
             0];        % mol I fed
    moles = gibbsminsolve_Cr_phasecorrected(gases,solids,input,'HSC');
    eqBal(1,n+1) = {[num2str(input(3)/2) ' mol O2']};
    eqBal(2,n+1) = {moles};


    figure;
    markers = '+o*.xsd';
    colors = 'rgbkmcy';


    hold;
    c = 1;
    m = 1;


    for z = 2:length(gases)+length(solids)+1
        plot(moles(:,1),moles(:,z),strcat(colors(c),markers(m)),'MarkerSize',
8);
        c = c + 1;
        if c == 8
            m = m + 1;
            c = 1;



        end
    end
    legend([gases solids])
    xlabel('Temperature (K)');ylabel('Number of Moles');
```

The full code for the "gibbsminsolve_Cr_phasecorrected.m" of this example is shown below:

```matlab
function [moles] = gibbsminsolve_Cr_phasecorrected(gases,solids,beq,database)
global specs;
if strcmp(database,'NIST') == 1
    specs = createSpeciesNIST();
elseif strcmp(database,'HSC') == 1
    specs = createSpeciesHSC();
else
    error('Input name of thermodynamic database.');
end
R = 0.008314;  % gas constant [kJ/mol*K]
Po = 0.986923267;  % standard state pressure [atm]
T = [1 100 200 298.15 300 400 500 600 700 800 900 1000 1100 1200 1300 1400
1500 1600 1700 1800 1900 2000];    %temperature range in Kelvin
```

```matlab
P = 1e-5;    %Total operating pressure in atm
lenGas = length(gases);
lenSol = length(solids);
Ggas = zeros(length(gases),1);
Gsol = zeros(length(solids),1);
x0 = [1 1 1 1 1 1 1 1 1 1 1 1 1 1 1 1 1 1 1 1 1 1 1];
LB = zeros(1,lenGas+lenSol);
for t = 1:length(T);
    for n = 1:lenGas  %make array of G_f/RT values for gases
        for m = 1:length(specs.gas)
            if strcmp(gases{n},specs.gas(m).name) == 1
                Aeq(:,n) = specs.gas(m).bal;
                Ggas(n) = specs.gas(m).Gf(t)/R/T(t);
                break;
            elseif m == length(specs.gas)
                str = gases{n};
                error(['Input compound ' str ' is not in list.']);
            end
        end
    end

    for n = 1:lenSol  %make array of Gf/RT values for solids
        for m = 1:lenSol
            if strcmp(solids{n},specs.solid(m).name) == 1
                Aeq(:,n+lenGas) = specs.solid(m).bal;
                Gsol(n)       =         specs.solid(m).Gf(t)/R/T(t)        +
specs.solid(m).molvol*101.325*(P-Po)/R/T(t);
                break;
            elseif m == length(specs.solid)
                str = solids{n};
                error(['Input compound ' str ' is not in list.']);
            end
        end
    end

    options = optimset('Algorithm','sqp');
    [x,f] = fmincon(@gibbsArray,x0,[],[],Aeq,beq,LB,[],[],options);

    moles(t,1) = T(t);
    moles(t,2:length(x)+1) = x;
    gibbs(t,1) = T(t);
    gibbs(t,2) = f*R*T(t);
end


function F = gibbsArray(nj)
    ntot = sum(nj(1:lenGas));

    F   =   sum(nj(1:lenGas)'.*(Ggas  +  log(nj(1:lenGas)'/ntot*P/Po)))  +
sum(nj(lenGas+1:lenGas+lenSol)'.*Gsol);
end

end
```

M. Gaussian

M.1. Gaussian Introduction

GAUSSVIEW program was used to compute thermochemical values of various compounds. Calculations were based on a white paper published by Orchterski [1]. Gaussian calculates optimal geometry and frequency of gaseous compounds using density functional theory. Theoretical thermochemical data can then be calculated from the output of the geometry optimization simulation and a frequency optimization calculation. Total electronic energy, ε_o is the relevant output from geometry optimization. Frequency optimization gives values for zero point correction (ε_{zpe}), thermal energy (E_{tot}), thermal enthalpy correction (H_{Corr}), and thermal free energy correction (G_{corr}).

The heat of formation for a molecule at 0 K is given by:

$$\Delta_f H^0(M, 0K) = \sum_j x_j \Delta_f H^0(j, 0K) - \sum D_0(M)$$

Where x_j is the atoms of j in molecule M, $\Delta_f H^0(j, 0K)$ is the heat of formation of atom j at 0K, and sum(D_0) is the atomization energy.

$$\sum D_0(M) = \sum x_j \varepsilon_0(j) - \left(\varepsilon_0(M) + \varepsilon_{zpe}(M)\right)$$

The heat of formation for a molecule at 298K is given by:

$$\Delta_f H^0(M, 298K) = \Delta_f H^0(M, 0K) + \left(H_{Corr}(M) - \varepsilon_{zpe}(M)\right) - \sum_j x_j H_{Corr}(j)$$

Gibbs free energy is given by:

$$G = H - TS$$

So that

$$\Delta_f G^0(M, 298K) = \Delta_f H^0(M, 298K) - T\left(\sum_j x_j S_{Corr}(j) - S_{Corr}(M)\right)$$

Where:

$$S_{Corr} = \frac{(H_{Corr} - G_{Corr})}{T^0}$$

M.2. Sample Calculations with SiH$_4$

Examples of calculating heat of formation of formaldehyde and bond dissociation energy of SiH$_4$ are discussed here. A comparisons of theoretical calculation and experimental values published by Casserly [2] is shown in Table M-1.

Table M-1 Output from Gaussian simulations, units are in Hartrees/molecule. *Hcorr for atomic species have been taken from literature [3].

Species	ε	ε_{ZPE}	H_{corr}*	G_{corr}	S_{corr}
Si	-289.39	0.0000	1.23E-03	-1.57E-02	6.07E-05
C	-37.86	0.0000	3.98E-04	-1.45E-02	5.67E-05
O	-75.09	0.0000	1.66E-03	-1.50E-02	5.81E-05
H	-0.50	0.0000	1.61E-03	-1.07E-02	4.36E-05
H_2CO	-114.55	0.0265	3.03E-02	4.86E-03	8.54E-05
SiH_4	-291.92	0.0311	3.51E-02	1.19E-02	7.79E-05
SiH_3	-291.26	0.0211	2.51E-02	4.87E-04	8.26E-05

Using data from Table M-2, values for heat of formation and Gibbs free energy of formation can be calculated.

Table M-2 values for heat of formation and Gibbs free energy of formation can be calculated.

Species	ΣD_0	$\Delta_f H^0(0K)$*	$\Delta_f H^0(298K)$			$\Delta_f G^0(298K)$
			Calculation	Gleason	Experimental[4,5,6]	
Si	0.00	106.52	107.23	107.23	107.55	107.23
C	0.00	169.98	171.21	171.21	171.29	171.21
O	0.00	58.98	59.42	59.43	59.55	59.42
H	0.00	51.63	52.10	52.10	52.10	52.10
H_2CO	358.47	-26.25	-27.16	-27.10	-26.00	-5.31
SiH_4	304.66	8.38	6.08	6.15	8.20	35.58
SiH_3	215.53	45.88	44.56	44.60	48.50	65.01

Bond dissociation can then be calculated with the following:

$$\Delta_{BDE}H^0(298K) = \sum_j x_j \Delta_f H^0(products,298K) - \sum_j x_j \Delta_f H^0(reactnts,298K)$$

Similarly for the Gibbs energy of bond dissociation:

$$\Delta_{BDE}G^0(298K) = \sum_j x_j \Delta_f G^0(products,298K) - \sum_j x_j \Delta_f G^0(reactnts,298K)$$

Table M-3 Bond dissociation energy of silane, units in kCal/mol.

Source	$\Delta G(298K)$	$\Delta H(298K)$
Calculation	81.52	90.58
Gleason	80.85	90.55
Experimental	N/A	91.1

M.3. References

[1] Ochterski, J. W. Thermochemistry in Gaussian. www. gaussian.com (accessed December 9, 2015)

[2] Casserly, T. B. and Gleason, K. K., Plasma Process. Polym. 2005, 2, 669-678

[3] Curtiss, L. A., et al., J. Chem. Phys. 106, 1063 (1997)

[4]Q. Z. Zhang, S. K. Wang, J. H. Zhou, Y. H. Gu, J. Phys. Chem.A 2002, 106, 115.

[5] G. Rauhut, P. Pulay, J. Phys. Chem. 1995, 99, 3093.

[6] M. W. Wong, Chem. Phys. Lett. 1996, 256, 391.

N. HSC Database

N.1. HSC Operating Procedure

1. Run HSC. The menu shown below in Fig. N-1 should appear.
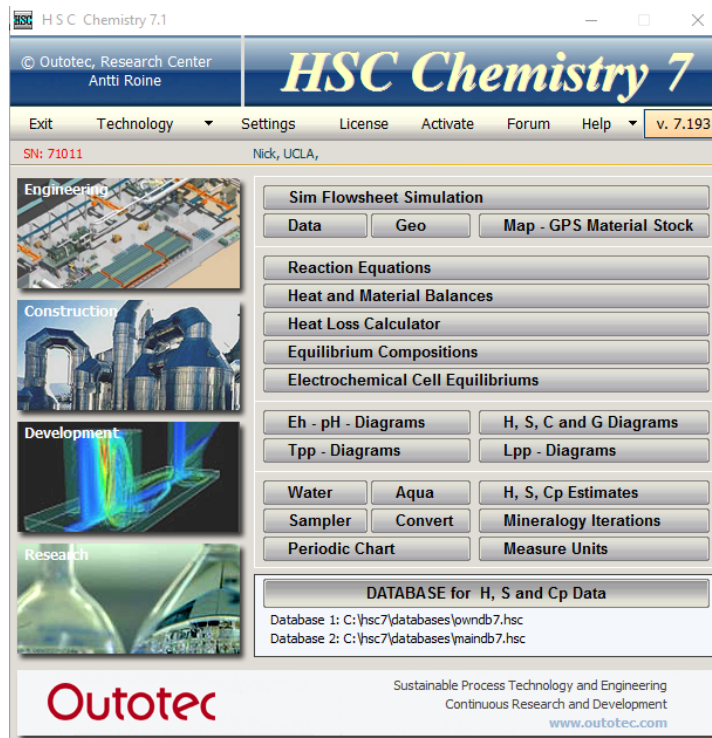
Figure N-1 Main Menu of HSC Chemistry 7.

2. Click on "DATABASE for H, S and Cp Data". The menu shown in Fig. N-2 below should appear.
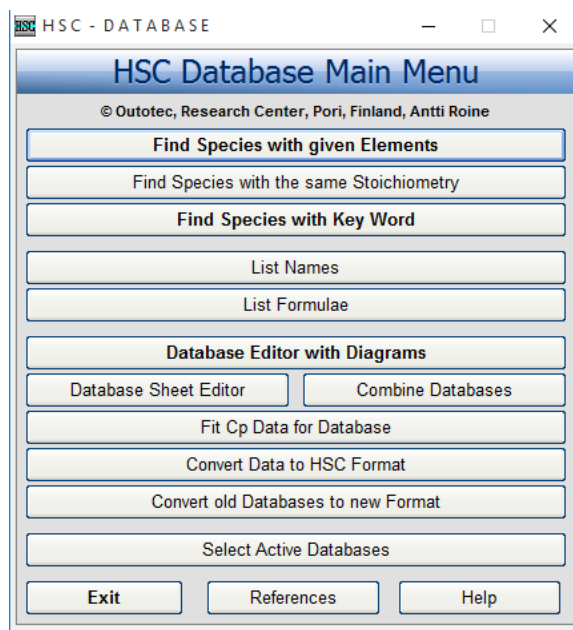
Figure N-2 HSC Database Main Menu.

3. Click on "Database Editor with Diagrams". The screen shown in Fig. N-3below should appear.
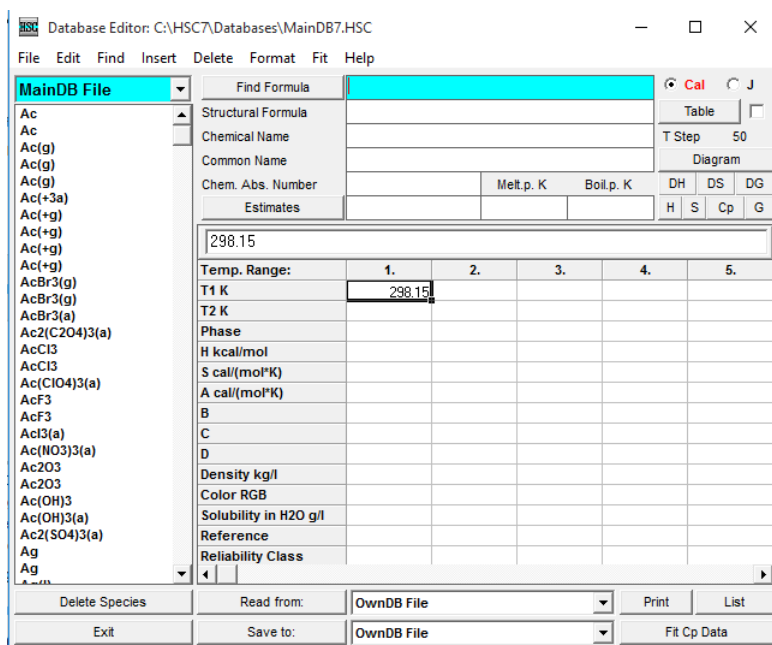
Figure N-3 Database Editor.

4. Values can be set to be reported in joules and calories using the radio buttons in the top right hand corner. The database can be searched by entering a formula in the "Find Formula" field highlighted in teal and clicking on "Find Formula". The desired species can be selected from the list on the left hand side.

5. Once a desired species has been found, thermodynamic data can be displayed using the "Table" button in the upper right hand corner. Clicking "Table" should bring up two

320

screens, shown below in Fig. N-4 and Fig. N-5. SiO_2 is being used as an example compound.

Figure N-4 Reaction Equations.

Figure N-5 Thermodynamic Results.

6. Results format can be cycled between Normal and Delta using the radio buttons beneath "Format of Results". The table of values given in Fig. N-4 can be updated by pressing the "Calculate" button in the lower right of Fig. N-4. The temperature range can be altered by changing the temperature values in Fig. N-4.

O. Etching of carbon-doped silicon dioxide

Gases primarily used in etching interlayer dielectric materials include SF_6 and perfluorocarbons (PFC) such as CF_4. These etchants generally have high global warming potentials (GWP), making their increased usage undesirable (Table O-1). In this work, a systematic study based on the assessment of various non-PFC yet halogen-based gases utilizes Gibbs free energy minimization to identify the thermodynamically favored etch products for etching carbon doped silica films. This technique operates under the precept that a system at equilibrium will tend to have a minimum total Gibbs free energy.

Gibbs minimization assists in the identification and quantification of species predicted to form at equilibrium (Figure O-1 a,b,c). Once identified, these products can be used in conjunction with idealized surface-gas reactions (Table O-2) and volatility diagrams (Figure O-2) to screen various chemistries. The viability of a large number of etchants was assessed using thermodynamic analysis to calculate the partial pressure of the main etch product—SiF_4—as a function of the etchant pressure. Both CF_4 and CHF_3 with H_2 were selected to explore the effects of differing amounts of additive hydrogen. Based on our thermodynamic analysis, H_2 is an effective addition to fluorocarbon etchants, resulting in increased partial pressure of the etch product (Figure O-2).

For this study, special focus is placed on the use of partially hydrogenated fluorocarbons, e.g. CHF_3, as well as additive H_2, to allow for independent control of the F/H ratio and observation of its influence on etch rate with the aim of supplanting a portion of fluorocarbon gas usage with hydrogen while potentially enhancing or maintain the etch rate of each material. Introduction of hydrogen is believed to target and liberate the carbon present within the silica structure through formation of volatile organic species such as CH_4. For a simple system such as etching SiO_2 with CF_4, Gibbs minimization predicts production of SiF_4 and CO_2 (Figure O-1a). Upon introduction of a small fraction of hydrogen by changing the etchant to CHF_3, the product distribution becomes significantly more complex (Figure O-1b). This distribution only evolves further upon introduction of molecular hydrogen (Figure O-1c), suggesting that, among the typical products of SiF_4 and CO_2, HF, CO, and CH_4 have may be generated.

In an effort to identify viable plasma parameters, preliminary experiments were performed using CF_4 with 1400W source power to study the effect of substrate bias—and thus ion energy—on the etch rate of each of the three materials. At lower bias values, most notably those below 10W, a net deposition was observed on the medium carbon doped silica film, while very little etch was seen on the low carbon doped film (Figure O-3). X-ray photoelectron spectroscopy (XPS) analysis was performed to elucidate the surface composition of the medium carbon doped film at this plasma condition. Detailed scans for Si 2p (Figure O-4a) show the expected Si-O, Si-C, Si-Si bonding states for the blank film (red); however, no Si signal was detected in the apparent deposited film. The C 1s spectra (Figure O-4b) of the blank film (red) shows C-C and C-Si bonding states, likely from surface hydrocarbon contamination and substrate composition. Post-etch (blue), the carbon spectrum broadens significantly, showing signals indicative of $C-F_3$, $C-F_2$, C-F, and $C-CF_x$ bonding states, evidence of fluorocarbon polymer deposition. Together with the survey scan (Figure O-4c), the loss of detectable Si, emergence of F 1s peak, and broadening of the C 1s suggest that at lower bias powers a

fluorocarbon layer is deposited from reactive species within the plasma, a phenomenon seen previously in etch studies performed on silica films using fluoroalkane etchants.

Etch rate studies were performed in conjunction with optical emission spectroscopy (OES) on the three (low, medium, high carbon content) blanket thick films supplied by Intel using CF_4 and CHF_3 with 25%, and 50% additive H_2. The absolute intensity of the atomic fluorine emission peaks at 685.6 and 703.7nm (Figure O-5) were recorded at each of the plasma conditions. A noticeable increase in emission intensity at both wavelengths of atomic fluorine is observed for the CF_4 chemistry with 25% H_2 before decreasing steadily to a minimum intensity at 50% H_2 (Figure O-6a). Identical behavior can be seen in the etch rate across all three blank thick films (Figure O-6b), suggesting a correlation between the presence of fluorine radical and etch rate within the system.

Although not identical, the observed negative effect of hydrogen addition on the emission intensity of atomic fluorine for CHF_3 discharge also can be seen in the decreasing etch rate of all three films (Table O-6c). This overarching decrease could indicate that an optimal feed composition of hydrogen exists and must be examined through the use of smaller increments of additive H_2. OES studies of CHF_3 repeated under identical plasma conditions but with smaller increments of %H_2 are summarized in Figure O-7. A noticeable maximum in the intensity is seen at 10% H_2, warranting further investigation to determine if an optimized amount of hydrogen could further correlate to an increase in etch rate. Through the utilization of an 85 nm Ti hard mask, CF_4, CF_4 with 25% H_2, CHF_3, and CHF_3 with 25% H_2 were all successful in patterning the three levels of carbon doped silica while maintaining good profile features (Table O-3).

Despite developing a guideline for analyzing the reactions occurring between the gas and silica surfaces and screening various plasma chemistries, a key component is missing in terms of understanding the formation and deposition of polymeric species. A large part of future work will be devoted to developing a model for and experimentally probing the reactions occurring only within the gas phase itself. Use of the Gibbs minimization technique has so far been focused on equilibrium between the surface and gas phases. However, it is believed that thermodynamic analysis can be extended to model the gas phase, providing insight into which polymerizing species may be present. This information would a more complete understanding of the competing etch and deposition mechanisms.

Table O-1 Global warming potentials of various chemistries in semiconductor processes. The two etchants investigated in this work, CF_4 and CHF_3 and their respective environmental and emissions data are bolded.

Chemistries	Atmospheric conc. in 2015 (ppt)	Atmospheric conc. in 2005 (ppt)	Con. since 1994 & 1998 (ppt)	Annual emission in late 1990s (Gg)	Radiative efficiency (W/m²/ppb)	Lifetime (year)	Global Warming Potential
CO_2	403×10^6	379×10^6	358×10^6*	-	-	variable	1
CH_4	7×10^5	7×10^5	2×10^5*	-	-	12.2	21
N_2O	326×10^5	275×10^3	311×10^3*	-	-	120	310
$CHClF_2$	-	-	105×10^3*	-	-	12.1	1400
CF_4	76	74	-	~15	0.1	50,000	6500
CCl_2F_2	-	-	503×10^3*	-	-	102	7100
C_2F_6	-	2.9	3.4	~2	0.26	10,000	9200
CHF_3	21	18	22	~7	0.19	270	11700
SF_6	-	5.6	7.1	~6	0.52	3,200	23900
NH_3	-	-	-	0.054	-	2 hrs	0
NF_3	<0.1	-	-	~2.3	0.21	740	16800
C_2F_4	-	-	-	-	-	1.9 days	<1
C_6F_6	-	-	-	-	-		<1
CF_3I	-	-	-	-	-	2 days	1
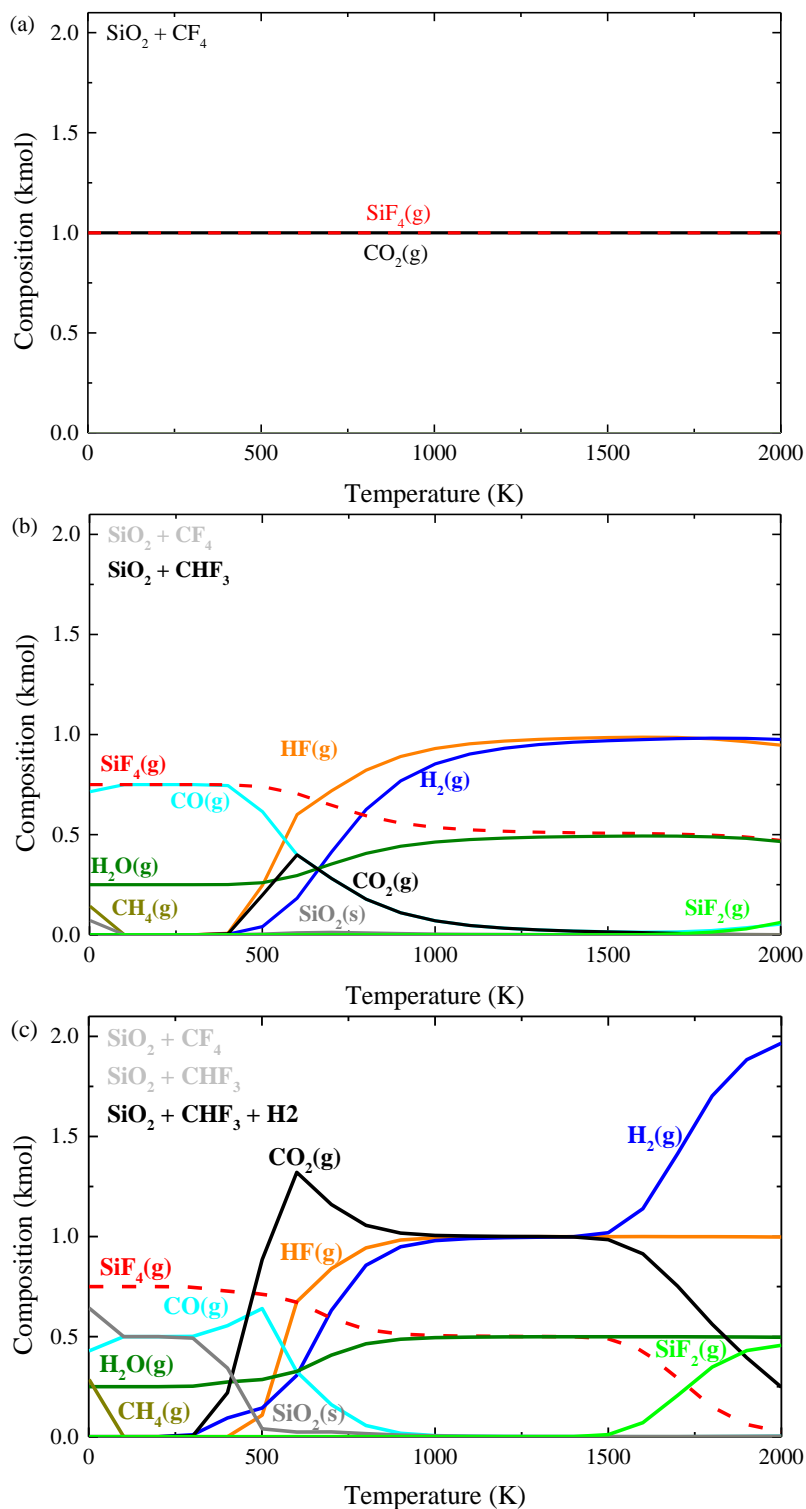
Figure O-1 Temperature-dependent product distribution of (a) SiO_2 + CF_4 (b) SiO_2 + CHF_3, and (c) SiO_2 + CHF_3 + H_2 as calculated through use of minimization of Gibbs free energy. Feed composition consists of 1 kmol of SiO_2, CF_4, CHF_3, and H_2 at 7.6 mTorr (10^{-5} atm).

Table O-2 Proposed surface-gas reactions for etching of silica species in CF_4 with H_2.

	Reaction	G (eV)
1	$SiO_2(c) + 2CF_4(g) \rightarrow SiF_4(g) + 2COF_2(g)$	-1.92
2	$2SiO_{1.5}CH_3(c) + 2CF_4(g) \rightarrow 2SiF_4(g) + COH_2(g) + CH_4(g) + 2CO(g)$	-5.24
3	$2SiOCH_2(c) + 2CF_4(g) \rightarrow 2SiF_4(g) + C_2H_4(g) + 2CO(g)$	-5.87
4	$SiO(CH_2)_2(c) + CF_4(g) \rightarrow SiF_4(g) + CO(g) + C_2H_4(g)$	-2.67
5	$SiOCH_2(c) + CF_4(g) + H_2(g) \rightarrow SiF_4(g) + CO(g) + CH_4(g)$	-3.82
6	$SiO(CH_2)_2(c) + CF_4(g) + 2H_2(g) \rightarrow SiF_4(g) + CO(g) + 2CH_4(g)$	-4.43
7	$2SiO_{1.5}C_2H(c) + 2CF_4(g) + 5H_2(g) \rightarrow 2SiF_4(g) + 3CO(g) + 3CH_4(g)$	-8.33
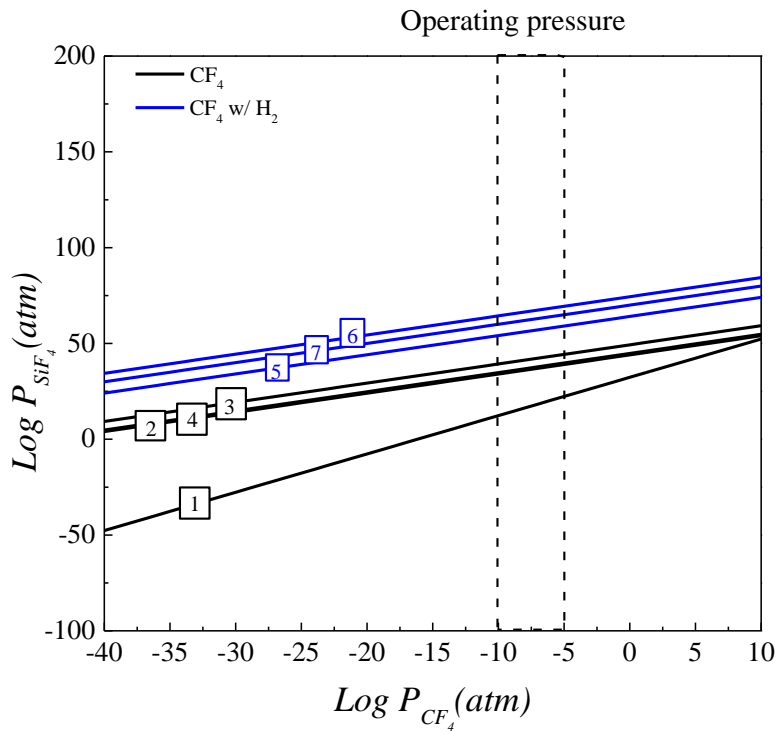
Figure O-2 Volatility diagram based upon reactions proposed in Table 2. Utilizing the Gibbs free energy of reaction allows for formulation of a functional relationship between the partial pressure of the etch product (SiF_4) and the etchant (CF_4).
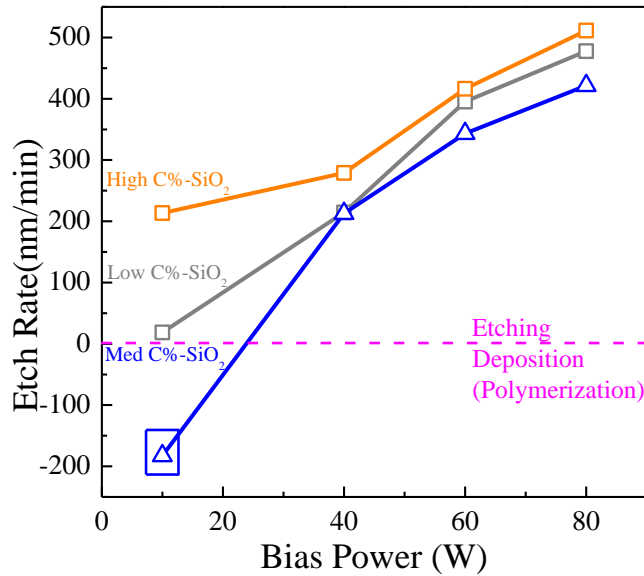
Figure O-3 A study of the effects of substrate bias power on the etch rates for all three (low, medium, and high) levels of carbon doped silica blank thick films. Deposition (negative etch rate values) occurs on the medium C%-SiO_2 at reduced bias powers suggesting that ion enhanced etch plays a significant role in a net etch of this material. XPS analysis was performed on the 1400W/10W condition and is shown below in blue.
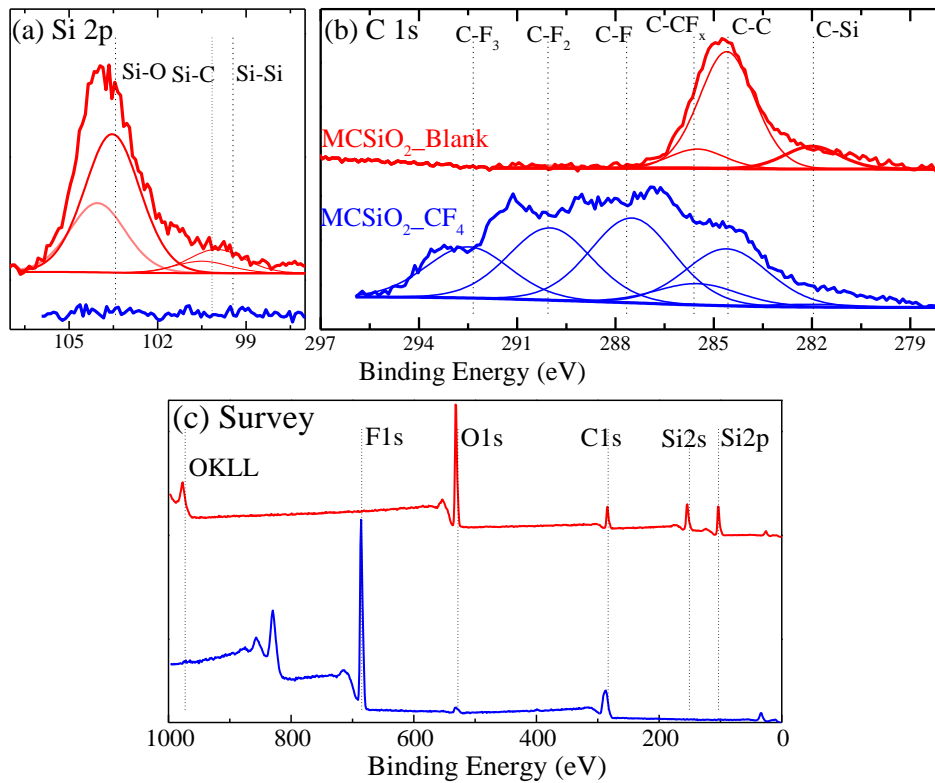
Figure O-4 XPS surface analysis of medium carbon doped silica blank thick film (red) and etched by pure CF_4 at 1400W with 10W bias (blue) showing (a) detailed Si 2p, (b) C 1s, and (c) Survey scans.

327
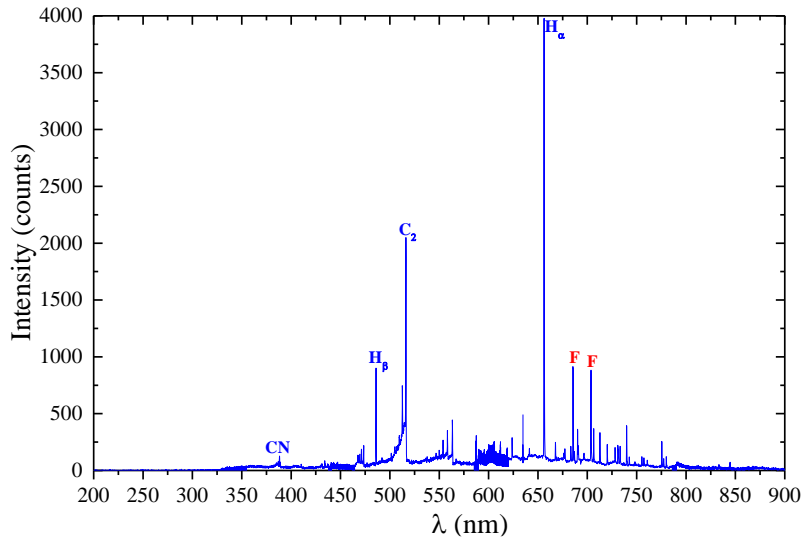
Figure O-5 Optical emission spectrum of CHF$_3$ plasma with 600W source power, 40W bias power, and operating pressure of 6 mTorr. Primary and secondary atomic fluorine emission peaks (highlighted in red) measured at 685.6 and 703.7 nm.
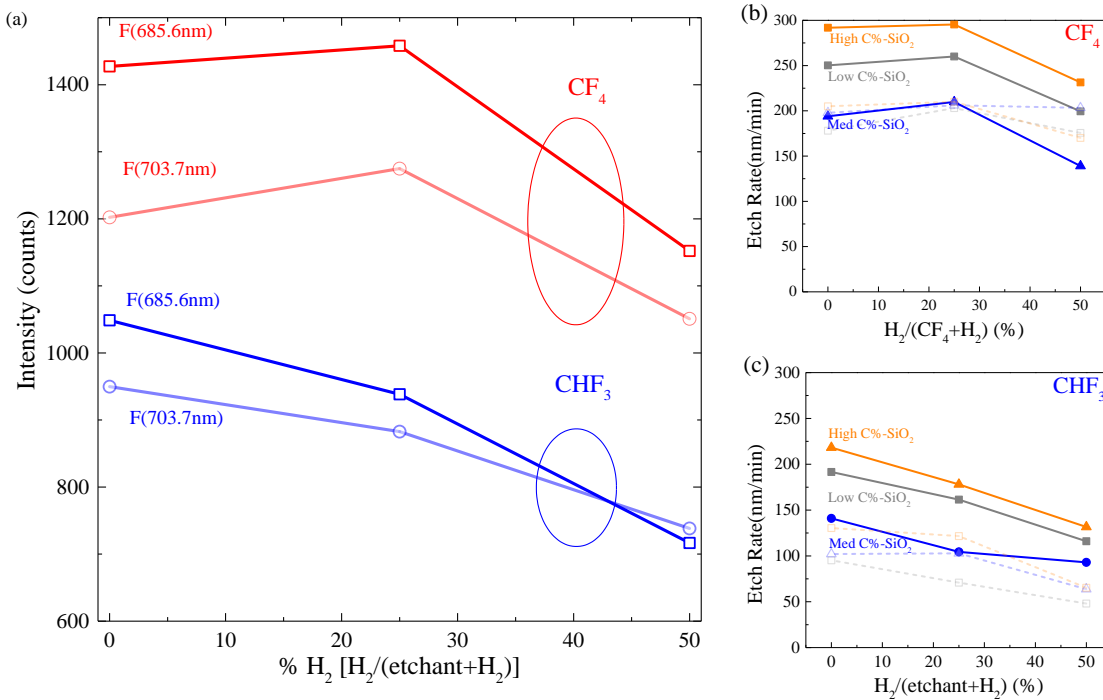
Figure O-6 (a) Atomic fluorine emission intensities at 685.6 and 703.7nm wavelengths as a function of %H$_2$ in feed gas for CF$_4$ (red) and CHF$_3$ (blue) at 600W source power and 40W bias power. (b) Etch rate as a function of %H$_2$ in CF$_4$. (c) Etch rate as a function of %H$_2$ in CHF$_3$.
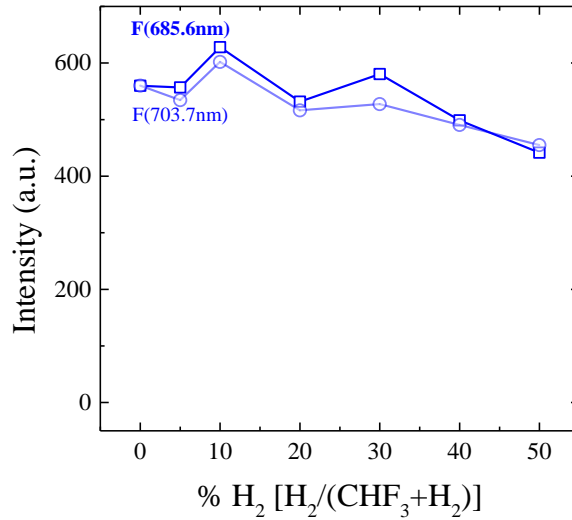
Figure O-7 Atomic fluorine intensities at 685.6 and 703.7nm wavelengths as a function of %H_2 in CHF_3 discharge at 600W source power and 40W bias power.

Table O-3 SEM images of etched carbon doped silica films in CF_4 and CHF_3 with 25% H_2 under 600W source power and 40W bias power.

	High C% doped SiO₂	Low C% doped SiO₂		Med. C% doped SiO₂
CF_4			CHF_3	
CF_4 / 25% H_2			CHF_3 / 25% H_2	

BIBLIOGRAPHY

Allender, D., J. Bray and J. Bardeen (1973). "Model for an Exciton Mechanism of Superconductivity." Physical Review B **7**(3): 1020-1029.

Amorim, J., H. S. Maciel and J. P. Sudano (1991). "High-Density Plasma Mode Of An Inductively Coupled Radio-Frequency Discharge." Journal Of Vacuum Science & Technology B **9**(2): 362-365.

Andriesse, M. S., T. Zijlstra and E. van der Drift (2000). "High speed anisotropic dry etching of CoNbZr for next generation magnetic recording." Journal of Vacuum Science & Technology B **18**(6): 3462-3466.

Andriesse, M. S. P., E. van der Drift and W. G. Sloof (2001). "High speed, dry etching of Fe for integration of magnetic devices in microelectronics." Journal of Vacuum Science & Technology B **19**(6): 2901-2905.

Antonov, V. E. (2002). "Phase transformations, crystal and magnetic structures of high-pressure hydrides of d-metals." Journal of Alloys and Compounds **330–332**(0): 110-116.

Apatiga, L. M. and V. M. Castano (2006). "Magnetic behavior of cobalt oxide films prepared by pulsed liquid injection chemical vapor deposition from a metal-organic precursor." Thin Solid Films **496**(2): 576-579.

Argyle, M. D. and C. H. Bartholomew (2015). "Heterogeneous Catalyst Deactivation and Regeneration: A Review." Catalysts **5**(1): 145-269.

Aspnes, D. E. (1982). "Optical-Properties of Thin-Films." Thin Solid Films **89**(3): 249-262.

Aston, F. W. (1920). "Isotopes and atomic weights." Nature **105**: 617-619.

Auciello, O. and D. L. Flamm (1989). Plasma Diagnostics: Discharge parameters and chemistry, Academic Press.

Axford, S. D. T., J. M. Goodings and A. N. Hayhurst (1998). "Mass-spectrometric sampling of ions from flames at atmospheric pressure: The effects of applied electric fields and the variation of electric potential in a flame." Combustion and Flame **114**(3-4): 294-302.

Aygen, S. and R. Vaneldik (1989). "A Spectroscopic and Mechanistic Study of the Enolization and Diol Formation of Hexafluoroacetylacetone in the Presence of Water and Alcohol." Chemische Berichte **122**(2): 315-320.

Baibich, M. N., J. M. Broto, A. Fert, F. N. Vandau, F. Petroff, P. Eitenne, G. Creuzet, A. Friederich and J. Chazelas (1988). "Giant Magnetoresistance of (001)Fe/(001) Cr Magnetic Superlattices." Physical Review Letters **61**(21): 2472-2475.

Bardeen, J., L. N. Cooper and J. R. Schrieffer (1957). "Theory of Superconductivity." Physical Review **108**(5): 1175-1204.

Barreca, D., C. Massignan, S. Daolio, M. Fabrizio, C. Piccirillo, L. Armelao and E. Tondello (2001). "Composition and microstructure of cobalt oxide thin films obtained from a novel cobalt(II) precursor by chemical vapor deposition." Chemistry of Materials **13**(2): 588-593.

Beck, W. (1965). "Infrared Spectra of Inorganic and Coordination Compounds." Kolloid-Zeitschrift and Zeitschrift Fur Polymere **202**(2): 171-&.

Behrisch, R. and W. Eckstein (2007). Sputtering by particle bombardment : experiments and computer calculations from threshold to MeV energies. Berlin ; New York, Springer.

Bennett, M. A., G. A. Heath, D. C. R. Hockless, I. Kovacik and A. C. Willis (1998). "Alkene complexes of divalent and trivalent ruthenium stabilized by chelation. Dependence of coordinated alkene orientation on metal oxidation state." Journal of the American Chemical Society **120**(5): 932-941.

Booth, J. P., O. Joubert, J. Pelletier and N. Sadeghi (1991). "Oxygen atom actinometry reinvestigated: Comparison with absolute measurements by resonance absorption at 130 nm." Journal of Applied Physics **69**(2): 618-626.

Booth, J. P. and N. Sadeghi (1991). "Oxygen and fluorine atom kinetics in electron cyclotron resonance plasmas by time-resolved actinometry." Journal of Applied Physics **70**(2): 611-620.

Braunstein, P. (2004). "Functional ligands and complexes for new structures, homogeneous catalysts and nanomaterials." Journal of Organometallic Chemistry **689**(24): 3953-3967.

Butler, W. H., X. G. Zhang, T. C. Schulthess and J. M. MacLaren (2001). "Spin-dependent tunneling conductance of Fe vertical bar MgO vertical bar Fe sandwiches." Physical Review B **63**(5).

Cabrera, N. and N. F. Mott (1948). "Theory of the Oxidation of Metals." Reports on Progress in Physics **12**: 163-184.

Caminati, W. and J. U. Grabow (2006). "The C-2v structure of enolic acetylacetone." Journal of the American Chemical Society **128**(3): 854-857.

Carcia, P. F., A. D. Meinhaldt and A. Suna (1985). "Perpendicular Magnetic-Anisotropy in Pd/Co Thin-Film Layered Structures." Applied Physics Letters **47**(2): 178-180.

Chae, H., S. A. Vitale and H. H. Sawin (2003). "Silicon dioxide etching yield measurements with inductively coupled fluorocarbon plasmas." Journal of Vacuum Science & Technology A: Vacuum, Surfaces, and Films **21**(2): 381-387.

Chase, M. W. (1998). NIST-JANAF Thermochemical Tables. Woodbury, New York, American Chemical Society
American Institute of Physics.

Chen, F. F. (2015). Introduction to Plasma Physics and Controlled Fusion, Springer International Publishing.

Cherrington, B. E. (1982). "The use of electrostatic probes for plasma diagnostics—A review." Plasma Chemistry and Plasma Processing **2**(2): 113-140.

Cho, H., K. P. Lee, K. B. Jung, S. J. Pearton, J. Marburger, F. Sharifi, Y. B. Hahn and J. R. Childress (2000). "Corrosion-free dry etch patterning of magnetic random access memory stacks: Effects of ultraviolet illumination." Journal of Applied Physics **87**(9): 6397-6399.

Cho, H. J., J. D. Choe, L. Ming, K. Jin Young, C. Sung Hoon, C. W. Oh, Y. Eun-Jung, K. Dong-Won, P. Donggun and K. Kim (2004). Fin width scaling criteria of body-tied FinFET in sub-50 nm regime. Device Research Conference, 2004. 62nd DRC.

Coburn, J. W. and M. Chen (1980). "Optical emission spectroscopy of reactive plasmas: A method for correlating emission intensities to reactive particle density." Journal of Applied Physics **51**(6): 3134-3136.

Coburn, J. W. and H. F. Winters (1979). "Ion-Assisted and Electron-Assisted Gas-Surface Chemistry - Important Effect in Plasma-Etching." Journal of Applied Physics **50**(5): 3189-3196.

Coburn, J. W. and H. F. Winters (1979). "Ion- and electron-assisted gas-surface chemistry—An important effect in plasma etching." J. Appl. Phys. **50**: 3189-3196.

Coburn, J. W. and H. F. Winters (1979). "Plasma etching—A discussion of mechanisms." J. Vac. Sci. Technol. **16**: 391-403.

Colinge, J. P., M. H. Gao, A. Romano-Rodriguez, H. Maes and C. Claeys (1990). Silicon-on-insulator 'gate-all-around device'. Electron Devices Meeting, 1990. IEDM '90.

Cruden, B. A., M. V. V. S. Rao, S. P. Sharma and M. Meyyappan (2002). "Neutral gas temperature estimate in CF4/O2/Ar inductively coupled plasmas." Applied Physics Letters **81**(6): 990-992.

Cui, J. P., Y. Z. He, S. Wang, J. Wang and B. C. Fan (2000). "Temperature measurement of reflected shock wave by using chemical indicator." Acta Mechanica Sinica **16**(1): 63-69.

Cullity, B. D. (1972). Introduction to magnetic materials. Reading, Mass.,, Addison-Wesley Pub. Co.

Czech, Z. and M. Wojciechowicz (2006). "The crosslinking reaction of acrylic PSA using chelate metal acetylacetonates." European Polymer Journal **42**(9): 2153-2160.

DeHoff, R. T. (1993). Thermodynamics in Materials Science. New York, McGraw-Hill.

Denbroeder, F. J. A., H. C. Donkersloot, H. J. G. Draaisma and W. J. M. Dejonge (1987). "Magnetic-Properties and Structure of Pd/Co and Pd/Fe Multilayers." Journal of Applied Physics **61**(8): 4317-4319.

Dennard, R. H., Gaenssle.Fh, H. N. Yu, V. L. Rideout, E. Bassous and A. R. Leblanc (1974). "Design of Ion-Implanted Mosfets with Very Small Physical Dimensions." Ieee Journal of Solid-State Circuits Sc **9**(5): 256-268.

Djayaprawira, D. D., K. Tsunekawa, M. Nagai, H. Maehara, S. Yamagata, N. Watanabe, S. Yuasa, Y. Suzuki and K. Ando (2005). "230% room-temperature magnetoresistance in CoFeB/MgO/CoFeB magnetic tunnel junctions." Applied Physics Letters **86**(9).

Donnelly, V. M. (1996). "A simple optical emission method for measuring percent dissociations of feed gases in plasmas: Application to Cl2 in a high-density helical resonator plasma." J. Vac. Sci. Technol. A **14**: 1076-1087.

Donnelly, V. M. and M. V. Malyshev (2000). "Diagnostics of inductively coupled chlorine plasmas: Measurements of the neutral gas temperature." Applied Physics Letters **77**(16): 2467.

Donnelly, V. M. and M. J. Schabel (2002). "Spatially resolved electron temperatures, species concentrations, and electron energy distributions in inductively coupled chlorine plasmas, measured by trace-rare gases optical emission spectroscopy." Journal of Applied Physics **91**(10): 6288.

Douglas, B. E., J. G. Brushmiller and R. A. Haines (1963). "Circular Dichroism of Coordination Compounds .1. Splitting Patterns for Potassium Ethylenediaminetetraacetatocobaltate(Iii) and Model Compounds." Inorganic Chemistry **2**(6): 1194-&.

Doyle, B. S., S. Datta, M. Doczy, S. Hareland, B. Jin, J. Kavalieros, T. Linton, A. Murthy, R. Rios and R. Chau (2003). "High performance fully-depleted tri-gate CMOS transistors." Electron Device Letters, IEEE **24**(4): 263-265.

Drews, T., J. Supel, A. Hagenbach and K. Seppelt (2006). "Solid state molecular structures of transition metal hexafluorides." Inorganic Chemistry **45**(9): 3782-3788.

Ellingham, H. (1944). "Transactions and Communications." Journal of the Society of Chemical Industry **63**(5): 125-160.

Evans, U. R. (1960). The corrosion and oxidation of metals; scientific principles and practical applications. London, E. Arnold.

Fahlman, B. D. and A. R. Barron (2000). "Substituent effects on the volatility of metal beta-diketonates." Advanced Materials for Optics and Electronics **10**(3-5): 223-232.

Farkas, J., K. M. Chi, M. J. Hampden-Smith, T. T. Kodas and L. H. Dubois (1993). "Etching of copper and copper oxide at high rates via generation of volatile copper species." Materials Science and Engineering: B **17**(1): 93-96.

Ferain, I., C. A. Colinge and J. P. Colinge (2011). "Multigate transistors as the future of classical metal-oxide-semiconductor field-effect transistors." Nature **479**(7373): 310-316.

Freindorf, M., C. M. Marian and B. A. Hess (1993). "Theoretical study of the electronic spectrum of the CoH molecule." J. Chem. Phys. **99**: 1215-1223.

Fu-Liang, Y., C. Hao-Yu, C. Fang-Cheng, H. Cheng-Chuan, C. Chang-Yun, C. Hsien-Kuang, L. Chi-Chuang, C. Chi-Chun, H. Huan-Tsung, C. Chih-Jian, T. Hun-Jan, Y. Yee-Chia, L. Mong-Song and H. Chenming (2002). 25 nm CMOS Omega FETs. Electron Devices Meeting, 2002. IEDM '02.

Fujiwara, H. (2007). Spectroscopic ellipsometry: principles and applications. Chichester, England; Hoboken, NJ, John Wiley & Sons.

Gajek, M., J. J. Nowak, J. Z. Sun, P. L. Trouilloud, E. J. O'Sullivan, D. W. Abraham, M. C. Gaidis, G. Hu, S. Brown, Y. Zhu, R. P. Robertazzi, W. J. Gallagher and D. C. Worledge (2012). "Spin torque switching of 20 nm magnetic tunnel junctions with perpendicular anisotropy." Appl. Phys. Lett. **100**(13): 132408.

Gajek, M., J. J. Nowak, J. Z. Sun, P. L. Trouilloud, E. J. O'Sullivan, D. W. Abraham, M. C. Gaidis, G. Hu, S. Brown, Y. Zhu, R. P. Robertazzi, W. J. Gallagher and D. C. Worledge (2012). "Spin torque switching of 20 nm magnetic tunnel junctions with perpendicular anisotropy." Applied Physics Letters **100**(13).

George, M. A., D. W. Hess, S. E. Beck, J. C. Ivankovits, D. A. Bohling and A. P. Lane (1995). "Reaction of 1,1,1,5,5,5-Hexafluoro-2,4-Pentanedione (H(+)Hfac) with Cuo, Cu2o, and Cu Films." Journal of the Electrochemical Society **142**(3): 961-965.

George, M. A., D. W. Hess, S. E. Beck, J. C. Ivankovits, D. A. Bohling and A. P. Lane (1995). "Reaction of 1,1,1,5,5,5-Hexafluoro-2,4-Pentanedione (H(+)Hfac) with Cuo, Cu2o, and Cu Films (Vol 142, Pg 961, 1995)." Journal of the Electrochemical Society **142**(5): 1732-1732.

George, M. A., D. W. Hess, S. E. Beck, K. Young, D. A. Bohling, G. Voloshin and A. P. Lane (1996). "Reaction of 1,1,1,5,5,5-hexafluoro-2,4-pentanedione (H(+)hfac) with iron and iron oxide thin films." Journal of the Electrochemical Society **143**(10): 3257-3266.

Gloersen, P. G. (1976). "Masking for Ion-Beam Etching." Solid State Technology **19**(4): 68-73.

Goodings, J. M., J. Z. Guo, A. N. Hayhurst and S. G. Taylor (2001). "Current-voltage characteristics in a flame plasma: analysis for positive and negative ions, with applications." International Journal of Mass Spectrometry **206**(1-2): 137-151.

Gorbenko, O. Y., A. R. Kaul, A. A. Molodyk, V. N. Fuflyigin, M. A. Novozhilov, A. A. Bosak, U. Krause and G. Wahl (1997). "MOCVD of perovskites with metallic conductivity." Journal of Alloys and Compounds **251**(1-2): 337-341.

Greenwood, N. N. and A. Earnshaw (1984). Chemistry of the elements. Oxford, Oxfordshire; New York, Pergamon Press.

Greenwood, N. N. and A. Earnshaw (1998). Chemistry of the elements, 2nd ed. Oxford; Boston, Butterworth-Heinemann.

Gshneider, K. A. (1964). In Solid State Physics. New York, Academic Press.

Gulbranse, E. A. and S. A. Jansson (1972). "High-Temperature Oxidation, Reduction, and Volatilization Reactions of Silicon and Silicon-Carbide." Oxidation of Metals **4**(3): 181-&.

Gulbransen, E. A. (1970). "Thermochemistry and Oxidation of Refractory Metals at High Temperature." Corrosion **26**(1): 19-&.

Habeeb, J. J., D. G. Tuck and F. H. Walters (1978). "Direct Electrochemical Synthesis of Some Metal Chelate Complexes." Journal of Coordination Chemistry **8**(1): 27-33.

Hagström, S., C. Nordling and K. Siegbahn (1964). "Electron spectroscopy for chemical analyses." Physics Letters **9**(3): 235.

Haines, R. A. and B. E. Douglas (1965). "Circular Dichroism of Coordination Compounds .V. Pentadentate Ethylenediaminetetraacetic Acid Complexes of Cobalt(3)." Inorganic Chemistry **4**(4): 452-&.

Hamid, M., M. Zeller, A. D. Hunter, M. Mazhar and A. A. Tahir (2005). "Redetermination of bis(2,4-pentanedionato)-palladium(II)." Acta Crystallographica Section E-Structure Reports Online **61**: M2181-M2183.

Hampdensmith, M. J. and T. T. Kodas (1995). "Chemical-Vapor-Deposition of Copper from (Hfac)CuI Compounds." Polyhedron **14**(6): 699-732.

Harper, J. M. E., J. J. Cuomo and H. R. Kaufman (1982). "Technology and Applications of Broad-Beam Ion Sources Used in Sputtering .2. Applications." Journal of Vacuum Science & Technology **21**(3): 737-756.

Hauffe, K. (1965). Oxidation of metals. New York,, Plenum Press.

Henne, A. L., M. S. Newman, L. L. Quill and R. A. Staniforth (1947). "The Alkaline Condensation of Fluorinated Esters with Esters and Ketones." Journal of the American Chemical Society **69**(7): 1819-1820.

Hidaka, J. and B. E. Douglas (1964). "Circular Dichroism of Coordination Compounds .2. Some Metal Complexes of 2,2]-Dipyridyl + 1,10-Phenanthroline." Inorganic Chemistry **3**(8): 1180-&.

Hidaka, J. and B. E. Douglas (1964). "Circular Dichroism of Coordination Compounds .4. Some Metal Complexes with Dithiooxalic Acid." Inorganic Chemistry **3**(12): 1724-&.

Ho, C. S., C. W. Lam, M. H. Chan, R. C. Cheung, L. K. Law, L. C. Lit, K. F. Ng, M. W. Suen and H. L. Tai (2003). "Electrospray ionisation mass spectrometry: principles and clinical applications." Clin Biochem Rev **24**(1): 3-12.

Hopwood, J. (1992). "Review of inductively coupled plasmas for plasma processing." Plasma Sources Science and Technology **1**(2): 109.

Hsiao, R. (1999). "Fabrication of magnetic recording heads and dry etching of head materials." IBM Journal of Research and Development **43**(1-2): 89-102.

Huang, X., W. Lee, C. Kuo, D. Hisamoto, L. Chang, J. Kedzierski, E. Anderson, H. Takeuchi, Y. Choi, K. Asano, V. Subramanian, T. J. King, J. Bokor and C. Hu (1999). "Sub 50-nm FinFET: PMOS " IEEE Electron Device Letters **99**: 67.

Ikeda, S., J. Hayakawa, Y. Ashizawa, Y. M. Lee, K. Miura, H. Hasegawa, M. Tsunoda, F. Matsukura and H. Ohno (2008). "Tunnel magnetoresistance of 604% at 300 K by suppression of Ta diffusion in CoFeB/MgO/CoFeB pseudo-spin-valves annealed at high temperature." Applied Physics Letters **93**(8).

Ikeda, S., J. Hayakawa, Y. M. Lee, F. Matsukura, Y. Ohno, T. Hanyu and H. Ohno (2007). "Magnetic tunnel junctions for spintronic memories and beyond." IEEE Transactions on Electron Devices **54**(5): 991-1002.

Ikeda, S., K. Miura, H. Yamamoto, K. Mizunuma, H. D. Gan, M. Endo, S. Kanai, J. Hayakawa, F. Matsukura and H. Ohno (2010). "A perpendicular-anisotropy CoFeB-MgO magnetic tunnel junction." Nature Materials **9**(9).

Isakova, V. G., I. A. Baidina, N. B. Morozova and I. K. Igumenov (2000). "gamma-Halogenated iridium(III) acetylacetonates." Polyhedron **19**(9): 1097-1103.

ITRS(2011) "Emerging Research Devices (ERD)." International Technology Roadmap for Semiconductors.

Jablonski, A. and C. J. Powell (2002). "The electron attenuation length revisited." Surface Science Reports **47**(2-3): 35-91.

Jain, A., T. T. Kodas and M. J. HampdenSmith (1995). "Thermal dry-etching of copper using hydrogen peroxide and hexafluoroacetylacetone." Thin Solid Films **269**(1-2): 51-56.

Jaklevic, R. C., A. H. Silver, J. Lambe and J. E. Mercereau (1964). "Quantum Interference Effects in Josephson Tunneling." Physical Review Letters **12**(7): 159-&.

Jensen, A. W. and B. A. O'Brien (2001). "Simple preparation and NMR analysis of mer and fac isomers of tris(1,1,1-trifluoro-2,4-pentanedionato)cobalt(III) - An experiment for the inorganic chemistry laboratory." Journal of Chemical Education **78**(7): 954-955.

Jones, S. W. (2004). "Exponential trends in the integrated circuits industry." ICKnowledge.

Jong-Tae, P., J. Colinge and C. H. Diaz (2001). "Pi-Gate SOI MOSFET." Electron Device Letters, IEEE **22**(8): 405-406.

Jung, K. B., H. Cho, Y. B. Hahn, D. C. Hays, E. S. Lambers, Y. D. Park, T. Feng, J. R. Childress and S. J. Pearton (1999). "Comparison of Cl-2/He, Cl-2/Ar, and Cl-2/Xe plasma chemistries for dry etching of NiFe and NiFeCo." Journal of the Electrochemical Society **146**(4): 1465-1468.

Jung, K. B., J. Hong, H. Cho, S. Onishi, D. Johnson, Y. D. Park, J. R. Childress and S. J. Pearton (1999). "Parametric study of NiFe and NiFeCo high density plasma etching using CO/NH3." Journal of the Electrochemical Society **146**(6): 2163-2168.

Jung, K. B., J. Hong, H. Cho, S. Onishi, D. Johnson, Y. D. Park, J. R. Childress and S. J. Pearton (1999). "Patterning of NiFe and NiFeCo in CO/NH3 high density plasmas." Journal of Vacuum Science & Technology a-Vacuum Surfaces and Films **17**(2): 535-539.

Jung, K. B., E. S. Lambers, J. R. Childress, S. J. Pearton, M. Jenson and A. T. Hurst (1997). "High rate dry etching of Ni0.8Fe0.2 and NiFeCo." Applied Physics Letters **71**(9): 1255-1257.

Kang, S. W., H. U. Kim and S. W. Rhee (1999). "Dry etching of copper film with hexafluoroacetylacetone via oxidation process." Journal of Vacuum Science & Technology B **17**(1): 154-157.

Kastenmeier, B. E. E., P. J. Matsuo, J. J. Beulens and G. S. Oehrlein (1996). "Chemical dry etching of silicon nitride and silicon dioxide using CF4/O-2/N-2 gas mixtures." Journal Of Vacuum Science & Technology A-Vacuum Surfaces And Films **14**(5): 2802-2813.

Kaufman, H. R. (1978). "Technology of Ion-Beam Sources Used in Sputtering." Journal of Vacuum Science & Technology **15**(2): 272-276.

Kaufman, H. R., J. J. Cuomo and J. M. E. Harper (1982). "Technology and Applications of Broad-Beam Ion Sources Used in Sputtering .1. Ion-Source Technology." Journal of Vacuum Science & Technology **21**(3): 725-736.

Kaufman, H. R., J. M. E. Harper and J. J. Cuomo (1979). "Focused Ion-Beam Designs for Sputter Deposition." Journal of Vacuum Science & Technology **16**(2): 179-180.

Kaufman, H. R., J. M. E. Harper and J. J. Cuomo (1979). "Focused Ion-Beam Designs for Sputter Deposition." Journal of Vacuum Science & Technology **16**(3): 899-905.

Kiihamaki, J. and S. Franssila (1999). "Pattern shape effects and artefacts in deep silicon etching." Journal Of Vacuum Science & Technology A-Vacuum Surfaces And Films **17**(4): 2280-2285.

Kinoshita, K., H. Utsumi, K. Suemitsu, H. Hada and T. Sugibayashi (2010). "Etching Magnetic Tunnel Junction with Metal Etchers." Jpn. J. Appl. Phys. **49**.

Kinoshita, K., K. Yamada and H. Matsutera (1991). "Reactive ion etching of Fe-Si-Al alloy for thin film head." IEEE T. Magn. **27**: 4888-4890.

Kittel, C. (1948). "On the Theory of Ferromagnetic Resonance Absorption." Physical Review **73**(2): 155-161.

Kleiner, R., D. Koelle, F. Ludwig and J. Clarke (2004). "Superconducting quantum interference devices: State of the art and application's." Proceedings of the Ieee **92**(10): 1534-1548.

Kortshagen, U., N. D. Gibson and J. E. Lawler (1996). "On the E - H mode transition in RF inductive discharges." Journal of Physics D: Applied Physics **29**(5): 1224.

Kruck, T. and M. Schober (1997). "Low-temperature dry etching of copper using a new chemical approach." Microelectronic Engineering **37-8**(1-4): 121-126.

Kulkarni, N. S. and R. T. DeHoff (2002). "Application of Volatility Diagrams for Low Temperature, Dry Etching, and Planarization of Copper." J. Electrochem. Soc. **149**: G620-G632.

Kulkarni, N. S. and R. T. DeHoff (2002). "Application of volatility diagrams for low temperature, dry etching, and planarization of copper." Journal of the Electrochemical Society **149**(11): G620-G632.

Laegreid, N. and G. K. Wehner (1961). "Sputtering Yields of Metals for Ar+ and Ne+ Ions with Energies from 50 to 600 Ev." Journal of Applied Physics **32**(3): 365-&.

Lamprey, H. (1960). "Properties and Applications of Metal Acetylacetonates." Annals of the New York Academy of Sciences **88**(2): 519-525.

Layadi, N., V. M. Donnelly and J. T. C. Lee (1997). "Cl-2 plasma etching of Si(100): Nature of the chlorinated surface layer studied by angle-resolved x-ray photoelectron spectroscopy." Journal of Applied Physics **81**(10): 6738-6748.

Lee, H., Y.-H. A. Wang, C. K. A. Mewes, W. H. Butler, T. Mewes, S. Maat, B. York, M. J. Carey and J. R. Childress (2009). "Magnetization relaxation and structure of CoFeGe alloys." Applied Physics Letters **95**(8): -.

Lee, J. M., K. M. Chang, I. H. Lee and S. J. Park (2000). "Cl2 - Based Dry Etching of GaN and InGaN Using Inductively Coupled Plasma The Effects of Gas Additives." J. Electrochem. Soc. **147**: 1859-1863.

Lee, R. E. (1979). "Microfabrication by Ion-Beam Etching." Journal of Vacuum Science & Technology **16**(2): 164-170.

Lee, W. T., L. Ford, P. Blowers, H. L. Nigg and R. I. Masel (1998). "Why do heats of adsorption of simple gases on platinum surfaces vary so little with surface structure?" Surface Science **416**(1-2): 141-151.

Leskela, M. and M. Ritala (2002). "Atomic layer deposition (ALD): from precursors to thin film structures." Thin Solid Films **409**(1): 138-146.

Lide, D. R. (1995). CRC Handbook of Chemistry and Physics. New York, CRC Press.

Lin, W.-C., C.-J. Tsai, B.-Y. Wang, C.-H. Kao and W.-F. Pong (2013). "Hydrogenation induced reversible modulation of perpendicular magnetic coercivity in Pd/Co/Pd films." Applied Physics Letters **102**(25): -.

Litvak, H. E. (1996). End point control via optical emission spectroscopy. The 3rd International Workshop on Advanced Plasma Tools for Etching, Chemical Vapor Deposition, and Plasma Vapor Deposition: Sources, Process Control, and Diagnostics, San Jose, California (USA), AVS.

Liu, C. T. and B. E. Douglas (1964). "Circular Dichroism of Coordination Compounds .3. Cobalt(3) Complexes of Optically Active Amino Acids." Inorganic Chemistry **3**(10): 1356-&.

Liu, X., W. Zhang, M. J. Carter and G. Xiao (2011). "Ferromagnetic resonance and damping properties of CoFeB thin films as free layers in MgO-based magnetic tunnel junctions." Journal of Applied Physics **110**(3): -.

Lou, V. L. K., T. E. Mitchell and A. H. Heuer (1985). "Graphical Displays of the Thermodynamics of High-Temperature Gas-Solid Reactions and Their Application to Oxidation of Metals and Evaporation of Oxides." Journal of the American Ceramic Society **68**(2): 49-58.

Lou, V. L. K., T. E. Mitchell and A. H. Heuer (1985). "REVIEW—Graphical Displays of the Thermodynamics of High-Temperature Gas-Solid Reactions and Their Application to Oxidation of Metals and Evaporation of Oxides." J. Am. Ceram. Soc. **68**: 49-58.

Luo, Y.-R. (2003). Handbook of bond dissociation energies in organic compounds. Boca Raton, Fla., CRC Press.

Malyshev, M. V. and V. M. Donnelly (2000). "Diagnostics of chlorine inductively coupled plasmas. Measurement of electron temperatures and electron energy distribution functions." Journal of Applied Physics **87**(4): 1642.

Malyshev, M. V. and V. M. Donnelly (2001). "Diagnostics of inductively coupled chlorine plasmas: Measurement of electron and total positive ion densities." Journal of Applied Physics **90**(3): 1130.

Mane, A. U., K. Shalini, A. Wohlfart, A. Devi and S. A. Shivashankar (2002). "Strongly oriented thin films of Co3O4 deposited on single-crystal MgO(100) by low-pressure, low-temperature MOCVD." Journal of Crystal Growth **240**(1-2): 157-163.

Maruyama, T. and T. Nakai (1991). "Cobalt Oxide Thin-Films Prepared by Chemical Vapor-Deposition from Cobalt(Ii) Acetate." Solar Energy Materials **23**(1): 25-29.

Mathon, J. and A. Umerski (2001). "Theory of tunneling magnetoresistance of an epitaxial Fe/MgO/Fe(001) junction." Physical Review B **63**(22).

Mayne, K. I. (1952). "MASS SPECTROMETRY." Reports on Progress in Physics **15**: 24-48.

Mcbride, J. R., G. W. Graham, C. R. Peters and W. H. Weber (1991). "Growth and Characterization of Reactively Sputtered Thin-Film Platinum Oxides." Journal of Applied Physics **69**(3): 1596-1604.

McNevin, S. C. and G. E. Becker (1985). "Investigation of kinetic mechanism for the ion-assisted etching of Si in Cl2." J. Vac. Sci. Technol. B **3**: 485-491.

Merlino, R. L. (2007). "Understanding Langmuir probe current-voltage characteristics." American Journal of Physics **75**(12): 1078-1085.

Miyazaki, T. and N. Tezuka (1995). "Giant Magnetic Tunneling Effect in Fe/Al2o3/Fe Junction." Journal of Magnetism and Magnetic Materials **139**(3): L231-L234.

Miyoshi, Y., Z. L. Petrovic and T. Makabe (2002). "Transition between capacitive and inductive mode in inductively coupled plasma observed by emission computerized tomography." Ieee Transactions On Plasma Science **30**(1): 130-131.

Moore, G. E. (1965). "Cramming more components onto integrated circuits." Electronics **8**: 114-117.

Moore, G. E. (1998). "Cramming more components onto integrated circuits (Reprinted from Electronics, pg 114-117, April 19, 1965)." Proceedings of the IEEE **86**(1): 82-85.

Mosquera, A., D. Horwat, L. Vazquez, A. Gutierrez, A. Erko, A. Anders, J. Andersson and J. L. Endrino (2012). "Thermal decomposition and fractal properties of sputter-deposited platinum oxide thin films." Journal of Materials Research **27**(5): 829-836.

Mott-Smth, H. M. and I. Langmuir (1926). "The theory of collectors in gaseous discharges." Physical Review **28**(4): 0727-0763.

Mott, N. F. (1940). "The theory of the formation of protective oxide films on metals, II." Transactions of the Faraday Society **35**(3): 0472-0482.

Nakatani, I. (1996). "Ultramicro fabrications on Fe-Ni alloys using electron-beam writing and reactive-ion etching." IEEE Transactions on Magnetics **32**(5): 4448-4451.

Nigg, H. L., L. P. Ford and R. I. Masel (1999). "The surface chemistry of 1,1,1-trifluoro-2,4-pentanedione on clean and oxygen pre-covered Cu(210) - A comparison with 1,1,1,5,5,5-hexafluoro-2,4-pentanedione and 2,4-pentanedione surface chemistry on the same surfaces." Surface Science **419**(2-3): 97-103.

Nigg, H. L. and R. I. Masel (1998). "The surface chemistry of hexafluoroacetylacetone on clean and oxygen pre-covered Cu(210): a temperature-programmed desorption study." Surface Science **409**(3): 428-434.

Nigg, H. L. and R. I. Masel (1998). "Surface reaction mechanisms of trifluoracetylacetone on clean and pre-oxidized Ni(110): An example where etching chemistry does not follow volatility trends." Journal of Vacuum Science & Technology a-Vacuum Surfaces and Films **16**(6): 3259-3265.

Nigg, H. L. and R. I. Masel (1999). "Surface reaction pathways of 1,1,1,5,5,5-hexafluoro-2,4-pentanedione on clean and pre-oxidized Ni(110) surfaces." Journal of Vacuum Science & Technology A **17**(6): 3477-3480.

Niu, H. and R. S. Houk (1996). "Fundamental aspects of ion extraction in inductively coupled plasma mass spectrometry." Spectrochimica Acta Part B-Atomic Spectroscopy **51**(8): 779-815.

Okano, K., T. Izumida, H. Kawasaki, A. Kaneko, A. Yagishita, T. Kanemura, M. Kondo, S. Ito, N. Aoki, K. Miyano, T. Ono, K. Yahashi, K. Iwade, T. Kubota, T. Matsushita, I. Mizushima, S. Inaba, K. Ishimaru, K. Suguro, K. Eguchi, Y. Tsunashima and H. Ishiuchi (2005). Process integration technology and device characteristics of CMOS FinFET on bulk silicon substrate with sub-10 nm fin width and 20 nm gate length. Electron Devices Meeting, 2005. IEDM Technical Digest. IEEE International.

Ono, K. and M. Tuda (1997). Profile evolution during cold plasma beam etching of silicon.

Ordal, M. A., R. J. Bell, R. W. Alexander, L. L. Long and M. R. Querry (1985). "Optical properties of fourteen metals in the infrared and far infrared: Al, Co, Cu, Au, Fe, Pb, Mo, Ni, Pd, Pt, Ag, Ti, V, and W." Applied Optics **24**(24): 4493-4499.

Orland, A. S. and R. Blumenthal (2005). "Magnetic metal etching with organic based plasmas. I. CO/H-2 plasmas." Journal of Vacuum Science & Technology B **23**(4): 1589-1596.

Orland, A. S. and R. Blumenthal (2005). "Metal etching with organic based plasmas. II. CO/NH3 plasmas." Journal of Vacuum Science & Technology B **23**(4): 1597-1602.

Osaka, T., T. Yokoshima, D. Shiga, K. Imai and K. Takashima (2003). "A High Moment CoFe Soft Magnetic Thin Film Prepared by Electrodeposition." Electrochemical and Solid-State Letters **6**(4): C53-C55.

Palik, E. D. (1985). Handbook of optical constants of solids. Orlando, Academic Press.

Palik, E. D. (1991). Handbook of optical constants of solids II. Boston, Academic Press.

Palik, E. D. and G. Ghosh (1998). Handbook of optical constants of solids. San Diego, Academic Press.

Parkin, S., X. Jiang, C. Kaiser, A. Panchula, K. Roche and M. Samant (2003). "Magnetically engineered spintronic sensors and memory." Proceedings of the IEEE **91**(5): 661-680.

Patterson, D., T. Anderson, N. Cardwell, R. Fromm, K. Keeton, C. Kozyrakis, R. Thomas and K. Yelick (1997). "A case for intelligent RAM." Micro, IEEE **17**(2): 34-44.

Perry, W. L., A. Jain, T. T. Kodas and M. J. Hampdensmith (1995). "Selective Chemical-Vapor-Deposition on Excimer-Laser-Patterned Polytetrafluoroethylene from Hexafluoroacetylacetonate Copper(I) Vinyltrimethylsilane." Thin Solid Films **262**(1-2): 7-11.

Pettiford, C., A. Zeltser, S. D. Yoon, V. G. Harris, C. Vittoria and N. X. Sun (2006). "Effective Anisotropy Fields and Ferromagnetic Resonance Behaviors of CoFe/PtMn/CoFe Trilayers." Magnetics, IEEE Transactions on **42**(10): 2993-2995.

Phillips, S. L. and D. L. Perry (1995). <u>Handbook of inorganic compounds</u>, Boca Raton : CRC Press.

Pierson, H. O. (1999). <u>Handbook of chemical vapor deposition</u>. Norwich, NY, Noyes Publications.

Sbiaa, R., H. Meng and S. N. Piramanayagam (2011). "Materials with perpendicular magnetic anisotropy for magnetic random access memory." <u>Physica Status Solidi-Rapid Research Letters</u> **5**(12): 413-419.

Schennach, F. (2012). <u>Oxidation of Two Different Pt-Aluminised Bond Coats</u>. Doctor of Philosophy, University of Birmingham.

Senocq, F., M. Urrutigoity, Y. Caubel, J. P. Gorrichon and A. Gleizes (1999). "Preliminary studies of Ni(dmen)(2)(CF3CO2)(2), Ni(deen)(2)(CF3CO2)(2) and Ni(en)(CF3C(O)CHC(O)CF3)(2) as precursors for metalorganic chemical vapour deposition: structures, thermal behaviours and vapour pressures." <u>Inorganica Chimica Acta</u> **288**(2): 233-238.

Sha, L. and J. P. Chang (2004). "Plasma etching of high dielectric constant materials on silicon in halogen chemistries." <u>Journal Of Vacuum Science & Technology A</u> **22**(1): 88-95.

Shalhoub, G. M. (1980). "Co(Acac)3 - Synthesis, Reactions, and Spectra - an Experiment for General-Chemistry." <u>Journal of Chemical Education</u> **57**(7): 525-528.

Siegbahn, K., E. F. Barnett, Fellnerf.H and D. Hammond (1972). "Electron Spectroscopy With Monochromatized X-Rays." <u>Science</u> **176**(4032): 245-&.

Silver, A. H. and Zimmerma.Je (1967). "Quantum States and Transitions in Weakly Connected Superconducting Rings." <u>Physical Review</u> **157**(2): 317-&.

Slaughter, J. M. (2009). "Materials for Magnetoresistive Random Access Memory." <u>Annual Review of Materials Research</u> **39**: 277-296.

Sletten, G. and P. Knudsen (1972). "Preparation of Isotope Targets by Heavy-Ion Sputtering." <u>Nuclear Instruments & Methods</u> **102**(3): 459-&.

Smith, H. I., Melngail.J, Williams.Rc and W. T. Brogan (1973). "Ion-Beam Etching of Surface Gratings." <u>Journal of Vacuum Science & Technology</u> **10**(6): 1127-1127.

Smith, W. R. (1996). "HSC chemistry for Windows, 2.0." <u>Journal of Chemical Information and Computer Sciences</u> **36**(1): 151-152.

Steger, R. and R. Masel (1999). "Chemical vapor etching of copper using oxygen and 1,1,1,5,5,5-hexafluoro-2,4-pentanedione." <u>Thin Solid Films</u> **342**(1-2): 221-229.

Steinbrüchel, C. (1985). "A simple formula for low-energy sputtering yields." <u>Appl. Phys. A-Mater</u> **36**: 37-42.

Stuart, R. V. and G. K. Wehner (1962). "Sputtering Yields at Very Low Bombarding Ion Energies." Journal of Applied Physics **33**(7): 2345-&.

Sun, J. Z. (2000). "Spin-current interaction with a monodomain magnetic body: A model study." Physical Review B **62**(1): 570-578.

Tamirisa, P. A., G. Levitin, N. S. Kulkarni and D. W. Hess (2007). "Plasma etching of copper films at low temperature." Microelectronic Engineering **84**(1): 105-108.

Tamirisa, P. A., G. Levitin, N. S. Kulkarni and D. W. Hess (2007). "Plasma etching of copper films at low temperature." Microelectron. Eng. **84**: 105-108.

Tanuma, S., C. J. Powell and D. R. Penn (1994). "Calculations of Electron Inelastic Mean Free Paths .5. Data for 14 Organic-Compounds over the 50-2000 Ev Range." Surface and Interface Analysis **21**(3): 165-176.

Thomas, M. E., M. P. Hartnett and J. E. Mckay (1988). "The Use of Surface Profilometers for the Measurement of Wafer Curvature." Journal of Vacuum Science & Technology a-Vacuum Surfaces and Films **6**(4): 2570-2571.

Tiitta, M. and L. Niinistou (1997). "Volatile Metal β-Diketonates: ALE and CVD precursors for electroluminescent device thin films." Chemical Vapor Deposition **3**(4): 167-182.

Tompkins, H. G. and W. A. McGahan (1999). Spectroscopic ellipsometry and reflectometry: a user's guide. New York, Wiley.

Vandelft, F. C. M. J. M. (1995). "Structuring Magnetic Thin-Films by Means of Plasma-Etching." Journal of Magnetism and Magnetic Materials **140**: 2203-2204.

Wagner, C. (1958). "Passivity during the Oxidation of Silicon at Elevated Temperatures." J. Appl. Phys. **29**: 1295-1297.

Wagner, C. (1969). "Distribution of Cations in Metal Oxide and Metal Sulphide Solid Solutions Formed during Oxidation of Alloys." Corrosion Science **9**(2): 91-&.

Wang, D. X., C. Nordman, J. M. Daughton, Z. H. Qian and J. Fink (2004). "70% TMR at room temperature for SDT sandwich junctions with CoFeB as free and reference layers." IEEE Transactions on Magnetics **40**(4): 2269-2271.

Wang, J., Y. Yun and E. I. Altman (2007). "The plasma oxidation of Pd(100)." Surface Science **601**(16): 3497-3505.

Weast, R. C. (1988). CRC handbook of chemistry and physics. Boca Raton, FL, CRC Press.

Wolf, R. E. (2005). What is ICP-MS? … and more importantly, what can it do? . I. PerkinElmer. PerkinElmer, Inc., USGS/CR/CICT.

343

Wu, F., G. Levitin and D. W. Hess (2010). "Low-Temperature Etching of Cu by Hydrogen-Based Plasmas." <u>ACS Applied Materials & Interfaces</u> **2**: 2175-2179.

Wu, F., G. Levitin and D. W. Hess (2010). "Patterning of Cu Films by a Two-Step Plasma Etching Process at Low Temperature." <u>J. Electrochem. Soc.</u> **157**: H474-H478.

Wu, F., G. Levitin and D. W. Hess (2011). "Mechanistic considerations of low temperature hydrogen-based plasma etching of Cu." <u>J. Vac. Sci. Technol. B</u> **29**: 011013.

Xue, Z. G., J. C. Daran, Y. Champouret and R. Poli (2011). "Ligand Adducts of Bis(acetylacetonato)iron(II): A H-1 NMR Study." <u>Inorganic Chemistry</u> **50**(22): 11543-11551.

Yakushiji, K., T. Saruya, H. Kubota, A. Fukushima, T. Nagahama, S. Yuasa and K. Ando (2010). "Ultrathin Co/Pt and Co/Pd superlattice films for MgO-based perpendicular magnetic tunnel junctions." <u>Applied Physics Letters</u> **97**(23).

Yinon, J. and F. S. Klein (1971). "The quadrupole and its applications in vacuum technology and mass spectrometry." <u>Vacuum</u> **21**(9): 379-383.

You, J. Q. and F. Nori (2011). "Atomic physics and quantum optics using superconducting circuits." <u>Nature</u> **474**(7353): 589-597.

Yuasa, S., T. Nagahama, A. Fukushima, Y. Suzuki and K. Ando (2004). "Giant room-temperature magnetoresistance in single-crystal Fe/MgO/Fe magnetic tunnel junctions." <u>Nature Materials</u> **3**(12): 868-871.

Zhang, B., R. J. Wang, D. Q. Zhao, M. X. Pan and W. H. Wang (2004). "Properties of Ce-based bulk metallic glass-forming alloys." <u>Physical Review B</u> **70**(22).

Zheng, Y., R. Zhang and L. Chen (2012). Ellipsometry and Its Applications in Stoichiometry. <u>Ellipsometry and Its Applications in Stoichiometry, Stoichiometry and Materials Science - When Numbers Matter</u>. D. A. Innocenti, InTech**:** 49.

Zollner, S. (2000). "Ellipsometry of Platinum Films on Silicon." <u>Physica Status Solidi (A)</u> **177**(2): r7-r8.